Physicochemical characterization and biocompatibility studies of persistent luminescence nanoparticles for preclinical diagnosis applications

A doctoral thesis submitted to

Universidad de Guanajuato
Campus Guanajuato
División de Ciencias Naturales y Exactas

and

Université Pierre et Marie Curie
Chimie Moléculaire de Paris Centre
Unité de Technologies Chimiques et Biologiques pour la Santé

for the degree of Doctor en Química de la Universidad de Guanajuato and Docteur de Chimie Moléculaire de Paris Centre

Author
Gonzalo Ramírez García

Supervised by

Prof. Anne Varenne   **Prof. Silvia Gutiérrez Granados**
Prof. Nathalie Mignet   **Prof. Minerva Martínez Alfaro**

July 2016

CERTIFICATE OF APPROVAL

This manuscript has been read and approved by the Examining Committee
constituted by:

Dr. ÁVILA-RODRÍGUEZ Mario
President of the jury
(UGTO)

Dr. MÉNAGER Christine
President of the jury
(UPMC)

Dr. DÍAZ-MUÑOZ Mauricio
Rapporteur
(UNAM)

Dr. KUHN Alexander
Rapporteur
(ENSCBP)

Dr. CRUZ-JIMÉNEZ Gustavo
Examiner
(UGTO)

Dr. BEDIOUI Fethi
Examiner
(ENSCP)

STATEMENT OF ORIGINALITY

This is to certify the originality of this thesis, and that its content is the product of my own work. This thesis has not been submitted for any degree or other purposes.

M.Sc. RAMÍREZ-GARCÍA Gonzalo

ACKNOWLEDGEMENTS

PREFACE

The present work represents the fulfillment of a jointly supervised doctoral thesis between the University Pierre et Marie Curie, PARIS VI, and the University of Guanajuato according to the applicable terms and conditions for the preparation of the thesis established in agreement by the above mentioned universities. The research has been carried out in the laboratories of the Unité de Technologies Chimiques et Biologiques pour la Santé (Paris, France), and the laboratories of the División de Ciencias Naturales y Exactas of the University of Guanajuato (Guanajuato, Mexico).

This thesis has been directed by a multidisciplinary group integrated by Anne Varenne, Nathalie Mignet, Silvia Gutiérrez Granados and Minerva Martínez Alfaro. Fanny d'Orlyé and Cyrille Richard have also supervised and participated fruitfully in the discussion of the entire work.

This manuscript is presented in English, and it includes an extended summary in French.

The general objective of this work has been to develop and apply methodologies for characterization of physicochemical properties and biocompatibility of persistent luminescence nanoparticles for preclinical diagnosis applications.

The present thesis is actually relevant in three senses: first, the development of methodologies for determination of nanoparticle physicochemical properties (Chapter II), the evaluation of their interactions with proteins (Chapters III-V), and thirdly, the application of these methodologies in combination with a complete set of biocompatibility studies to characterize the recently developed $ZnGa_{1.995}Cr_{0.005}O_4$ nanoparticles (Chapter VI and VII), which are a great promise in the field of the biological imaging for a wide range of applications.

The global conclusions of this research are presented in the last section of this manuscript.

As a result of this collaboration, the next publications on indexed journals were achieved or are expected:

Gonzalo Ramírez-García, Fanny d'Orlyé, Silvia Gutiérrez-Granados, Minerva Martínez-Alfaro, Nathalie Mignet, Cyrille Richard, Anne Varenne. *Functionalization and characterization of persistent luminescence nanoparticles by dynamic light scattering, laser Doppler and capillary electrophoresis.* **Colloids and Surfaces B Biointerfaces**, 2015. **136**: p. 272-281.

Gonzalo Ramírez-García, Silvia Gutiérrez-Granados, Marco A. Gallegos-Corona, Lourdes Palma-Tirado, Fanny d'Orlyé, Anne Varenne, Nathalie Mignet, Cyrille Richard, Minerva Martínez-Alfaro. *Acute, short and long-term toxicity of persistent nanophosphors in mice.* (Submitted)

Gonzalo Ramírez-García, Fanny d'Orlyé, Silvia Gutiérrez-Granados, Minerva Martínez-Alfaro, Nathalie Mignet, Cyrille Richard, Anne Varenne. *Electrokinetic Hummel-Dreyer characterization of nanoparticle-plasma protein corona: the non-specific interactions between PEG-modified persistent luminescence nanoparticles and bovine serum albumin.* (Submitted)

Photo-activation enhances the toxicity of persistent luminescence nanoparticles in breast cancer cells. (Under revision)

A quantitative method to optimize the PEGylation of persistent luminescence nanoparticles thus increasing their permanency in blood circulation: evaluation of the nanoparticle interactions with human serum albumin. (Under revision)

Comparative and competitive interactions between PEGylated persistent luminescence nanoparticles and apolipoprotein-e versus albumin: analysis in a binary system of proteins. (Under revision)

The essence of each one of these works is presented in the next chapters.

ABSTRACT

Nowadays engineered nanoparticles surround us, leading to many and highly valuable applications in different domains. Thanks to their unique properties they are revolutionizing and pushing up varied research areas including biomedical, material, physics and chemistry sciences, and thereby our society. Nevertheless, those properties are hardly dependent on the nature, size, shape, surface chemistry and chemical environment of these materials. The use of nanoparticles for biomedical applications implies the knowledge of their physicochemical parameters in physiologically relevant media.

Zinc gallate nanoparticles doped with chromium ($ZnGa_{1.995}Cr_{0.005}O_4$) are innovative persistent luminescence materials with particular optical properties allowing their use for *in vivo* imaging. They offer the promise of revolutionary tools for biological imaging with applications such as cellular tracking or tumor detection. They can be excited in the tissue transparency window by visible photons and emit light for hours after the end of the excitation. This allows observing the probe without any time constraints nor autofluorescence signals produced by biological tissues when using fluorescent probes.

In the first chapter, a brief review describing the relevance of the $ZnGa_{1.995}Cr_{0.005}O_4$ nanoparticles and their applications is presented. Thereafter, the nanoparticle functionalization effects on their physico-chemical properties and on their colloidal stability and applications are described. Some important aspects about NPS pharmacokinetic and their biocompatibility are also presented in order to lay the groundwork for the toxicity studies presented in Chapters VI and VII. Finally, the state of the art and trends about the characterization of NPS by means of electrokinetic methodologies and the parameters obtained from the electrophoretic profiles are reviewed with emphasis on the NPs characterization for biomedical applications and their interactions with biomolecules.

Modification of the surface of these nanoparticles is essential to be colloidally stable not only for cell targeting applications but also for proper distribution in living organisms. The use of different methods for controlling and characterizing the functionalization process is imperative to better understand the subsequent interactions with biological elements. The optimization of the $ZnGa_{1.995}Cr_{0.005}O_4$ synthesis with various functional groups on their surface (-OH, aminosilane and PEG) and their physic-chemical characterization have been explored for the first time in this work by means of dynamic light scattering, laser Doppler electrophoresis in combination with capillary electrophoresis. The results are presented in Chapter II. Special interest was focused in the latter method in order to evaluate its potential for the evaluation of colloidal and chemical properties and stability of functionalized nanoparticles. The hydrodynamic diameter, zeta potential, electrophoretic dispersion, stability over time and aggregation state of persistent luminescence nanoparticles under physiological-based conditions have been studied for each functional state. This thorough control increases our knowledge on these nanoparticles for subsequent interactions and toxicological studies and ultimately medical application.

The knowledge of the magnitude of the interactions between nanoparticles and plasma proteins could help determining the role played by this protein corona in the fate of the nanoprobes. In this sense, the nanoparticle surface passivation is therefore a very crucial challenge in biomedicine. In Chapter III we developed herein for the first time an electrokinetic Hummel and Dreyer method for quantitatively characterize protein corona formation on nanoparticles. This strategy was designed and optimized to evaluate the non specific binding of Bovine Serum Albumin with the PEG-functionalized $ZnGa_{1.995}Cr_{0.005}O_4$ persistent luminescence nanoparticles developed for *in vivo* biological imaging. The binding strength and the number of binding sites were determined at different ionic strengths. This methodology opens the way to an easy, low sample- and time-consuming evaluation of the impact of NPs surface nature on protein-corona formation and therefore on their potential for various bio-medical applications. As the first application of this method, in the Chapter IV the effect of the reaction time during aminosilanation step on the interactions between PEGylated nanoparticles and Human Serum Albumin was quantitatively evaluated in order to determine the optimal conditions for polyethylene glycol anchorage. The obtained results are in good agreement with the previous *in vivo* observations, since the lower the aminosilanation time, the stronger the interactions with proteins. Thereby, this methodology can help in the optimization and control of the production of functionalized nanoparticles for increase their permanence in blood circulation before the *in vivo* analysis.

In Chapter V, a second step for a better understanding of protein corona, three different strategies were used to compare the interactions between the PEGylated $ZnGa_{1.995}Cr_{0.005}O_4$ and Human Serum Albumin (the most abundant serum protein) or Apolipoprotein-E (ApoE) (which has been related to the active transport of nanoparticles or molecules through the blood brain barrier) by means of electrokinetic CE: i) interaction of injected nanoparticles with single proteins in the BGE, under the same analytical conditions, comparison of the electrophoretic profiles and determination of the binding parameters, ii) incubation of the NPs with one of the proteins and then electrokinetic separation in a separation media including the second protein, and vice versa, and iii) evaluation of the nanoparticle/protein interaction in a binary system of both proteins mixed at different ratios. These analytical methodologies show the application of capillary electrophoresis in the Hummel-Dreyer and Affinity modes according to the interaction parameters, for the evaluation of interactions between the persistent luminescence nanoparticles and two plasma proteins in a comparative and competitive system, resulting in a higher affinity between the PEGylated nanoparticles and the ApoE in comparison to the Human Serum Albumin. These observations may open interesting prospects for brain blood barrier translocation by the persistent luminescence nanoparticles or other contrast agent or delivery nanoparticles, and thereby for their application in optical imaging or therapeutics into the brain zone.

During the persistent luminescence, the most part of the energy is slowly emitted as photons, however, some of the electrons in the conduction band can reduce the molecular oxygen to produce superoxide anion ($O_2^{\bullet-}$). In Chapter VI, we evaluated the light effect on the reactive oxygen species production by irradiated or non-irradiated ZGO persistent luminescence nanoparticles. Their influence in oxidative stress induction and their cytotoxic effect on MCF-7 and MDA-MB-231 human breast cancer cells were also analyzed. The results indicated that reactive oxygen species

production was stimulated by exposition of the hydroxylated persistent luminescence nanoparticle to UV and visible light, and the corresponding oxidative stress induced in cells after internalization can be directly related to their dose-dependent inhibition of cell viability. On the other hand, PEGylated nanoparticles were not uptake by cells, and cell viability was not altered by these nanoparticles. This study reveals the importance of consideration of light irradiation for the study of luminescent nanoparticles toxicity, and a novel possible application in photodynamic therapy.

Despite the attractive optical properties of the $ZnGa_{1.995}Cr_{0.005}O_4$ persistent luminescence nanoparticles, their use demands extensive toxicological evaluation (Chapter VII). A complete set of mice were treated with a single intravenous administration of hydroxylated or PEGylated nanoparticles at different concentrations and then a set of standard tests were carried out 1 day, 1 month and 6 months after the administration in order to evaluate their acute, sub-chronic and long term *in vivo* effects. Hydroxylated nanoparticles induced some important health alterations at the higher dose both at short and at long term exposition. High concentrations of hydroxylated nanoparticles generate structural alterations at histological level, endoplasmic reticulum damage and oxidative stress in liver, as well as rising in white blood cells counts. On the contrary, no clinical sign related to PEGylated nanoprobes treatments were noted during our *in vivo* experiments, denoting the protective effect of PEG-functionalization and thereby their potential as safe *in vivo* diagnostic probes.

As a global conclusion, this work demonstrates the efficiency and high potential of electrokinetic methodologies for the physicochemical characterization of the recently synthesized $ZnGa_{1.995}Cr_{0.005}O_4$ persistent luminescence nanoparticles and their interactions with biomolecules. The knowledge of this information in addition to the *in vitro* and *in vivo* biocompatibility studies can thereafter potentiate their biological applications.

These methodologies developed in this work could be further used for other types of NPs and proteins.

LIST OF CONTENTS

ACRONYMS AND SYMBOLS

Acronyms	Details
ACB	*Ammonium carbonate buffer*
ACE	*Affinity capillary electrophoresis*
AFM	*Atomic force microscopy*
ApoE	*Apolipoprotein-E*
APTES	*3-Aminopropyl triethoxysilane*
BBB	*Blood brain barrier*
BGE	*Background electrolyte*
BSA	*Bovine Serum Albumin*
CE	*Capillary electrophoresis*
CZE	*Capillary zone electrophoresis*
DAPI	*4´,6-diamidino-2-phenylindole*
DDABr	*Didodecyldimethylammonium bromide*
DFM	*Dark-field microscopy*
DLS	*Dynamic light scattering*
DMF	*N,N-Dimethylformamide*
DMSO	*Dimethyl sulfoxide*
DNA	*Deoxyribonucleic acid*
DSC	*Differential scanning calorimetry*
EC	*Electrochemical detector*
EDTA	*Ethylenediaminetetraacetic acid*
ELS	*Evaporative light scattering*
FACE	*Frontal analysis capillary electrophoresis*
FACMCE	*Continuous frontal analysis in a microchip electrophoresis format*
FRET	*Förster resonance energy transfer*
FTIR	*Fourier transform infra-red spectroscopy*
GRAN	*Granulocytes*
HCT	*Hematocrit*
HD	*Hummel-Dreyer capillary electrophoresis method*
HEPES	*4-(2-Hydroxyethyl)piperazine-1-ethanesulfonic acid*
HGB	*Hemoglobin*
HPLC	*High performance liquid chromatography*
HSA	*Human Serum Albumin*
IC_{50}	*Inhibitory dose at 50%*
IS	*Ionic strength*
LDE	*Laser Doppler electrophoresis*
LDV	*Laser Doppler velocimetry*
LED	*Light-emitting diode*
LIF	*Laser induced fluorescence detector*
LYM	*Lymphocytes*
MEKC	*Micellar electrokinetic chromatography*
$MeO\text{-}PEG_{5kDa}\text{-}NHS$	*Methoxypolyethylene glycol N-hydroxysuccinimide (5000 Dalton)*
MOPS	*Morpholino propanesulfonic acid*
MS	*Mass spectrometry*

Acronyms	Details
NECEEM	*Non-equilibrium CE of equilibrium mixtures*
NM	*Nanomaterial*
NMR	*Nuclear magnetic resonance*
NOx	*Nitric oxide metabolites*
NP	*Nanoparticle*
PAGE	*Polyacrylamide gel electrophoresis*
PDI	*Polydispersity index*
PEG	*Polyethylene glycol*
PLNPs	*Persistent luminescence nanoparticles*
PLT	*Platelets*
POx	*Aqueous peroxides*
PZC	*Point of zero charge*
QD	*Quantum dot*
RBC	*Red blood cells*
ROS	*Reactive oxygen species*
SEM	*Scanning electron microscopy*
TDA	*Taylor dispersion analysis*
TEM	*Transmission electron microscopy*
VACE	*Vacancy affinity capillary electrophoresis*
VPM	*Vacancy peak method*
WBC	*White blood cells*
XRD	*X-ray diffraction*
XTT	*2,3-bis(2-methoxy-4-nitro-5-sulfophehyl)-2H-tetrazolium-5-carboxanilide*
ZGO-NH$_2$	*Aminosilane-functionalized $ZnGa_{1.995}Cr_{0.005}O_4$ nanoparticles*
ZGO-NPs	*$ZnGa_{1.995}Cr_{0.005}O_4$ nanoparticles*
ZGO-OH	*Hydroxyl-functionalized $ZnGa_{1.995}Cr_{0.005}O_4$ nanoparticles*
ZGO-PEG	*Pegylated $ZnGa_{1.995}Cr_{0.005}O_4$ nanoparticles*

Symbol	Details
A_c	Vacancy peak area obtained during HD calibration
A_s	Vacancy peak area of the sample in the HD method
A_λ	Absorbance at given wavelength (λ)
a	Hydrodynamic radius
C	Molar concentration
D_H	Hydrodynamic diameter
$\Lambda^0_{counter}$	Limit equivalent conductance of the counter ion
E	Electric field
e	Elementary electric charge
η	Vicosity
ε	Molar extinction coefficient
ε_0	Electric permittivity of vacuum
ε_r	Relative electric permittivity
k	Boltzmann constant
κ	Debye-Hückel parameter (reciprocal thickness of the ion cloud)
Ka	Binding constant
l	Light pathway in cm
L	Ligand
$[L]_b$	Bound ligand concentration
$[L]_T$	Total ligand concentration
$[S]_b$	Bound substrate concentration
$[S]_T$	Total substrate concentration
$m_{counter}$	Ionic drag coefficient of the counterion
μ_E	Electrophoretic mobility
n	Number of binding sites on a substrate
N_A	Avogadro number
n_H	Cooperativity
$O_2^{\bullet-}$	Superoxide anion
R_H	Hydrodynamic radius
S	Substrate
T	Temperature
v	Electrophoretic velocity
V_A	Attraction potential energy
V_R	Repulsion potential energy
V_T	Total potential energy
z	Charge number of the counterion
ζ	Zeta potential

INDEX OF FIGURES AND TABLES

CHAPTER I

ANEXE-1

TABLES

CHAPTER I

CHAPTER III

CHAPTER IV

CHAPTER V

CHAPTER VI

CHAPTER VII

ANEXE-1

CHAPTER I.

THEORETICAL FRAGMENT

1.1. PERSISTENT LUMINESCENCE NANOPARTICLES FOR BIOMEDICAL IMAGING

1.1.1. Luminescent nanoparticles for optical imaging

Optical imaging is a rapidly developing field of research aimed at noninvasively interrogating animals for disease progression, evaluating the effects of a drug, assessing the pharmacokinetic behavior, or identifying molecular biomarkers of diseases [1]. The first medical imaging was realized in the late 1895 by Wilhelm Röntgen shortly after he discovered X-ray and applied it to capture the images of the bones of a hand on film [2]. The immediate consequence of this discovery triggered intense development of new imaging technologies, such as X-ray computed tomography, magnetic resonance imaging, positron emission tomography, ultrasound and optical imaging, that are indispensable to medicine diagnostic [2, 3]. These imaging technologies differ predominantly in resolution, penetration depth, temporal resolution and energy expended for generation of the image.

Today, these modern imaging technologies coupled with newly developed imaging probes facilitate the integration of complex biological and physical phenomena into the rapid visualization process at a molecular level [4-6]. A pre-requisite of molecular imaging is precisely the development of specific, targeted imaging contrast agents to assess the biological processes, hence different kind of compounds with optical properties are being studied [7].

Nanotechnology is emerging as a versatile tool for biomedical applications, and the field of optical imaging is not excluded. Nanomaterials possess at least one dimension between 1 and 100 nm, and at this scale, unique physical, chemical and optical properties have been discovered. In the Figure 1.1 is illustrated an approximate comparison of the nanoparticle size with other relevant structures.
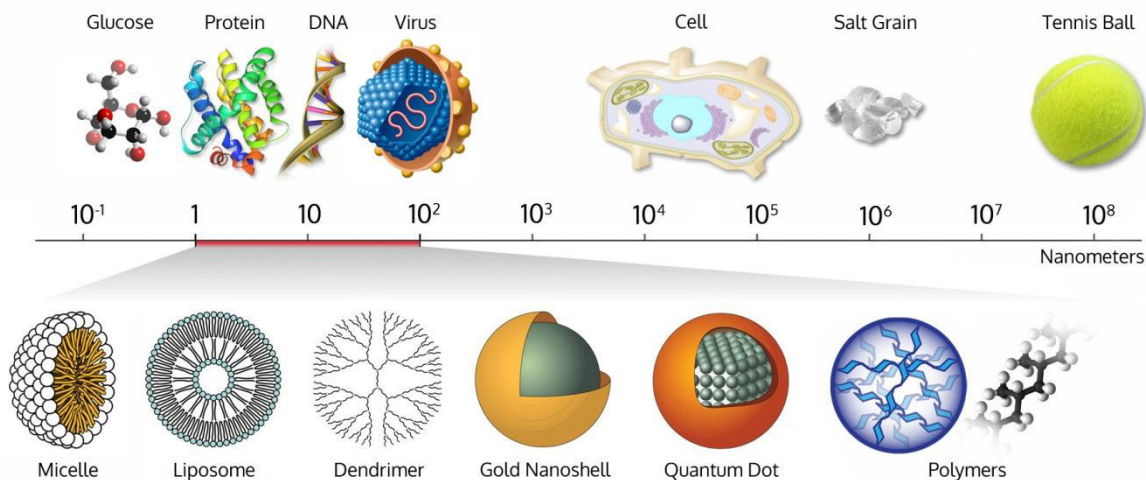
Fig. 1. 1. Relative size of nanoparticles [8].

In addition, the nanoparticle size influences the capacity to interact with molecules or cellular elements in living organisms, which enhance their applications, i.e. luminescent nanoparticles for biomedical imaging.

Luminescence is an emission of light by a substance not resulting from heat, and it can be described according to excitation source and the duration of the emission after the end of the excitation in fluorescence (nanoseconds) or phosphorescence (some seconds) [9]. Certain features of luminescent nanoparticles, such as multi-functionality, multivalency, and the ability to carry large payloads have made them the subject of intense researches, and a great variety of configurations have been synthesized, i.e. semiconductor quantum dots, fluorophore-encapsulated silica nanoparticles, gold nanoclusters, carbonaceous materials (carbon-dots, nanodiamonds), up-conversion nanoparticles, metal oxide nanoparticles, rare earth nanoparticles, etc. [10-12].

However these nanomaterials present several limitations such as short light emission time, low sensibility (especially due to tissue autofluorescence under external illumination) and weak tissue penetration of low wavelength excitation light [13, 14]. Current optical imaging probe applications are hampered by poor sensitivity, being one of the principal reasons to develop new luminescent nanomaterials. Innovative materials with a property known as persistent luminescence promise surpass some of these disadvantages.

1.1.2. Persistent luminescence nanoparticles

The persistent luminescence is the optical phenomenon presented by some compounds whose light emission remains for extended periods of time after the excitation source has been turned off, with a record of time of more than several hours [15, 16].

The well-documented history of persistent luminescence as a phenomenon dates from the beginning of the 17th century, when an Italian shoemaker, V. Casciarolo [17], observed strong luminescence from the mineral barite ($BaSO_4$) in its reduced form (BaS) containing different trace impurities, later to be known as "Bologne stone". Several books were written about this "miraculous" phenomenon (Figure 1.2).

Despite no explanation being found for the persistent luminescence, the applications were taken into use until the 20th century, principally as luminous paints, which were based on persistent luminescence from the different sulphide materials such as copper-doped BaS, showing both weak and short light emission [18].

The introduction of the rare earth based phosphors to ameliorate these limitations takes place in the 1960s, however, a negative collateral effect was incorporated: the afterglow, by which the emission was retarded and in many cases weakened as result of the formation of traps to store the excitation energy [17].
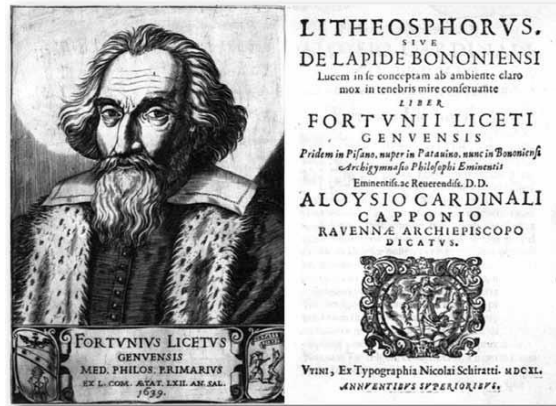
Fig. 1. 2. The book Litheosphorus Sive de Lapide Bononiensi by Fortunius Licetus (Bologna, Italy, 1640) on the persistent luminescence of the Bologna stone [17].

Due to this problem, persistent luminescence remained almost disregarded until 1995, when the new persistent luminescence era was born with the Eu^{2+} doped and rare earth (R^{3+}) co-doped alkaline earth aluminates ($MAl_2O_4:Eu^{2+},R^{3+}$; being M Ca and Sr) synthesis [19].

Since then, a lot of new compounds have been developed. Presently, there are Eu^{2+} based persistent luminescence phosphors emitting across all the visible electromagnetic spectra (Figure 1.3). However, for these materials the persistent luminescence is not so long nor strong at the red region, representing a predicament for some applications [17].
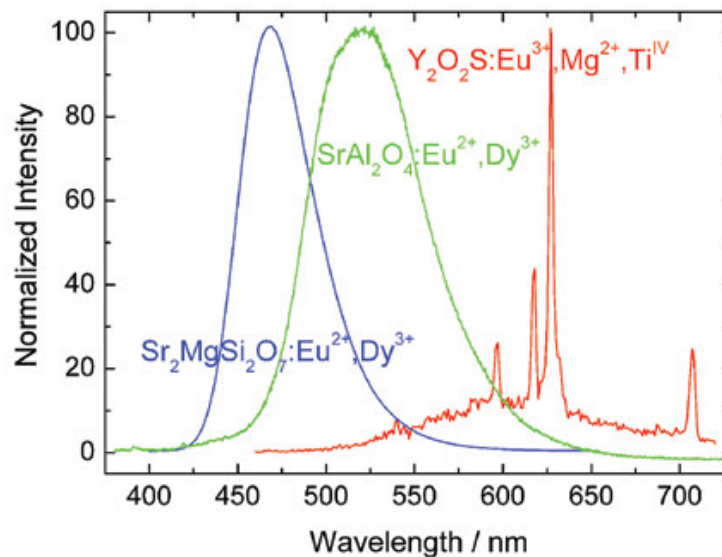
Fig. 1. 3. The luminescence spectra of the blue emitting $Sr_2MgSi_2O_7:Eu^{2+},Dy^{3+}$, green emitting $SrAl_2O_4:Eu^{2+},Dy^{3+}$, and red emitting $Y_2O_2S:Eu^{3+},Mg^{2+},Ti^{IV}$ phosphors after UV excitation [17].

During the past few decades, the research on persistent luminescence materials has been focused mainly on Eu^{2+}-doped compounds. Actually, they represents only 20% of the total number of known persistent phosphorous, which has increased to over 200. Other compounds are not based on Eu^{2+}, but rather, on intrinsic host defects, transition metals or trivalent rare earths (cerium, terbium, dysprosium, etc.) [17]. For an extensive list of the actually known persistent nanomaterials, we could refer to the reviews from *Smet P. et al.* [20] and from *Viana B. et al.* [21]. These kinds of materials have been principally used in safety indications, road signs, safety clothing, billboards, toys, graphic arts and interior decoration [22] (Figure 1.4).

Fig. 1. 4. Persistent luminescence applications [22].

Their use in the form of nanoparticulate materials for biomedical applications for *in vivo* imaging has been barely suggested for the first time in 2007 by *de Chermont et al.* [14]. Contrary to classical fluorescent probes that need to be constantly excited to produce a signal, persistent luminescence nanoparticles have the capacity to store excitation energy in traps and then to emit light for a long period of time, from dozen of minutes to hours upon thermal activation [23]. This property is of particular interest for *in vivo* bioimaging applications since it allows complete avoidance of the autofluorescence signal coming from endogenous chromophores also excited when using fluorescent probes. Due to this series of advantages, the research regarding biomedical applications has increased since the pioneer work presented in 2007 (Figure 1.5) (adapted from [24], and actualized).
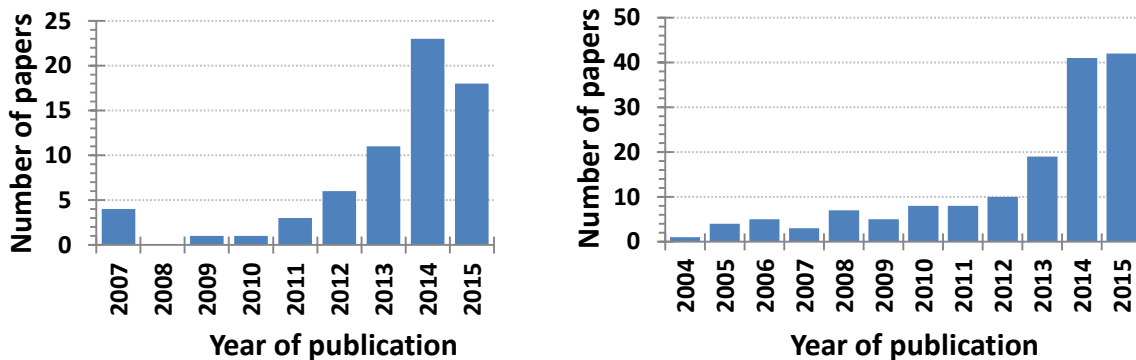
Fig. 1. 5. Number of papers published (from Web of Science). At the left side, with the key words "persistent luminescence" and "in-vivo imaging" ; at the right side with the key words "persistent luminescence" and "nanoparticles" (adapted from [24]).

The exact models to explain the persistent luminescence phenomena are far from being understood. In general, a persistent luminescence process requires the presence of abundant traps able to trap carriers such as electrons, holes, or pairs of both, and immobilize them for a long period of time and thereby, retain the energy for a long period of time before being emitted as photons for example by thermal activation [25]. Taking into account the current models, it is necessary to consider the matrix, the dopants and co-dopants agents when designing persistent luminescence materials because their selection can impact directly on the intensity and duration of persistent luminescence, ranging from seconds to hours, and in the emission wavelength. Furthermore, the thermal bleaching and interaction of the dopants with electron traps, recombination centers or crystal lattice, are of particular significance because persistent luminescence has been related with the defects in the molecular network and with the concentrations of the elements present in it [26].

The main requirements that the persistent luminescence materials must fulfill for *in vivo* biomedical imaging purposes are the followings [21]:

i) Nanometric size (< 100 nm)
ii) Persistent emission over hours
iii) Intensive emission in the tissue transparency window
iv) Adequate functionalization
v) Chemical and colloidal stability in aqueous solution

The tissue transparency window (also called "biological optical window" or simply "therapeutic window") is the region of the electromagnetic spectrum in which tissues are most transparent, as said, between 600 nm and 1300 nm. This region is demarcated by the combination of absorption of lower wavelength light by the important tissue chromophores (oxy and deoxyhemoglobin and melanin) together with reduced light scattering at longer wavelengths and the occurrence of water absorption at wavelengths greater than 1300 nm (See Figure 1.6) [27].
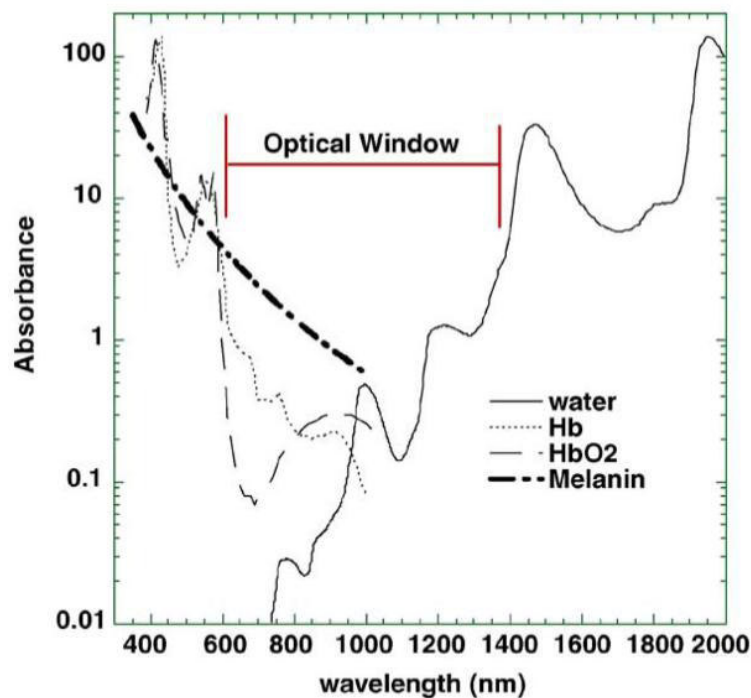
Fig. 1. 6. Absorption spectra of important chromophores present in mammalian tissues [27].

In the past five years, the research in biomedical imaging has been principally focused on developing highly sensitive and efficient red/near-infrared emitting nanophosphorous in order to overcome the intrinsic autofluorescence limitations in small animals [21].

1.1.3. $ZnGa_{1.995}Cr_{0.005}O_4$ persistent luminescence nanoparticles

The zinc gallate and its analogous chromium doped material ($ZnGa_2O_4:Cr^{3+}$) have initially attracted serious attention as a bulk material due to their near-infrared persistent luminescence presented after UV excitation [28, 29].

The $ZnGa_2O_4:Cr$ phosphor has a cubic normal spinel crystal structure with Fd_3m space group (Figure 1.7). The unit cell contains 8 tetrahedral cations, 16 octahedral cations and 32 oxygen anions. The normal spinel $ZnGa_2O_4$ has tetrahedrally coordinated Zn sites surrounded by 4 oxygens and octahedrally coordinated Ga sites surrounded by 6 oxygen molecules [30].

The optical proprieties of this kind of compounds at their pure and/or chromium doped configuration have been also investigated in nanoscale materials [24, 31, 32].
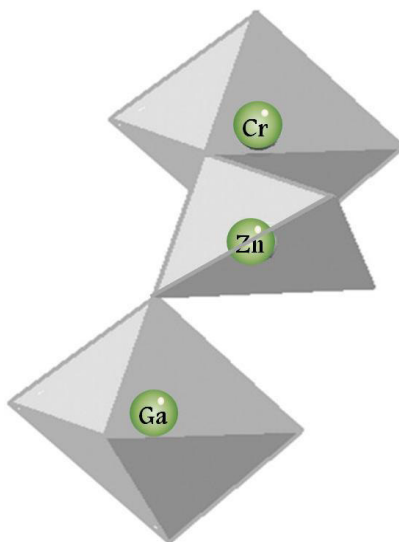
Fig. 1. 7. Crystalline spinel structure of ZnGa$_2$O$_4$:Cr [30].

The more recently reported chromium-doped zinc gallate ZnGa$_{1.995}$Cr$_{0.005}$O$_4$ nanoparticles (ZGO-NP), a chromium-doped binary oxide having also an ordinary spinel structure has denoted attractive optical properties due to its long persistent luminescence besides the capacity to be re-activated *in vivo* through living tissues using highly penetrating low energy photons by simple two minutes illumination under a simple orange/red LEDs source [33].
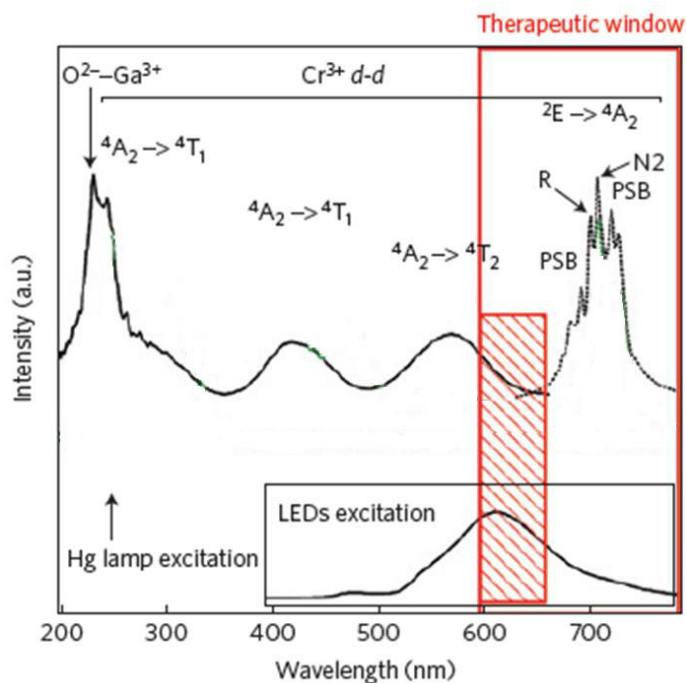
Fig. 1. 8. Photoluminescence excitation (solid line) and emission (dotted line) spectra of ZGO-NP [33].

The excitation spectrum of photoluminescence in ZGO-NP is composed by four broad bands covering a wide spectral region from ultraviolet to red light (Figure 1.8, solid black line) [33].

The band at 245nm corresponds to an excitation greater than the bandgap of $ZnGa_2O_4$, the band at 290nm and bands in the range 425-560nm correspond to Cr^{3+} d-d transitions [34]. The $^4A_2 \rightarrow {}^4T_2$ absorption band partly corresponds to a region of weaker absorption of tissues (red rectangle). The photoluminescence emission spectrum of ZGO-NP (Figure 1.8, dotted line) is composed of ^2E (^2G)$\rightarrow {}^4A_2$ (^4F) lines of Cr^{3+} ions. Ideal Cr^{3+} ions are located in a trigonally distorted octahedral environment at a Ga^{3+} site. They are denoted as Cr_R and emit R-lines accompanied at room temperature by intense phonon sidebands. Some other Cr^{3+} ions, denoted as Cr_{N2}, have an antisite corresponding to Ga in Zn site and viceversa with weaker phonon sidebands (PSB) [29, 35, 36]. In addition, the ZGO-NP show intense long-lasting phosphorescence centered on 695nm [29]. The optical UV-excitation leads to the creation of electrons/holes that become trapped at specific defects of the crystal and enable the material to store the excitation light. At the end of the excitation, the carriers are slowly released from the trapping defects located at about 0.6-1.0 eV below the conduction band by thermal assistance [25] or by light in the case of photostimulated phosphors, and radiatively recombine at Cr^{3+} ions to produce a persistent luminescence. The mechanism proposed to explain the persistent luminescence in ZGO-NP is presented in Figure 1.9 [33].
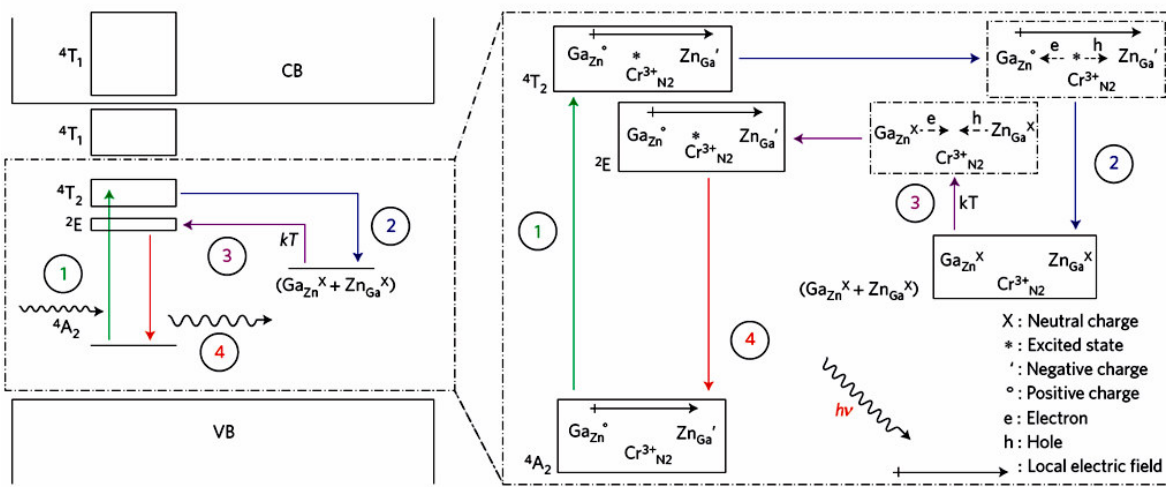
Fig. 1. 9. Schematization of the mechanism proposed for the persistent luminescence induced by LED excitation. Conduction band (CB) and valence band (VB) [33].

Trapping of a defect pair (electron-hole) after LED excitation could be related to a permutation of Ga and Zn (antisite defects) close to Cr^{3+} ions. A Ga ion in a Zn site is a positively charged defect ($Ga_{Zn}°$) and Zn in a Ga site is a negatively charged defect (Zn_{Ga}'). When localized close to Cr^{3+}, these defects create a local electric field providing a driving force for charge

separation. In step 1, Cr^{3+} is promoted to one of its excited states ($^4T_2$ with orange/red LED excitation). The excited Cr^{3+} will induce a redistribution of charge in the Zn_{Ga}'-Cr^{3+*}-Ga_{Zn}° complex (step 2). As the two antisite defects become neutralized, the electric field at the origin of the charge separation is suppressed, and the electron-hole pair remains trapped in the Cr^{3+} vicinity as a neutral antisite defect. The reverse process (detrapping) is induced by thermal activation (step 3), leading to an excited Cr^{3+}_{N2} followed by the emission from the ^2E state (step 4). In this mechanism, the excitation (electron-hole pair) is directly trapped at neighbouring defects of Cr^{3+} [24, 33].

Due to these properties, the ZGO-NP have revealed their ability to show a near infra-red persistent luminescence following an ultraviolet excitation or an orange/red illumination by a LED source (in the form of a raw powder or suspension in water) (Figure 1.10)[33].
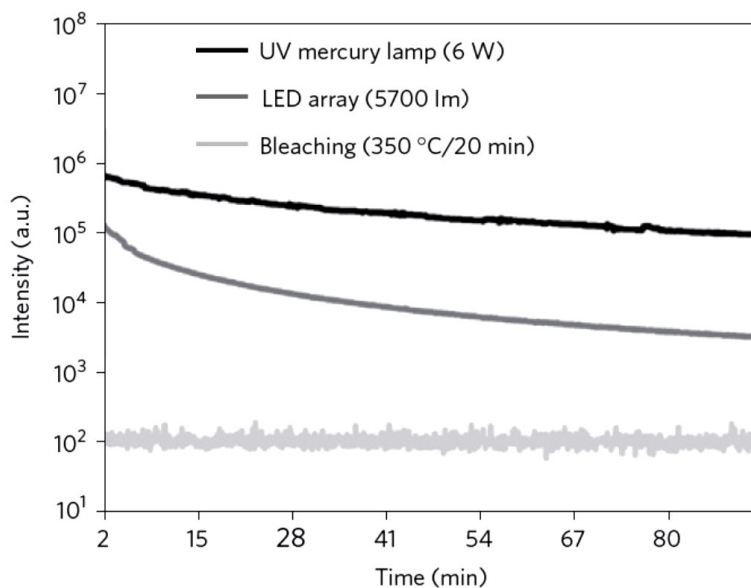
Fig. 1. 10. Room-temperature persistent luminescence decay curves of bleanched ZGO-NP. Excitation was applied during 2 min under ultraviolet light or LED array sources. Un-excited ZGO-NP (by isolating them in the darkness for at least one week before the analysis) were used as background reference [33].

In this figure, the light emission lasts for at least 90 min after the end of the excitation, and continue with considerable intensity. This exclusive property permits the ZGO-NPs either to be excited before the administration into the observation animals (by UV- or LED-light), or to excite them once inside the specimen (by LED-light) (see Figure 1.11) [33].
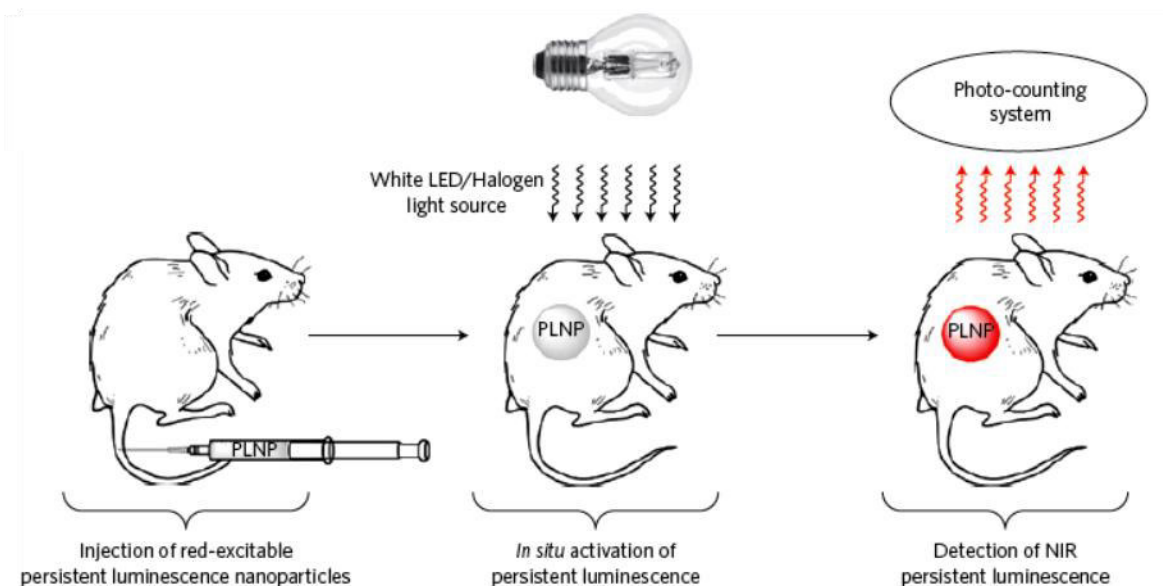
Fig. 1. 11. Schematic representation of the in vivo imaging after in situ activation of the ZGO-NP [33].

Such property indicates that optical imaging observations with ZGO-NP can be done without time constraints, meaning a great advantage over other luminescent or persistent luminescence nanoparticles. A head to head comparison of the ZGO-NP with commercially available 705 nm emitting QDs revealed one crucial advantage of the persistent luminescence for *in vivo* applications over classical fluorescence techniques: in spite of the clear superiority of QDs over ZGO-NP regarding absolute sensitivity and total emitted light, the ZGO-NPs returns a far better target to background ratio and thereby better sensitivity respect to the QDs, but also ensures real-time imaging of the physiological phenomenon studied *in vivo*, avoiding the undesirable autofluorescence effects [33].

After proper surface modifications, the primary applications of the ZGO-NP have been the nanoparticle-biodistribution assays, the RAW cell *in vivo* tracking, and the passive *in vivo* targeting of tumors in rats[33, 37]. Due to their advantages, numerous biomedical applications can be envisaged for the ZGO-NP considering the possibility of different functional groups addition on their surface [21].

1.1.4. Modification and functionalization of nanoparticles

For NPs to be successfully used as luminescent labels, two main requirements must be met: First, good stability in physiological conditions, and then, the presence of some functional groups on their surface to allow further conjugation with biologically active molecules or, in another hand, to avoid natural detection by immune cells [38, 39].

Methods for the functionalization of inorganic NPs for bioimaging applications are rather diverse. In general, such NPs are modified in two steps, the first being surface activation, the second being conjugation [12]. Numerous methods to functionalize NP are available depending on the kind of species to be immobilized. These range from polymers such as poly(ethylene glycol) to proteins, fluorophores or oligomers. Both physical adsorption and covalent binding have their merits and are widely used. Quality criteria of the final product include colloidal stability in water, biocompatibility, cell permeability, and a brightness that enables even minute quantities of NPs to be discerned from an often strongly fluorescent background [40, 41].

It is well known that the biological activity of nanoparticles is significantly dependent on their size and shape, but also on their surface decoration. Nanoparticles have been functionalized with specific targeting moieties, biocompatible polymers, cell penetrating, stealth, stimulus-sensitive or imaging agents to improve their applications [42] (Figure 1.12).
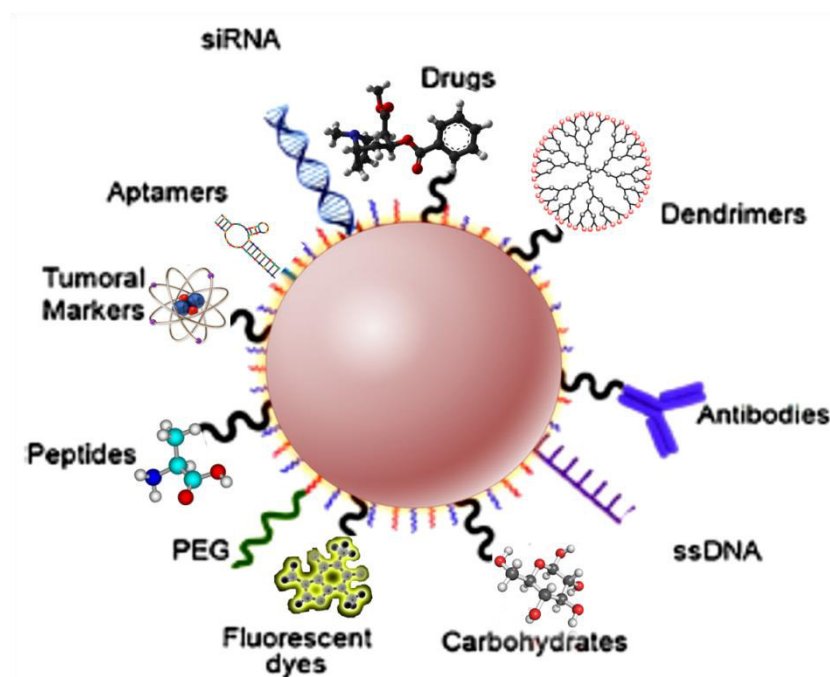
Fig. 1. 12. Functional decoration of nanoparticles (adapted from [42]).

The surface density of functional groups is of high priority, considering most applications are based principally on the surface region of nanomaterials [43]. For example, it has been shown the possibility to functionalize the surface of ZGO-NPs with small molecules such with amine, carboxylic acid functions or with PEG chains, and that their biodistribution in healthy mice is highly dependent on their diameter and surface coating [44].

1.1.4.1. Passive and active targeting

The need to optimize the therapeutic ratio in which a treatment affects cancer cells versus healthy tissues leads to the idea that it is necessary to have a treatment that could act as the "magic bullet" to selectively recognize cancer cells. Nanoparticle platforms offer a variety of potentially efficient solutions for the development of targeted agents that can be exploited for cancer diagnosis and treatment [45]. There are two ways by which targeting of nanoparticles can be achieved, namely passive and active targeting.

Passive targeting involves the unspecific tumor signaling by means of nanomaterials with long blood retention time. It is naturally based on the pathophysiological vascular architecture of many tumors, which are ascribed to the presence of fenestrations in the imperfect tumor blood vessels and to the poor lymphatic drainage in the tissue. The combination of these two phenomena was coined as the enhanced permeation and retention effect (EPR) [46, 47]. Nanomaterials with *in vivo* hydrodynamic diameters above the glomerular filtration threshold and blood residence times of at least 6 h substantially accumulate and retain in tumors through the enhanced permeability and retention effect [48, 49].

Active targeting, also called ligand-mediated targeting, involves immobilization of affinity ligands on the surface of NPs for specific retention and uptake by the targeted disease cells. To that end, ligands are selected to bind surface molecules or receptors over-expressed in diseased organs, tissues, cells or subcellular domains [50, 51]. Active targeting facilitates the lively uptake of nanoparticles by the tumor cells themselves. A variety of targeting molecules including small organic molecules, peptides, aptamers, carbohydrates as well as proteins, receptors, oligomers or antibodies and their fragments have been exploited for active targeting of nanomaterials so far [45].

An alternative targeting technique is making use of probes and nanomaterials with sensing capability. This enables not intrinsically fluorescent-biochemical species to be imaged. Examples include imaging of the distribution of chemical species such as pH values [52], glucose, calcium (II)[12] or oxygen [53], and also as nanosensors for temperature analysis in the living health and tumor cells [54].

Both active and passive targeting molecules induce the nanoparticles to change their transport properties and performance inside the organism, so it´s necessary to understand the possible routes and final facts destined for them.

1.2. PHARMACOKINETICS OF NANOPARTICLES FOR BIOLOGICAL IMAGING

Despite the enormous potential of NPs as multimodality agents with both diagnostic and therapeutic capabilities, challenges for extended biological and medicinal applications remain. Primarily, this includes particle biocompatibility and toxicity as well as unfavorable pharmacokinetics and biodistribution interfering with diagnostic imaging. Due to the great variety of recently developed nanomaterials, it is practically impossible to establish a sequence of rules determining their toxicity fact; however, nanoparticle pharmacokinetics is a strongly determinant of their biocompatibility. Pharmacokinetic analysis is routinely performed for drugs or chemicals before they can be applied for medical purposes. By that, some important concepts involved in the nanoparticle pharmacokinetics such as their administration, biodistribution, protein corona formation, cellular uptake and interactions with biomolecules, their metabolism and potential toxic effect, and finally, their elimination from the body are introduced in the next sections.

1.2.1. Administration of manufactured nanoparticles

There are four common routes through which a person can be exposed to manufactured nanomaterials: ingestion, injection, transdermal delivery, and inhalation; the most part of the nanocompounds for medical applications have been administered by these ways [55]. However, a great variety of routes of administration for nanoparticles in preclinical studies has been studied ever in order to improve clinical outcomes [56]. The route of administration of nanoparticles to rats has shown to be a determinant parameter on their distribution in tissues and excretion rate and thereby, their applicability or injurious effects [57]. However, the route for nanoparticle administrations depends principally on their applications and chemical properties. For example, the most part of nanoparticles intended for use as imaging agents are administered via intravenous injection. According to nanoparticle properties, the route for administration could be chosen and possibly alternated by the operator; however, a most difficult challenge is to control their distribution inside the specimen.

1.2.2. Nanoparticle biodistribution

Developing agents with ideal pharmacokinetic behavior will reduce toxicity risks due to minimized exposure times as a consequence of rapid removal from the body. A combination of key factors including size, shape, composition, surface chemistry and charge affects tremendously the pharmacokinetics and biodistribution of NPs *in vivo* [10, 58].

Nanoparticles have been used as optical imaging agents, drug carriers and other applications, in which adequate biodistribution is essential item [59]. During systemic circulation after intravenous administration, NPs encounter blood as a highly complex fluid composed of a wide variety of substances including salts, sugars, proteins as well as amino acids that can destabilize NPs and can cause their aggregation. Depending on the surface properties of the NPs, biological macromolecules, such as serum proteins and lipids adsorb nonspecifically and a dynamic

biomolecular corona is formed. This opsonization consequently leads to NP recognition as well as uptake by mononuclear phagocytic cells.

1.2.2.1. Protein corona formation

The biomolecules such as proteins present in biological fluids, entering in contact with the nanoparticle surface, can be progressively and selectively adsorbed forming the so-called protein corona, which may play a key role in the *in vivo* biological fate establishing a new identity of the nanosized materials [60]. The protein corona may influence cellular uptake, biodistribution, inflammation, accumulation, degradation and clearance of the nanoparticles [61].

Fundamentally, all interactions between the nanoparticle–corona complex and the biological machinery are mediated by physical forces common to all molecular systems (for example, van der Waals, electrostatic and others) [62]. Proteins in corona are in a constant adsorption/desorption process between the surrounding proteins in the biological fluid and the nanoparticle surface, establishing an equilibrium according to the relative affinity of their interactions [63] (see Figure 1.13). Depending of the surface chemistry of the NPs, biomolecules in the environment can adsorb strongly to the bare NP surface, forming a tightly bound layer of biomolecules, the so called "hard corona", in immediate contact with the nanoparticle. Other biomolecules, the "soft corona", have a residual affinity on the nanoparticle-hard corona complex (primarily to the hard corona itself), but this is much lower, so those molecules are in rapid exchange with the environment [60].
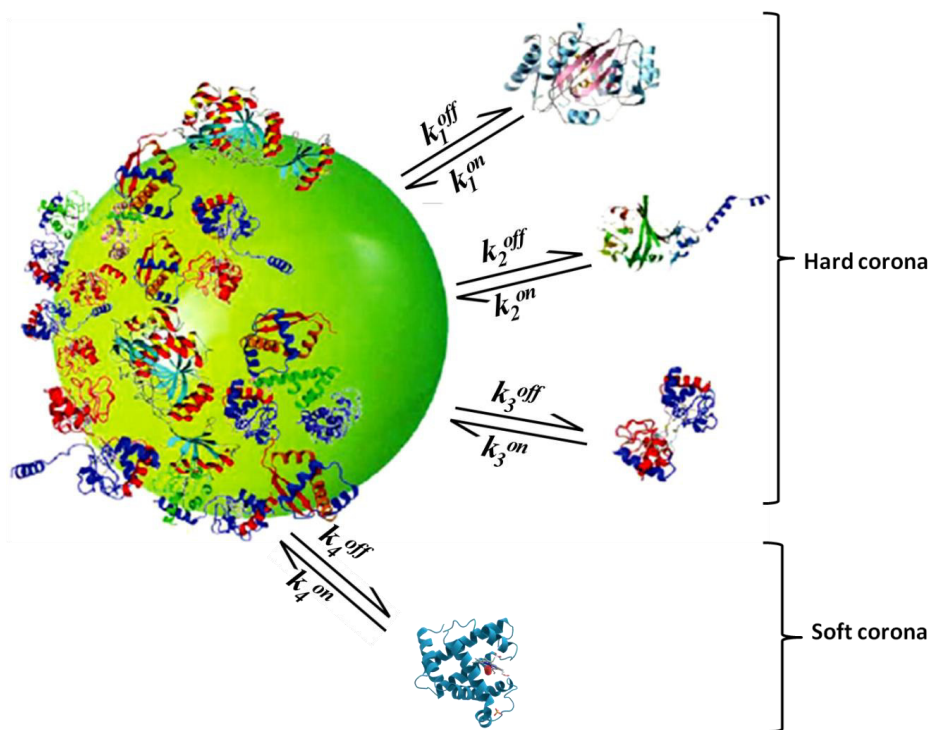
Fig. 1. 13. The nanoparticle-corona complex in a biological system (Adapted from [60]).

The composition of the corona is absolutely assorted and can be easily varied even in the same organism. Some of the parameters altering their composition are the nanoparticle size, shape, roughness, surface functionalization and protein abundance [64, 65].

The fact that the biomolecular corona defines the biological interactions of nanoparticles has been considered surprising because we often classify substances according to the "intrinsic" properties of the bare material, rather than "extrinsic" properties derived from the environment [60]. As an example, the apolipoproteins, which are abundant in the corona of very different nanomaterials are important to the nanoparticle transport process, specifically for crossing biological barriers [66-69]. Other proteins in corona have been involved in cellular uptake by different mechanisms [70, 71].

1.2.2.2. Cellular uptake and interactions

The knowledge of the underlying mechanism of cellular uptake is an important step towards understanding the biological fate of nanoparticles, both the adverse and favorable aspects. The interaction of nanomaterials with cells and lipid bilayers is critical in many applications such as photodynamic therapy, imaging, and drug/gene delivery, and is strongly related to their toxicity.

The plasma membrane is a dynamic structure of lipid bilayers and membrane proteins that segregate the cytoplasm from the external medium and regulates the transport of matter into cells. Cell membranes are somewhat permeable and allow only small molecules to pass through. Uptake of nanoparticles through the plasma membrane is a subject poorly known; however, diverse mechanisms about the internalization processes of nanomaterials by cells through endocytosis have been studied [72].

Endocytosis is a form of active transport in which a cell takes in any objects by enclosing them in vesicles or vacuoles pinched off from its cytoplasmic membrane in an energy dependent manner. The principal endocytosis pathways described for nanoparticle uptake are mainly via phagocytosis, pinocytosis, and caveolae-dependent or clathrin-mediated transport [62, 73, 74]. These mechanisms are schematized in Figure 1.14.

Phagocytosis is mainly conducted by specialized mammalian cells (like monocytes, macrophages, and neutrophils) to engulf solid particles with diameters > 750 nm by the cell membrane to form an internal phagosome [75, 76]. Smaller particles ranging from a few to several hundred nanometers are internalized by pinocytosis or macropinocytosis, which occurs in almost all cell types. Energy-dependent clathrin-mediated endocytosis is probably the primary characterized mechanism for the cellular uptake of nanoparticles [77-79], in which cargo is deposited in small endocytic vesicles (usual diameter < 100 nm) that fuse with early endosomes [80]. More recently, a plethora of additional mechanisms have emerged that use clathrin-independent pathways, many of them relying on the cholesterol dependent clustering of lipid-anchored proteins into diverse micro-domains [81]. Caveolae/lipid rafts, consisting of plasma membrane invaginations of 50 to 80 nm in size, contain cholesterol, sphingolipids, and caveolins [82]. Note that for endothelial cells, the

caveolae-mediated endocytosis is the important cellular uptake pathway for nanoparticles [83-85]. Each type of nanoparticle exhibits a preferred pathway for cellular internalization.
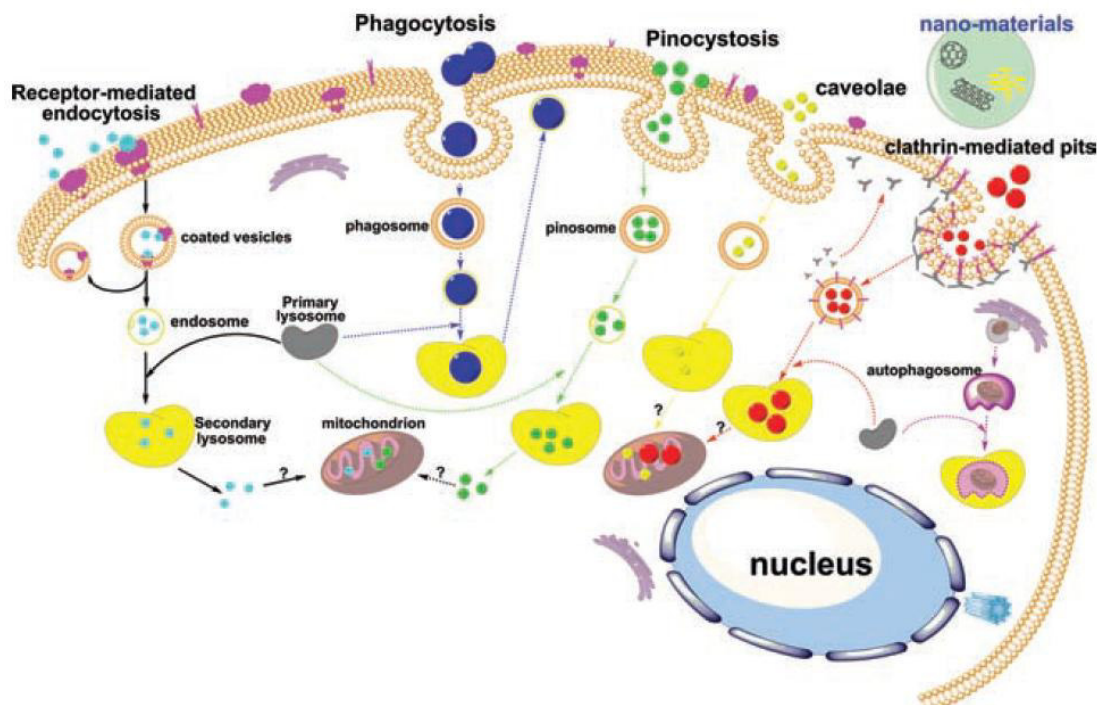
Fig. 1. 14. Schematic of the known pathways for nanoparticle internalization [72].

In general, the physiological behavior and pharmacokinetic parameters of nanoparticles can be optimized by adjusting their size, composition, shape, and surface characteristics such as charge and hydrophobicity, which are also key mediators of potential toxicity [86, 87]. One aspect of nanoparticle structure that may influence toxicity is the identity and charge of ligand molecules used to functionalize the NP surface, as an example, acute exposure toxicity assays show that overall the negatively charged AuNPs tested are orders of magnitude less toxic than the positively-charged AuNPs [88].

1.2.3. Metabolism

After uptake of nanoparticles by cells, the next important question is their intracellular location and translocation, which is directly related to the cytotoxicity or medical functions of the internalized nanoparticles. Generally, after entering cells, the internalized nanoparticles are normally translocated via either endosomal and/or lysosomal vesicles which contain varying amounts of hydrolases and hence lead to the rapid destruction and degradation of the internalized nanoparticles [89-91].

As practically all NPs are internalized by cultured cells through endocytic mechanisms, their surrounding pH will shift from 7.4 in the extracellular medium over 6.0 (early endosomes) to 4.5 (lysosomes). As NPs often have a high surface charge density, the local pH at the NP surface can often be even lower or higher than the global value of their surroundings [92]. Along with the pH differences, NPs will also be exposed to various degradative enzymes, such as cathepsin L, which has recently been suggested to be able to degrade nearly all bioconjugated particles [93].

Once the nanoparticles are inside the cells, the main cellular responses of nanoparticles suggested by the experimental results include anti-oxidative response, pro-inflammatory effects, lysosome permeation, mitochondrial membrane potential decrease, Ca^{2+} release, caspase activation, cell apoptosis, and cell death. Some of the cell-signaling pathways can be activated by the nanoparticle interactions, for example, through proinflammatory cytokines such as the mitogen-activated protein kinase (MAPK) and nuclear factor-kappa B (NF- κB) cascades [72].

Upon degradation of the coating molecules, the acidic environment of the endosomes can lead to acid etching of the NPs, resulting in the generation of free ions from the NP surface and gradually decrease the NP core diameter [94]. The metabolism of the nanoparticles can conduce to a complete loss of NP functionality, and in addition the leached metal ions can potentially also affect cell homeostasis.

1.2.3.1. Nanoparticle toxicity

The safe use of inorganic nanoparticles (NPs) in biomedical applications remains an unresolved issue. The assessment of NP safety has been complicated due to a great diversity in: i) types of NPs ii) stabilizing coating agents, iii) physicochemical parameters of the NPs (diameter, surface charge, surface topography, surface area), iv) incubation conditions (time and concentration), v) type of cells vi) type of assay vii) possible interference of the NPs with the assay readout [94].

Regardless of the intrinsic differences between the various types of NPs, at least six mechanisms by which they affect homeostasis at the cellular level can be grouped: i) oxidative stress, ii) alteration of cell morphology and cytoskeleton, iii) deregulation of the intracellular signaling pathways, iv) release of toxic components of the nanoparticles, v) interactions with biomolecules, and vi) effects of application of external physical stimuli for nanoparticle performance. They will be briefly discussed in the next paragraphs.

Initially, the generation of reactive oxygen species (ROS) by cells and the consequent oxidative stress induction upon exposure to NPs is quite a common phenomenon [95, 96]. When cells are exposed to environmental stress such as pathogens or heat, they can generate chemically active oxygen-containing molecules. These ROS molecules can be subdivided into two different types, being radical ROS (nitric oxide or hydroxide radicals) and non-radical ROS (hydrogen peroxide). Most cells have defense mechanisms such as the glutathione redox system, which can buffer a certain amount of ROS. When the increase in ROS species is too high, cells are prone to

undergo various negative effects. In general, small and transient increases in ROS can be tolerated by most cell types, whereas higher levels which persist over a longer time period are more likely to result in cell damage [94, 96, 97]. NPs have been described to possibly generate ROS by different mechanisms [98]:

a) Nanomaterials present in the acidic environment of lysosomes can induce ROS by direct reactivity of their surface coating, degradation of the coating and direct interaction of the acidic media on the metal surface or degradation of the whole nanoparticle and production of ions (Fe^{2+}, Cd^{2+}), which can induce ROS species by various chemical reactions [99, 100].
b) Nanomaterials can also directly interact with oxidative organelles such as the mitochondria by destabilizing the outer membrane, deregulating the mitochondrial membrane potential and hereby disrupting the electron transport chain of the oxidative phosphorylation [101].
c) Nanoparticles can directly interact with redox active proteins such as NADPH oxidase and hereby stimulate large ROS production in cells of the immune system [98].
d) Interaction of nanoparticles with surface located receptors can lead to receptor activation and triggering of intracellular signaling cascades (activation of second messenger or calcium waves), finally resulting in expression of stress response genes which can up-regulate ROS [98].

Cell morphology and cytoskeleton defects are also common toxic effects originated by nanoparticles. As NPs have certain physical dimensions, the intracellular volume they occupy can lead to alterations in cellular morphology or affect the structure of the cellular cytoskeleton network. It was hypothesized that the mere physical presence of high amounts of nanoparticles enclosed in large and bulky lysosomal structures typically located in the perinuclear region, sterically hindered the cytoskeleton network and hereby induced the remodeling of the actin network [102, 103]. Nanoparticles have also shown to disrupt actin fibers and tubulin network of human umbilical vein endothelial cells and also impeded the maturation of focal adhesion complexes, which link the cytoskeleton network to the extracellular matrix. These cytoskeletal deformations also decreased the capacity of human umbilical vein endothelial cells for vascular network formation [104].

Nanoparticles can alter the balance of cellular homeostasis and thereby the complex intracellular signaling pathways, resulting in a cascade of possible effects. These interactions can occur by several mechanisms, such as: i) genotoxic effects caused by high levels of ROS [105], ii) altered protein or gene expression due to the perinuclear localization of the particles which may hinder the functioning of the transcription and translation machinery [106], iii) altered protein or gene expression levels due to leaching of free metal ions [107], iv) altered activation status of proteins by interfering with stimulating factors such as cell-surface receptors [108], or v) altered gene expression levels in response to the cellular stress that the NPs induce [109].

Degradation of the nanoparticles and the consequent release of their components is other frequently founded mechanism for nanotoxicity [110-112]. For example, the time-dependent destabilization of QDs where release of free Cd^{2+} was found to increase with aging of the QDs, altering the intracellular microenvironment by the presence of the cadmium [113]. It is important to

study the kinetics and extent of intracellular NP degradation and to quantify the release of any (toxic) ions. If degradation is observed, acute cytotoxicity and the induction of ROS should be studied as well [94].

The nanoparticle interactions with biological elements are also a mechanism by which they can induce toxicity. The high surface area and high local charge densities generate a large area which can interact with surrounding biological molecules (as the protein corona). The mere presence of serum proteins in the surrounding media of NPs will automatically lead to a tight association of both entities [114]. These proteins interacting with NPs undergo conformational changes. These conformational changes could have profound effects on cellular well-being since our immune system may then not recognize these proteins as native but rather as foreign objects and may try to eliminate them, inducing then autoimmunity. Binding of serum proteins to NPs may also directly affect their endocytic route and degree of cytotoxicity [115]. NPs can also interact directly with other biological molecules, such as lipids. Depending on the surface charge density, NPs can directly adhere to lipid membranes and induce structural defects, leading to cellular penetration of the particles. This direct penetration into the cell opens a path for intracellular delivery bypassing the endocytic machinery, but could also induce specific toxic effects [116].

In order to fully exploit the properties of the NPs, external stimuli are often required (e.g. exposure to a magnetic field or light) in order to put the NPs to full use. However, these external factors can also induce alterations in the NPs which lead to potential toxic effects or directly influence cell homeostasis. Quite often, these traits (fluorescence quantum yield, magnetic moment) are linked to the NP structure and surface properties and will therefore be greatly affected by NP degradation, protein binding or alterations to the immediate NP environment [117-120].

A complete set of toxicity tests to screen the adverse effects caused by the nanoparticle administration must be defined in terms of the nanoparticle properties and applications. Due to the enormous quantity of nanomaterials and their properties, each list trying to enclose every possible parameter will be incomplete. However, a great variety of reviews enlisting numerous probes to evaluate nanoparticle safety and biocompatibility exist in the literature [55, 94, 121-124] (just to mention some recent or relevant examples), and can help for this objective.

After the cellular uptake, intracellular location, translocation of nanoparticles, and possible metabolic effects, the next question is their function, biological consequence and finally the elimination by the body.

1.2.4. Clearance of nanoparticles

The circulation of nanomaterials in bloodstream is critical for their delivery, dynamics of tissue redistribution, and the overall targeting of drug carriers to specific cells and organs.

The physicochemical interactions occurring between nanomaterials and the biological medium after their introduction into living systems may further influence the blood circulation and clearance profiles. For example, the protein corona formation consequently leads to NP recognition

as well as uptake by mononuclear phagocytic cells, to removal from the circulation and despite their very small size to accumulation in the organs of the mononuclear phagocyte system such as liver and spleen [125]. These interactions can alter properties such as agglomeration, phase transformations, dissolution, degradation, protein adsorption, and surface reactivity [126]. However, the lung, liver, spleen and kidney are the major distribution sites and target organs for nanomaterials exposure, and their clearance patterns in these organs are critical for understanding the nanomaterials *in vivo* fate (Figure 1.15) [126].
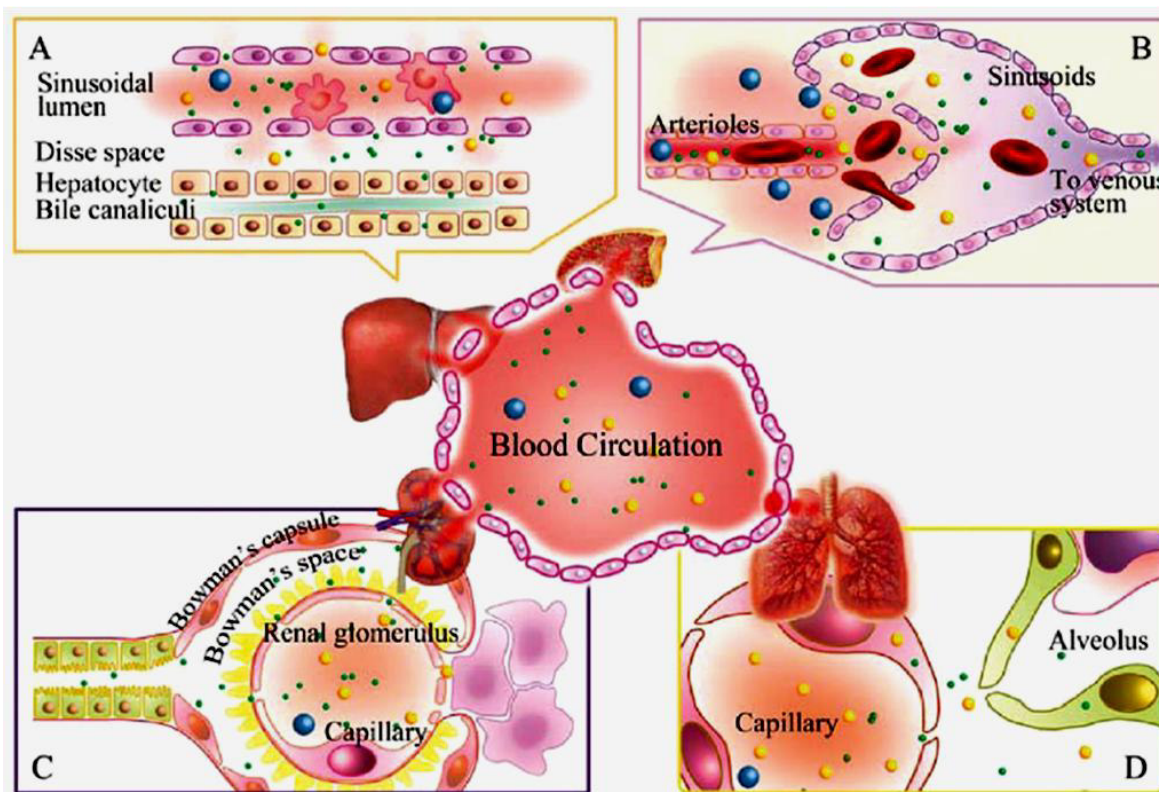
Fig. 1. 15. The tissue-specific extravasation of nanomaterials. A) Liver, B) spleen, C) kidney, and D) lung [126].

The mechanisms and parameters describing the preference for any of the above enlisted organs to nanoparticle clearance will be briefly mentioned in the next lines.

The lung is in direct contact with the environment, and is likely to be the first port of entry for the inhaled nanoparticles (from the environment or from pharmaceutical formulations in aerosols) into the body. Airway and alveolar macrophages are at the forefront of lung defense. Phagocyte uptake, in concert with mucociliary transport, is the main mechanism for foreign intruder removal; however this mechanism is size-selective and quite inefficient for nanomaterials smaller

than 100 nm [127-129]. In case of nanoparticle agglomeration once they are in contact with biological systems, with remarkably enlarged size and varied shape they are always found in alveoli during the initial stage of exposure. These agglomerates are large enough to be efficiently eliminated by phagocytic uptake followed by mucociliary movement [129, 130]. Other mechanisms like macropinocytosis or pinocytosis, that is, clathrin- or alveolae-mediated endocytosis [72], are possible but so far seem not to induce nanomaterial accumulation in macrophages and lead to macrophage-associated removal of nanomaterials [129]. Intracellular particle dissolution is an additional clearance pathway; its rate depends on particle physicochemical characteristics such as size, density, surface area, and chemical composition [131].

Upon intravenous injection, circulating NPs distribute in the body and flow along with the blood stream into the kidneys [132]. These organs possess innumerable microscopic filtration units called renal corpuscles, each of which is composed of the glomerulus (a dense capillary network) and a Bowman's capsule. The endothelium of the glomerular capillaries possesses pores (fenestrae) and is surrounded by the highly negatively charged glomerular basement membrane. Since fenestrae and slit pores have a maximal diameter, glomerular filtration is highly dependent on molecule size [126, 133]. As a consequence, nanoparticles with an *in vivo* hydrodynamic diameter <6 nm are filtered charge-independently, while those >8 nm bypass the filtration process, remain in the circulation and exit the glomerulus via the efferent arterioles. NPs within the 6-8 nm range are filtered through the glomerular capillary wall depending on their charge. Particles with cationic surfaces are more readily filtered than their equally sized counterparts possessing anionic surfaces due to electrostatic repulsion by negative charges of the glomerular basement membrane. After transglomerular passage into the Bowman's space, nanoparticles may be reabsorbed within the proximal tubule, transported from the lumen to the renal interstitium and further into the circulatory system [134, 135]. NPs remaining in the non-reabsorbed filtrate (tubular fluid) pass through to the collecting duct to form urine, which finally exits the kidneys, enters the bladder through the ureters and is excreted via the urethra. While renal elimination minimizes the residence time of NPs in the body, it is nonetheless considered as the preferred route for the removal of non-biodegradable materials. In particular, renal clearance is a highly desirable trait for diagnostic NPs in order to reduce retention in non-targeted tissue, to achieve reasonable signal-to-background ratios shortly after injection by efficient excretion of unbound probe from the body and to minimize NP toxicity [10]. For larger non- biodegradable particles, the reticulum endothelial system (i.e. liver and spleen) represents the only alternative mode of elimination.

Liver is the main organ of metabolic clearance of most drugs and xenobiotics. NPs bypassing the renal filtration process will inevitably end up in the spleen and in the liver [126]. The latter organ has a dual vascular supply, whereas it receives oxygenated, arterial blood from the hepatic artery as well as blood that have previously passed through the intestine and spleen via the hepatic portal vein. Both, venous as well as arterial blood is mixed in the liver capillaries (sinusoids) and then exits the liver through the hepatic veins. The hepatic sinusoids are lined mainly by liver sinusoidal endothelial cells and resident liver macrophages (Kupffer cells). Both cell types, also collectively referred to as scavenger cells, are responsible for most of the liver uptake of

intravascular NPs [136-138]. The very thin liver sinusoidal endothelial cells act as a filter between the lumen of the hepatic sinusoids and the surrounding hepatocytes, which is achieved by the presence of numerous transcellular pores in liver sinusoidal endothelial cells (fenestrae, with diameters ranging from 50-300 nm in humans) [139]. Soluble substances and NPs smaller than these pores pass from the sinusoids into a sub-endothelial space and come directly in contact with underlying hepatocytes. Upon internalized, NPs are subjected to intracellular enzymatic breakdown potentially leading to the disruption of the surface coating, dissolution of ions out of the inorganic crystal core as well as release of their components [140, 141]. After being degraded by these cells, NP metabolites are potentially secreted by hepatocytes into the bile and finally excreted with the faces [126, 142]. As mentioned above, Kupffer cells and liver sinusoidal endothelial cells represent the major cell types responsible for liver uptake and metabolism of NPs. The uptake and accumulation of nondegradable can stimulate free radical release which may result in cell damage and inflammation [143-145].

By its side, in sinusoidal spleen, blood flows through the discontinuous capillary into splenic venous system. Large entities sized above 200 nm may be cleared from blood by splenic filtration [126, 146].

According to the basic principle for safety, biomedical agents should be effectively cleared from the body and have little accumulation within the organs. The efficient clearance of nanomaterials determines the balance between nanomaterial-induced activity and toxicity. So far, most *in vivo* studies indicate that nanomaterials shown unspecific uptake in the reticulum endothelial system, have high tendency to accumulate within the organs over an extended time, and are slowly degraded or excreted from the body [126].

The physicochemical properties of nanomaterials change dynamically *in vivo* thereby making the prediction of their metabolism and final fact in the organism a complex and difficult task. The knowledge of some parameters as size, surface charge density and stability are paramount during nanoparticle formulation, or once they have been submitted to biologically relevant conditions.

1.3. COLLOIDAL STABILITY OF NANOPARTICLES

For all their applications, the stability of nanoparticles dispersions is paramount. The kind of nanoparticle instability may share some different effects on living organisms.

Stability issues associated with nanosuspensions can be categorized as physical and chemical stability. The common physical stability issues include sedimentation/creaming, agglomeration, crystal growth and change of crystallinity state. Although sedimentation is one of the key issues for colloidal suspension, the reported studies examining sedimentation issues in aqueous-based nanosuspensions are very scarce. This could be due to (i) surfactants that are generally used in most of the nanosuspensions to inhibit particle agglomeration in the medium, which alleviates the sedimentation issues and (ii) the small nano-sized particles significantly reduce the sedimentation rate [147].

Nanoparticles can either settle down or cream up in a suspension depending on the density relative to the medium, and according to Stokes´ law the viscosity, particle size, and densities of dispersed phase and dispersant play a determinant role in sedimentation rate [148]. The large surface area of nanoparticles creates high total surface energy, which is thermodynamically unfavorable. Accordingly, the particles tend to agglomerate to minimize the surface energy. Agglomeration can cause a variety of issues for nanosuspensions including rapid settling/creaming, crystal growth and inconsistent dosing [149].

Stability is one of the critical aspects in ensuring safety and efficacy of intravenously administered nanosuspensions. For example, during nano-drugs administration, formation of larger particles a big as 5 µm could lead to capillary blockade and embolism, or deposition in different organs, causing severe healthy problems [147, 150]. The kind of nanoparticle instability may share some different effects in living organisms. For instance particle agglomeration could be a major issue in pulmonary drug delivery since it affects deposition amount/site, and thus, drug efficacy. On the other hand, agglomeration in intravenous formulations can cause blood capillary blockage and obstruct blood flow [151, 152].

The physicochemical characteristics of the surrounding media of the NP such as pH, ionic strength, nature of solvent, and electrolytes, etc., and the presence of organic components, like natural organic matter, polysaccharides and proteins, can also affect suspension stability and lead to NP agglomeration/aggregation, further affecting the exposed area and dissolution of the particles. Both, the kinetics of dissolution and the saturation concentration may vary for the same NP when suspended in different exposure media [153].

1.3.1. The role of attraction and repulsion forces in colloidal stability

There are two main mechanisms through which colloidal suspensions can be stabilized in both aqueous and non-aqueous medium: steric stabilization and electrostatic repulsion [148, 154].

In steric stabilization, amphiphilic non-ionic stabilizers are usually utilized to provide steric stabilization which is dominated by solvation effect. As the non-ionic stabilizers are introduced into nanosuspensions, they are absorbed onto the particles through an anchor segment that strongly interacts with the dispersed particles, while the other well-solvated tail segment extends into the bulk medium. In addition to solvation, the stabilizing moiety needs to be sufficiently long and dense to maintain a steric barrier that is capable of minimizing particle–particle interaction to a level that the Van Der Waals attractive forces are less than the repulsive steric forces [155].

Built on the basis of Gouy-Chapman model of the particle-solution interface, DLVO theory [156] developed in 1940's by Derjaguin and Landau, and Verwey and Overbeek, separately, explained the stability of colloids by drawing a balance between the repulsive electric double layer forces and the attractive, short-range Van Der Waals forces. The electrical double layer consists of two layers: Stern and Gouy layers. They are represented in the Figure 1.16 [147].
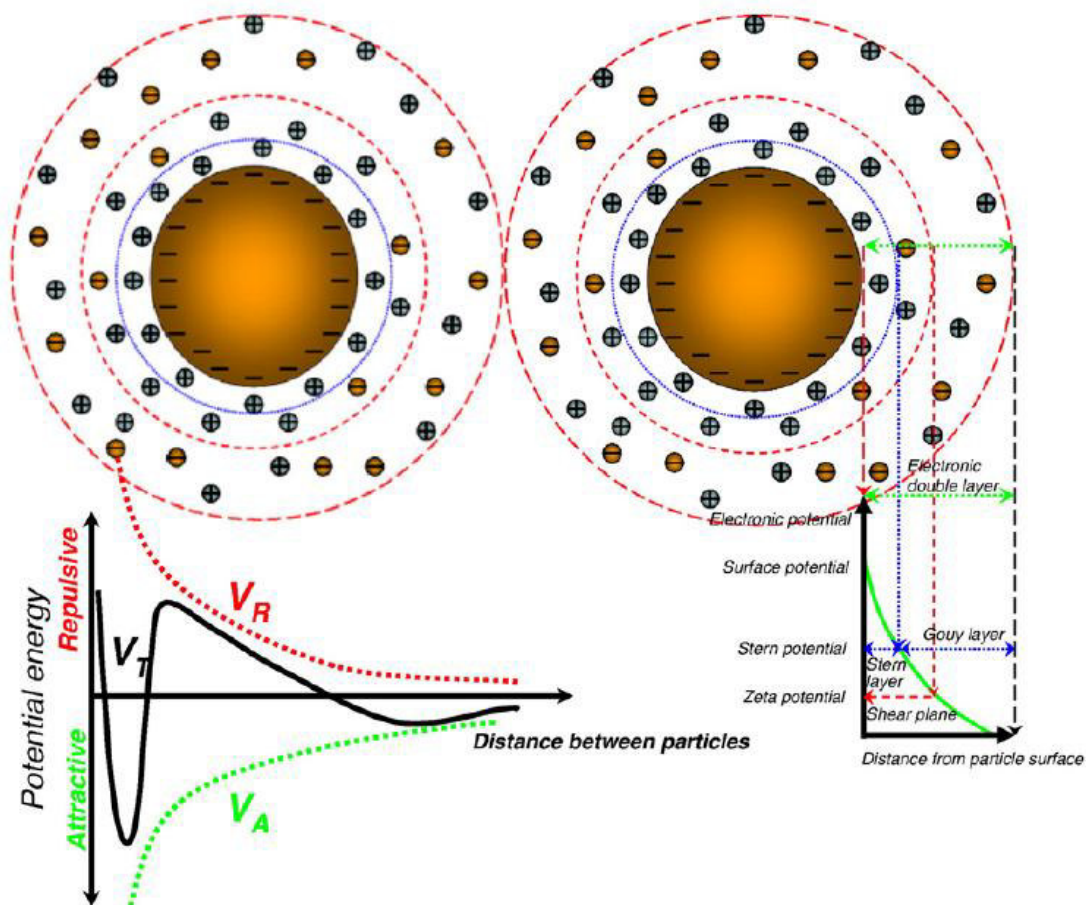
Fig. 1. 16. Illustration of attractive and repulsive forces between nanoparticles according DLVO theory [147].

The first one is composed of counter ions attracted toward the particle surface to maintain electrical neutrality of the system, while the second one is composed essentially by a diffusion layer of ions [147].

According to the nomenclature of DLVO theory, the total potential energy (V_T) is given by the sum of repulsion (V_R) and attraction (V_A) potentials. The repulsive forces (V_R) are originated from the overlapping of electrical double layer surrounding the particles in the medium, and thus preventing colloidal agglomeration. On the other side, the attractive forces (V_A) are produced by chemical interactions. V_R is extremely sensitive to ion concentration in the medium. As the ion strength is increased in the medium, the thickness of electrical double layer decreases due to screening of the surface charge. This causes decrease in V_R, increasing the susceptibility of the dispersed particles to form aggregates. By its side, V_A is determined by the Hamaker constant, particle size and inter-particulate distance while V_R depends on particle size, distance between the particles, ion concentration, dielectric constant of the medium and zeta potential [148, 157].

1.3.1.1. Zeta-potential

Zeta potential (ζ-potential) is the electrical potential at the shear plane which is the boundary of the surrounding liquid layer attached to the moving particles in the medium. The high absolute value of zeta potential generates a repulsive electrostatic force between the particles, which is a key property of an agglomeration resistant suspension. The suspension is more stable at higher ζ-potentials [158, 159]. The electrostatic stability of a suspension is widely considered to be sufficient when the absolute ζ-potential value is 30 mV or higher.

ζ-potential is sensitive to the surrounding medium basically in two different ways. The surface charge of nanoparticles in most cases is originated from the pH-dependent ionization of the surface groups. The influence of pH changes can be characterized by determining the isoelectric point [160]. The isoelectric point is pH value where zeta potential reaches the zero value.

For biomedical applications the dissolution medium must satisfy some conditions such as isotonicity, i.e. a solution having the same ionic concentration as the other solution with which it is compared. The isotonic concentration of an aqueous solution can be estimated by comparing its freezing point depression to an isotonic sodium chloride solution. Two solutions with the same freezing point depression have the same osmotic pressure, and they are referred to as isosmotic. For example, an queous 0.9 w/v % (150 mM) solution of sodium chloride is isotonic with blood, thus creating a minimal change to the osmotic pressure of blood when injected [161].

Another impact of the medium arises from the fact that zeta potential is calculated from particle mobility measurement, in which the adsorbed surface layer cannot be distinguished from the moving body [162]. The Zeta potential is a powerful indicator of nanoparticles surface charge density, and suspension stability in a biologically relevant medium [158]. Size and surface charges of NPs are strong determinants of the biokinetic fate in the organism. In example, surface charge

affects the biodistribution of NP so that positively charged particles accumulate more in the kidneys while negative and non-charged particles showed a higher accumulation in the liver [163].

Differently to the Nerst potential (the potential at the surface of the nanoparticle), the ζ-potential can be easily accessible by measuring the electrophoretic mobility once the nanoparticle is submitted to an external electric field. Therefore, the measurement of the ζ-potential has become essential for nanoparticle research. However, the interpretation of nanoparticle electrophoretic mobility can be a complex undertaking [159].

The choice of the adequate model to convert electrophoretic mobility into zeta potential is not an easy task, and a complete set of parameters and theoretical calculations must be considered to obtain more reliable values. A complete guide for this purpose was reported by *Delgado et al.* [164], and the most actualized model has been reported by *Pyell et al.* [165]. Their use and application will be properly described in the Chapter II of this work for the ζ-potential calculation of the ZGO-NPs.

Different methods are currently used to determine the electrophoretic mobility of the nanoparticles and thereby the ζ-potential, and in combination with the DLVO theory are greatly applied to determine and optimize nanoparticle stability. The determination of ζ-potential as well as the characterization of the other parameters defining the nanoparticles is mandatory for their applications in the biomedical field.

1.4. ELECTROKINETIC METHODS FOR NANOPARTICLE CHARACTERIZATION

Nowadays engineered nanoparticles (NPs) surround us, leading to many and highly valuable applications in different domains such as electronics, pharmaceutics, cosmetic, food or material industries. Thanks to their unique properties they are revolutionizing and pushing up different research areas including biomedical, material, physics and chemistry sciences, and thereby our society. Nevertheless, those properties are hardly dependent on the nature, size, shape, surface chemistry and chemical environment of these materials [166, 167]. Moreover, their use for biomedical applications implies the study of other important parameters such as biocompatibility, colloidal stability in physiological environments, possible biomolecule interactions (i.e. the so-called protein corona) and the final fate of these NPs, among others [168, 169]. Therefore, a detailed characterization of the entire NP is crucial not only for the improvement of their design, synthesis, properties and applications but also to better understand their behavior and final fate in physiological media and *in vivo* systems. Regarding these concerns the development of reliable analytical methodologies and the adaptation of existing ones to the nanoscale level of analysis is a present demand to perform adequate NP characterization.

Among the different methods commonly used to attempt this objective [167, 170, 171], electrokinetic separation methods have been recently proved as attractive and powerful ones for the complete physicochemical characterization of NPs and the study of their behavior in physiological environments. Initially, the general techniques for size and ζ-potential determination are briefly described on this section. Herein, some concepts of the electrokinetic methods along with the parameters and information that could be obtained will be detailed. Relevant examples to illustrate the recent developed methodologies for NPs characterization and evaluation of their behavior in biological systems will then be given. Finally, some trends and research lines envisaged in this domain will be discussed.

1.4.1. General methods for nanoparticle size distribution and ζ-potential determination

Particle size and size distribution are the key parameters used for evaluating the properties and physical stability of nanoparticles. A variety of techniques, including dynamic light scattering, laser diffraction, and coulter counter, are commonly used to measure the particle size and size distribution [147, 172, 173] (Table 1-1)

Table 1- 1. Commonly used techniques to evaluate the stability of nanoparticles.

Measured parameters	Techniques	Remarks
Particle size and size distribution	DLS	*Pros*: rapid, non-invasive *Cons*: limited measure range; apply only to liquid suspension.
	Laser diffraction	*Pros*: wide measurement range, rapid, non invasive, apply to both liquid suspension and dry powder samples. *Cons*: particles are assumed to be spherical
	Coulter counter	*Pros*: precise *Cons*: apply only to spherical particles
Particle size and morphology	SEM/TEM	*Pros*: evaluate both particle morphology and size, very small quantity of sample required *Cons*: challenging to acquire statistical size distribution, usually invasive, time-consuming
	AFM	*Pros*: non-invasive, evaluate both particle morphology and size, very small quantity of sample required *Cons*: challenging to acquire statistical size distribution, time consuming
Sedimentation/ creaming	Visual observation/laser backscattering/near infrared transmission	-
Particle surface charge/zeta potential	Laser Doppler electrophoresis	-
Crystallinity state	XRD/DSC	-
Chemical stability	HPLC/FTIR/NMR/MS	-

DLS : Dynamic light scattering ; SEM : Scanning electron microscope, TEM: Transmission electron microscope; AFM: Atomic force microscope; XRD: X-ray diffraction; DSC: Differential scanning calorimetry; HPLC: High performance liquid chromatography; FTIR: Fourier transform infra-red spectroscopy; NMR: Nuclear magnetic resonance; and MS: Mass spectrometry.

Dynamic light scattering (also known as photon correlation spectroscopy and quasi-elastic light scattering) is one of the most popular methods for determining size and size distribution of nanoparticles in a suspension [150]. The principle of this technique is to monitor the temporal fluctuation of the elastic scattering intensity of light, i.e., Rayleigh scattering, induced from the Brownian motion of the particles/molecules of a size much smaller than the incident light wavelength, at a fixed scattering angle [174-176]. However this is an expensive technique and it is unsuitable for accurate quantification due to frequently observed presence of impurities or interferences [173]. The mean particle size and distribution indicated as polydispersity index (PDI)

are the typical measured parameters of this technique. A PDI value of 0.1 to 0.25 indicates a narrow size distribution while a PDI greater than 0.5 refers to a broad distribution [150].

By its side, laser Doppler electrophoresis (also known as electrophoretic light scattering) is also a commonly used technique to measure zeta potential. This technique evaluates electrophoretic mobility of suspended particles in the medium and then is transformed by mathematical equations into zeta potential. In a LDE experiment, a laser beam is split into reference and excitation beams (Figure 1.17A). The excitation beam is directed through the sample while an electric field E is applied to induce NP electrophoresis (Figure 1.17B). Upon recombination of the scattered and reference beams, a difference frequency is produced, which is measured by the LDE detector to provide the particle electrophoretic drift velocity v. Even though an alternating electric field (at kHz frequencies) is often applied, the NP response at sub-MHz frequencies is quasi-steady [159].
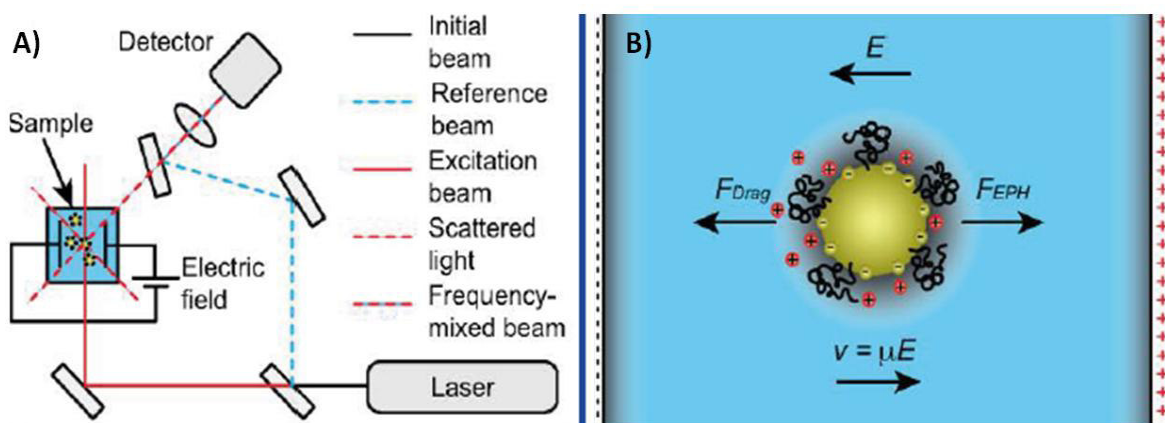
Fig. 1. 17. Schematic laser Doppler electrophoresis setup (A), and migration of a nanoparticle as an effect of the applied electric field [159].

Both LDE and DLS are very popular techniques due to its accessibility through the well known ZetaSizer instrument, from Malvern.

Recent progress in the development of functional, versatile NP for use in workable devices has led to the need for methods for monitoring NP properties, such as size distribution, surface charge, and reaction efficiencies of various surface functionalization strategies [177]. Instrumental tools for determining nanocrystals size and size distribution have been well established for NP characterization. However, elucidation of surface properties, particularly in solution, is less well developed. For example, modification of a crystal surface to provide water solubility by exchanging hydrophobic surface ligands with hydrophilic ligands or formation of a lipid bilayer with amphiphiles can drastically affect nanocrystals properties such as hydrodynamic radii, zeta potential, NP diffusion rates, cytotoxicity, luminescence quantum efficiency, and longevity.

However, techniques such as TEM (transmission electron microscopy) and X-ray diffraction can only probe the nanocrystal inorganic core and not the surface coating. As well, even when UV-Vis and DLS have been applied to estimate properties of NPs, such as hydrodynamic radius and solution stability [178], these techniques typically require large sample concentrations and are often at the lower edge of the size range capabilities of most DLS instruments. So, the development of innovative techniques allowing characterizing nanoparticles in relevant aqueous media and giving additional or complementary information is necessary.

1.4.2. Capillary electrophoresis: Principles

Capillary electrophoresis (CE) is an analytical method based on the separation of the analytes under an electric field, within a capillary, leading to different electrophoretic mobilities. It is a powerful analytical technique with exceptional separation mechanism, speed, efficiency and versatility. Generally, separation takes place in narrow-bore capillaries (10–100 μm internal diameter, and a length in the range of 10-100 cm) filled with buffer solution and subjected to high electric fields (typically 5–30 kV) (See Figure 1.18). The essential instrumentation of CE is simpler than in other techniques, consisting only of electrodes, a capillary, a power supply, a sample introduction system and the detector. The detection can be on-line [ultraviolet/diode-array (UV/DAD), spectrophotometric, spectrofluorimetric and electrochemical detectors] or off-line [mass spectrometer (MS)] [179].
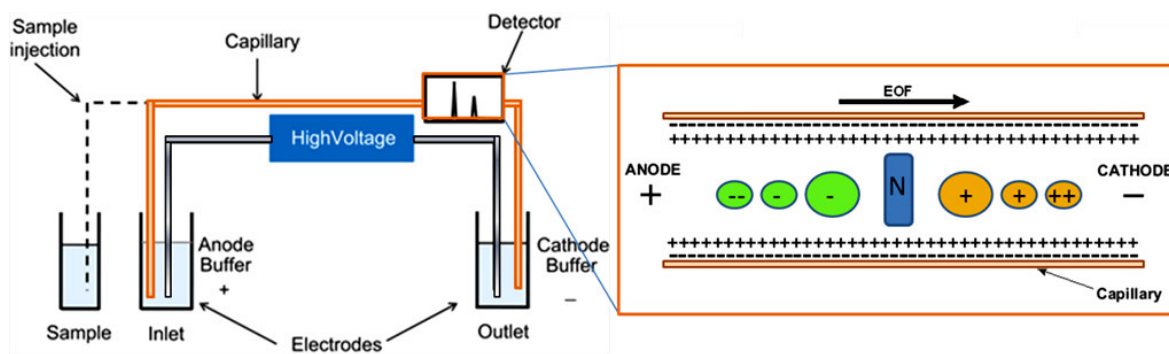
Fig. 1. 18. Standard capillary electrophoresis setup.

Analytes are separated on the basis of their differential mobilities in the running buffer, consisting of a buffer with possible additives such as micelles, ligands.... Accordingly, driving forces in CE are electrophoretic migration, the electroosmotic flow (EOF) and, in some modalities, the distribution of the analyte with pseudostationary phases [180-182].

CE presents several advantages, such as high separation efficiency in aqueous, hydro-organic or organic media, low sample and products consumption, simple sample preparation, accurate

quantitative analysis, reduced analysis time and a high degree of automation [66, 183]. In comparison to other separation methods, the separation capillary is free of stationary phase, therefore allowing mimic the *in vivo* conditions for the study of biochemical events without any competing interaction [184-188]. This property is important as it permits the characterization of surface-functionalized NPs, describing nanoparticle-ligand binding, which is a key parameter in production control and stability of nanoparticles, and therefore, its quality and application [189, 190]. A full list of the capillary electrophoresis applications for nanoparticle characterization is detailed below. Particular emphasis is put in the characterization of nanoparticles used for biomedical applications and in the CE electrophoresis applications to better understanding of the NP behavior in biological systems.

1.4.3. Applications of electrokinetic methods for nanoparticle characterization: the current context

Capillary electrophoresis (CE), the most employed format of electrokinetic separations, provides a high-resolution separation method of any type of compounds in a complex mixture, based on intrinsic molecular properties such as charge, frictional forces, and hydrodynamic radii.

Capillary electrophoresis has shown to be able to separate, identify, and characterize different small objects, including from small molecules til microorganisms [191]. By using this method, particles of different nature have been separated: synthetic based on polystyrene, ,latex and other polymers, inorganic (gold, silver, silica, iron (III), alumina, etc.), quantum dots, carbon nanotubes, and biological entities (lipoproteins, viruses, cells), etc. [184-186]. CE has been evidenced as an attractive approach for NP physico-chemical characterization and thereby, contributes to the development of new nanomaterials for biomedical applications. An actualized summary of the CE applications for NP characterization and optimization is presented in the Figure 1.19 [192].

The electrophoretic mobility, that is calculated from measured migration time and experimental parameters such as capillary total length, length to detector and applied voltage, allows the determination of several physicochemical parameters of nanomaterials including equivalent spherical diameter, ζ-potential, surface charge density, grafting rates and binding parameters. Furthermore the colloidal stability can be estimated from the electrophoretic profiles and eventual size and ζ-potential variations [193]. For such purpose different CE working modes (e.g. capillary zone electrophoresis CZE, micellar electrokinetic chromatography MEKC, frontal analysis capillary electrophoresis FACE and affinity capillary electrophoresis ACE) and mathematical approaches that relate the electrophoretic mobility with those parameters, have been proposed [194-197]. Finally, it should be mentioned a strategy that is gaining more and more relevance in the NP characterization domain that is the Taylor dispersion analysis (TDA). Although it is not an electrokinetic method by itself, the CE instrument fulfills the requirements for performing this kind of analysis. TDA is an absolute method for determining the diffusion coefficient of a given sample in a laminar flow [198]. This diffusion coefficient allows for the determination of the mean hydrodynamic radius and the size distribution of a given particle population. This approach nevertheless suffers from a lack of selectivity. However, this drawback

has been overcome with promising results by the online coupling of CE and TDA, constituting a trending topic in the domain [199]. Thus, CE could be exploited for NP separation and then the dispersion of each separated sample zone could be estimated by TDA all in a single run.
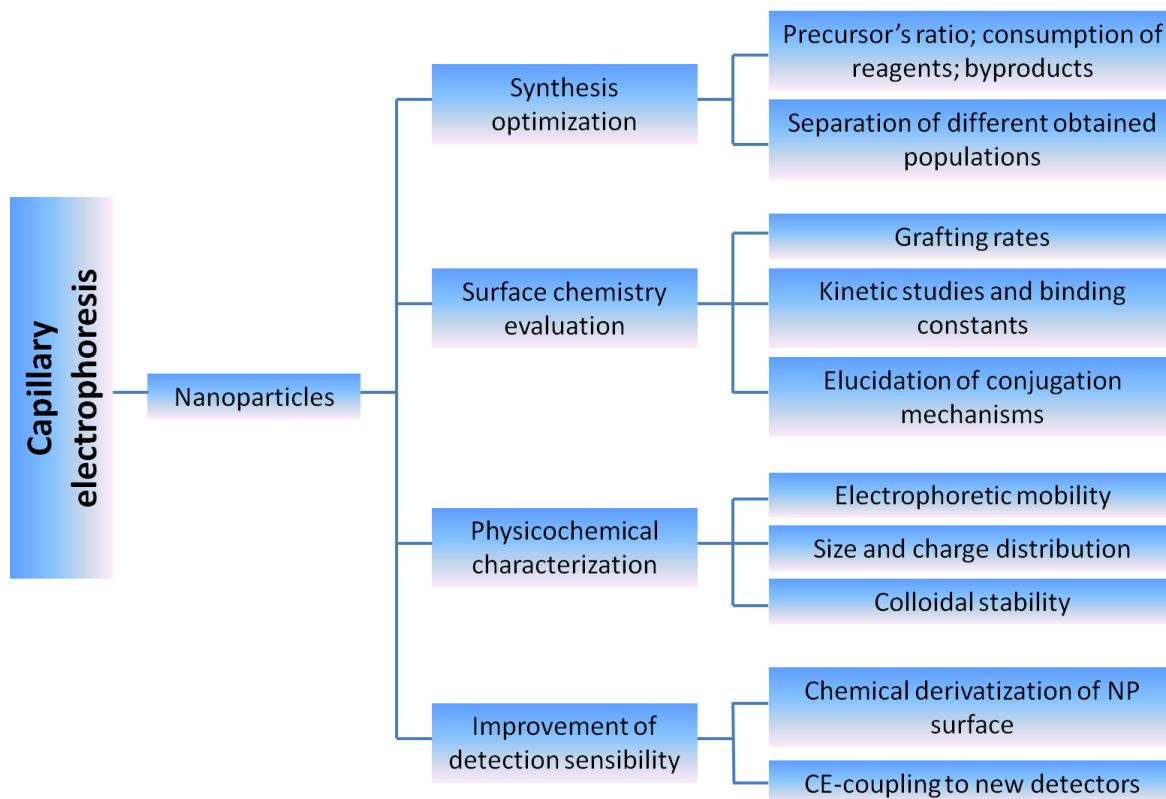
Fig. 1. 19. A comprehensive scheme for the control and optimization of nanoparticle synthesis and properties based on analytical electrokinetic methodologies (Adapted from [192]).

Another important application of CE is the determination of NPs-biomolecule interactions (namely proteins, peptides, DNA, RNA, aptamers and dendrimers in the current research context), uptake and interactions of NPs with viruses. The estimation of binding information using CE methods can be done by measuring the signal of either free or conjugated biomolecule or NP in function of their respective concentrations. Thus, different interaction parameters can be obtained by subsequent data treatment using well-defined mathematical models relating the concentration of biomolecules bound to NPs, i.e. binding constants, number of binding sites, binding saturation, kinetics, stoichiometry and cooperativity [169, 200]. This specific CE application will be described and exemplified in the last section of the theoretical fragment.

Nevertheless, CE also has its own limitations to be applied for the characterization of nanomaterials. Generally is accepted that electrophoretic migration of nanoparticles is much more complex phenomenon than migration of a typical solute.

Theoretical principles of separations of micro and nanoparticles by CZE: In an electrolyte solution, a charged particle is surrounded by the "ionic atmosphere" which is a diffusive part of the electric double layer. During electrophoresis, the particle´s translational motion results from the balance of three forces: i) The driving force is exerted on the particle by the external electric field (due to the particle´s electrokinetic charge) and is balanced by ii) the Stokes viscous drag and by iii) an "additional" hydrodynamic force – the electrophoretic retardation, for small particles it is balanced mainly by the "ordinary" hydrodynamic resistance (the Stokes drag) [187, 201]. As a precise operational limitations, NP adsorption onto the capillary wall, intra-capillary floculation phenomenon, detection sensitivity and lack of reference materials. Concerning NP adsorption, capillary inner wall modifications are required for the separation of positively charged NPs [202, 203], either by permanent or dynamic coatings. In addition, analytical standards and reference materials are not generally available for nanoparticles at the moment; consequently, development of precise quantitative methods for the analysis of nanoparticles in real samples is still difficult [59].

Although their limitations, CE offers very interesting performances the sensitivity is one of its weak points. Great efforts are being done to increase detection sensitivity by coupling CE to highly sensitive and specific detectors such as laser induced flurescence (CE-LIF), electrochemical (CE-EC) and inductive-coupled plasma mass spectrometry (CE-ICP-MS) detectors. Regarding the evaluation of NP-biomolecule interactions, the difficulty to separate and quantify adsorbed proteins onto NPs from the serum with sufficient sensitivity remains a challenge [66], and the most part of the publications reporting the use of CE-based binding assays are relatively simple in composition, involving normally the interaction of the NPs with individual and pure biomolecules and rarely in a mixture of them.

Once critically revised the performances of CE, some selected examples showing the more representative and recent applications of this technique for the characterization of NPs and their evaluation in biologically relevant systems will be addressed. In this regard CE offers a unique vision being useful not only to assess the physicochemical properties of NPs but also to control and optimize their synthesis and surface modification. This section non-exhaustively describes recently developed and relevant CE methodologies for the physicochemical characterization of NPs as well as for the design and optimization of NP synthesis and surface modification procedures. Special emphasis is putted in the characterization of nanomaterials with potential biomedical applications. The different selected publications are presented according to NP nature, so as to allow the reader to have a general overview on the topic. Due to their relevance, we consider the characterization of nanoparticles used as drug delivery systems in a separate sub-section.

1.4.3.1. Noble-metal nanoparticles

Noble-metal NPs composed of gold and silver are the most studied. In general, this kind of NPs is very attractive for the scientific community due to their optoelectronic, photo-thermal and catalytic properties, which hardly depend on their size, shape and surface chemistry. Therefore a complete characterization is required to enhance their potential applications in fields such as biosensing, imaging or catalysis.

As mentioned above, the electrophoretic mobility is the key value to estimate characteristic parameters of NPs population using different mathematical approaches. In this sense, *Ute Pyell et al.* [165] have recently developed a new approximation that consists in a simplification of Oshsima's model [196], neglecting the impact of the electrolyte co-ion on particle electrophoretic mobility, and that describes properly the electrophoretic behaviour of Au-NPs. This approach is only valid for NPs with electric charges homogenously distributed and located within a very thin shell close to the surface of shear and for diluted NP dispersions (negligible interparticle interactions) in any buffered electrolyte. To go deeper, the authors combined CE and TDA methodologies in order to analyse Au-NP functionalized with different hydrophilic polymer coatings and thus estimated their ζ-potential, surface charge density, effective charge number and size distribution (monomodal, bimodal or multimodal). In a further experiment using CE+TDA approach they performed the transformation of the intensity-weighted electrophoretic mobility distribution profile of a given NP population into intensity-weighted hydrodynamic radius distribution [204] providing a calibration-free strategy for the accurate determination of NP size.

But CE methodologies are also used for monitoring the surface modification of NPs. For example, the on-line ligand exchange and the formation of self-assembled-monolayers of thiolated ligands over the surface of Au- and Ag-NPs have been recently reported [205]. For such purpose the NPs were injected into the capillary whereas the ligands were present as additives in the background electrolyte (BGE). The ligand exchange mechanism was observed thanks to significant shifts in the electrophoretic mobility of the NPs due to the modification of their surface charge. In addition, based on the differential affinity of evaluated ligands (thioctic acid and thiomatic acid) for each kind of NPs, the authors were able to separate mixtures having components of similar size and shape.

Detection sensitivity is another important issue in the development of CE methodologies for NP characterization. In the particular case of noble-metal NPs, inductively coupled plasma mass spectrometry (ICP-MS) is being investigated as highly sensitive detector for coupling to CE. ICP-MS detector is ideal for the analysis of metal NPs because it allows selective and sensitive metal quantification at very low concentration levels (ppt) in complex matrices and enables discriminating between metal NPs and the ionic forms of the respective dissolved elements. In this context, some pioneering works should be mentioned [206-208]. They apply different modes of CE (CZE and MEKC) to perform the separation, identification, size characterization and speciation of various metal NPs (Au, Ag, Pt and Pd) in complex matrices (dietary supplements, consumer products, river water and wastewater samples). MEKC was used to improve the resolution capacity of CE. Authors

observed that the addition of surfactants (at concentrations above their CMC) such as SDS improved the resolution of the size-based separation technique. These CE-ICP-MS methodologies provide unique and valuable information remarking their high resolution (being able to distinguish NP fractions of less than 10 nm) and speciation capability, good linear relationship between the electrophoretic mobility and the NP size (allowing the transformation of the electropherogram in a size distribution function), quantitative recoveries and very low detection limits. Thus, a promising future can be envisaged for CE-ICP-MS-based methodologies, not only as a reliable NP characterization technique but also for the rapid screening of NP presence in different samples or for the quality control of commercial products containing these materials. The coupling of CE to other detection systems such as dark-field microscopy (DFM) [209] and evaporative light scattering (ELS) [210] have been also investigated. In the first case the visualization in real time of events that take place within the capillary is afforded. Thus DFM allows corroborating analytic expression for the electrophoretic mobility, observing the movement of individual Au-NP capped with different ligands that confers them different surface charges (see Figure 1.20).
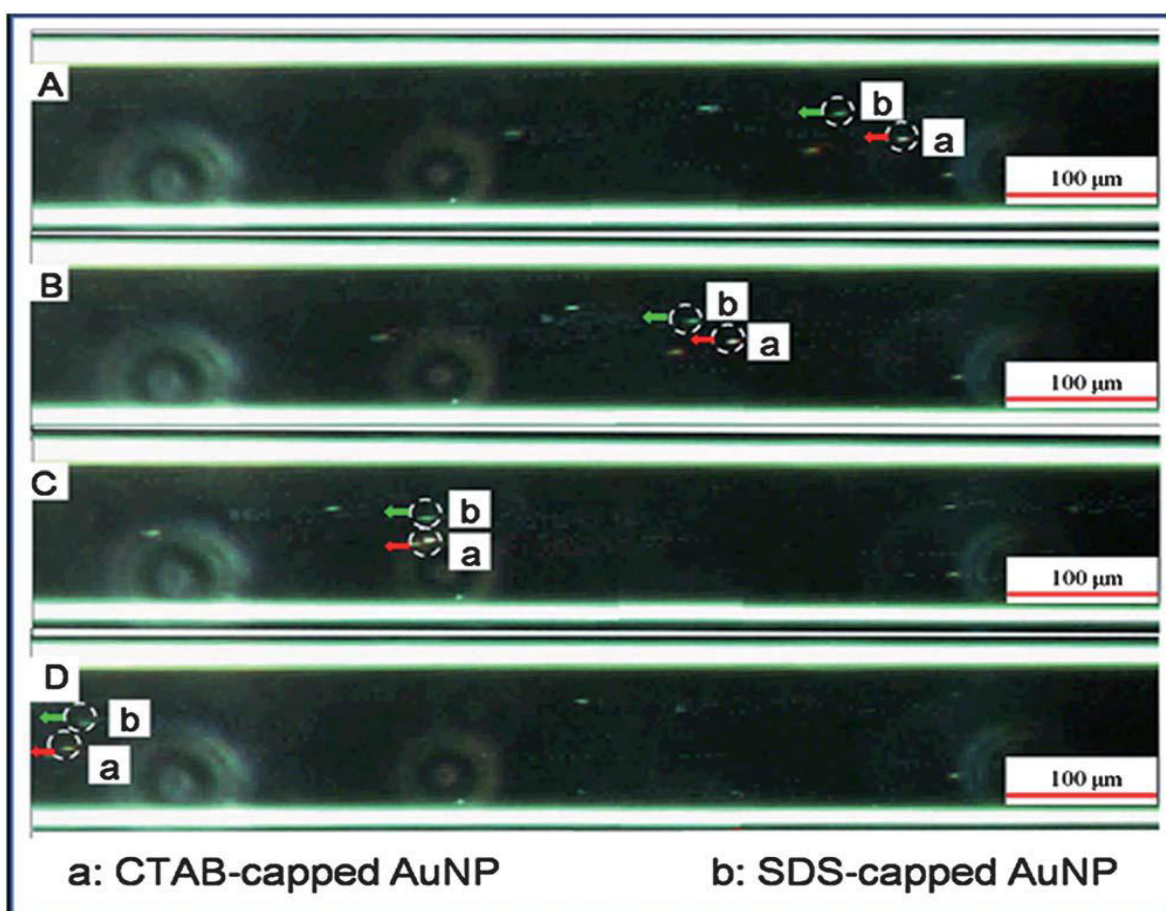
Fig. 1. 20. Electrophoretic behavior of positively charged AuNPs (single red CTAB-capped AuNP, a) and negatively charged AuNPs (single green SDS-capped AuNP, b) in situ visualized by capillary electrophoresis coupled to dark field microscopy detector. Conditions: 5 mM PBS (pH 9.0) ; electrokinetic injection,5 kV; separation voltage, 0.6 kV [210].

This system was applied for the size characterization of Au-NPs and authors envisaged promising applications in the investigation of NP-biomolecule interactions. ELS detector is presented as a promising detection alternative for CE. In this work authors are able to discriminate Au-NPs that only differ by 3 nm in size without the use of any additive in the BGE.

1.4.3.2. Quantum Dots

In 2014 two articles about this topic overview in depth the state of the art of CE methodologies for the analysis of QDs [211, 212]. Although they claim for reliable analytical standards to improve QD characterization and quantification using CE, they highlight that the latter is a powerful analytical tool not only to estimate fundamental parameters (size, size distribution, effective charge and concentration) but also to monitor and validate the synthetic process and to determine of the number of functions present at the surface of this nanomaterial. They also revised the different modes of CE (capillary zone electrophoresis, capillary gel electrophoresis, micellar electrokinetic chromatography and isotacophoresis) that are commonly used for the analysis and characterization of QDs, the use of additives or surfactants for the improvement of CE separation and the types of detection (UV-Vis and LIF) for the identification of QDs and their bioconjugates.

In the last year, the investigation focused on the determination of the number of ligands non-covalently attached to the surface of the QDs. In the work of *Vorácová et al.* [213] the electrophoretic mobility was correlated with the ζ-potential and thus the surface charges could be estimated as well as the number of ligands attached to the QD surface. In addition, the CZE methodology here developed also allowed the calculation of the binding constant of the ligands bond to QDs. The information provided by this CZE methodology is highly valuable because the knowledge of potential reactive sites for conjugation of QDs to biomolecules facilitates the design and the preparation of new nanoprobes. In addition, the knowledge of the binding constant permits the selection of appropriate conditions for both conjugation and purification processes.

1.4.3.3. Metal oxide nanoparticles

This group comprises a great number of different NPs (e.g. TiO_2, SiO_2, Fe_2O_3, etc.) that present a variety of interesting properties such as magnetism, persistent luminescence, conductivity or catalysis. CE has been widely employed for their characterization [214, 215]. In this section some of the lattest applications will be discussed.

An interesting parameter that can be assessed by CZE is the effective charge (q_{eff}) of a given object. This parameter controls the interactions between charged molecules. Its determination is based on the electrophoretic mobility and the diffusion coefficient (hydrodynamic radius) that can be obtained by CE and TDA analysis, respectively. Afterwards, different mathematical models (Nerst-Einstein, O'Brien-White-Ohshima, and Yoon and Kim) can be applied for the final estimation of the effective charge (q_{eff}), that are systematically compared in the work of *Ibrahim et al.* [197] in the case of small ions, polyelectrolytes and different NPs (magnetic beads, polystyrene

latex and cerium and titanium oxides). As for NPs, O'Brien-White-Ohshima and Yoon and Kim models turn out to be the most accurate for q_{eff}.determination.

1.4.3.4. Carbon-based nanomaterials

The carbon-based nanomaterials represent a wide family of nanomaterials on going from the fullerenes to the carbon dots. General properties that are appreciable in all of them are their stability and biocompatibility. Then, depending on each type of carbon-based nanomaterial, other optical, mechanical, thermal, catalytic and electric properties can be studied. Those features make them very attractive for numerous applications within biological systems, cosmetic products, electronics and photovoltaics. Some representative examples are selected to illustrate the use of CE for the characterization of the different types of these nanomaterials.

First CE methodologies have been optimized for the evaluation and control of the synthesis of carbon nanodots (C-dots). These NPs present a tunable photoluminescent emission, good photostability and excellent biocompatibility but their properties are highly dependent on their surface chemistry. In a recent publication [216] the group of Choi employed CZE for the control and optimization of the synthesis of C-dots. Here they evaluated the influence of the reaction time and molar ratio of NH_2/COOH precursors on the final composition of C-dots. The optimized CE methodology allowed obtaining information about the synthesis yields and grafting rates considering the relative increase observed for the peak intensity of each particle population.

The formation of nanoparticle aggregates is a current concern in the use of NPs. Frequently, it is the consequence of an inadequate colloidal dispersion or surface chemistry of NPs. This phenomenon can be evaluated by CE as performed in the cases of detonation nanodiamond (DND) [217] and fullerenes [218].

Although DND are increasingly used, some fundamental aspects regarding their characterization (e.g. wide type of surface chemistry, tendency to agglomerate, wide range of ζ-potential, physical and chemical heterogeneities) still remain a challenge in the understanding of their behaviour and properties. For such purpose *Duffy et al.* [217] developed a CZE methodology to evaluate the effect of BGE conditions (composition, concentration, and pH) on the electrophoretic behaviour of DND, as well as peak shape and tendency to agglomerate. They observed that the formation of aggregates is favoured by an increase in BGE ionic strength, due to counter-ion effect. Finally, they remarked the analytical performance CZE in terms of resolution and quantification of DND populations.

Fullerenes are well-known and studied nanomaterials and have been already characterized by CE as revised in a recent publication [219]. The last work found in the literature [218] deals with the study of the aggregation behaviour of both hydrophobic and hydrophilic fullerenes. The authors compare the performances of two CE modes (MEKC and CZE) using in both cases different concentrations of SDS as additive in the BGE. MEKC was applied with success for the analysis of hydrophobic fullerenes. Sharp peaks at identical migration time (migration time of the micelles)

were observed for all evaluated fullerenes indicating an absence of selectivity for hydrophobic fullerenes. MEKC was also applied for the characterization of hydrophilic fullerenes but in this case, higher buffer concentrations induced aggregation and consequently broad and distorted electrophoretic profiles. Nevertheless, the presence of SDS facilitated the separation of aggregates with different sizes or morphologies. In contrast, when working under CZE conditions (below CMC) sharper peaks were observed. These results in combination with the information provided by TEM and asymmetric field-flow field fractionation techniques (also allowing size determination) configure an interesting strategy for the evaluation of fullerene aggregation state of in aqueous solutions.

1.4.3.5. Polymeric nanoparticles

Polymeric NPs are promising materials for medical applications, such as drug delivery systems, thanks to their higher biocompatibility, low toxicity, drug carrying and controlled release capacities. Nevertheless, due to the large amount of parameters that affect their final properties (e.g. size distribution, chemical composition, hydrophilic/hydrophobic balance, surface effective charge, etc.) their characterization remains a challenging issue. In the last years different CE strategies have been proposed to carry out the characterization of these nano-objects.

In the first example, the size and effective charge of pGVE (hydrophilic polyglutamate backbone grafted with hydrophobic vitamin E) hydrogels, used as drug delivery systems, were determined by TDA and CE [220]. The TDA approach seemed suitable for the determination of the hydrodynamic radius of nanogels. The effective charge density was estimated by different electrophoretic approaches (Nerst-Einstein, O'Brien-White-Ohshima, Yoon and Kim) and resulting values compared to an indirect UV detection method. Only O'Brien-White-Ohshima and Yoon and Kim models led to results consistent with indirect UV detection measurements for the determination of the effective charge number per glutamate residue. In addition, authors demonstrated that the electrophoretic behaviour of such nanogels is similar to that of polyelectrolytes which is consistent with the high water content of pGVE.

The surface modification of dendrigraft poly-L-lysines has also been studied [221]. In this case the control of the click chemistry reaction, the kinetics and the characterization of final products were achieved by pressure assisted CE methodology. Thus, the purity and the homogeneity of these polymeric compounds could be controlled. In a further experiment TDA was applied to the final products to determine the diffusion coefficient and therefore the hydrodynamic radius of functionalized dendrigraft poly-L-lysines.

Finally, to prove the novel approach of the inline coupling between CE and TDA, *Oukacine et al.* [222] performed a size-based characterization of mixtures of 56 and 70 nm large nanolatexes. A scheme of the experimental set-up as well as the corresponding electrophero- and taylorgrams are presented in Figure 1.21.
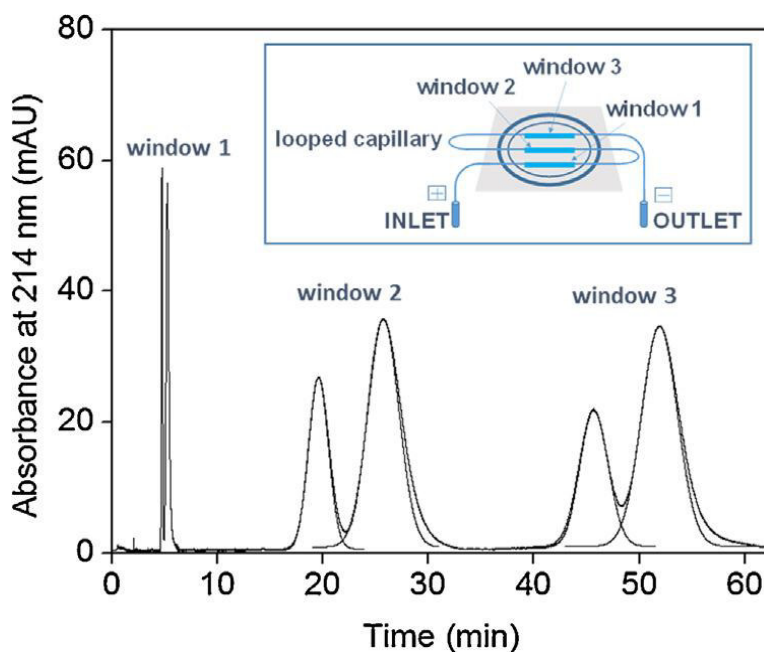
Fig. 1. 21. Online CE-TDA for the separation and the determination of the size of two nanolatexes (1.0 g/L and 2.5 g/L respectively). A schematic representation of the technical set-up is presented in the inset. Experimental conditions: fused silica capillary, 94 cm (27 cm to window 1, 42 cm to window 2, 57 cm to window 3) × 26 μm I.D.(365 μm O.D.). Hydrodynamic injection: 50 mbar, 28 s. Applied voltage: +30 kV during 6.2 min. Mobilizing pressure: 40 mbar. Electrolyte: 35.2 mM $Na_2B_4O_7$ + 1.0 mM Brij-35 (pH 9.2) [222].

As we can see, three windows are open in the capillary (Figure 1.21); the first one nearby the detector is the detection zone for the electrokinetic separation step. Once the separated zones passed the first detection window, the voltage was stopped and a pressure applied to further carry out TDA, peak broadening being monitored at the two other detection points. Thus, by combining the high separation performance of CE and the absolute size-based determination of TDA in one run a complete characterization of complex NP mixtures can be envisaged.

CE for the analysis of NPs as drug delivery systems with pharmaceutical relevance is another remarkable application. For the characterization of drug delivering NPs all the above mentioned CE modes have been applied to follow NP decomposition, concentration of free or encapsulated drug and the effects of the dispersion media [200].

1.4.4. Evaluation of nanoparticles as drug delivery systems

A relevant example of the characterization and evaluation of the performance of drug delivery systems by CE is the analysis of a platinum derivative-loaded polymeric micelles (PtDLPM) and their precursor (PEG-b-PGlu copolymer) [200]. The PEG-b-PGlu copolymer composition, separation and the quantification of the proportion of residual PGlu homopolymer in

the PEG-b-PGlu sample were performed by free solution CZE. This method allowed following the decomposition of PtDLPM incubated in a highly concentrated NaCl solution at room temperature. This mode brought also information on the sample polydispersity. MEKC showed hydrophobic interaction between SDS and both copolymer PEG-b-PGlu and polymeric micelles. A comparison of the interactions between PEG-b-PGlu unimers and polymeric micelles or surfactants was carried out by using the MEKC and Frontal Analysis Continuous Capillary Electrophoresis FACCE modes. The absence of adsorption of PEG-b-PGlu and PGlu onto the polymeric micelles has been demonstrated by FACCE. FACCE allows the determination of the concentrations of free ligand (and/or free substrate) at equilibrium conditions (Figure 1.22).
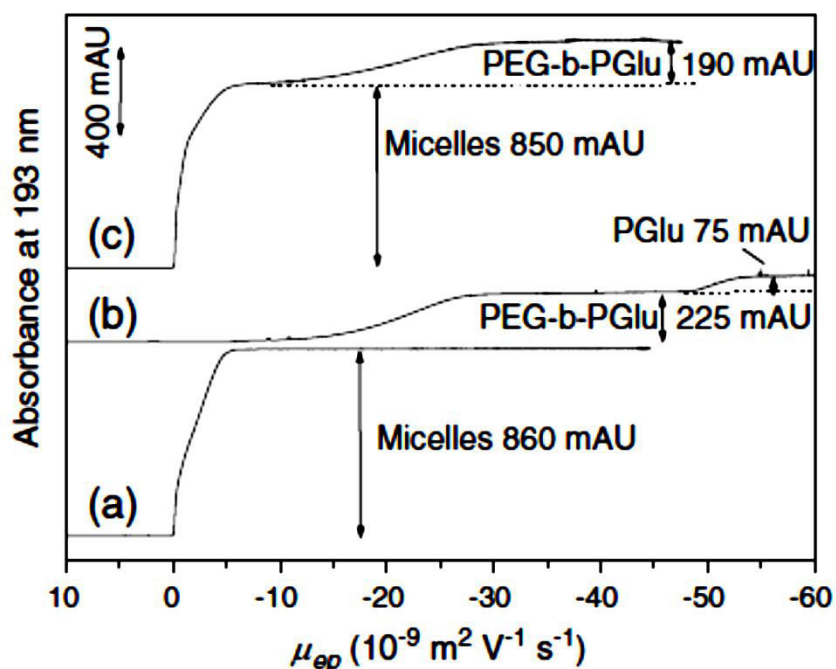
Fig. 1. 22. FACCE of polymeric micelles (a), PEG-b-PGlu (b) and their mixture (c) in effective mobility scale. Experimental conditions: electrolyte: 10 mM phosphate buffer (pH 7.2). Applied voltage: +10 kV. Samples: (a) polymeric micelles diluted at 33% v/v in the electrolyte, (b) PEG-b-PGlu at 3.8 g/L, (c) polymeric micelles diluted at 33.3% v/v in the electrolyte containing PEG-b-PGlu at 3.8 g/L [200].

Species separated by electrophoresis appear as discrete and progressive plateaus in the electropherograms. Electropherogram (c) demonstrated that PEG-b-PGlu does not adsorb onto the surface of polymeric micelles since the height of the PEG-b-PGlu plateau was not significantly affected by the presence of polymeric micelles. The latest resulted particularly suitable for the study of interacting systems whatever the kinetics of interaction. The results show the relevance and adequacy of CE to study these systems.

In the pharmaceutical and biomedical sciences, liposomes (with sizes between 20 nm – 10 µm) can be assimilated as NPs and find use as models of biological membranes, partitioning medium and as drug carriers. The use of CE and liposome electrokinetic chromatography for the characterization of liposomes in a pharmaceutical context has been reviewed by *Franzen et al.* [223]. A considerable number of studies indicate that capillary electrophoresis may have a role in the characterization of liposome drug delivery systems, for the investigation of encapsulation efficiency and drug leakage. In addition, CE has been also applied for determination of liposome/water partitioning and characterization of drug–liposome interactions.

1.4.6. Current trends in capillary electrophoresis for nanoparticle characterization

Electrokinetic methods have demonstrated to be powerful analytical tools for the separation and whole characterization of physicochemical properties of NPs as well as to help in the design and control of NPs synthesis and surface modification processes. In addition, the inline coupling of CE to TDA offers to the user an absolute technique for NP characterization overcoming the limitation of the lack of reference materials.

Further experimentation with CE using capillaries with different inner surface chemistries should be evaluated with the goal of calculating binding parameters for a wide range of proteins and NPs. The analysis and characterization of different NPs physicochemical parameters in more complex media is also suggested in order to obtain more accurate information for the prediction of NPs performance.

Although not presented here, another active research line must be highlighted, that comprises the uses of NPs in CE not as the object of study but as a tool for the improvement of both the separation process and the sensitivity of CE. In this sense, the main lines of investigation focus on capillary coatings [224], electrode modifications [225], addition of NPs into the BGE [226], and enhancement of the signal detection, for example in the CE-based immunoassays [227]. Another tendency in which tremendous efforts are being done and with very promising results is the miniaturization, i.e., the insertion of the CE-based methodologies into a chip or a microscope slide [228, 229].

1.5. CAPILLARY ELECTROPHORESIS METHODOLOGIES FOR THE EVALUATION OF INTERACTIONS BETWEEN NANOPARTICLES AND BIOMOLECULES

Numerous electrokinetic methods have been reported for the study of non-covalent intermolecular associations. Protein–drug, peptide–peptide, carbohydrate–drug and antigen–antibody binding are a few examples [189, 190]. This property is important because it permits the characterization of surface-functionalized nanoparticles, describing nanoparticle-ligand binding nature, which is a key parameter in production control and stability of nanoparticles, and therefore, its quality and application.

The high surface area over volume ratio increase the NP surface available for interaction with cellular components; however, this interaction depends on different conditions, fundamentally the functional groups present on the surface, and its electrical charge [44, 230, 231]. Noncovalent interactions play a key role in many biochemical processes related to for example drug targets or protein-protein interactions [232].

Proteins are the key for the biodistribution of the nanoparticles, controlling their transport, uptake, delivery and active targeting. The adsorption of plasma proteins onto NPs dictates their residence time in blood and ultimate destination [233, 234]. If the nanoparticles are resistant to nonspecific adsorption of serum proteins, their residence time in the blood is increased, and this facilities passive tumor targeting [235, 236]. When suppression of protein adsorption onto nanoparticles is desired, passivating surfaces against nonspecific interactions have been developed by the attachment of several specific molecules on the surface of nanoparticles [237-239]. The PEGylation (anchorage of polyethylene glycol molecules) has been the standard procedure to make protein-repellent surfaces [240].

Some parameters for the study of molecular association as association constants, binding constants, dissociation constants, partition coefficients can be determined with a variety of different capillary electrophoresis (CE) approaches. These methodologies have been traditionally applied for the study between a smaller molecule or ion (i.e., the solute, drug or analyte of interest) and a larger entity (e.g., proteins, micelles, polymers, cyclodextrins, etc.) [241].

The determination of the physico-chemical parameters of NPs and their performance in biologically relevant systems could strengthen their applications in the biomedical fields. Qualitative and quantitative information of the interaction between NPs and biological elements can be assessed by diverse modes in CE. Dynamic equilibrium approaches in which one partner of the interaction is in the sample and the other one in the electrolyte are the more commonly used methods when fast reactions ($t_{binding} \ll t_{CE}$) occur. In that case, some methods such as ACE and FACE exploit changes in electrophoretic mobility or plateau height, respectively, to determine the binding parameters. For relatively weak interactions between NPs and proteins occur, the Hummel-Dreyer method has been presented has the alternative to obtain binding parameters [242]. In addition, the so-called electrophoretically mediated microanalysis (EMMA) has been also applied to evaluate interactions with relative fast kinetics reactions inside the capillary [243]. When a slow

reaction occurs ($t_{binding} \gg t_{CE}$), an incubation of the reaction mixture for a certain period of time prior to analysis is then necessary and the binding parameters are obtained by monitoring the changes in the electrophoretic mobility or the plateau heights by using CZE or FACE, respectively [169, 244]. Some significant examples of these subjects are described in the next paragraphs. The analysis of NPs as drug delivery systems with pharmaceutical relevance and the obtained parameters are also analyzed in the last part of this section.

1.5.1. Evaluation of interactions between nanoparticles and proteins

The fate of NPs *in vivo* is closely related to their interactions with plasma proteins. They can induce the NP detection by immune system or facilitate active targeting to cells or tumors. Analytical methodologies such as CE have been developed to characterize the NPs-protein or peptide binding. In this section we present some representative examples about this topic. The albumin has been principally used as a model protein for evaluation of NPs interactions with proteins, however other specific proteins or natural or synthetic peptides have also been analysed.

The use of CE methodologies to evaluate protein-NPs interactions is attractive from different points of view. In the review of *Aleksenko et al.* [169], they show the applicability of this methodology for the evaluation and determination of interaction parameters between individual proteins and multiplex NPs for tumor detection applications (QDs, AuNPs and iron oxide NPs) by different CE approaches, principally ACE methods, getting the percentage of conjugate, binding constant, efficiency of conjugation, binding saturation, binding kinetics, stoichiometry and cooperativity. Detectors such as LIF, fluorescence, UV, ICP-MS, or electrochemical ones [225, 245] were used.

When the analysis of the NP-protein interactions is performed, two possible situations can be visualized: i) Stable NPs-protein complexes or ii) Short-lived complexes with fast association/dissociation rates. The choice of the adequate mode in CE for the evaluation of NP-protein interactions can be only verified by pilot experimental results.

The selection of the adequate CE mode for analysis of interactions of bovine serum albumin (BSA) with the gold and super paramagnetic Fe_3O_4 NPs, was emphasized in the work of *Li et al.* [244]. Depending on the complex dissociation rate, binding situations were studied with two CE operation modes: CZE and ACE. Interactions of BSA with the Fe_3O_4 NPs and with the AuNPs displayed slow and fast binding kinetics, respectively and were therefore characterized by ACE and CZE, respectively. The impacts of the physicochemical properties of NPs and the incubation buffer on NP-protein interaction were evaluated on the basis of the dissociation constant (Kd) and the binding saturation constant (n) values to interpret the interaction driving forces.

Another innovative methodology for the study of quantum dots and protein interactions inside a capillary was applied by *Wang et al.* [243], the so called electrophoretically mediated microanalysis (EMMA). Particularly, QDs and protein were subsequently injected into a capillary. As QDs migrated slower than albumin (which was injected in second place), a micromixing

occurred due to their differential mobility when electric field was applied. Therefore, QDs and albumin were mixed and interacted inside the capillary; and the online separation and detection were then achieved permitting the QDs/proteins interaction kinetic studies using the Hill's equation. This methodology is supposed to be useful only for relative fast kinetics reactions, the limiting parameter being the separation time.

As previously indicated, CE has the advantage to allow physiologically relevant media to be employed as BGE, which improves their use for characterization of NPs in view of biomedical applications. In a recent work, a CZE method for the analysis of the interactions between gold NP and proteins (albumin and transferrin) in real human serum samples was optimized with emphasis on compatibility with physiological conditions [246]. The mechanism and kinetics of interaction between CdSe/ZnS QDs and a multivalent ligand, the denatured BSA (dBSA) were obtained by CE with (CE-FL) detector in different pH and ionic strengths. They revealed that the binding sites on the QDs surface have different priorities that can lead to hierarchical assembly of the ligand, and that these ligands can be kinetically favoured resulting in low-degree displacement due to multivalent thiol groups on the NP surface [247]. Figure 3 shows a series of electropherograms of dBSA and QDs mixtures at different ratios, allowing to obtain different informations about interactions by means of a classic CZE experiment considering the kinetic aspect: i) Different species of free QDs (peak 1) and bound QDs (peaks 2 to 4) could be separated in the electropherograms because multiple QDs–protein pre-saturation intermediates were formed. ii) The distribution of QD–dBSA complex population is altered by the coupling time at the same molar ratio. iii) At a 2:1 molar ratio, little changes were observed (Figure 1.23a). However, at 4:1 and 6:1 molar ratios, the population of QDs–dBSA complex species rapidly increased over time, and free QDs significantly decreased (Figures 1.23b and 1.23c). At a 8:1 molar ratio, no free QDs could be observed after mixing for 10 min (Figure 3d). The interaction kinetics of QDs with dBSA manifested a bi-phasic kinetics with a linear initial stage followed by a saturating stage.

The binding of a model protein (BSA) to gold NPs (AuNPs) as a function of particle shape (spherical and rod-shaped), size, and surface charge was investigated by ACE and compared with steady-state fluorescence quenching titration [202], finding similar binding constants within an order of magnitude no matter the NP shape or surface charge, even for neutral PEGylated NPs. However, in that work, some difficulties occurred to analyze positively charged NPs due to capillary wall interactions. This problem could be eliminated by chemically modifying the capillary inner wall by means of capillary preconditioning with didodecyldimethylammonium bromide, which prevented from positively charged NP adsorption and preserved high analytical performances [203].

Other alternative method for the evaluation of protein-corona on NPs is the electrokinetic Hummel-Dreyer method (CE-HD). This method has been recently used for the first time for quantitative characterization of the non specific binding between the PEG-functionalized $ZnGa_{1.995}Cr_{0.005}O_4$ persistent luminescence NPs used in biological imaging and the BSA as a model protein [242]. The binding constant and the number of binding sites were determined at different ionic strengths. This method has shown to be sufficiently sensitive to detect small changes in the

magnitude of binding parameters, and allowed to highlight the screening effect of the BGE counter-ions on the NP surface, indicating that electrostatic interactions occur between PEGylated $ZnGa_{1.995}Cr_{0.005}O_4$ and BSA. This method can be used in the case in which relatively weak interactions between NPs and proteins are suspected, particularly when NP surface has been passivated to avoid their detection by the immune system.
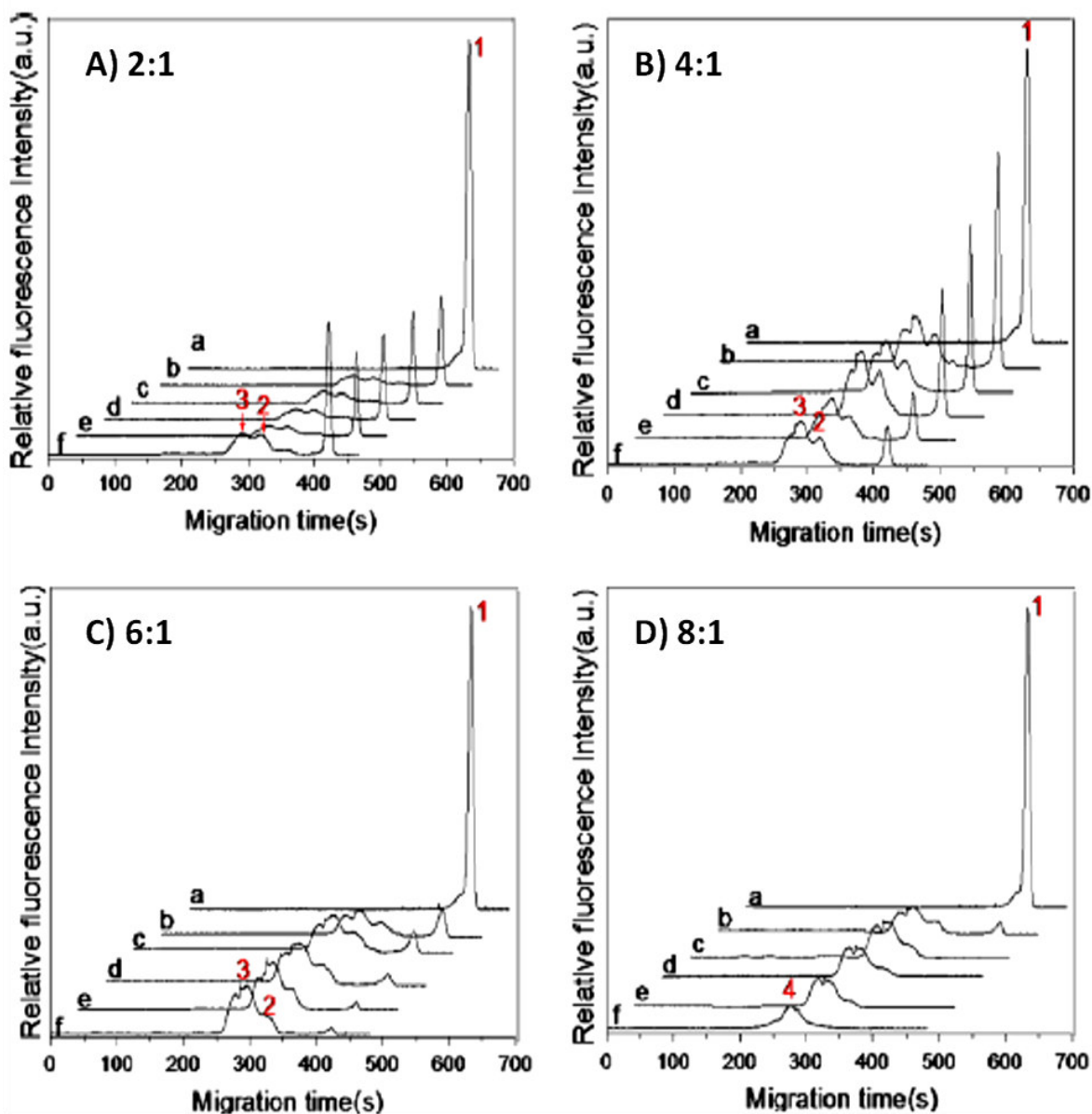
Fig. 1. 23. CZE of QDs-dBSA self-assembled at different dBSA/QD ratios (A, 2:1; B, 4:1; C, 6:1; D, 8:1. Incubation time : without BSA (a) ; with BSA 0 min (b), 10 min (c), 20 min (d), 30 min (e), 60 min (f) [247].

1.5.2. Interaction of nanoparticles with other biomolecules and biological systems

The evaluation of the interaction between NPs and biomolecules by CE is clearly not limited to proteins. However only a few studies of NP interactions with other kinds of biomolecules such as peptides, DNA, oligonucleotides, aptamers and virus have been presented in the literature.

CE has been applied for the evaluation of interactions of more specific peptides, permitting the evaluation of punctual biochemical events. In the works of *Brambilla et al.* [67, 183], they demonstrated by CE-LIF and complementary techniques the influence of poly(alkyl cyanoacrylate) and poly(lactic acid) NPs (PEGylated or not) on the behavior of monomeric and soluble oligomeric forms of $A\beta_{1-42}$ peptide at concentrations close to physiological conditions. Indeed, their progressive production, accumulation, and aggregation leads to the formation of amyloid plaques in the brain, which is one of the different physiopathological hallmarks related to Alzheimer disease. In that work, CZE was crucial in evidencing that PEGylated NP influence on $A\beta_{1-42}$ aggregation kinetics at 37 °C by means of the appearance of "spike-shape" peaks likely due to the formation of bigger aggregates networked with NPs via $A\beta$ oligomeric bridges.

Aptamers and peptides with specific molecular recognition and their interactions with NP have been also assessed by CE. CdSe/ZnS QDs probes for targeted delivery to mouse and human cells using aptamer GS24 and peptide T7 specific to mouse/human transferrin receptors were developed. By means of the evaluation of the interactions, CE was used to investigate the optimal ratios for conjugation of QDs to aptamer and peptide [248]. The continuous frontal analysis in a microchip electrophoresis format (FACMCE) was used to evaluate the interactions in a more complex system, the aptamer-conjugated to fluorescent maghemite NPs and a lysozyme (the aptamer target) in different BGE natures and composition [228, 249, 250]. This technique enabled to determine the number of binding sites on the substrate and the dissociation constant, and thereby to demonstrate the preservation of the targeting functionality of the lysozyme-binding aptamer after conjugation with NPs.

An alternative CE method to indicate the interaction between luminescent NPs and ligands consists in the use of the Förster resonance energy transfer (FRET) from QDs to surface bound fluorescent ligands [251]. That work demonstrated that the FRET between ligands and QDs could be readily detected by CE-FL, which together with the migration times of the fluorescent peaks provided an indication of the binding interaction between polyhistidine peptide dendrimer and QDs in a complex binding solution (cell lysate). CE with in-line fluorescence measurement could detect multiple emission channels simultaneously or even record the whole fluorescence spectrum during electrophoresis. So, the decrease of the donor emission and the increase of the acceptor emission due to Föster resonance energy transfer (FRET) could be monitored at the same time. Since the emission signals at both channels are measured under the same excitation condition, the ratio of the integrated peak areas at two channels renders a valid measure of the relative FRET efficiency.

The interaction between NPs with chicken genomic DNA and 500 bp DNA fragment was observed employing CZE with LIF detector and gel electrophoresis, and the result relies on possible

matching between QDs size and the size of DNA major grove [252]. In another work of *Stanisavljevic et al.* [253], CZE with both LIF and UV detectors and gel electrophoresis were used for QDs characterization and for monitoring the interaction of the pair biotin/streptavidin. A linkage was used as streptavidin modified QDs to label and detect biotinylated oligonucleotide cancer sequence of BCL-2 and a sequence of hepatitis B virus (HBV). The interaction of QDs was verified also by a second oligonucleotide fragment, specific for hepatitis B virus labeled with biotin (HBV-biotin). This detection might help to have fast diagnosis of these diseases.

1.5.3. Current trends in the capillary electrophoresis application for the determination of nanoparticle/biomolecules interactions

Various CE modes can be applied in the separation and characterization of multiplex NPs and their conjugates with biomolecules in simulated physiological conditions. The different qualitative and physicochemical parameters for the interactions can help to predict the fate of NPs in biological systems, such as their biodistribution, drug delivery performance, and in general their cellular uptake or interactions with biological elements. Despite the great advances of CE methodologies for NP-biomolecule interactions, many CE modes for evaluation of binding parameters such as Hummel-Dreyer (HD), vacancy ACE (VACE), vacancy peak method (VPM), non-equilibrium CE of equilibrium mixtures (NECEEM) and many other methodologies remain unexplored and could be potentially exploited in order to obtain different and complementary information about binding parameters.

Considering the current trends for NPs studies and the power of CE, the CE characterization of interactions between NPs and specific proteins or different kinds of biomolecules is a challenging task in a near future.

OBJECTIVES

General objective

Develop and apply novel methodologies for characterization of physicochemical properties and biocompatibility of persistent luminescence nanoparticles for preclinical diagnostics applications.

Particular objectives

➢ Characterize the $ZnGa_{1.995}Cr_{0.005}O_4$ persistent luminescence nanoparticles by capillary electrophoresis and compare the results with the obtained ones by dynamic light scattering and laser Doppler electrophoresis.

➢ Evaluate the biocompatibility of $ZnGa_{1.995}Cr_{0.005}O_4$ nanoparticles in mice at acute, short and long-term.

➢ Evaluate the photo-activation effects on the toxicity of persistent luminescence nanoparticles in breast cancer cells.

➢ Develop a capillary electrophoresis methodology to determine the non-specific interactions between nanoparticles and single proteins.

➢ Compare the magnitude of the interactions between PEGylated persistent luminescence nanoparticles and Apolipoprotein-e versus Albumin in a binary system of proteins.

CHAPTER II.

FUNCTIONALIZATION AND CHARACTERIZATION OF ZnGa$_{1.995}$Cr$_{0.005}$O$_4$ PERSISTENT LUMINESCENCE NANOPARTICLES BY DYNAMIC LIGHT SCATTERING, LASER DOPPLER AND CAPILLARY ELECTROPHORESIS

CHAPTER II

FUNCTIONALIZATION AND CHARACTERIZATION OF ZnGa$_{1.995}$Cr$_{0.005}$O$_4$ PERSISTENT LUMINESCENCE NANOPARTICLES BY DYNAMIC LIGHT SCATTERING, LASER DOPPLER AND CAPILLARY ELECTROPHORESIS
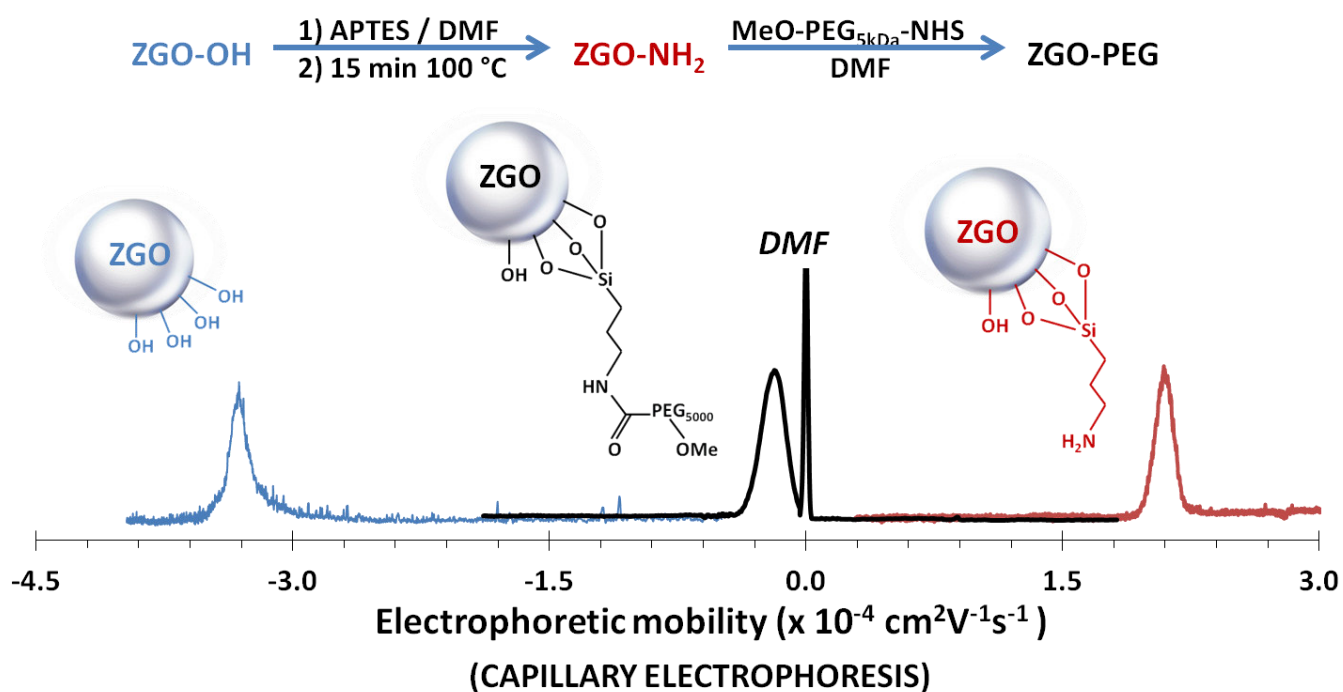
Zinc gallate nanoparticles doped with chromium (III) (ZnGa$_{1.995}$O$_4$:Cr$_{0.005}$) are innovative persistent luminescence materials with particular optical properties allowing their use for *in vivo* imaging. They can be excited in the tissue transparency window by visible photons and emit light for hours after the end of the excitation. This allows to observe the probe without any time constraints and without autofluorescence signals produced by biological tissues. Modification of the surface of these nanoparticles is essential to be colloidally stable not only for cell targeting applications but also for proper distribution in living organisms. The use of different methods for controlling and characterizing the functionalization process is imperative to better understand the subsequent interactions with biological elements. In this chapter, the characterization and optimization of a classic functionalization sequence, starting with hydroxyl groups (ZGO-OH) at the nanoparticle surface, followed by an aminosilane-functionalization intermediate stage (ZGO-NH$_2$) before PEGylation (ZGO-PEG) is explored for the first time. Dynamic light scattering and laser Doppler electrophoresis were used in combination with capillary electrophoresis to characterize the nanoparticle functionalization processes and control their colloidal and chemical stability. The hydrodynamic diameter, zeta potential, electrophoretic mobility, stability over time and aggregation state of persistent luminescence nanoparticles under physiological-based solution conditions have been studied for each functional state. Additionally, a new protocol to improve ZGO-NH$_2$ stability based on a thermal treatment to complete covalent binding of (3-Aminopropyl)triethoxysilane onto the particle surface has been optimized. This thorough control increases our knowledge on these nanoparticles for subsequent toxicological studies and ultimately medical application.

2.1. BACKGROUND AND JUSTIFICATION

Optical imaging is a rapidly extending research field aiming at non-invasively interrogating animals for disease evaluation and progression *in vivo*, assessing drug pharmacokinetic behavior or identifying molecular biomarkers of disease in preclinical studies [1]. The preparation of materials to overcome the disadvantages of conventional optical markers such as classical quantum-dots and organic dyes mainly due to a non negligeable autofluorescence signal coming from endogeneous chromophores also excited when using such probes *in vivo*, is currently intensively investigated. In this context, materials whose light emission remains for extended periods (hours) of time after light excitation is stopped have been synthesized, and currently known as persistent luminescence materials [16, 23, 37, 254-259]. In this context, materials based on chromium-doped zinc gallate (ZnGa$_2$O$_4$:Cr(III)) have attracted serious attention due to their bright near-infrared persistent luminescence after ultraviolet (UV) excitation [29]. The optical properties of undoped zinc gallate have also been investigated in nanoscale materials [31, 32]. Thus, the most recently reported chromium-doped zinc gallate ZnGa$_{1.995}$Cr$_{0.005}$O$_4$ nanoparticles (ZGO-NPs), a chromium-doped binary oxide, has shown attractive optical properties due to its long persistent luminescence besides

CHAPTER II

FUNCTIONALIZATION AND CHARACTERIZATION OF ZnGa$_{1.995}$Cr$_{0.005}$O$_4$ PERSISTENT LUMINESCENCE NANOPARTICLES BY DYNAMIC LIGHT SCATTERING, LASER DOPPLER AND CAPILLARY ELECTROPHORESIS

its capacity to be re-activated *in vivo* through living tissues using highly penetrating low-energy orange/red photons [33].

In order to successfully use nanoparticles as luminescent probes *in vivo*, their surface properties should be thoroughly controled. Indeed surface functionalization should firstly provide a good dispersibility, a hight stability in aqueous solutions, to prevent natural detection by immune cells, and finally allow further conjugation with biologically active molecules [38, 39, 260]. First, colloidal stability is one of the critical aspects for employing nanoprobes *in vivo*. For example, during nano-drug intravenous administration, formation of larger particles as big as 5 µm could lead to capillary blockade and embolism or deposition in different organs, causing severe health problems [147, 150]. Three main mechanisms are involved in nanoparticle colloidal stability both in aqueous and non-aqueous media: electrostatic repulsion, sterical stabilization and electrosterical repulsion (both electrostatic and sterical mechanisms at the same time) [147, 148]. The physicochemical properties of the dispersion media such as pH, ionic strength, composition and concentration, as well as the presence of a complex matrix (natural organic matter, polysaccharides and proteins) can also affect nanoparticle suspension stability and lead to agglomeration/aggregation [153]. Second, the surface density of functional groups is of high priority considering that most applications are mainly based on interactions with the nanomaterial surface [43, 44, 240]. Thus, nanoparticle size and surface charge are strong determinants of their pharmacokinetic in living organisms [163].

Recent progress in the development of functional, versatile nanoparticles for use in feasible devices has led to the need for methods allowing efficient nanoparticle properties monitoring [172]. Furthermore, in a sequential surface modification, a precise control of each functionalization step is very important to optimize the overall process and nanoparticle performances. Among currently used techniques, electron microscopy provides information on particle shape and real diameter [261], whereas dynamic light scattering (DLS) gives access to hydrodynamic diameter via the Stokes-Einstein equation [262]. Micro-electrophoresis [263] and laser doppler velocimetry (LDV) [187, 262, 263] are applied for measuring electrophoretic mobilities, which can be converted into zeta potentials (ζ) using proper models based on both nanoparticle and solvent properties [263]. A complete guideline to chose the adequate model for this propose has been reported by *Delgado et al.* [164], and novel approximations have been recently proposed by *Pyell et al.* [165].

Capillary electrophoresis (CE) has been applied to nanoparticles characterization [200, 203, 207, 210, 213, 264], providing information on both size and surface charge density, while leading to low sample consumption and fast analysis. The selectivity of this separation method also allows simultaneous characterization of mixtures of organic [187, 265] or inorganic [185, 266, 267] particle populations differing in size, charge or chemical composition, as well as detection of impurities present in the suspensions [268].

This chapter is focused on the combined use of dynamic light scattering (DLS), laser doppler electrophoresis (LDE), and capillary zone electrophoresis (CZE) to control and optimize the synthesis and functionalization of ZGO-NPs and determine their colloidal stability through time

CHAPTER II

FUNCTIONALIZATION AND CHARACTERIZATION OF ZnGa$_{1.995}$Cr$_{0.005}$O$_4$ PERSISTENT LUMINESCENCE NANOPARTICLES BY DYNAMIC LIGHT SCATTERING, LASER DOPPLER AND CAPILLARY ELECTROPHORESIS

when dispersed in different physiological buffers. Surface charge density (zeta potential) and hydrodynamic diameter were determined at each step of the surface functionalization by LDE and DLS. An efficient separation of these nanoparticles was simultaneously performed on the same sample by CZE for a batch to batch quality control allowing determination of particle zeta potential, polydispersity and colloidal stability. Thus, by means of the study of this sequence of functionalization, involving negatively (ZGO-OH), positively (ZGO-NH$_2$) charged nanoparticles as well as neutral (ZGO-PEG) ones; we could compare the influence of different surface functional groups on the electrophoretic behavior of ZGO-NPs.

2.2. MATERIALS AND METHODS

Zinc nitrate hexahydrate and N,N-dimethylformamide (DMF) were purchased from Fluka (France). Gallium oxide and chromium (III) nitrate nonahydrate were acquired from Alfa Aesar chemicals (USA). α-Methoxy-ω-N-hydroxysuccinimide poly(ethylene glycol) (PEG 5000 Da) was purchased from Iris Biotech GmbH (Germany). (3-Aminopropyl)-triethoxysilane (APTES), 3-(N-Morpholino)propanesulfonic acid (MOPS), 4-(2-Hydroxyethyl)piperazine-1-ethanesulfonic acid (HEPES), sodium phosphate monobasic dehydrate, sodium phosphate dibasic, citric acid and didodecyldimethylammonium bromide (DDABr) were purchased from Sigma-Aldrich (France). Finally, for capillary activation and modification standard 1.0 M NaOH solution Normadose were purchased from VWR (Strasbourg, France).

ZnGa$_{1.995}$Cr$_{0.005}$O$_4$ nanoparticles were synthesized by a two step hydrothermal and calcination process as described by *Maldiney et al.* [33]. Briefly, 8.94 mmol gallium oxide are mixed with 10 mL of concentrated nitric acid (35 wt %) and let react in a Teflon-lined stainless steel autoclave at 150 °C overnight to form gallium nitrate. A mixture of 0.04 mmol chromium nitrate and 8.97 mmol zinc nitrate in 10 mL water was added to gallium nitrate in acidic medium under vigorous stirring. 7.5 mL of ammonia solution (30 wt%) was added to the resulting solution until precipitation at pH 7.5. Resulting dispersion was then stirred for 3 hours at room temperature, and transferred into a 25 mL Teflon-lined stainless steel autoclave and heated for 24 hours at 120 °C. The resulting material was washed with water and ethanol, and then dried at 60 °C for 2 hours. The resulting powder was finally sintered in air atmosphere at 750 °C for 5 hours [33].

Hydroxylation was performed by basic wet grinding of the powder (100 mg) for 15 minutes, with an agate mortar and pestle in minimal quantity of 5.0 mM NaOH solution. After re-dispersion of the resulting material in 5.0 mM NaOH solution (10 mL), the resulting suspension was vigorously stirred overnight at room temperature. Nanoparticles with an hydrodynamic diameter of 90 nm were selected from the whole polydisperse colloidal suspension by centrifugation on a SANYO MSE Mistral 1000 at 4500 rpm for 7 minutes. They were located in the supernatant (assessed by DLS). The supernatants were gathered and concentrated to a final suspension, in which hydroxylated nanoparticles (ZGO-OH) concentration was evaluated by determining the sample weight after drying.

CHAPTER II

FUNCTIONALIZATION AND CHARACTERIZATION OF ZnGa$_{1.995}$Cr$_{0.005}$O$_4$ PERSISTENT LUMINESCENCE NANOPARTICLES BY DYNAMIC LIGHT SCATTERING, LASER DOPPLER AND CAPILLARY ELECTROPHORESIS

ZGO-OH were rinsed twice in water and twice in DMF. Aminosilane-coated nanoparticles (ZGO-NH$_2$) were obtained by adding 20 µL of APTES to a suspension of 5.0 mg ZGO-OH dispersed in 2.0 mL DMF. The reaction mixture was sonicated for the first 2 minutes using a Branson Ultrasonic Cleaner 1210 and kept under vigorous stirring for 5 hours at room temperature in a glass round flask. The nanoparticles were then washed from the unreacted APTES by three successive centrifugation/redispersion steps in DMF [33]. An additional thermal-curing step to improve the stability of the aminosilane layer in aqueous media was studied. A round flask containing dry ZGO-NH$_2$ was placed for 15 minutes in an oven at temperatures ranging from 100 to 200 ° C. Their colloidal stability was then evaluated by CE and DLS after several sonication steps and the results were correlated to the chemical stability of the aminosilane layer on the nanoparticle surface.

Finally, PEGylated nanoparticles (ZGO-PEG) were obtained by reacting 10 µmol MeO-PEG$_{5kDa}$-NHS (50 mg) with 5.0 mg ZGO-NH$_2$ nanoparticles in 1.0 mL DMF. To ensure a maximum PEG functionality, this last step was achieved overnight, under vigorous stirring at 90 °C [33]. This sequential functionalization process is summarized in Figure 2.1.
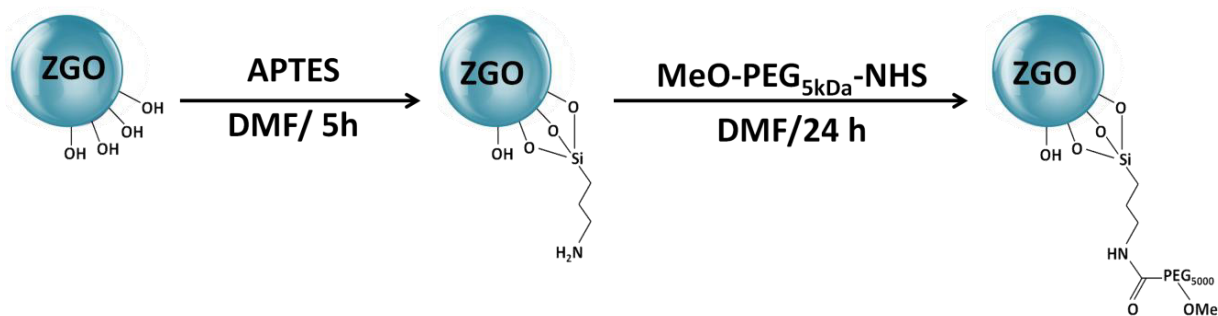
Fig. 2. 1. Sequential surface functionalization of ZnGa$_{1.995}$Cr$_{0.005}$O$_4$ nanoparticles.

5.0 mM NaOH was used as suspension storage medium for ZGO-OH, and DMF for ZGO-NH$_2$ and ZGO-PEG. Before analysis, nanoparticles were washed three times, alternating pelleting by centrifugation and redispersion by ultrasound in storage medium. Thereafter, nanoparticles were finally redispersed in buffer solution.

Nanoparticle size was characterized by DLS measurements with a Nano ZS Zetasizer instrument (Malvern Instruments, Southborough, MA), which is based on the intensity fluctuations of back-scattered (178∘) laser light, caused by the Brownian motion of nanoparticles. A Branson Ultrasonic Cleaner 1210 was used for sample sonication.

Zeta potential was estimated from electrophoretic mobility measurements by LDE with a Nano ZS Zetasizer instrument (Malvern Instruments, Southborough, MA).

CHAPTER II

FUNCTIONALIZATION AND CHARACTERIZATION OF ZnGa$_{1.995}$Cr$_{0.005}$O$_4$ PERSISTENT LUMINESCENCE NANOPARTICLES BY
DYNAMIC LIGHT SCATTERING, LASER DOPPLER AND CAPILLARY ELECTROPHORESIS

Electrophoretic separations were performed with a 7100 model Capillary Electrophoresis System (Agilent Technologies, Waldbronn, Germany). 50 µm id x 35 cm fused-silica capillaries (detection length, 26.5 cm) from Polymicro Technologies (Phoenix, AZ, USA) were used after activation by successive flushes (925 mbar) with 1.0 M NaOH (15 min), 0.1 M NaOH (15 min) and H$_2$O (5 min), respectively. Injections were performed hydrodynamically applying 20 mbar at the capillary inlet for 10 s (approx. 10 nL) unless otherwise specified. Successive injection zones were performed in the following order: neutral marker (DMF), particle sample and electrophoretic buffer. The applied voltage was 12 kV unless otherwise specified, with positive polarity at the capillary inlet for bare fused-silica capillaries, and negative polarity for DDABr coated capillaries. The temperature of the capillary cartridge was set at 25 ° C. The detection wavelength was 200 nm.

Hydroxylated and PEGylated ZGO-NPs were separated in bare fused silica capillaries after activation and a 3 min conditioning (flush at 925 mbar) with background electrolyte (BGE) . DDABr-modified capillaries were used in the case of ZGO-NH$_2$ to prevent NP adsorption on capillary wall. DDABr modification of the capillary column was performed as reported before [269]. The initial capillary modification procedure consisted in a 5 min flush (925 mbar) with a 0.1 mM DDABr solution in 10 mM HCl, followed by a 3 min flush (925 mbar) with the BGE to move out the excess of surfactant and equilibrate the capillary. Between each run, capillaries were rinsed with water for 1 min and regenerated with the DDABr solution for 2 min before conditionning with BGE for 1 min.

Electrophoretic mobility were obtained from migration time measured at the center of area distribution of the peaks. Then, the mathematical model to convert the electrophoretic mobility obtained by both CE and LDE into zeta potential is an Ohshima´s equation [196] modification proposed by Pyell [165] (here called Ohshima-Pyell equation), and its choice and parameters are briefly discussed in the next section.

2.3. RESULTS AND DISCUSSION

A functionalization sequence was set up to synthesize ZGO-NPs with different surface chemistry: ZGO-OH, then ZGO-NH$_2$, and finally ZGO-PEG (Figure 2.1).

Therefore, the sequential surface functionalization was characterized through the determination of a number of physico-chemical parameters such as NP surface charge density through their zeta potential (by CE and LDE), hydrodynamic diameter (by DLS), point of zero charge (PZC) (by CE and LDE) and colloidal stability (by CE and DLS) when dispersed in various aqueous media. The choice of characterization medium is of high importance, since it should be close to physiological conditions to estimate NP colloidal stability for further use in biological applications or simulations.

2.3.1. ZGO-OH: Point of zero charge

The hydroxyl groups on the surface of ZGO-NPs produce electrostatic repulsions and thereby prevent their aggregation when dispersed in aqueous solution. Nanoparticles with an average hydrodynamic diameter of 90 nm in 5 mM NaOH were selected from the whole polydisperse colloidal suspension by differential centrifugation.

First ZGO-NPs were characterized in terms of point of zero charge and colloidal stability. The effect of pH on particle zeta potential and hydrodynamic diameter was studied by DLS in 30 mM citrate buffers at various pH, ranging from 2.0 to 5.5 (Figure 2.2).
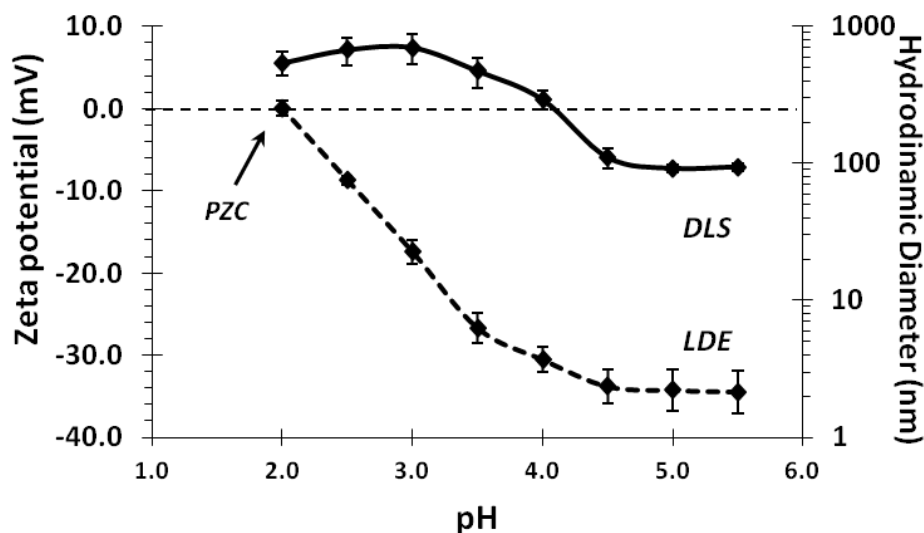
Fig. 2. 2. Characterization of ZGO-OH suspensions (1.0 mg/mL) in terms of zeta potential (dashed line) and hydrodynamic diameter (continuous line) estimated by LDE and DLS, respectively, in a 30 mM citrate buffer pH 2.0 to 5.5 (n= 4 repetitions, and error bars represent standard deviation).

Under these conditions their point of zero charge was estimated about pH 2.0, and their colloidal stability evidenced at pH above 4.5, where no variations in hydrodynamic diameter were evidenced.

2.3.2. Ionic strength effect on ZGO-OH colloidal stability at physiological pH: Use of adequate mathematical models for ζ-potential determination

To deeper evaluate the colloidal stability according to experimental conditions, the influence of the chemical nature of buffer solutions, including anionic and zwitterionic buffers, was tested. The obvious aggregation of ZGO-OH in 10 mM MOPS and HEPES zwitterionic buffers at pH 7.0-7.4 was noted (results not shown), suggesting electrostatic interactions between nanoparticles and positive sites in the zwitterionic molecules of the buffer. On the other hand, ZGO-OH presented a

CHAPTER II

FUNCTIONALIZATION AND CHARACTERIZATION OF ZnGa$_{1.995}$Cr$_{0.005}$O$_4$ PERSISTENT LUMINESCENCE NANOPARTICLES BY DYNAMIC LIGHT SCATTERING, LASER DOPPLER AND CAPILLARY ELECTROPHORESIS

good colloidal stability in 30 mM phosphate buffers pH 7.0-8.0 and in 30 mM citrate buffers pH 4.5-5.5, as evidenced by stable hydrodynamic diameter values about 90 nm. This hypothesis was confirmed when monitoring colloidal aggregation kinetics by means of DLS for the first 3 hours after ending NP sonication. The generated count rate, defined as the number of detected photons per second, which is useful for determinating the sample concentration, declined markedly between ZGO-OH dispersions in zwitterionic buffers to those in anionic media, indicating aggregation (results not shown).

The colloidal stability was studied based on the measurement of particle hydrodynamic diameter and its evolution over the time (till 3 hours). It was estimated in pH 7.4 phosphate buffer at different ionic strengths (from 10 to 100 mM) and different NP concentrations (from 0.1 to 1 mg/mL). Corresponding results are shown in Figure 2.3A for ZGO-OH suspensions at 1.0 mg/mL.
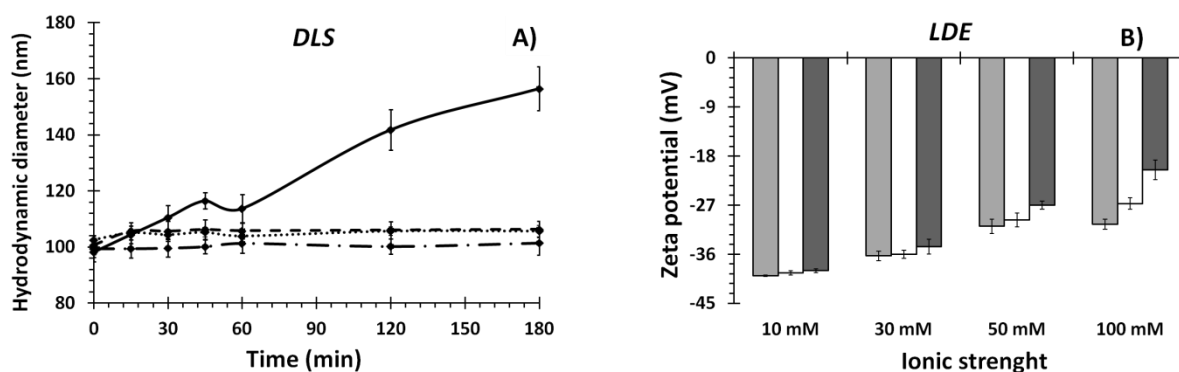
Fig. 2. 3. *Hydrodynamic diameter (at 1.0 mg/mL) in phosphate buffers (pH 7.4) at different ionic strengths (----- 10 mM, –·– 30 mM, ······ 50 mM, and —— 100 mM) estimated by DLS (A) and zeta potential estimated by LDE (B) of ZGO-OH at different NP concentrations (▨ 0.1, ▢ 0.5, and ▦ 1.0 mg/mL) (n= 4 repetitions, and error bars represent standard deviation).*

Similar results (not shown) where obtained for suspensions at 0.1 and 0.5 mg/mL. In the case of ZGO-OH concentrations equal to or higher than 0.5 mg/mL, a light increase in particle hydrodynamic diameter was evidenced immediately in the 100 mM ionic strength buffer. This may be due to random association of some nanoparticles without reaching aggregation at this point, but which is consistent with an aggregation expected to be induced by increasing salt concentration. In the same experimental conditions, ZGO-OH zeta-potential were estimated (Figure 2.3B).

In this work, the Ohshima-Pyell equation [165] was used to convert the electrophoretic mobility (μ_E) into zeta potential (ζ). This expression allows to distinguish between the stronger influence of the counterion mobility and the lower influence of the co-ion mobility, permitting to extend the applicability of the Ohshima´s equation[196] to buffered electrolytes [165] (eq. 2.1):

CHAPTER II

FUNCTIONALIZATION AND CHARACTERIZATION OF ZnGa$_{1.995}$Cr$_{0.005}$O$_4$ PERSISTENT LUMINESCENCE NANOPARTICLES BY DYNAMIC LIGHT SCATTERING, LASER DOPPLER AND CAPILLARY ELECTROPHORESIS

$$\mu_E = \frac{2}{3}\frac{\varepsilon_r \varepsilon_0 \zeta}{\eta}\left[f_1(\kappa a) - \left(\frac{ze\zeta}{kT}\right)^2 f_3(\kappa a) - m_{counter}\left(\frac{ze\zeta}{kT}\right)^2 f_4(\kappa a)\right] \qquad \text{Eq. 2.1}$$

Where ε_r is the relative electric permittivity, ε_0 the electric permittivity of vacuum, η the vicosity, e the elementary electric charge, k the Boltzmann constant, z the charge number of the counterion, T the absolute temperature, $m_{counter}$ the dimensionless ionic drag coefficient of the counterion, and can be defined as (Eq. 2.2) :

$$m_{counter} = \frac{2\varepsilon_r \varepsilon_0 kTN_A}{3\eta z\Lambda^0_{counter}} \qquad \text{Eq. 2.2}$$

in which N_A is the Avogadro number and $\Lambda^0_{counter}$ the limiting equivalent conductance of the counter ion. The functions $f_1(\kappa a)$, $f_3(\kappa a)$ and $f_4(\kappa a)$ are given by equations 2.3 to 2.5:

$$f_1(\kappa a) = 1 + \frac{1}{2[1+2.5/\{\kappa a(1+2e^{-\kappa a})\}]^3} \qquad \text{Eq. 2.3}$$

$$f_3(\kappa a) = \frac{\kappa a(\kappa a + 1.3e^{-0.18\kappa a}+2.5)}{2(\kappa a+1.2e^{-7.4\kappa a}+4.8)^3} \qquad \text{Eq. 2.4}$$

$$f_4(\kappa a) = \frac{9\kappa a(\kappa a + 5.2e^{-3.9\kappa a}+5.6)}{8(\kappa a+1.55e^{-0.32\kappa a}+6.02)^3} \qquad \text{Eq. 2.5}$$

Where κ is the Debye-Hückel parameter, the reciprocal thickness of the ion cloud, and a the sphere radius, which can be approximated by the number-weighted mean hydrodynamic radius of the investigated nanoparticles population.

As expected in our work, when increasing ionic strength and NP concentration, absolute zeta potential values decrease. Indeed, a reduction in the thickness of the diffuse double layer (due to screening of the surface charge) by increasing ionic strength is predicted by the electrical double layer theory. Concomitantly, higher NP concentrations facilitate inter-particle interactions due to greater proximity [147, 270]. These results are in good accordance with the particle size measurements, indicating the higher the zeta potential, the more stable the dispersion.

2.3.3. pH effect on ZGO-OH colloidal stability at fixed ionic strength

The pH effect on colloidal stability was also investigated in 30 mM ionic strength phosphate buffers in various pH range from 6 to 8, including physiological pH 7.4 (Figure 2.4).
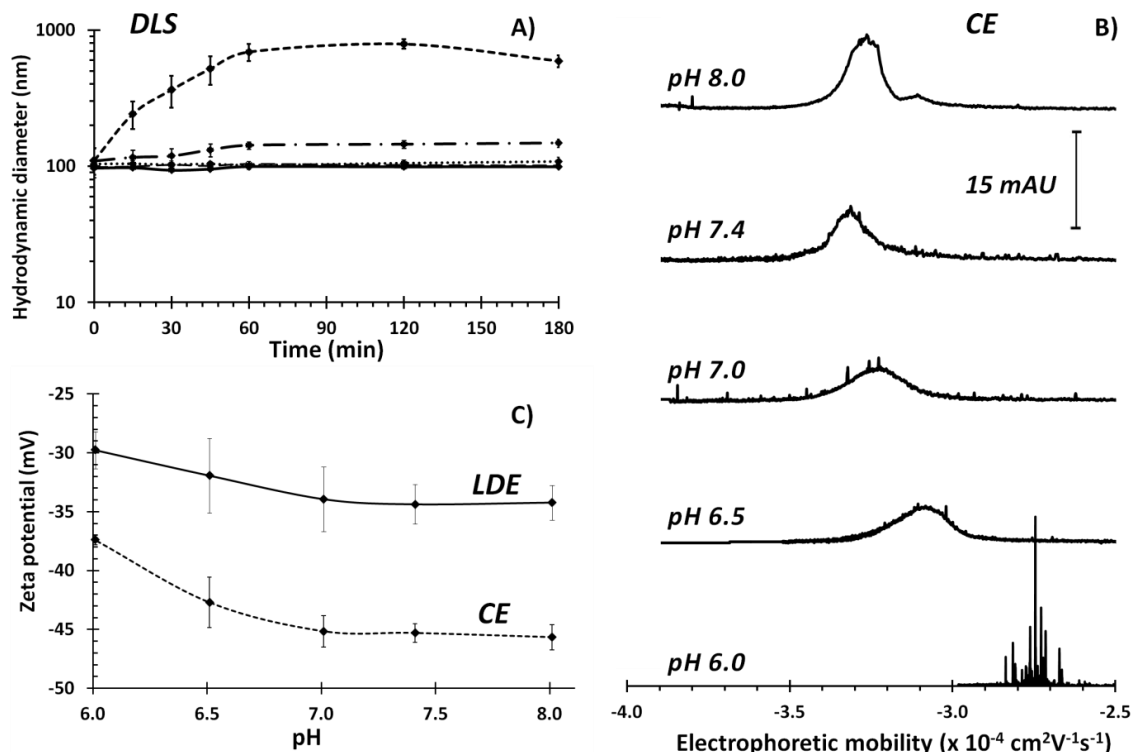
Fig. 2. 4. *Hydrodynamic diameter (at 1.0 mg/mL) and at different pH values (pH 6.0 -----, 6.5 –·–, 7.0 ······, 7.4 ———, and 8.0 ——) estimated by DLS (A), electrophoretic profiles (at 0.2 mg/mL) obtained by CZE (B) and zeta potential derived from mobility measurements either by CZE (dashed line) or by LDE (continuous line) (C) of ZGO-OH in 30 mM phosphate buffers. Separation conditions: bare fused silica capillary column: 50.0 μm i.d., 35.0 cm total length, 26.5 cm effective length; injection: 10 s at 20 mbar; applied voltage: 12 kV; UV absorption detection at 200 nm; capillary temperature: 25 ◦C. (n= 4 repetitions, and error bars represent standard deviation).*

A gradual increase in particle hydrodynamic diameter over time was evidenced only at pH 6.5 and below (Figure 2.4A), indicating the beginning of particle aggregation. Zeta potentials determined from mobility measurements by both LDE and CE were constant over the pH range 7.0-8.0 (Figure 2.4C). However, for values lower than pH 6.5, mobility decreases slightly in absolute value. Besides the displacement of the electrophoretic peaks (Figure 2.4B) severe aggregation at pH 6.0 has been evidenced by spiky profiles corresponding to aggregates migrating at random velocity. It has to be noted that the zeta potential values determined by LDE and CE for ZGO-OH in the same conditions (30 mM phosphate buffer solutions in a pH gradient ranging from 6 to 8) present the same evolution, but not the same value (See Figure 2.4C). Absolute values of zeta potential derived from mobility measurements by CE were roughly 11.0 mV higher with respect to those obtained by LDE. This divergence is usually observed in the literature, where a tendency towards higher absolute electrophoretic mobilities determined by CE is remarked respect to LDE or another similar techniques as LDV [265, 271, 272]. One hypothesis for this discrepancy could be interactions between the nanoparticles and the capillary wall (i.e. adsorption), resulting in some retention and thus in an apparent increase of mobility measured by CE [187, 223]. However,

CHAPTER II

FUNCTIONALIZATION AND CHARACTERIZATION OF ZnGa$_{1.995}$Cr$_{0.005}$O$_4$ PERSISTENT LUMINESCENCE NANOPARTICLES BY DYNAMIC LIGHT SCATTERING, LASER DOPPLER AND CAPILLARY ELECTROPHORESIS

absolute electrophoretic mobilities in CE were in the broad value domain of the electrophoretic mobility obtained by LDE.

2.3.4. Amelioration of the ZGO-NH$_2$ synthesis by a thermal step

One of the most commonly used surface modification process to afford NP biocompatibility involves first the functionalization by aminosilanes or organoalkoxysilanes as "precursors" [273]. The host materials and solvents should be dried carefully prior to adding precursors to avoid self-condensation of precursors in the presence of H$_2$O. Three different side reactions can occur during amino-functionalization by trialkoxy silanes on glass substrates and nanostructures (Figure 2.5) [274, 275].
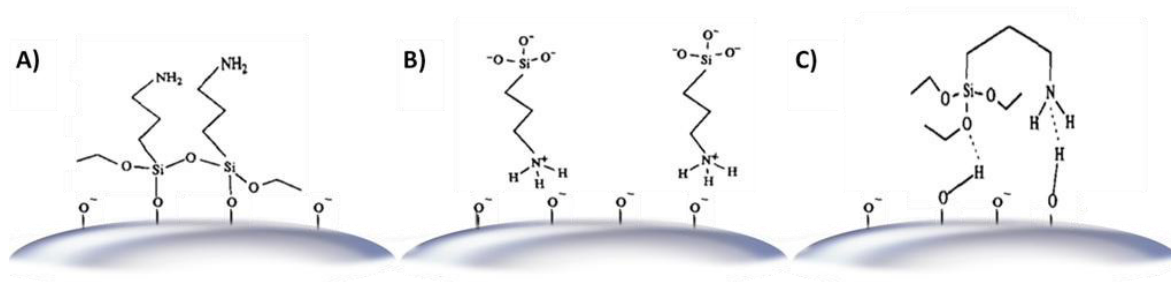
Fig. 2. 5. Surface bounded APTES: a) covalently, b) electrostatically, and c) by means of hydrogen bond.

The first one corresponds to covalent bond between oxygen originated from the surface of functionalized materials, and the silicon and siloxane (-Si-O-Si-) resulting from the partial hydrolysis of the alkoxysilane molecules during the silanization reaction in anhydric conditions. The second one corresponds to electrostatic interaction between the amino-group and deprotonated hydroxyl groups on the nanoparticle surface. Finally, hydrogen bond is possible between the hydrogen in the amino-group and the oxygen on the nanoparticle surface.

In order to obtain stable nanoparticles with a greater size uniformity, covalently linked groups are preferred, the link being performed by either post-synthetic grafting with organosilanes bearing amino groups or co-condensation methods [43, 276]. In this study, the former method was chosen by reacting APTES with the free hydroxyl groups of ZGO-OH.

By means of conventional methodologies, the obtained amino surface is not chemically stable through washing and conditioning steps in aqueous and organic solvents. A method to implement a stable aminosilane layer over nanoparticles is proposed in this work, inspired from the work published by *Vandenberg et al.* [277], where a 3-aminopropyltriethoxy silane layer was deposited over bulk silicon surfaces and stabilized by post-synthetic curing step consisting in a thermal treatment (200 °C for 15 minutes). The subsequent drying and heating process consists in a drying step with absolute ethanol after washing with DMF. Ethanol was then volatilized by the application of compressed air to dryness in a glass round flask. The flask was then placed in an oven at 100,

CHAPTER II

FUNCTIONALIZATION AND CHARACTERIZATION OF ZnGa$_{1.995}$Cr$_{0.005}$O$_4$ PERSISTENT LUMINESCENCE NANOPARTICLES BY DYNAMIC LIGHT SCATTERING, LASER DOPPLER AND CAPILLARY ELECTROPHORESIS

150 or 200 ° C for 15 minutes. After this step, the NPs were redispersed in aqueous solvents (MOPS and HEPES zwitterionic buffers or citrate and phosphate anionic buffers) by sonication. NP size and zeta potential were measured after each one of the redispersion processes by DLS and LDE, respectively (Figure 2.6).
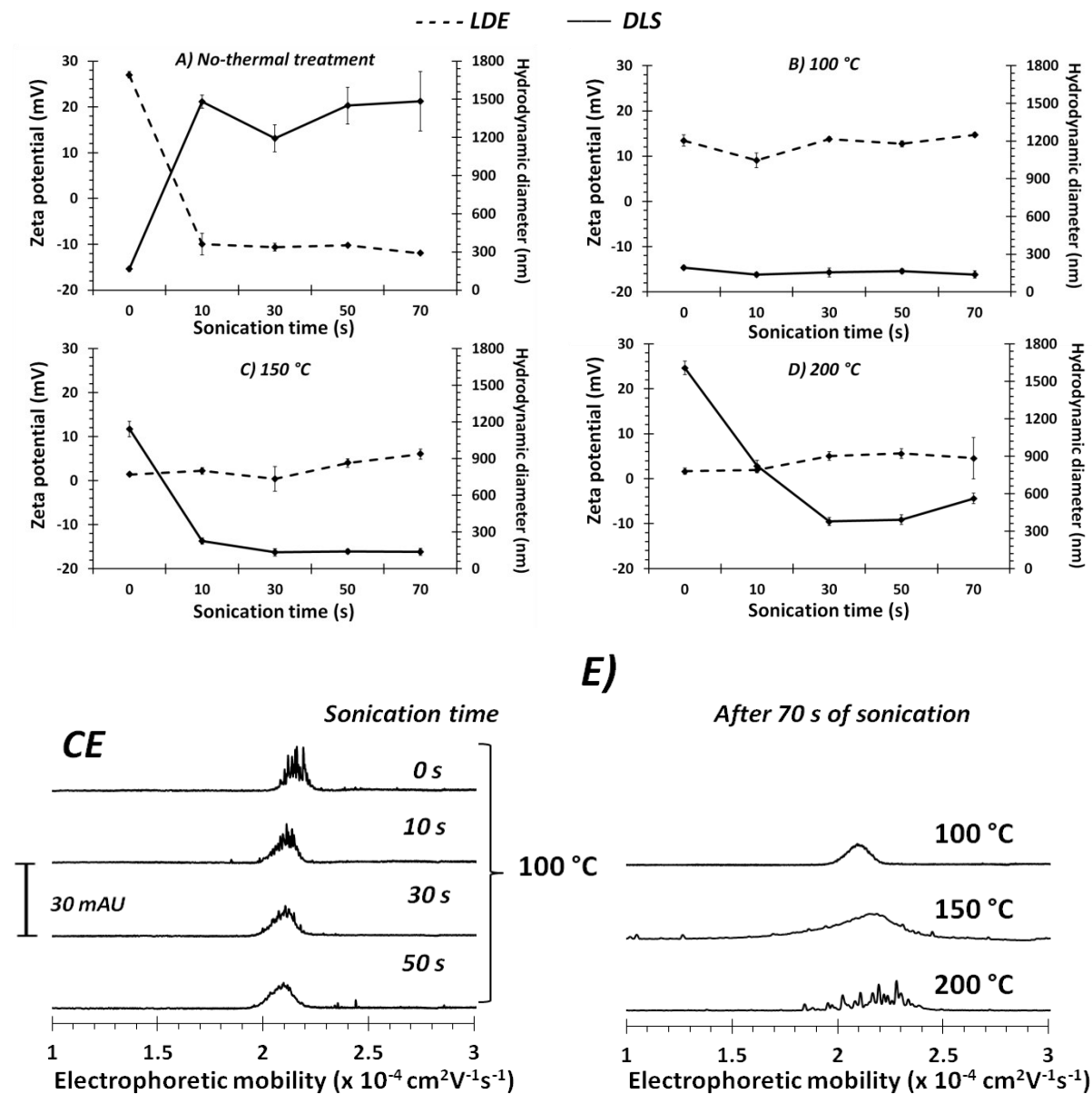
Fig. 2. 6. *Influence of the thermal treatment on the hydrodynamic diameter (continuous lines) and zeta potential (dashed lines) of ZGO-NH$_2$ (1.0 mg/mL) estimated by DLS and LDE in 20 mM MOPS (pH 7.4). A) No thermal treatment, B) 100 °C/15 minutes, C) 150 °C/15 minutes, D) 200 °C/15 minutes (n= 4 repetitions, and error bars represent standard deviation). E) Electrophoretic profiles of ZGO-NH$_2$ (0.2 mg/mL) during pre-conditioning after thermal treatment steps in 10 mM MOPS (pH 7.4). Separation conditions: DDABr modified capillary column: 50.0 μm i.d., 35.0 cm total length, 26.5 cm effective length; injection: 10 s at 20 mbar; applied voltage: -10 kV; UV absorption detection at 200 nm; capillary temperature: 25 ∘C.*

CHAPTER II

FUNCTIONALIZATION AND CHARACTERIZATION OF ZnGa$_{1.995}$Cr$_{0.005}$O$_4$ PERSISTENT LUMINESCENCE NANOPARTICLES BY DYNAMIC LIGHT SCATTERING, LASER DOPPLER AND CAPILLARY ELECTROPHORESIS

An obvious aggregation was noticed with just the naked-eye in anionic buffers but not in zwitterionic ones. Electrostatic interactions between positive residual amino-groups on the NP surface and anionic buffers can contribute to colloidal aggregation. This phenomenon is emphasized by the presence of multivalent ions such as phosphates and citrates. The strong suppression of the electrostatic repulsion between two charged colloidal particles by multivalent ions can be caused by their relatively strong screening, and by the close encounter between nanoparticles and thereby, their aggregation [278]. As the best dispersion media were the zwitterionic buffers, only MOPS and HEPES were considered for further experiments.

Figure 2.6A corresponding to ZGO-NH$_2$ that did not undergo the optimized subsequent drying and heating process shows a drop in zeta potential and a concomitant increase in hydrodynamic radius after the first sonication step, which can be explained by a partial sequential removal of the aminosilane layer. The sonication step seems critical in the loss of the aminosilane layer, altering directly NP physical stability as dramatic aggregation is observed. On the other hand, the influence of thermal treatment on ZGO-NH$_2$ is shown on Figures 2.6 B-D, for 100, 150 and 200 °C thermal treatment, respectively. For a 100°C heating treatment, the ZGO-NH$_2$ retained initial zeta potential and hydrodynamic diameter values before sonication (13.4 mV and 140 nm, respectively). For a 150°C and 200°C thermal treatment, initial zeta potential values were lower (close to zero) than for the two previously described conditions. The sonication process allowed to increase these values until ζ= 6.0 mV for a 150°C thermal treatment, whereas zeta potential remained almost constant for a 200°C thermal treatment (ζ= 4.6 mV). A stable hydrodynamic diameter (145 nm) was reached after sonication steps for the NPs heated at 150 °C, while NPs treated at 200 °C remained clustered after sonication. The optimal conditions seem to be obtained for a 100 °C thermal treatment, which allows obtaining slightly positive NPs (zeta potential between 9.0 and 18.7 mV) with an average hydrodynamic diameter of 140-145 nm.

To date, capillary electrophoresis has been generally applied to negatively charged nanoparticles since positively charged nanoparticles can lead to fused-silica capillary inner wall adsorption [264]. Cationic colloids have therefore received little attention so far [203, 264, 279-281]. Thus, different strategies for capillary wall modification aiming at preventing wall adsorption have been developed [279]. In this study we employed the DDABr dynamic modification of silica capillaries according to previous report in order to avoid cationic nanoparticles adsorption to the capillary wall [269]. Successsive CZE separations of ZGO-NH$_2$ at the various stages of the treatment were performed in these modified capillaries by using MOPS or HEPES as background electrolyte. Figure 2.6E shows the electrophograms of the 100°C-treated ZGO-NH$_2$ at the different sonication steps. From the electrophoretic profiles, an aggregation phenomenon prior to sonication is evidenced (spiky profiles), that completely disappears after one minute sonication. In the zone delimited by a square is presented the sonication step corresponding to 70 s. With the 150°C thermal treatment, DLS measurements indicated that the NPs were apparently stable after the sonication step, according to their hydrodynamic size, however a high polydispersity index (pdi= 0.21), in comparison to relatively low polydispersity index (pdi= 0.09) for 100 °C, was obtained and consistent with NP peak broadening evidenced in CZE that announces the beginning of an agregation. For the 200°C treated nanoparticles, the electrophoretic profile for the last sonication

CHAPTER II

FUNCTIONALIZATION AND CHARACTERIZATION OF ZnGa$_{1.995}$Cr$_{0.005}$O$_4$ PERSISTENT LUMINESCENCE NANOPARTICLES BY DYNAMIC LIGHT SCATTERING, LASER DOPPLER AND CAPILLARY ELECTROPHORESIS

step evidenced an obvious aggregation phenomenon, which is in accordance with previous results by DLS and LDE. More extended sonication times were evaluated, and the different thermally treated NPs showed similar behavior with respect to the corresponding profile after 70 s of sonication.

It has previously been observed that silanes first adsorb and subsequently covalently react with the surfaces [277]. In not-cured materials, APTES seems to be linked mainly by weak bonds, as the redispersion in water and wash steps cause the sequential removal of these non-covalently bounded APTES. Mild temperature-curing at 100 and 150 °C seem to result in covalent bonding of initially absorbed APTES to the nanoparticle surface. Thereby, the remaining weakly bounded APTES (by electrostatic interactions or by means of hydrogen bond) are thus removed by subsequent washing and sonication steps, allowing only the presence of covalently attached APTES. At 200 °C, APTES evaporation (boiling point: 217 °C) can occur leading to a lower zeta potential and accordingly nanoparticle aggregation.

2.3.5. Ionic strength effect on ZGO-NH$_2$ colloidal stability at physiological pH

After functionalization was stabilized, colloidal stability was tested. Figure 2.7 presents the hydrodynamic diameter and zeta potentials of ZGO-NH$_2$ in HEPES and MOPS at different ionic strengths (from 10 to 30 mM) and pH (7.0 and 7.4).
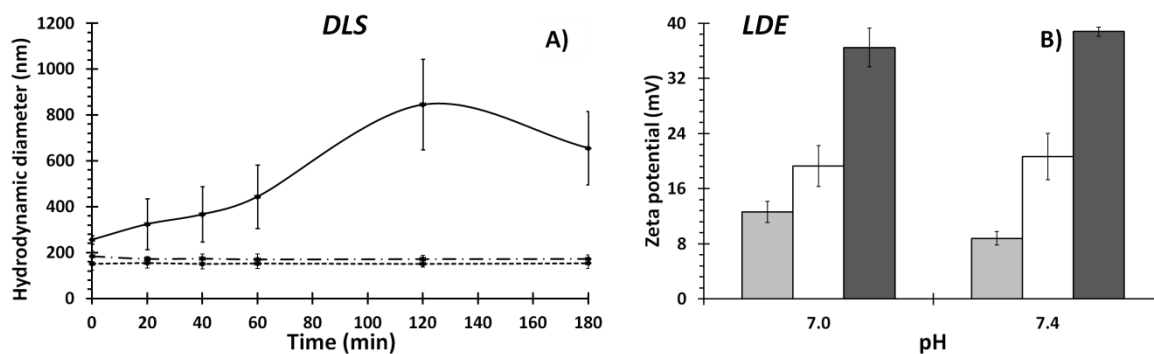
Fig. 2. 7. Hydrodynamic diameter estimated by DLS of ZGO-NH$_2$ (1.0 mg/mL) in HEPES (left) and zeta potential estimated by LDE of ZGO-NH$_2$ (0.2 mg/mL) in MOPS (right) at various ionic strengths (—— or ▨ : 30 mM ; ······ or □ : 20 mM ; –·– or ■ : 10 mM) (n= 4 repetitions, and error bars represent standard deviation).

Zeta potential was similar in both buffers at these pH values. While increasing the buffer ionic strength, the zeta potential decreased as expected, explaining the beginning of an aggregation consistent with the destabilization observed over time in 30 mM ionic strength buffers. For these ZGO-NH$_2$ NPs, similar zeta-potential values were derived from mobility measurements either by CE (ζ= 38.8±3.0mV) or LDE (ζ= 37.9±1.6mV) under the same analytical conditions (pH 7.4 and 10 mM MOPS).

CHAPTER II

FUNCTIONALIZATION AND CHARACTERIZATION OF ZnGa$_{1.995}$Cr$_{0.005}$O$_4$ PERSISTENT LUMINESCENCE NANOPARTICLES BY
DYNAMIC LIGHT SCATTERING, LASER DOPPLER AND CAPILLARY ELECTROPHORESIS

It is generally believed that a zeta potential greater than ± 20 mV is sufficient to maintain a stable formulation with a combined electrostatic and steric stabilization [282-284]. As evidenced by the hydrodynamic diameter measures over time, a zeta potential above 14.7 mV was sufficient to maintain the colloidal stability of ZGO-NH$_2$ in 20 mM MOPS and HEPES buffers. In addition to colloidal stability characterization, we developed for the first time a protocol (thermal treatment) to obtain chemically stable ZGO-NH$_2$.

2.3.6. Ionic strength effect on the ZGO-PEG colloidal stability at physiological pH

So as to help for nanoparticle stabilization in aqueous solutions, an inert hydrophilic molecular chain such as polyethyleneglycol (PEG) can be introduced on its surface [285, 286]. PEG has also been the most studied polymer used to decrease the detection of nanoparticles by the mononuclear phagocyte system [240]. For this purpose, ZGO-NH$_2$ were further modified to obtain a PEG coating, in order to reduce interactions with various proteins and biological elements, and thereby improve their biodistribution and application in biological imaging [37].

As for ZGO-OH and ZGO-NH$_2$, different separation media (at pH 7.4, for mimicking physiological media) were studied. ZGO-PEG colloidal stability was studied in 30-150 mM phosphate, MOPS and HEPES buffers. In this wide ionic strength range, the ZGO-PEG hydrodynamic diameter was constant (about 180 nm) at least during the first 3 hours after ending sonication in both anionic and zwitterionic buffers. Figure 2.8A shows the results for ZGO-PEG dispersed in phosphate buffer solutions. While performing CE separation in bare-fused silica capillaries in pH 7.4 phosphate buffer in this range of ionic strength, ZGO-PEG migrated as a peak near to the electroosmotic marker with a very slightly negative electrophoretic mobility (Figure 2.8B). This is in accordance with a quasi-neutral surface charge density of the ZGO-PEG due to the presence of PEG layer. As expected, electroosmotic mobility (first peak) decreased upon ionic strength increase; however, particle electrophoretic profile and mobility were unaltered at ionic strengths ranging from 30 to 150 mM, indicating quite constant particle properties in terms of hydrodynamic size and surface charge as well as colloidal stability (Figure 2.8A and 2.8B).

CE and LDE techniques allowed to study the ionic strength effect on the ZGO-PEG zeta potential in 30-150 mM phosphate and MOPS buffers (Figure 2.8C). It has to be noted that 150 mM ionic strength was chosen as it can mimic the osmotic pressure of the blood [161]. The results indicate that ZGO-PEG zeta potential is very low either in anionic or zwitterionic buffers. Furthermore, it was shown that this residual charge is dependent on the buffer nature, i.e. a slightly negative zeta value was obtained in phosphate buffer, whereas a slightly positive one was determined for MOPS and HEPES. This could be explained by the presence on the ZGO-PEG of residual amino groups that were not functionalized [37]. These residual positive charges can interact electrostatically with the counter-ion of the buffer (MOPS, HEPES and phosphate), leading to an overall slightly positive residual surface charge for the two zwitterionic buffers and an overall slightly negative one for phosphate. Only slight differences in ζ were found by comparing CE and LDE (less than 1.0 mV). Therefore, the ZGO-PEG colloidal stability within time was demonstrated in these classical dispersion solutions, indicating their adequacy for biocompatibility.
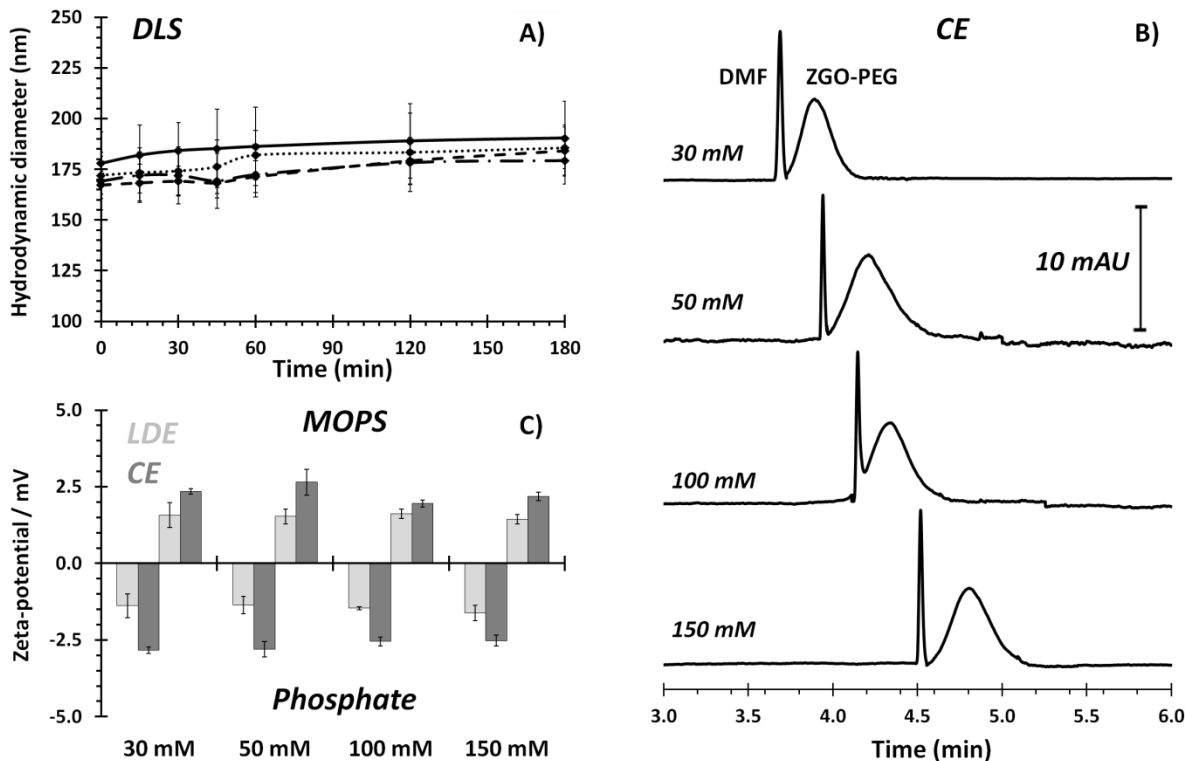
Fig. 2. 8. *A) Hydrodynamic diameter of ZGO-PEG estimated by DLS (1.0 mg/mL). B) Electrophoretic profiles of ZGO-PEG (0.2 mg/mL), and C) Zeta potential of ZGO-PEG estimated by LDE ☐ and CE ☐ (0.2 mg/mL) in phosphate and MOPS buffers pH 7.4 at various ionic strengths (----- 30 mM, –·– 50 mM, ······ 100 mM, and ⎯⎯ 150 mM). (n= 4 repetitions, and error bars represent standard deviation). CE separation conditions : Separation conditions: bare fused silica capillary column: 50.0 μm i.d., 35.0 cm total length, 26.5 cm effective length; injection: 10 s at 20 mbar; applied voltage: 12 kV; UV absorption detection at 200 nm; capillary temperature: 25 ∘C. Peak at left corresponds to EOF (0.01% DMF).*

2.4. PARTIAL CONCLUSIONS

In the present chapter we characterized ZGO persistent luminescence nanoparticles after their synthesis and functionalization by a successive mechanism to sequentially obtain hydroxylated, aminosilanated and PEGylated NPs. Various buffers of different nature, pH and ionic strength were employed as dispersion media for DLS and LDE characterization as classical techniques and for CE separations as an alternative emerging methodology. The characterizations at each step allowed (1) verifying of the effective functionalization, (2) to optimize the different steps in terms of reaction conditions and washing procedures, (3) to identify the best conditions to mimic physiological ones and allow colloidal stability. A new protocol to improve ZGO-NH$_2$ stability consisting in thermal treatment so as to complete covalent binding of APTES initially adsorbed into the surface was established, consisting in a 100 °C/15 min heating step. This optimization is of great importance for

CHAPTER II

FUNCTIONALIZATION AND CHARACTERIZATION OF $ZnGa_{1.995}Cr_{0.005}O_4$ PERSISTENT LUMINESCENCE NANOPARTICLES BY DYNAMIC LIGHT SCATTERING, LASER DOPPLER AND CAPILLARY ELECTROPHORESIS

NP functionalization as most literature protocols use APTES as a reaction intermediate. The buffer media was found to have a significant effect on the zeta potential of functionalized ZGO NPs. Among them, phosphate buffer proved to be an adequate dispersion medium (in terms of electrostatic stability) for negative or neutral NPs, while zwitterionic buffers (MOPS and HEPES) was adequate for positive and neutral NPs. For ZGO-PEG, colloidal stability was obtained in 150 mM phosphate, HEPES and MOPS at pH 7.4, which are classically used as biological buffers. The interest of employing CE for nanoparticle characterization was again demonstrated in this study, allowing a very quick and easy characterization with minimal amount of nanoparticles independently of the surface charge density. Thanks to the electrophoretic profiles, stability, polydispersity, size characterization and zeta potential could be determined in various buffers. This new generation of ZGO-NPs could lead to biocompatible persistent luminescence nanoparticles not only for cell targeting applications but also for proper distribution in living organisms.

CHAPTER III.

ELECTROKINETIC HUMMEL-DREYER CHARACTERIZATION OF NANOPARTICLE-PLASMA PROTEIN CORONA: THE NON-SPECIFIC INTERACTIONS BETWEEN PEG-MODIFIED PERSISTENT LUMINESCENCE NANOPARTICLES AND BOVINE SERUM ALBUMIN
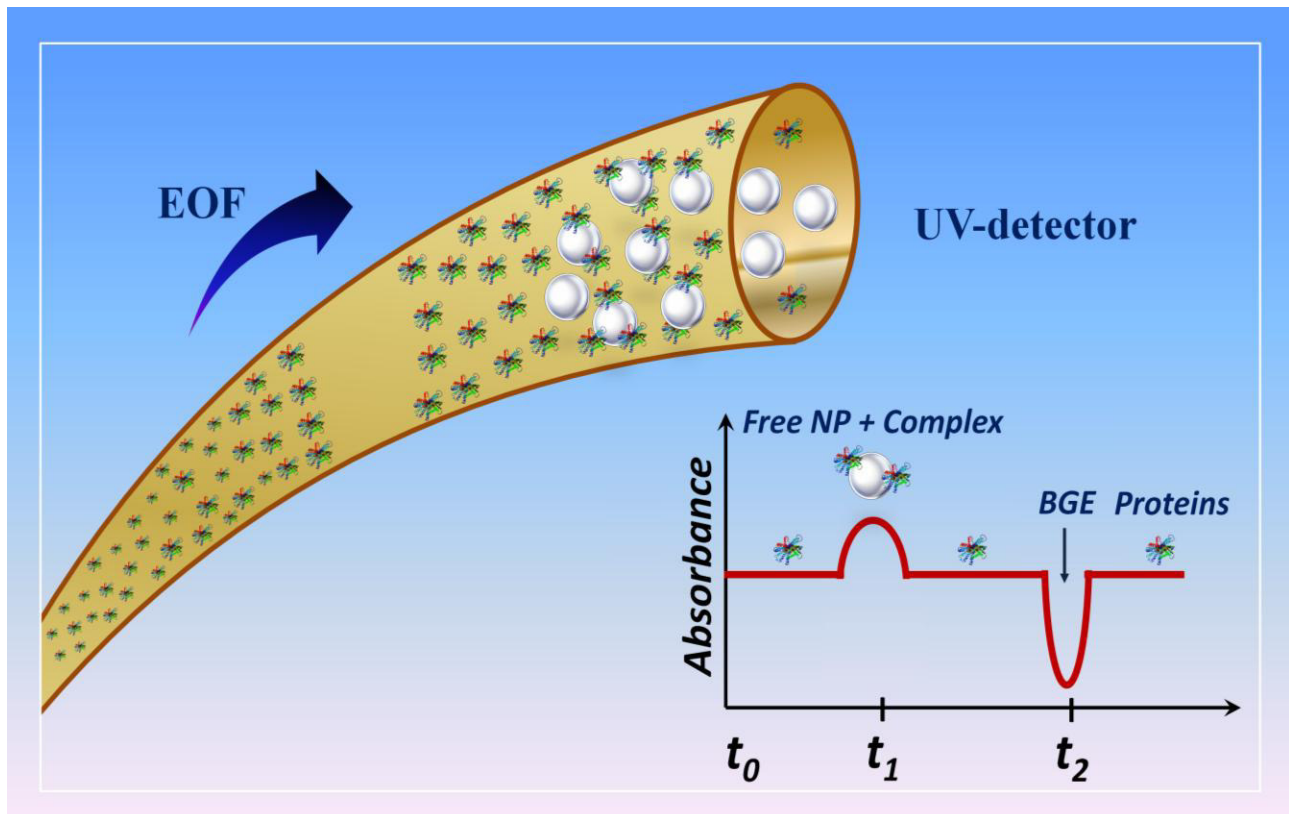
Nanoparticles (NPs) play an increasingly important role in the development of new biosensors, contrast agents for biomedical imaging and targeted therapy vectors thanks to their unique properties as well as their good detection sensitivity. However, a current challenge in developing such NPs is to ensure their biocompatibility, biodistribution, bioreactivity and *in vivo* stability. In the biomedical field, the adsorption of plasmatic proteins on the surface of NPs impacts on their circulation time in blood, degradation, biodistribution, accessibility, the efficiency of possible targeting agents on their surface, and their cellular uptake. NP surface passivation is therefore a very crucial challenge in biomedicine. We developed herein for the first time an electrokinetic Hummel and Dreyer method to quantitatively characterize the formation of protein corona on the surface of NPs. This strategy was designed and optimized to evaluate the non specific binding of bovine serum albumin with the recently discovered PEG-functionalized $ZnGa_{1.995}Cr_{0.005}O_4$ persistent luminescence NPs developed for *in vivo* biological imaging. The binding strength and the number of binding sites were determined at different ionic strengths. This methodology opens the way to an easy, low sample- and low time-consuming evaluation of the impact of NP surface modification on protein-corona formation and therefore on their potential for various bio-medical applications.

3.1. BACKGROUND AND JUSTIFICATION

Optical imaging is a rapidly extending research field aiming at non-invasively interrogating animals for preclinical studies [1]. The structural design of NPs for biomedical imaging continues to expand and diversify [287]. In this sense, some materials present innovative properties such as persistent luminescence, in which the light emission remains for extended periods of time (up to hours) after light excitation is stopped [16, 23, 255-259]. This property allows observations without time constraints, and also avoids autofluorescence signals produced by biological tissues when using and exciting fluorescent probes [33]. The recently synthesized persistent luminescence PEG-functionalized $ZnGa_{1.995}Cr_{0.005}O_4$ (ZGO-PEG) NPs are a hold great promise for the non-invasive exploration and *in vivo* detection of multiple disease markers using this properties [33]. To go further in the potentials of these NPs, it is necessary to evaluate their interactions with plasma proteins in order to predict and improve their *in vivo* biodistribution, biocompatibility and behavior [288]. Indeed, the adsorption of plasmatic proteins on the surface of NPs directly impacts the NP circulation time in blood and degradation, their biodistribution, accessibility, the efficiency of possible targeting agents on their surface, and their cellular uptake [37, 44, 233, 234]. The high surface/volume ratio of NP increases the potential for interaction with macromolecules and cellular components; however, this interaction depends on their size, on the nature of the functional groups on the surface and on the particle overall surface charge density [44, 230]. In the absence of nonspecific adsorption of serum proteins, the NP residence time in the blood is increased, which enhances passive tumor targeting [235, 236]. So as to avoid protein adsorption, the NP surface passivation is therefore a crucial challenge [237-239]. One of the most currently applied strategies

involves the use of polyethylene glycol (PEG) coatings to limit these nonspecific interactions [44, 64, 240].

Various analytical methodologies have been reported in the literature to study NP/protein interactions, i.e. circular dichroism [289], quartz crystal microbalance [290], scattering correlation spectroscopy [291], dynamic light scattering (DLS)[238] and some spectroscopic methods such as localized surface plasmon resonance, fluorescence and surface-enhanced Raman scattering fluorescence [292]. A few recent publications showed different ways by which capillary electrophoresis (CE), in zone or affinity mode, can be applied to evidence interactions between NPs used as contrast agents in biological systems and proteins.[169] CE shows various advantages such as short time analysis, small sample volume consumption, simplicity, cost-efficiency, high degree of resolution and efficiency [169, 293]. Methods to study and quantify binding parameters between a substrate and a ligand require careful determination of the concentration of bound or free ligand without disturbing the equilibrium between the two [294, 295]. CE has been used frequently for the determination of binding parameters, principally between drugs and proteins [293, 296]. The adsorption of plasmatic proteins onto pegylated NPs has also been qualitatively evaluated by different techniques, including direct injection CE [66, 183]. However, the use of CE-based methods for protein-NP interaction studies is still rather preliminary in character [169].

The CE methods for binding parameter determination can be subdivided according to considered experimental parameters: mobility shift for affinity (ACE) and vacancy affinity (VACE); plateau height for frontal analysis (FACE); peak area for direct sample injection, vacancy peak (VPCE) and Hummel-Dreyer (HDCE) and a combination of some of them in non-equilibrium conditions (Non-equilibrium capillary electrophoresis of equilibrium mixtures, NECEEM). The selection of one of these methods depends on the strength and kinetics of the interaction [296, 297].

In the present study the nonspecific interaction between persistent luminescence ZGO-PEG NPs and bovine serum albumin (BSA) was quantified by HDCE. To our knowledge, HDCE has not been previously reported in the literature for the evaluation of the interactions in liquid phase between NPs and proteins. Our HDCE-based method was designed and optimized so as to access both the binding constant and the number of proteins bound onto NP surface. This methodology seems very useful to identify the most appropriate coating in order to limit non-specific interactions between nanoprobes and proteins prior to biodistribution studies in small animals.

3.2. MATERIALS AND METHODS

Bovine serum albumin (BSA) (chromatographically purified, ≥ 98 %), sodium phosphate monobasic dehydrate, sodium phosphate dibasic, aminopropyltriethoxysilane (APTES), dimethylformamide (DMF) were purchased by Sigma-Aldrich. Gallium oxide and chromium nitrate were provided from Alfa Aesar chemicals, zinc nitrate from Fluka and α-methoxy-ω-N-hydroxysuccinimide polyethylene glycol (5000 Da) (PEG) from Iris Biotech GmbH. Phosphate

buffer (PB) solutions (pH 7.4) were prepared at various ionic strength (IS), then sonicated and filtered through 0.2 µm nylon syringe filters (Corning, NY, USA) before use.

ZnGa$_{1.995}$Cr$_{0.005}$O$_4$ nanoparticles were prepared using a low temperature hydrothermal synthesis process as described by *Maldiney et al.* [33]. The resulted hydroxylated material (ZGO-OH) was fractioned by repeated centrifugation steps and the 90 nm NP fraction (hydrodynamic diameter) were collected, considering a PDI lower than 0.1 as a quality parameter. Further surface modification was performer according our previous report (Chapter II) [193].

Nanoparticle size and zeta potential were determined by DLS and Laser Doppler Electrophoresis (LDE) measurements in background electrolyte (BGE) consisting in PB (pH 7.4) at various IS, with a Nano ZS Zetasizer instrument (Malvern Instruments, France). The morphology of the NPs were assessed using a JEOL JEM-1010 Transmission Electron Microscope (TEM) equipped with an ORIUS digital camera, by GATAN operated at 90 kV. Electrophoretic separations were performed with a Model BioFocus 3000 CE system equipped with a UV–Vis absorbance detector, a power supply and automatic sample changer, which were purchased from Bio-Rad (San Francisco, CA, USA). BioFocus system integration software (Bio-Rad) was used for data collection and treatment. 50 µm id x 31 cm fused-silica capillaries (detection length, 26.5 cm) from Polymicro Technologies (Phoenix, AZ, USA) were used after activation by successive flushes (925 mbar) with 1.0 M NaOH (15 min), 0.1 M NaOH (15 min) and H$_2$O (5 min), respectively. Injections were performed hydrodynamically applying 20 mbar at the capillary inlet for 10 s. The applied voltage was 12 kV, with positive polarity at the capillary inlet. The temperature of the capillary cartridge was set at 25 °C. The detection wavelength was 200 nm. Zeta potential was also derived from particle electrophoretic mobility estimated from particle migration time measured at peak apex as for LDE measurements, both of them using the Ohshima-Pyell equation [165].

The HDCE protocol consists in three steps: capillary preconditioning (capillary filled with solutions of proteins at varying concentrations in BGE), external calibration (injection and separation in the preconditioned capillary of a zone of the corresponding BGE free of protein) and then sample separation (injection and separation in the preconditioned capillary of a zone of a 0.2 mg/mL NP dispersion in the corresponding BGE free of protein, which corresponds to an equivalent molar concentration of 3.88 nM considering an average solid radius of 15 nm and a density of 6.055 g/cm^3 [298, 299]. The preconditioning step consists in successive injection zones in the following order: 0.1 M NaOH (1 min), BGE (1 min), protein solutions (2 min) at varying concentrations (0.10, 0.15, 0.20, 0.25, 0.30, 0.60 and 0.90 µM) in BGE of varying IS (30, 60, 100 and 150 mM). The separation was repeated four times for each sample. Afterwards, electroosmotic mobility was measured (injection of 0.001% DMF in BGE) and a supplementary rinsing step was applied every four measures, consisting in successive flushes of 0.1 M NaOH, H$_2$O, BGE, for 3 min each.

For each BGE containing proteins, viscosity and conductivity measurements were carried out according a capillary electrophoresis method as described by *Francois et al.* [300].

CHAPTER III

ELECTROKINETIC HUMMEL-DREYER CHARACTERIZATION OF NANOPARTICLE-PLASMA PROTEIN CORONA: THE NON-SPECIFIC INTERACTIONS BETWEEN PEG-MODIFIED PERSISTENT LUMINESCENCE NANOPARTICLES AND BOVINE SERUM ALBUMIN

For all the experiments realized in this work arithmetic mean values were obtained from four independent measures for each analysis. For the numerical analysis, the peak area was normalized by the peak migration time.

3.3. RESULTS AND DISCUSSION

The $ZnGa_{1.995}Cr_{0.005}O_4$ persistent luminescence NPs were synthesized with an average solid diameter of 20-40 nm and functionalized according to previous work [33, 193], leading to a PEG functionalization (Figure 3.1A). Independent nanoparticles with nearly spherical shape were observed.
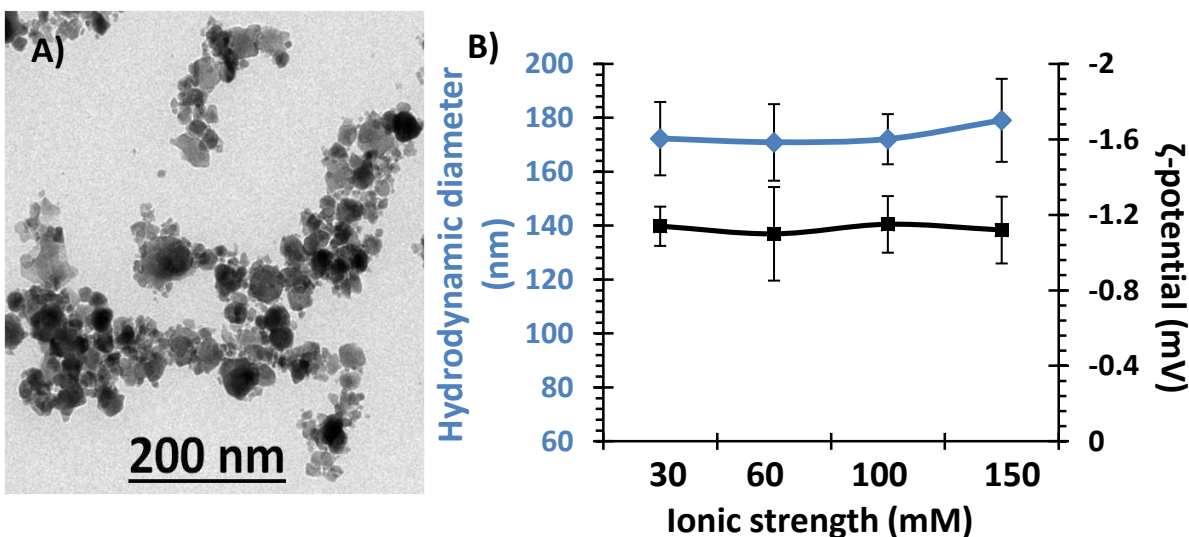
Fig. 3. 1. A) TEM image of the ZGO-PEG. B) Ionic strenght effect on the hydrodynamic diameter (diamonds) and ζ-potential (squares) of ZGO-PEG (0.2 mg/mL) in phosphate buffer solutions, pH 7.4, at varying ionic strength from 30 to 150 mM.

The colloidal stability and physicochemical properties of these NPs in suspensions (0.2 mg/mL) were evaluated and controlled by measuring their hydrodynamic diameter and zeta potential in phosphate buffer (pH 7.4) in the 30 to 150 mM ionic strength (IS) domain. The PEGylated NPs present hydrodynamic diameter of 174.5 ± 7.6 nm and a zeta potential of -1.2 ± 0.5 mV (Figure 3.1A). This thorough control proves that no aggregation occurs in the experimental conditions, preventing any measurement artifact. An extensive study of these properties has already been carried out by our group and reported in a previous work [193].

3.3.1. The Hummel-Dreyer method as a propose to determinate nanoparticle/protein interactions

As the ZGO-NPs were modified with PEG on their surface, interaction with plasmatic proteins should be low and non-specific, enhancing the permanence of the NPs in blood circulation

[37]. Depending on the relative strength and association/dissociation kinetics of a substrate/ligand interaction, different ways to address the binding parameters can be elected [169]. The interaction between BSA and ZGO-PEG NPs were initially investigated by different CE modes, including capillary zone electrophoresis and frontal analysis (FA), so as to estimate the most adequate CE format (data not shown). As the preliminary results did not show any appreciable change in the electrophoretic profiles while varying either the protein or the NP concentrations, the HDCE method was investigated.

The HDCE method, based on peak area measurements, permits the characterization of interactions with rapid dissociation kinetics [301]. The process developed in this work is illustrated in Figure 3.2. The capillary is filled with BGE containing the ligand "L" at varying known concentrations $[L]_t$ (step 1). An external calibration is performed by injection and separation of a constant volume of the BGE free of ligand or substrate (step 2). One "negative peak" appears, due to the local deficiency of L in the BGE. For interaction study, the same volume of substrate "S" at a fixed concentration $[S]_t$ (lower than $[L]_t$), dispersed in the BGE free of ligand is then injected and separated (step 3). Two peaks may appear in the electropherogram [241, 294, 301]. A "positive peak" corresponds to the free substrate, while a "negative peak" is caused by the local deficiency of L in the sample and by the complexation with the substrate. From the peak area of the "negative peak" and the external calibration, one can access to the concentration of ligand bound to the substrate $[L]_b$, and therefore to the binding constant and the number of binding sites.

For a NP-protein interaction system, the NP can be considered as the substrate (S) with multiple binding sites due to its major size, lower concentration, uniformity of functional groups, and capacity to form multiple and possibly similar binding sites for proteins on the surface. On the other hand, proteins can be considered as monovalent ligands (L) [244]. Assuming a system in which a protein can potentially bind to multiple independent binding sites on the NP surface, the interaction can be expressed as (Eq. 3.1):

$$S + nL \rightleftharpoons SLn \qquad \text{Eq. 3.1}$$

where n is the total number of binding sites. If we consider that the n independent sites have identical energy, the elementary interaction (between one protein molecule and one interaction site at the NP surface) is characterized by a binding constant K_a. The fraction of proteins actually bound per nanoparticle [294] can then be defined as "r" (Eq. 3.2):

$$r = \frac{[L]_b}{[S]_t} = n\,\frac{[L]Ka}{[L]Ka+1} \qquad \text{Eq. 3.2}$$

The "r" value varies from 0 to n. Eq. 3.2 can be linearized as follows (Eq. 3.3):

$$\frac{r}{[L]} = -K_a r + K_a n$$

Eq. 3.3

When plotting r/[L] versus r, one can access to the Scatchard plot, allowing for K_a determination (slope in absolute value) and n (x-intercept).
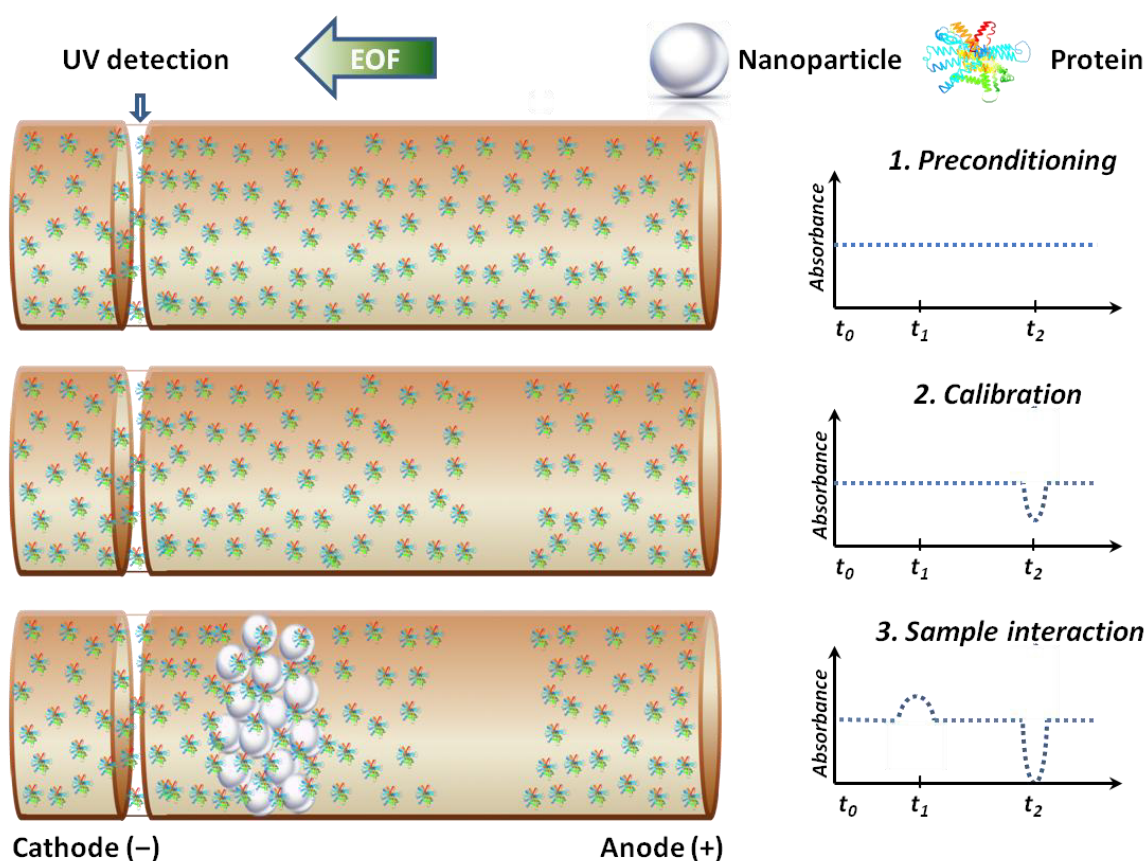
Fig. 3. 2. Schematic representation of the Hummel-Dreyer method for the evaluation of interactions between nanoparticles and proteins. EOF: Electroosmotic flow.

3.3.2. External calibration for the determination of the bound protein concentration

The viscosity and the conductivity of the BGE containing proteins were evaluated throughout the range of protein concentrations and BGE IS [300]. No significant variation in viscosity was

observed (8.5-9.0 $\times 10^{-4}$ Pa.s) and conductivity increased linearly with IS, whatever the protein concentration. Therefore, the changes in electrophoretic profiles in this study are only representative of the interaction between the ZGO-PEG NPs and BSA. Figure 3.3 presents as an example the electropherograms obtained for an external calibration performed in a 60 mM BGE containing BSA at a concentration, $[L]_t$, ranging from 0 to 0.9 µM.
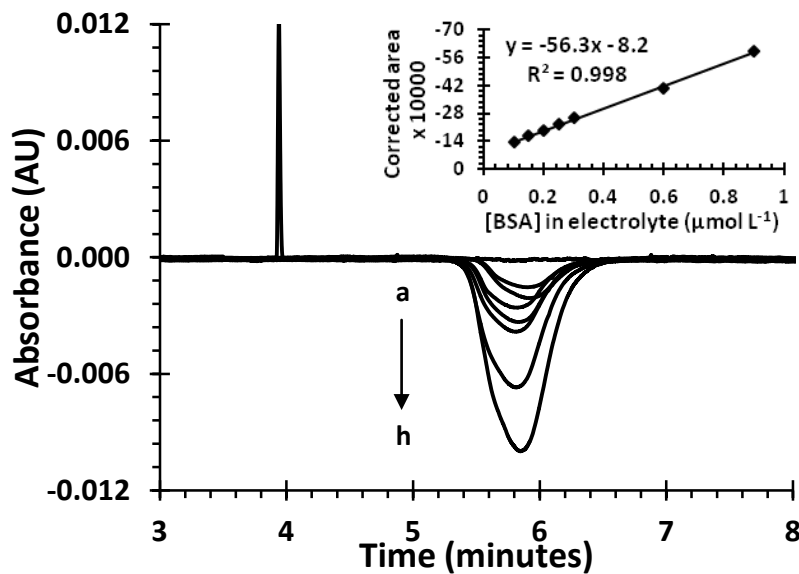
Fig. 3. 3. Representative electropherograms at λ = 200 nm for external calibration according Hummel-Dreyer method. Vacancy peaks corresponds to injections of background buffer (pH 7.4 phosphate buffer solution at 60 mM) in a capillary filled with buffer containing BSA at different concentrations (a-DMF, b-0.10, c-0.15, d-0.20, e-0.25, f-0.30, g-0.60 and h-0.90 µmol L^{-1}). The corresponding calibration curve is shown in the inset figure.

The "negative peak" is due to the vacancy of the protein, which is originated by the injection of BGE, and its area increases proportionally to $[L]_t$ in the capillary (see inserted calibration curve). The "positive peak" corresponds to the neutral marker (EOF). No shift or peak distortion in the electrophoretic mobility of the vacancy peak was detected, whatever $[L]_t$, indicating the absence of possible undesirable protein adsorption to capillary wall.

To assess interaction parameters with the NPs, 10 nL of a 3.88 nM ZGO-PEG NP dispersion were injected in the same conditions as for calibration. Whatever the IS, similar electrophoretic evolutions occurred, as presented in Figure 3.4 in the case of a 60 mM IS BGE.
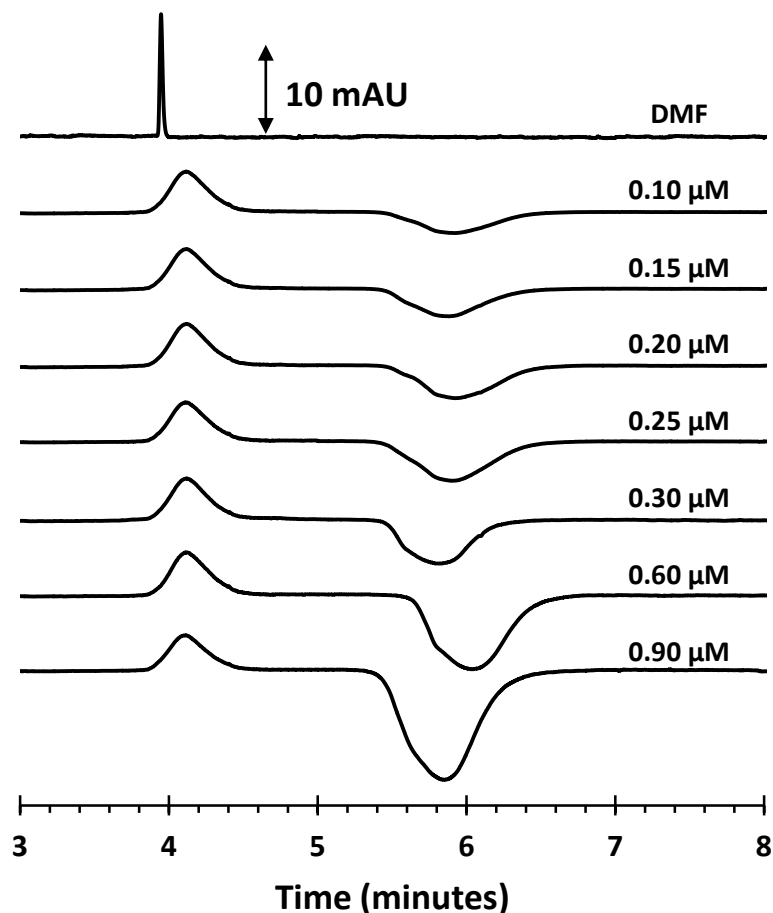
Fig. 3. 4. Electropherograms at λ = 200 nm characteristic of the BSA/ZGO-NP interaction at different protein concentrations in 60 mM IS phosphate buffer solutions (pH 7.4) implementing the Hummel-Dreyer method in CE.

In this figure, a "positive peak" appears at -1.2×10^{-5} cm^2.V^{-1}.s^{-1} corresponding to ZGO-PEG NPs, whatever the protein concentration in the BGE. This peak remains without appreciable change in shape and magnitude. The "negative peak" is due to the vacancy of the protein originating from the interaction with the injected NPs and the lack of ligand in the injected sample. As no peak distortion occurs while increasing protein concentration, the hypothesis of a rapid dissociation of the ZGO-PEG NP/BSA complex (S/L) seems valuable. In this study, no other peak corresponding to S/L could be identified; however, the variation in the "negative peak" area between calibration and sample separation (under the same experimental conditions) proves the presence of an interaction. Two hypotheses can emerge: (1) a fast dissociation of the complex compared to the electrokinetic separation time and/or (2) no significant difference in electrophoretic mobility between free and bonded NPs. The literature presenting HDCE for other S/L systems did not permit to identify any other peak neither [294, 296, 302-304].

3.3.3. Saturation curves and binding parameters determination

The bound ligand concentration $[L]_b$ could be estimated (Eq. 3.4) from the "negative" or vacancy peak area (A_c) obtained during calibration and the one arising from the injection of the substrate (A_s) for a given BSA content in the separation buffer, $[L]_t$ [294]:

$$[L]_{bound} = \frac{A_S - A_c}{A_c}[L]_t \text{ , with } A_c < A_s$$

Eq. 3.4

The $[L]_b$ quantification allows then to determine the binding isotherm, i.e. r versus $[L]_t$ (Figure 3.5A). It appears that $[L]_b$ decreases when IS increases, due to counter-ions condensation at the NP surface. Furthermore, the experimental conditions allow drawing a quite complete binding isotherm, which is convenient for further mathematical treatment. The linearization of this binding isotherm leads to the Scatchard plot (Figure 3.5B). The good repeatability of the measures (over four repetitions) reflects the good accuracy of this methodology, and allows the estimation of the association constant (K_a) and the number of binding sites (n) on each NP (Table 3-1). As expected from Figure 3.5A, K_a and n decrease when IS increases, due to counter-ion condensation and therefore competition to associate with NP surface, indicating that electrostatic interactions control ZGO-PEG NP/BSA association. No cooperativity was identified in the conditions experienced here, as the Scatchard plot is linear over the full concentration domain.
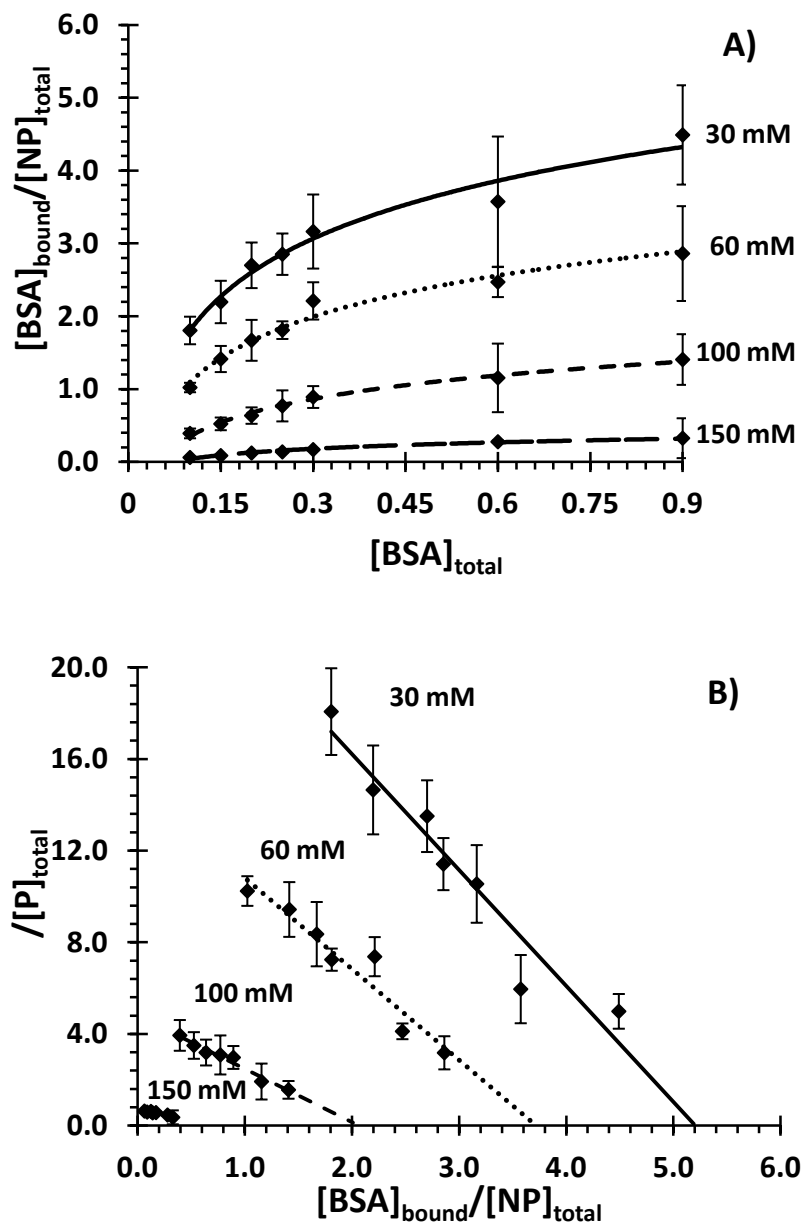
Fig. 3. 5. A) Binding isotherms characterizing the BSA/ZGO-PEG NP interaction in phosphate buffer (pH 7.4) at varying ionic strength. B) Scatchard plot. Error bars indicate the ± standard deviation of a set of four measurements performed on samples prepared independently at each concentration.

CHAPTER III

ELECTROKINETIC HUMMEL-DREYER CHARACTERIZATION OF NANOPARTICLE-PLASMA PROTEIN CORONA: THE NON-
SPECIFIC INTERACTIONS BETWEEN PEG-MODIFIED PERSISTENT LUMINESCENCE NANOPARTICLES AND BOVINE SERUM
ALBUMIN

Table 3- 1. Summary of model fitting parameters according to the Hummel-Dreyer method for BSA/ZGO-PEG complexes.

Parameter	Ionic strength			
	30 mM	60 mM	100 mM	150 mM
$K_{a\ Scatchard}$ (M^{-1})	$5.06 \pm 0.64 \times 10^6$	$3.98 \pm 0.38 \times 10^6$	$2.33 \pm 0.23 \times 10^6$	$9.53 \pm 0.18 \times 10^5$
n	5.21 ± 0.27	3.71 ± 0.13	2.06 ± 0.22	0.74 ± 0.15

Under experimental conditions best mimicking physiological conditions (i.e. 150 mM IS), the estimated K_a value was about 10^6 M^{-1}, and increased up to 5.10^6 M^{-1} over decreasing IS down to 30 mM. The binding parameters available in the literature are provided for a great diversity in NP nature (composition, size, shape, surface functionalization) and experimental conditions (pH, IS, methodology) making difficult a direct comparison between the obtained values and the referenced ones. K_a values describing the adsorption of serum proteins to nanomaterials and estimated using different methodologies may vary from approximately 10^4 to 10^9 M^{-1} [63]. For example, by means of ACE, the interaction between PEGylated gold-nanorods of smaller size than the NPs in this study (7.8 nm instead of 175 nm) and BSA was quantified and the K_a estimated to be equal to 1.53×10^4 M^{-1} (5 mM MOPS , pH 7.4) [202].

Albumin is well known for its ability to bind molecules of many types. The interaction of BSA, a "soft" protein, with surfaces is thought to be governed by an entropically favored conformational change that offsets the endothermicity of interactions [305, 306]. The flexibility of the albumin structure adapts it readily to ligands, and its three-domain design provides a variety of sites. BSA shows discrete binding sites with different specificities [307]. As we identified rather weak and fast-dissociating interactions between ZGO-PEG NPs and BSA, the ligand binding properties of albumin seem counteracted by the passivation effect of PEG chains immobilized on NP surface. These results are in good agreement with the long circulation time in blood of PEG passivated ZGO NPs evidenced after intravenous injection in mouse, proving the effectiveness of this surface treatment [37].

This HDCE methodology allows to quickly and easily determining binding parameters for this type of complexes. Contrary to other proposed methodologies, it permits to reach equilibrium directly into the capillary without additional pre-incubation steps that may alter the chemical integrity of the functional groups around the nanoparticles, as for example by means of hydrolysis reactions [308].

3.4. PARTIAL CONCLUSIONS

A main challenge in developing biomedical nanoprobes is to ensure their biocompatibility, bioreactivity and *in vivo* stability. For this purpose, a better understanding of the behavior of the NPs in biological fluids and a tailored surface chemistry for ensuring both particle stability and furtivity in blood circulation is necessary. We developed an electrokinetic Hummel-Dreyer method for a deeper and fast characterization of the nonspecific protein adsorption phenomenon on NP surface. This method does not require pre-incubation steps, which means that chemical equilibrium is not mechanically altered during sample preparation. The binding constant and number of binding sites were determined at different ISs. Increasing condensation of the BGE counter-ions at the nanoparticle surface affected the strength of the interaction that binds BSA to NPs, indicating the electrostatic nature of the BSA/ZGO-PEG NP interaction. In a 150 mM IS phosphate buffer (pH 7.4) the number of binding site and the binding constant were estimated equal to 0.74 and 9.53×10^5 M^{-1}, respectively. These results at different ionic strengths are consistent with a weak non-specific interaction that may be ensured by the NP surface PEGylation.

The Hummel-Dreyer method has shown to be sufficiently sensitive to detect small changes in the magnitude of association parameters. The non-specific interaction between PEG-functionalized $ZnGa_{1.995}Cr_{0.005}O4$ persistent luminescence nanoparticles and BSA as a model protein has been demonstrated quantitatively. This methodology opens the way for a better understanding of NP/protein interactions and for a prediction of NPs behavior in biological systems. This could guide future NP syntheses and functionalization for the design and performance improvement of new NPs in various domains such as diagnostic biosensors, biomedical imaging and targeted therapy.

The methodology presented in this Chapter will be applied in the next chapters. First, for the optimization of the aminosilanation time required in the sequence of the reactions used to obtain PEGylated nanoparticles (Chapter IV), and secondly, for the comparison of the interactions between HSA and ApoE (Chapter V).

CHAPTER IV.

A QUANTITATIVE METHOD TO OPTIMIZE THE PEGYLATION OF PERSISTENT LUMINESCENCE NANOPARTICLES THUS INCREASING THEIR PERMANENCY IN BLOOD CIRCULATION: NANOPARTICLE INTERACTIONS WITH HUMAN SERUM ALBUMIN
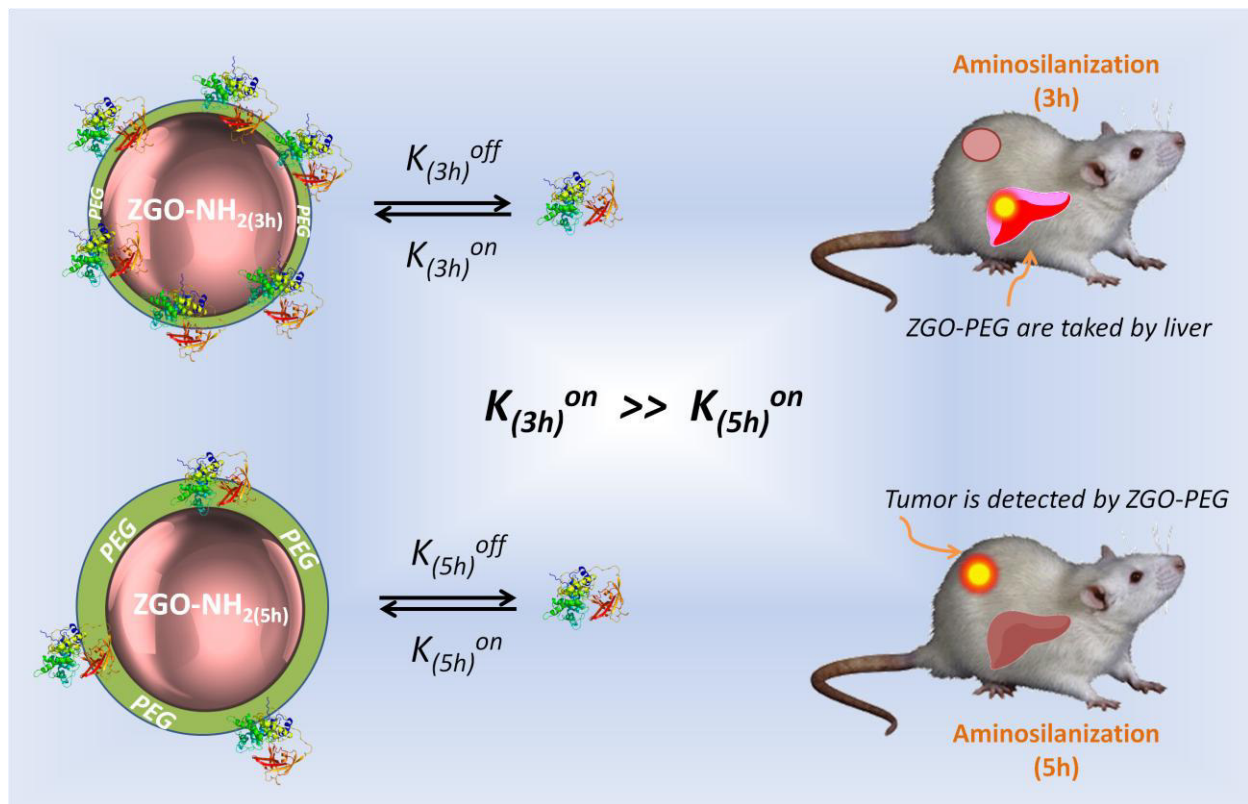
Adequate biodistribution is an indispensable parameter for NP biomedical applications. In optical imaging, the long permanency of nanoparticles in blood circulation enhances their tumor targeting applications. The anchorage of polyethylene glycol onto nanoparticles surface is the most used method to decrease their detection by the reticuloendothelial system. This recognition mechanism is mediated principally by opsonization, the labeling process in which the opsonin proteins present in the blood serum are adsorbed onto the nanoparticles, allowing macrophages of the mononuclear phagocytic system to recognize the nanoparticles, initiating the immune response. In order to decrease the proteins adsorption onto the surface of the $ZnGa_{1.995}Cr_{0.005}O_4$ persistent luminescence nanoparticles, they were PEGylated. For their functionalization, they were initially hydroxylated, then aminosilane groups were added, and finally PEGylated. In a recent precedent work [33], it has been shown that aminosilane layer thickness plays an important role on the *in vivo* biodistribution of the final PEGylated nanoparticles. In the present chapter, the effect of the reaction time during aminosilanization step on the PEG anchorage, and consequently on the interactions between the PEGylated nanoparticles and Human Serum Albumin was quantitatively evaluated. The Hummel-Dreyer capillary electrophoresis method was applied to determine the optimal conditions for PEG anchorage. The obtained results are in good agreement with the previous *in vivo* observations, since the lower the aminosilanization time, the higher the interactions with proteins. Thereby, this methodology can helps in the optimization and control of the production of functionalized nanoparticles to increase their permanence in blood circulation before the *in vivo* analysis.

4.1. BACKGROUND AND JUSTIFICATION

Protein adsorption is a key factor when testing biological responses to nanoparticles (NPs), as it may influence their biodistribution, therapeutic efficacy, uptake and toxicity [234, 309, 310]. When nanoparticles are injected or diluted in biological media, they are covered by a coating known as "protein corona", which confers a new identity to the particles and defines the rational strategy for clinically relevant formulation [311-313]. Binding of plasma proteins is also the primary mechanism for the reticuloendothelial system (RES) to recognize the circulating nanoparticles [314, 315]. The optimization of the surface coatings features is essential to decrease the clearance by the RES, for example functional groups density and content [44, 316, 317].

Modifying surfaces of NPs with polyethylene glycol (PEG), the so called PEGylation, is the most commonly used method to reduce NP interactions with proteins and thereby to increase the residence of NPs in the blood circulation[240, 318]. For tumor targeting and other applications, an adequate control of the PEGylation process is needed to produce functional nanoparticle formulations [319, 320]. PEGylated nanoparticles possess the ability to be passively accumulated in tumors by means of the enhanced permeability and retention effect [33, 321]. The longer the nanoparticles circulate, the higher the higher their probability to passively accumulate at the vicinity

CHAPTER IV

A QUANTITATIVE METHOD TO OPTIMIZE THE PEGYLATION OF PERSISTENT LUMINESCENCE NANOPARTICLES THUS
INCREASING THEIR PERMANENCY IN BLOOD CIRCULATION: NANOPARTICLE INTERACTIONS WITH HUMAN SERUM
ALBUMIN

of the tumor [322, 323]. The PEGylation of nanoparticles has shown not only to enhance blood circulation time, but also to limit the global sequestration within reticulum endothelial organs [324].

In a recent work [37], it has been shown in a reliable way the effect of aminosilanization time in the biodistribution and half life circulation of the recently synthesized $ZnGa_{1.995}Cr_{0.005}O_4$ persistent luminescence nanoparticles, which are a promise for biomedical imaging due to their optical properties [33]. There, the persistent luminescence was used to demonstrate the importance of the reaction time during aminosilanization in the functionalization sequence to obtain suitable PEGylated nanoparticles with increased circulation time in blood of living mice [37].

A better knowledge of the interactions between NPs and proteins is crucial for their safe and efficient applications in the field of nanomedicine, for example as specific nanodrugs, nanovaccines or imaging tools [325]. Therefore, the development of new strategies permitting the accurate determination of these interactions is paramount for the design and synthesis of new nanomaterials for biomedical applications. In that sense, capillary electrophoresis has been demonstrated to be a reliable tool to characterize nanoparticles and their interactions with biomolecules in physiologically relevant media [326] (Sections 1.4 and 1.5).

In the precedent chapter, we used the Hummel-Dreyer capillary electrophoresis (HDCE) method to measure the binding parameters between bovine serum albumin (BSA) and the ZGO-PEG persistent luminescence nanoparticles at different ionic strengths at physiological pH, obtaining the binding constant and number of binding sites. The aim of the present study was to apply this methodology for the evaluation of the interactions between PEG-functionalized ZGO persistent luminescence nanoparticles and human serum albumin. The effect of two aminosilanization times (3 and 5 hours) on protein interaction with the NPs was quantitatively compared in order to quantitatively evaluate the PEGylation conditions, and thereby, to optimize the permanency of the nanoparticles in blood circulation.

4.2. MATERIALS AND METHODS

Gallium oxide and chromium nitrate were provided from Alfa Aesar chemicals, zinc nitrate from Fluka and α-methoxy-ω-N-hydroxysuccinimide polyethylene glycol (5000 Da) from Iris Biotech GmbH. 3-aminopropyltriethoxysilane (APTES), dimethylformamide (DMF) were purchased from Sigma-Aldrich. Human serum albumin (HSA) was bought from LFB Biotechnologies (France), and dissolved in phosphate buffer solutions at pH 7.4 and various ionic strengths. Phosphate buffer was prepared in 150 mM initial ionic strength (IS) by dissolving the proper amounts of sodium phosphate monobasic dehydrate and sodium phosphate dibasic (from Sigma-Aldrich). The pH was adjusted to 7.4 by the addition of 1.0 M NaOH, and then sonicated and filtered through 0.2 μm nylon syringe filters (Corning, NY, USA) before use. Phosphate buffer was used as background electrolyte (BGE) for the size, zeta-potential and separation experiments.

Hydroxylated $ZnGa_{1.995}Cr_{0.005}O_4$ nanoparticles were prepared using a hydrothermal synthesis process as described in the Chapter II [33]. A little variation was implemented during aminosilanization step. Aminosilane-functionalized nanoparticles (ZGO-NH$_2$) were obtained by adding 20 µL of APTES to a suspension of 5.0 mg ZGO-OH dispersed in 2.0 mL DMF. The reaction mixtures were sonicated for the first 2 minutes using a Branson Ultrasonic Cleaner 1210 and kept under vigorous stirring for 3 or 5 hours at room temperature in a glass balloon flask. Particles were washed from the unreacted APTES by three centrifugation and redispersion steps in DMF. The resulting ZGO-NH$_2$(3h) and ZGO-NH$_2$(5h) were reacted overnight in parallel at 90 °C with 10 µmol α-Methoxy-ω-N-hydroxysuccinimide polyethylene glycol (5000 Da) in 1.0 mL DMF each one. The resulting ZGO-PEG NP were washed three times in water and re-dispersed in phosphate buffer at the corresponding ionic strength. Nanoparticle hydrodynamic size was determined by dynamic light scattering measurements in BGE at various IS, with a Nano ZS Zetasizer instrument (Malvern Instruments, France).

Electrophoretic separations were performed with a G7100A Capillary Electrophoresis system from Agilent Technologies equipped with a UV–Vis absorbance detector. 50 µm id x 35 cm fused-silica capillaries (detection length, 28.5 cm) from Agilent Technologies were used after activation by successive flushes (925 mbar) with 1.0 M NaOH (15 min), 0.1 M NaOH (15 min) and H$_2$O (5 min), respectively. Injections were performed hydrodynamically applying 20 mbar at the capillary inlet for 10 s. The applied voltage was 12 kV, with positive polarity at the capillary inlet. The temperature of the capillary cartridge was set at 25 °C. The detection wavelength was 200 nm. Zeta potential was derived from particle electrophoretic mobility estimated from particle migration time measured at peak apex as for laser Doppler electrophoresis measurements using the Ohshima-Pyell equation [165, 193]. The carrier electrolyte buffer was phosphate buffer solution pH 7.4 at variable ionic strength.

The HDCE protocole consists in three steps: capillary preconditioning (capillary filled with protein solutions in BGE at known concentration), external calibration (injection and separation of BGE without protein in the preconditioned capillary), and then sample separation (injection and separation of NPs dispersed in BGE at a fixed concentration (0.2 mg/mL, which corresponds to 3.88 nM considering an average solid radius of 15 nm and a density of 6.055 g/cm3 [298, 299] into the preconditioned capillary containing the protein). The preconditioning step consists in successive injection zones in the following order: 0.1 M NaOH (1 min), H20 (1 min), BGE (1 min), protein solutions (2 min) at varying concentrations (0.10, 0.15, 0.20, 0.25, 0.30, 0.60 and 0.90 µM) and in BGE of varying IS (30, 60, 100 and 150 mM). The separation was repeated four times for every sample. Afterwards, electrosmotic mobility was measured (injection of 0.001% DMF in BGE) and a supplementary rinsing step was applied each four measures, consisting in successive flushes of 0.1 M NaOH, H$_2$O, BGE, 3 min each.

In our precedent work [242] (Chapter III) it was demonstrated that viscosity and conductivity of the suspensions are not altered by the protein concentrations in the range tested here (0-0.90 µM).

For all the experiments realized in this work arithmetic mean values were obtained by four independent measures for each analysis. For the numerical analysis, the peak area was corrected in each case according to the migration time of the peak in order to avoid the effect of random variations in migration times.

4.3. RESULTS AND DISCUSSION

In this part of the work, two important aspects were studied simultaneously: i) the aminosilanization time effect (3 h versus 5 h) on the HSA interaction with ZGO-PEG, and ii) the applicability of the previously described Hummel-Dreyer method for the detection of the differences in the intensity of theses interactions.

4.3.1. Influence of the aminosilanization time effect on the size and ζ-potential of ZnGa$_{1.995}$Cr$_{0.005}$O$_4$ nanoparticles

In the Figure 4.1 is shown the sequence of reactions for nanoparticle PEGylation, in which the only difference is the reaction time during aminosilanization step (3 or 5 hours). The last step was done in parallel under the same conditions and reaction time.
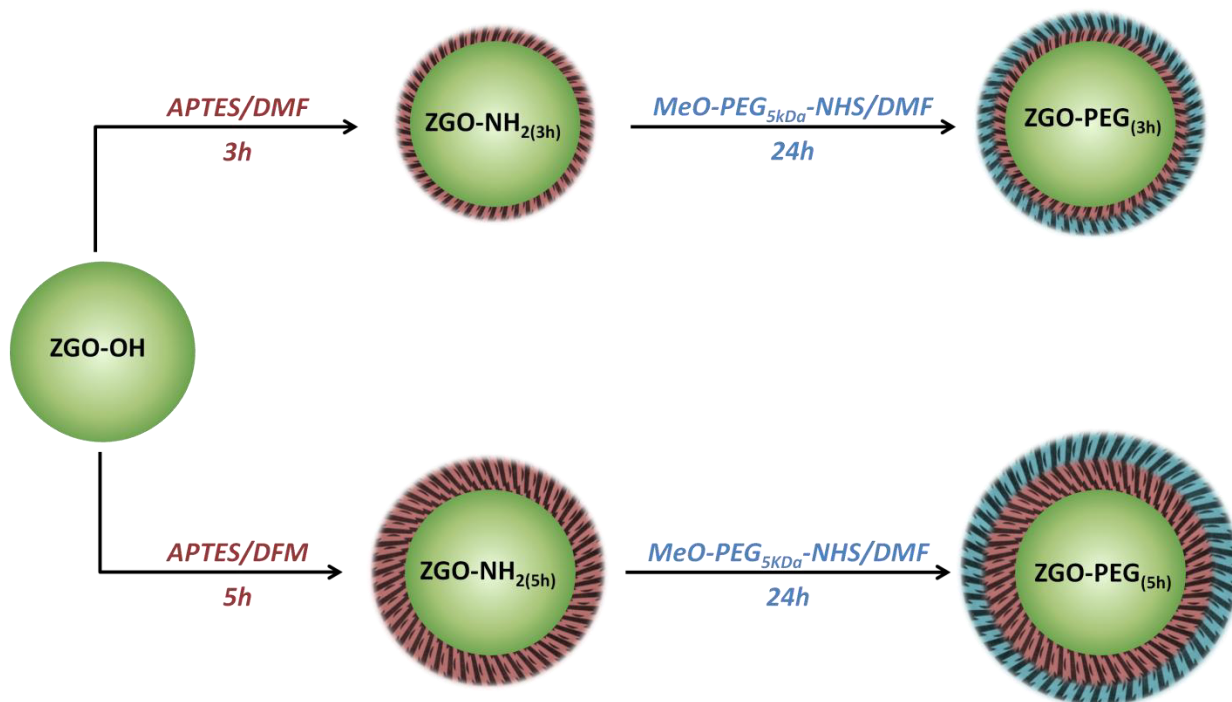
Fig. 4. 1. *Sequential surface functionalization of ZnGa$_{1.995}$Cr$_{0.005}$O$_4$ nanoparticles. The aminosilanization time was varied at 3 or 5 hours under the same reaction conditions. PEGylation reaction was carried out under the time and same reaction conditions in parallel.*

The colloidal characterization of these objects was carried out after every functionalization step in terms of hydrodynamic diameter and zeta potential (Table 4-1).

Table 4- 1. Size and zeta potential of sequentially functionalized ZGO-OH and ZGO-PEG in 30 mM phosphate buffer, and ZGO-NH$_2$ in 10 mM MOPS buffer (at pH 7.4).

Functional group	Size (nm) ± SD	Zeta potential (mV) ± SD
ZGO-OH	88.1 ± 2.4	-34.8 ± 1.8
ZGO-NH$_2$ (3h)	120.0 ± 3.8	29.4 ± 3.3
ZGO-NH$_2$ (5h)	154.2 ± 4.3	32.3 ± 4.4
ZGO-PEG (3h)	162.2 ± 0.8	-1.8 ± 0.7
ZGO-PEG (5h)	175.2 ± 1.6	-1.7 ± 0.9

The aminosilane and polyethylene glycol anchorages were verified by a significant increase in hydrodynamic size, independently of the aminosilanization time. The increase in hydrodynamic size after the aminosilanization step was higher for nanoparticles reacted 5 hours with APTES with respect to their analogous nanoparticles reacted only 3 hours. This observation indicates that the reaction time is a determining factor in the accumulation of aminosilane groups onto the nanoparticle surface.

One of the main issues in aminosilanization is the fact that there are many possible ways for APTES to interact with functional groups in the surfaces: via covalent attachment, hydrogen bonds, electrostatic attractions, two-dimensional self-assembly (horizontal polymerization), and multilayers (vertical polymerization) [327]. Some of the aminosilane groups can also be attached to the surface in oligomeric form in the excessive presence of water, which introduces additional disorder in the aminosilane layer [327]. As regarding the considerable increase in hydrodynamic size of our ZGO-NH$_2$ nanoparticles, we suspect that the formation of multi-layers of APTES (vertical polymerization) is the most prominent mechanism for aminosilane accumulation around the NP surface. The reproducibility of the aminosilane layer thickness and colloidal stability of our nanoparticles is enhanced by adequate water removal by varied wash steps with DMF after the precedent functionalization step (ZGO-OH). The increase in hydrodynamic size was also verified for the PEGylated nanoparticles but in a lesser extent. Even if the PEGylation step was carried out under the same reaction conditions for both ZGO-NH$_{2(3h)}$ and ZGO-NH$_{2(5h)}$, the aminosilanization step also impacts on the hydrodynamic size of the ZGO-PEG.

The zeta-potential variations also indicate the adequate functionalization after every step because the negative initial charge for hydroxylated nanoparticles was shifted to positive values after aminosilanization, and finally to quasi neutral values for PEGylated nanoparticles. No significant differences in zeta potential were found between ZGO-NH$_{2(3h)}$ and ZGO-NH$_{2(5h)}$ nor between ZGO-PEG$_{(3h)}$ and ZGO-PEG$_{(5h)}$. As no significant differences in surface charge were observed, the mechanism in which varied aminosilane layers are formed is supported.

CHAPTER IV

A QUANTITATIVE METHOD TO OPTIMIZE THE PEGYLATION OF PERSISTENT LUMINESCENCE NANOPARTICLES THUS INCREASING THEIR PERMANENCY IN BLOOD CIRCULATION: NANOPARTICLE INTERACTIONS WITH HUMAN SERUM ALBUMIN

A few recent publications have shown different ways by which capillary electrophoresis can be applied to characterize interactions between nanoparticles used as contrast agents in biological systems and proteins [169]. In this part of the work is presented an application of this capillary electrophoresis methodology for the evaluation of interactions between HSA and ZGO-NPs in order to improve the functionalization design and synthesis. The increase in the permanency of PEGylated nanoparticles in blood circulation could enhance the optical imaging applications, i.e. passive tumor detection. In this study the protein model was the HSA, the most abundant protein in human plasma, (55–60% of the total proteins) [328].

4.3.2. Aminosilanization time effect on the electrophoretic profiles for ZGO-PEG/human serum albumin interactions.

The HDCE method, based on peak area measurements, permits the characterization of interactions with rapid dissociation kinetics [301]. For a NP-protein interaction system, the NP can be considered as the substrate (S) with multiple binding sites due to its major size, lower concentration, uniformity of functional groups, and capacity to form multiple and possibly similar binding sites for proteins on the surface. On the other hand, proteins can be considered as monovalent ligands (L) [244]. The capillary is filled with BGE containing the ligand (L) at varying known concentrations [L]. An external calibration is performed by injection and separation of a constant volume of the BGE devoid of ligand or substrate. One "negative peak" appears, due to the local deficiency of ligand in the BGE. To determine the concentration of ligand bound $[L]_b$ to substrate, the same volume of substrate (S) at a fixed concentration $[S]_t$ dispersed in the same BGE is then injected and separated. Two peaks may appear in the electropherogram. The peak with positive absorbance corresponds to the free substrate, while the peak with negative absorbance is caused by the local deficiency of L in the sample. The area of the negative peak after substrate injection is expected to be bigger with respect to that observed during calibration at the same ligand concentration because some ligand molecules are sequestered by the substrate, causing the increase in the local deficiency of the ligand. From the peak area of the latest mentioned vacancy peak and the external calibration, one can access to the concentration of ligand bound to the substrate $[L]_b$ (equation 4.1), and therefore to the binding constant and the number of binding sites by using the Scatchard model (see Chapter III) [242].

$$[L]_b = \frac{A_s - A_c}{A_c}[L]_t \text{ , with } A_c < A_s \qquad \text{Eq. 4.1}$$

The representative electropherograms for the evaluation by the HDCE method of the interactions between PEGylated nanoparticles that were aminosilanated at different times and HSA are shown in Figure 4.2.
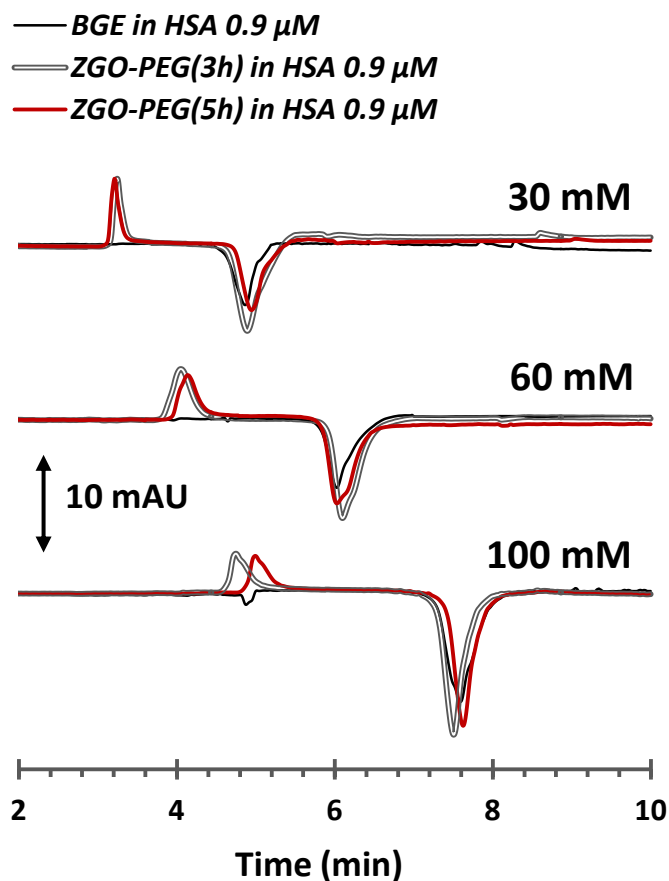
Fig. 4. 2. Representative electropherograms for the evaluation of interactions between ZGO-PEG(3h) or ZGO-PEG(5h) and HSA (0.9 µM) according to the Hummel-Dreyer method at different ionic strength.

So as to characterize the interaction between HSA and ZGO-PEG, various HSA concentrations in the 0.1 to 0.9 µM range were studied. Only the electropherograms for interactions with the higher analyzed HSA concentration (0.9 µM) are presented on this figure. Here is possible to distinguish the differences in magnitude for the negative peaks between the electropherograms for calibration with respect to the corresponding signals obtained when ZGO-PEG$_{3h}$ or ZGO-PEG$_{5h}$ were injected into the capillary preconditioned under the same conditions. By integration of these negative peak areas the respective ligand concentrations obtained. The resulting absolute values indicate that HSA affinity is higher with ZGO-PEG$_{3h}$ than with ZGO-PEG$_{5h}$. As expected, migration time for both nanoparticles and proteins increases upon ionic strength increases. The small differences in their retention time during the distinct analysis (i.e. calibration, interactions with ZGO-PEG$_{3h}$ or with ZGO-PEG$_{5h}$) at the same ionic strength are considered as random in this work. Peak areas were corrected respect to their corresponding migration time before to numeric analysis.

4.3.3. Saturation curves and binding parameters determination

In order to determine the binding parameters for the ZGO-PEG$_{(3h)}$ or ZGO-PEG$_{(5h)}$ and HSA, the free protein concentration was calculated using the external calibration for the different ionic strengths. The saturation curves were plotted and presented in the Figure 4.3.
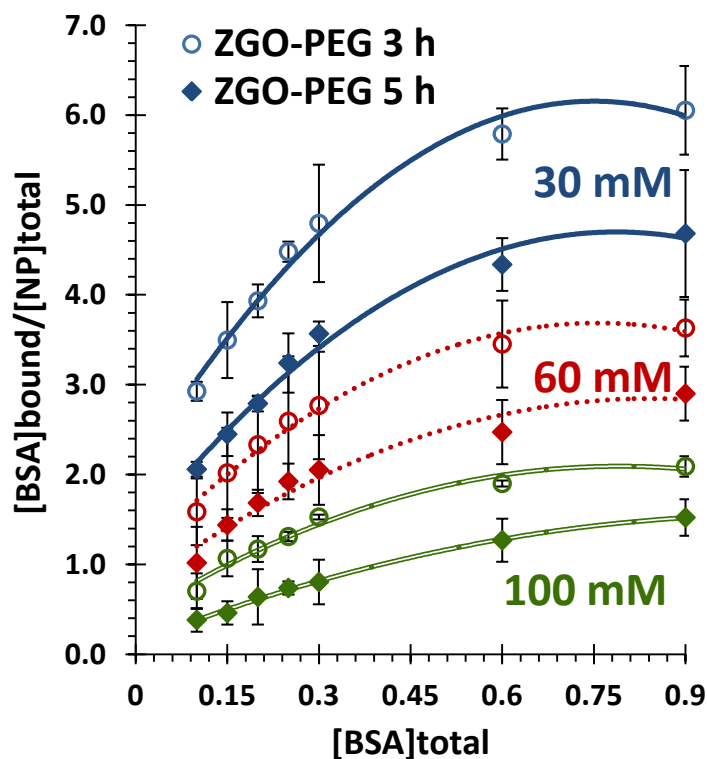
Fig. 4. 3. *Binding curves of the interactions between HSA and ZGO-PEG$_{3h}$ or ZGO-PEG$_{5h}$ in phosphate buffer (pH 7.4) at different ionic strengths as obtained from the Hummel-Dreyer methods. Error bars indicate the ± standard deviation of four replicates. Lines represent the non linear curve fitting of the experimental data.*

As previously noted by visual analysis considering the differences in the areas of the vacancy peaks, the HSA interaction with NPs were stronger for ZGO-PEG$_{3h}$ with respect to ZGO-PEG$_{5h}$ in all the analyzed ionic strength range. By means of an adequate mathematical model, the Scatchard equation [242] (Equation 3.3 of the precedent chapter), the saturation curves were linearized and presented in Figure 4.4.
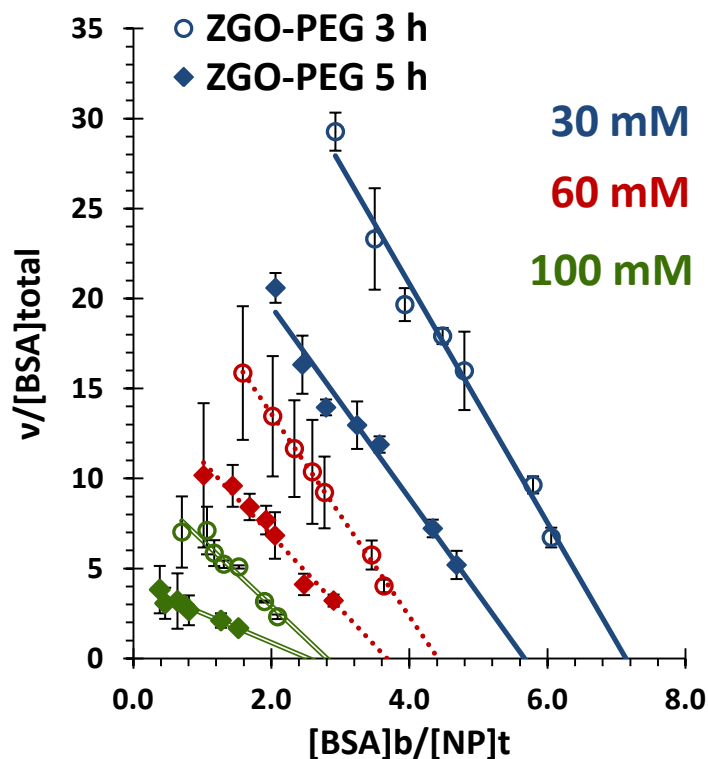
Fig. 4. 4. Scatchard plots for the interaction between HSA and ZGO-PEG$_{3h}$ (circles) or ZGO-PEG$_{5h}$ (diamonds) at 30, 60, and 100 mM (continuous, dotted and double lines, respectively) according to Scatchard equation. Error bars indicate the ± standard deviation of four sets of samples prepared by separate at each concentration.

From the Scatchard plots, the binding constant and number of binding sites could ce determined. Table 4-2 presents these values for the 3 ionic strengths experienced

Table 4- 2. *Summary of model fitting parameters according Hummel-Dreyer study for HSA/ZGO-PEG$_{3-5h}$ complexes.*

Parameter	IONIC STRENGTH					
	30 mM		60 mM		100 mM	
	3 h	5 h	3 h	5 h	3 h	5 h
$Ka_{Scatchard}$ (x10^6/M)	6.64±0.42	5.33±0.44	5.63±0.52	4.10±0.44	3.63±1.09	1.63±0.50
n	7.13±0.05	5.67±0.20	4.41±0.47	3.67±0.72	2.81±0.32	2.55±0.61

CHAPTER IV

A QUANTITATIVE METHOD TO OPTIMIZE THE PEGYLATION OF PERSISTENT LUMINESCENCE NANOPARTICLES THUS INCREASING THEIR PERMANENCY IN BLOOD CIRCULATION: NANOPARTICLE INTERACTIONS WITH HUMAN SERUM ALBUMIN

The decrease of the binding constant and number of binding sites when ionic strength increased is due to the increase in the ion concentrations surrounding the nanoparticle surface and the corresponding screening effect.

At a given ionic strength, the significant difference in binding constant for HSA interacting either with ZGO-PEG$_{3h}$ or ZGO-PEG$_{(5h)}$ indicates a higher affinity of HSA to ZGO-PEG$_{3h}$ than to ZGO-PEG$_{(5h)}$, demonstrating that a silanization step of 5 h leads to a more efficient passivation of the NP surface by PEG. This leads to a significative decrease in number of binding sites for the lower ionic strength (30 mM).

The polyethylene glycol forms a flexible layer on the surface of NPs, preventing the adsorption of proteins via steric hindrance [320, 329]. The reversible formation and dissociation of a ZGO-PEG/HSA complex into the capillary can be understood considering that interactions between both objects are due to coulombic forces between the proteins and nanoparticles surfaces, which are weaker with respect to the covalent bonds[325]. Other studies have recently shown the importance of the PEG density in the formulation of new nanocompounds. It has been suggested that the increase in PEG density reduces the hemolytic activity, suggesting the formation of a steric barrier [330]. Increasing PEG density seems to provide a stronger shield of the nanoparticle surface and reduce immunostimulatory potential, which may contribute to improved safety and reduced clearance by the mononuclear phagocyte system [330].

This CE methodology used in this work is therefore demonstrated as a quick and efficient tool for the optimization and control of the production of functionalized nanoparticles so as to increase their permanence in blood circulation, before the *in vivo* analysis. HDCE presents some important advantages with respect to the other techniques classically employed for the evaluation of interactions between NP and proteins., The Bradford method normally used to quantify the absorption of proteins onto nanoparticles [309, 331] shows some disadvantages with respect to CE because it requires higher protein concentrations and a longer sample treatment, *i.e.* pre-incubation and centrifugation steps, that could furthermore alter the stability of the formed complexes and highlight only strong protein interactions. A precise, quantitative determination of the interactions between nanoparticles and proteins requires *in situ* measurements in order to avoid protein adsorption or desorption processes during the experiment. 2D-PAGE has been also used to determine the interactions between nanoparticles and proteins [66, 317]. This methodology fails to be accurate in the case of plasma proteins which are represented by very few amounts in the blood or when the molecular weight is high [68]. However, this methodology implies a strong interaction between the interweave polyacrylamide structures of the gel used for the separation. Complementary analytical methods such protein Labchip, and western blot have also be employed for studying protein adsorption [68].

4.4. PARTIAL CONCLUSIONS

The present Hummel-Dreyer CE method allowed determining the aminosilanization-reaction time effect on the ZGO-PEG physicochemical properties (size, zeta-potential, binding constant and number of binding sites with HSA,) in a simple and direct way. This efficient methodology will help for the production of PEGylated nanoparticles with improved permanency in blood circulation, which enhances their biological imaging applications. This study permitted to accurately compare the interactions between two very similar NPs, of different PEGYlation protocols, with HSA, which could help to predict which of them will remain longer in blood circulations, giving place to a better distribution in living organisms. This work predicted the *in vivo* performance of the nanoparticles, as it was in good agreement with the previously reported studies on mice biodistribution of these NPs. The present work opens the way to the development of new strategies for NPs passivation against plasma proteins without the necessity of preliminary *in vivo* tests, which represent important infrastructure requirements and implicit ethical implications.

CHAPTER V.

COMPETITIVE INTERACTIONS BETWEEN PEGYLATED PERSISTENT LUMINESCENCE NANOPARTICLES AND APOLIPOPROTEIN-E VERSUS ALBUMIN: ANALYSIS IN A BINARY SYSTEM OF PROTEINS

CHAPTER V

COMPETITIVE INTERACTIONS BETWEEN PEGYLATED PERSISTENT LUMINESCENCE NANOPARTICLES AND
APOLIPOPROTEIN-E VERSUS ALBUMIN: ANALYSIS IN A BINARY SYSTEM OF PROTEINS
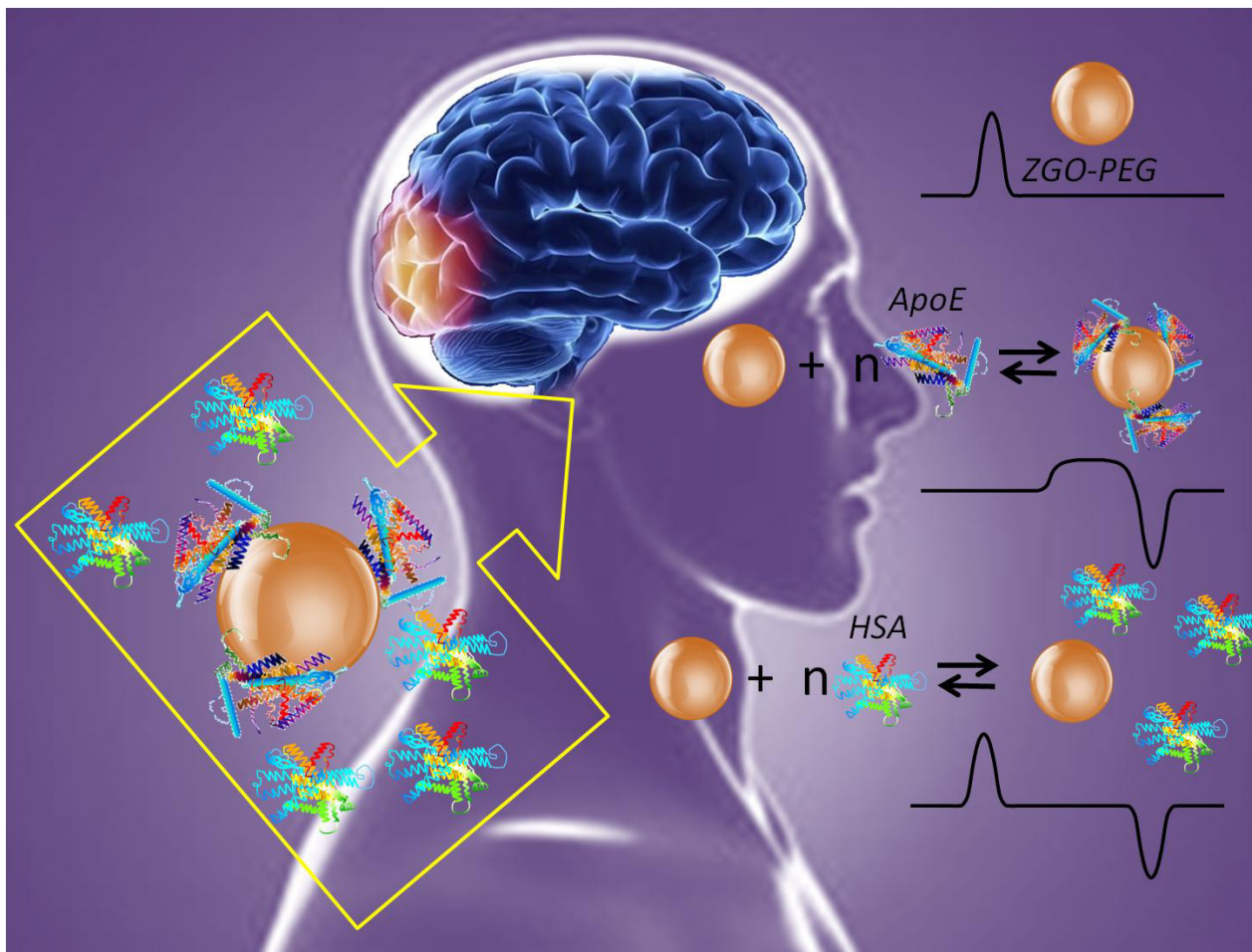
The knowledge of the magnitude of the interactions between nanoparticles (NPs) and plasma proteins could help determining the role played by these proteins in the fate of the nanoprobes. In this work three different strategies were used to compare the interactions between the PEGylated persistent luminescence $ZnGa_{1.995}Cr_{0.005}O_4$ NPs (ZGO-PEG) and human serum albumin (HSA) (the most abundant serum protein) versus apolipoprotein-E (ApoE) (which has been related to the active transport of NPs or molecules through the blood brain barrier) by means of capillary electrophoresis (CE): i) interaction of NPs with single proteins under the same analytical conditions and then comparison of their binding constants, ii) evaluation of the nanoparticle/protein interaction in a binary system of both proteins mixed at different ratios, and iii) incubation of the NPs with one of the proteins and then analysis of their interaction in a separation medium including a second protein, and vice versa. These analytical methodologies show the application of capillary electrophoresis Hummel-Dreyer and affinity capillary electrophoresis for the evaluation of interactions between persistent luminescence nanoparticles and two proteins in a comparative and competitive system, resulting in a higher affinity between the PEGylated nanoparticles and the ApoE with respect to the HSA. These observations may open interesting prospects for brain blood barrier translocation by the persistent luminescence nanoparticles or other contrast agent or delivery nanoparticles, and thereby for their application in optical imaging or therapeutics into the brain zone.

5.1. BACKGROUND AND JUSTIFICATION

In the current context of the nanomedicine, one of the most representative challenges is to successfully target therapeutic NPs to cells or organs of interest *in vivo* [168]. Some difficulties as the detection by the immune system [332], degradation [333], bioaccumulation by organs[37], or the presence of physical or physiological barriers [334, 335] avoid their adequate targeting and function.

The blood-brain barrier (BBB) is one of the most important and impermeable physiological barriers in the organism, and is involved in the regulation of the essential brain homeostasis. As a result of its properties, the BBB enables a protection of the brain from the peripheral circulation and toxic substances but restricts the transport of many therapeutically important drugs and nanodrugs from the blood into the brain [336, 337]. Only lipophilic and small hydrophobic molecules can cross the BBB by diffusion. Even so, an active specific transport mediated by peptides and proteins permits the flux of some large molecules [338].

There are three major strategies for delivering therapeutics into the brain, including i) invasive (principally by direct administration of drugs into the brain through a catheter), ii) pharmacological (modification of drugs to enable penetration through the BBB, for example by reducing the number of polar groups on the compound of interest, or increasing their lipophilicity, both of which can potentially reduce their activity) and iii) physiological methods (which are

CHAPTER V

COMPETITIVE INTERACTIONS BETWEEN PEGYLATED PERSISTENT LUMINESCENCE NANOPARTICLES AND
APOLIPOPROTEIN-E VERSUS ALBUMIN: ANALYSIS IN A BINARY SYSTEM OF PROTEINS

advantageous as they use naturally occurring internalizing receptors to assist in BBB translocation, for example by using peptides, proteins, antibodies or small molecules attached directly to the drug of interest, or by taking advantage of low-density lipoprotein receptor proteins, which are receptors that mediate the internalization and degradation of multiple ligands [337, 339, 340].

As for any biomaterials, once *in vivo* nanoparticles can interact with plasma biomolecules, forming new complex and dynamic entities in which an active exchange of proteins from solution to the NP surface and vice versa occurs [168]. A rapid formation of plasma protein corona affects critically the interaction of the nanoparticles with living systems, and thereby, the nanoparticle action or pathology [313]. In this sense, different kinds of NP have been successfully used for the transport of drugs across the BBB [341], and some early studies by *Kreuter J. et al.* [342-344] have verified a clear correlation between the ApoE adsorption onto the NP surface and the passage through this barrier.

Despite the precise mechanism for NP transport across the BBB is not well described, active endocytotic uptake mechanism has been proposed and shows the involvement of low density lipoprotein receptor on the uptake of the ApoE-covalently functionalized NPs into the brain capillary endothelial cells [345]. The participation of ApoE in the translocation of PEG/ poly(hexadecylcyanoacrylate) (PHDCA) NPs into rat brain endothelial cells has also been demonstrated [69]. In this case the NPs composed of an amphiphilic copolymer consisting of PEG (hydrophilic chains) and PHDCA (hydrophobic part) have shown a long circulating time in blood and an interesting ability to penetrate into healthy rat brain.

The increased use of imaging agents will help to diagnose brain cancer in earlier stages, in order to have the best survival probability, as well as to monitor brain tumors during the duration of a treatment regime [337]. The recently reported $ZnGa_{1.995}Cr_{0.005}O_4$ persistent luminescence nanoparticles (ZGO-NPs) represent a new generation of optical nanoprobes, whose persistent luminescence can be activated before administration on live systems, as well as *in vivo* through living tissues [33]. This *in situ* re-activation in the therapeutic window results in the ability to make observations of the probe without any time constraints, opening new perspectives for a great variety of diagnosis applications. For example, the PEGylated ZGO-NPs ability for *in vivo* passive tumor targeting has been demonstrated [33]. Despite the great number of applications of the ZGO-NPs, the BBB could limit their application for brain cancer research.

In a more general way, the need for studies considering the competitive adsorption of proteins from plasma is emphasized in order to improve the mechanistic investigations about the protein adsorption onto PEG modified nanoparticles [317]. Qualitative and quantitative information of NPs can be assessed by diverse modes in capillary electrophoresis (CE) [173, 182, 246], and some of the applications of this technique are the determination of NPs/biomolecule interactions. Different approaches in CE (principally ACE methods) have been used for the analysis of interactions between various types of NPs and proteins, getting the percentage of conjugate, binding constant, efficiency of conjugation, binding saturation, binding kinetics, stoichiometry and cooperativity [169, 243, 244, 246]. We have also demonstrated the application of the Hummel-

Dreyer method for the evaluation of interactions between the ZGO-PEG NPs and the bovine serum albumin (BSA). The capillary zone electrophoresis (CZE) has shown to be an important tool in the discovering of the involvement of ApoE in the NP translocation through the BBB [66, 68, 69]. CZE has also been used as a complementary method to show that the PEGylation could drastically increase both the blood half-life of the particles and the amyloid-beta peptide adsorption onto the surface without altering neither the ApoE adsorption from the serum nor the complement system activation in serum [67, 183].

In order to successfully deliver persistent luminescence NPs for optical imaging across the plasma membrane or epithelial and endothelial barriers, a permeation enhancing strategy must be employed, and the possibility to join ZGO-PEG with ApoE is evaluated in this work by means of the analysis of their interactions by using CE. This strategy can enhance the ZGO-PEG application for tumor brain detection and in general for optical imaging of the brain region.

5.2. MATERIALS AND METHODS

Ammonium carbonate buffer (ACB) was prepared in an initial ionic strength of 50 mM by dissolving the proper amounts of ammonium carbonate and ammonium bicarbonate (Sigma-Aldrich). The pH was adjusted to 8.0 by the addition of 1.0 M NaOH, and then sonicated and filtered through 0.2 μm nylon syringe filters (Corning, NY, USA) before use. Human Alipoprotein E (ApoE) was carefully diluted in ACB (the same buffer solution in which was supplied by Merk Millipore). Human serum albumin (HSA) was bought from LFB Biotechnologies (France) and also dissolved in ACB at corresponding ionic strength.

$ZnGa_{1.995}Cr_{0.005}O_4$ nanoparticles were prepared and functionalized as described in the Chapter II, and only protein interactions with ZGO-PEG were tested in the present work and not the ZGO-OH or ZGO-NH_2. The colloidal stability and physicochemical parameters of nanoparticles suspensions have been also properly characterized in Chapter II in order to avoid aggregations that can potentially interfere with the analysis [193].

A Model G7100A Capillary Electrophoresis system from Agilent Technologies equipped with a UV–Vis absorbance detector was used for the analysis. Separations were carried out using a fused silica capillary [37 cm (effective length 28.5 cm) X 50 μm I.D., purchased from Polymicro technologies (Phoenix, USA)]. Injection was performed hydrodynamically. The background electrolyte (BGE) was composed of ACB (pH 8.0) at different ionic strengths.

The method used for the different experiments realized in this work consists in four principal steps; i) equilibrium of the capillary, ii) capillary preconditioning with a BGE containing the protein or proteins of interest at different concentrations or ratios, iii) sample injection and iv) analysis of their interactions with the proteins contained into the BGE. Initially, capillary equilibrium step consisted in 2 minutes of 0.1 M NaOH, 2 minutes H_2O and 2 minutes of ACB at corresponding ionic strength. For preconditioning, 3 minutes of BGE (HSA, ApoE or their mixture at varied

concentrations and proportions dispersed in ACB solution at the corresponding ionic strength). For sample interactions, ZGO-PEG (at the fixed concentration of 0.2 mg/mL) were hydrodynamically injected applying 20 mbar at the capillary inlet for 10s for individual proteins and the pre-incubated mixture or 5s for interactions performed in a capillary filled with protein mixtures, and then an electric field was applied for electrophoretic separation (See the precise value in the footnote for every figure). Signal registration was made by UV-detector at $\lambda= 200$ nm. Between each sample (4 repetitions), the electropherogram of 0.001% DMF in BGE was obtained to control the electroosmotic flow. After each sample and DMF (4 replicates and one DMF measures), a supplementary rinsing step was applied, consisting in 3 minutes of 0.1 M NaOH, 3 minutes H_2O, and 3 minutes of ACB at corresponding ionic strength in order to renew the capillary surface and then avoid the non specific protein adsorption to the capillary. Finally, for the data interpretation, two different approaches in CE were applied, both of them with the same operational methodology: Hummel-Dreyer method (HD-CE) in the cases in which no shift in electrophoretic mobility of the involved species (protein, NPs or their complex) was detected upon protein concentration variation. In this case the injection of ACB solutions under the same analytical conditions was used for external calibration, and the peak areas were monitored to obtain the portion of protein bounded to NPs. The second method is the affinity capillary electrophoresis (ACE), in which shifts in the electrophoretic mobilities of the complex formed between the proteins and the NPs where detected when protein concentration was varied.

Each analysis in this work was performed four times to obtain representative values. Binding curves were analyzed using GraphpadPrism Version 5.00 (Graphpad Software, San Diego, CA) curve-fitting software for nonlinear regression.

5.3. RESULTS AND DISCUSION

The study of the biophysical parameters of NPs and their performance in biologically relevant systems could strengthen their applications in the biomedical fields. The CE has demonstrated to be an advantageous tool for the NP characterization in physiologically relevant media, and for the evaluation of the NP interactions with biomolecules.

The ZGO-PEG were initially synthesized as previously reported [33] with an average solid diameter of 30 nm and afterwards characterized in terms of hydrodynamic size and ζ-potential. The hydrodynamic diameter of the PEGylated NPs was 177.6 ± 7.6 nm in 30 mM ammonium carbonate buffer at pH 8.0 with a polydispersity index smaller than 0.1, demonstrating that quite monodisperse NP formulations were used. The zeta potential was slightly negative, with a value of -1.7 ± 0.6 mV. A further characterization of these NPs in physiologically relevant media can be reviewed in our previously reported work [193]. By means of the mentioned study we guarantee the colloidal stability of the ZGO-PEG above all the range of conditions used in the present work, and thus the variations in electrophoretic profiles can be attributed exclusively to the inter-protein or NPs/proteins interactions.

5.3.1. ZGO-PEG interactions with single proteins in the BGE

When the study of the NP-protein interactions is performed, two possible systems can be visualized: i) Stable NPs-protein complexes or ii) Short-lived complexes with fast association/dissociation rates. The choice of the adequate mode for the evaluation of NP-protein interactions in CE can be only verified by pilot experimental results. In the present work, a methodology consisting in the NP injection into a capillary previously preconditioned with protein suspensions at different concentrations was applied for the interaction studies, resulting in two different electrophoretic signals whever HSA or ApoE were analyzed under the same analytical conditions (Figure 5.1): either a variation in the vacancy peak area of HSA in the case of the ZGO-PEG interaction with HSA (Figure 5.1A), or a shift in electrophoretic mobility for complex formed between ZGO-PEG and ApoE (Figure 5.1B). These data resulted in a convenient analytical tool for a qualitative direct comparison of the interaction forces between ZGO-PEG and both HSA or ApoE proteins.
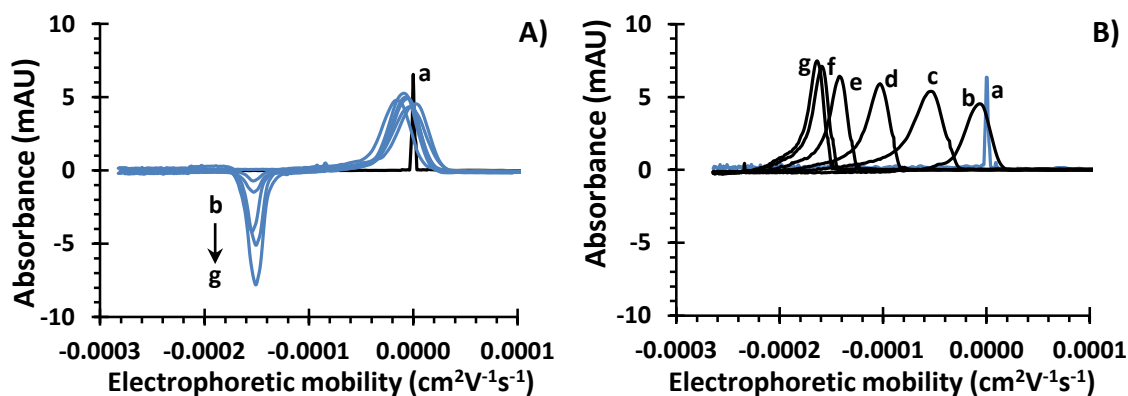
Fig. 5. 1. *Set of representative electropherograms obtained at λ = 200 nm with the Hummel-Dreyer/Affinity Capillary Electrophoresis method for A) HSA/ZGO-PEG and B) ApoE/ZGO-PEG interactions in ammonium carbonate buffer solutions (pH 8.0) at 30 mM ionic strength. E=14 kV. Peak identification: a) DMF, b) 0, c) 0.12, d) 0.24, e) 0.72, f) 0.96, g) 1.44 μM of the corresponding protein.*

The electrophoretic mobility values for HSA (M.W. 66 400 Da) and ApoE (M.W. 34 200 Da) as obtained by means of CZE when the proteins are injected in a capillary containing only BGE are slightly identical ($-1.52 \pm 0.12 \times 10^{-4}$ $cm^2V^{-1}s^{-1}$ and $-1.65 \pm 0.09 \times 10^{-4}$ $cm^2V^{-1}s^{-1}$, respectively). This is in coherence with their isoelectric points (4.7 and 5.5 respectively), leading to negative charges in the BGE of study (pH 8.0).

According to the Beer-Lambert law, the molar extinction coefficients could be determined with the CE apparatus in the experimental conditions (30 mM ACB) at 200 nm as $\varepsilon= 1.48 \times 10^{6}$ $cm^{-1}M^{-1}$ for HSA and $\varepsilon=1.17 \times 10^{5}$ $cm^{-1}M^{-1}$ for ApoE

CHAPTER V

COMPETITIVE INTERACTIONS BETWEEN PEGYLATED PERSISTENT LUMINESCENCE NANOPARTICLES AND
APOLIPOPROTEIN-E VERSUS ALBUMIN: ANALYSIS IN A BINARY SYSTEM OF PROTEINS

When studying the interaction between HSA and ZGO-PEG in 30 mM ACB at 30 mM, the electrophoretic evolution in function of the HSA concentration (from 0 to 1.44 μM) in the BGE corresponds to the Hummel-Dreyer mode: no significant shift in the electrophoretic mobility and shape of the ZGO-PEG peak was observed (Figure 5.1A). The migration time of the protein vacancy peaks remained unchanged whatever the HSA concentrations, and the calculated electrophoretic mobilities correspond to the above mentioned values for HSA as determined by CZE. From the vacancy peak area, interactions could be quantified (see Chapter III).

On the other hand, in the same experimental conditions, the migration time corresponding to the ZGO-PEG injected in the BGE containing the ApoE, increased upon ApoE concentration (Figure 5.1B). In this case, no signal corresponding to ApoE was detected. This indicates a stable complex between ZGO-PEG and ApoE. As ApoE is negatively charged in the experimental conditions, the complexation of ZGO-PEG with ApoE induces an increase (in negative value) of the electrophoretic mobility of the complex upon increasing ApoE concentration. As for HSA, analyses were also performed at IS 15 mM. This evolution corresponds to the classical affinity mode.

The electrophoretic mobility detected by CZE corresponds to these obtained for the formed complex with the ZGO-PEG at the highest ApoE concentration (electropherogram g in Figure 5.1B). The lower values obtained for ApoE (one order of magnitude) respect to the HSA ones can explain the differences in the electropherograms and why an ApoE signal was not detected at these concentrations.

The differences in the electrophoretic profiles for interactions between ZGO-PEG and HSA or ApoE can be explained in terms of their association/dissociation kinetics: the interactions between ZGO-PEG and HSA seem to occur with fast association/dissociation kinetics. This hypothesis is supported by the absence of variations in the shape and electrophoretic mobility of the ZGO-PEG, and the presence of a vacancy peak for HSA. On the other hand, the complex ZGO-PEG/ApoE seem to have a slower kinetics, giving place to a signal of the complex, with an electrophoretic mobility shift due to the increase in the presence of potentially-chargeable groups provided by the ApoE molecules around the surface of the PEGylated NPs.

The absence of shift in the electrophoretic mobility of ZGO-PEG when submitted to interaction with HSA compared to the mobility shift when submitted to interaction with ApoE, is a first indication of a higher stability of the ZGO-PEG/ApoE complex compared to their corresponding ZGO-PEG/HSA.

5.3.2. Determination of binding constants for ZGO-PEG interaction with HSA or ApoE

In order to obtain the ZGO-PEG/protein binding constants for both ApoE and HSA, two different analytical approaches can be applied. For HSA, the fraction "r" describing the ratio of the bound proteins $[L]_b$ to total NPs $[S]_t$, and for ApoE the fraction "v" being the ratio of the bound NPs $[S]_b$ to total NPs $[S]_t$ can be determined by changing the amount of protein present in the BGE during the separation.

When HDCE method is applied the bound protein concentrations $[L]_b$ are obtained, and then is possible to have access to the protein bound per NP fraction ($[L]_b/[S]_b$) by means of the equation 5.1 (previously described in Chapter III) [242, 294]:

$$[L]_b = \frac{A_{NP} - A_c}{A_c}[L]_t \qquad \text{Eq. 5.1}$$

In which A_c is the resulting negative or vacancy peak area of the calibration standard (obtained by BGE injection into the pre-filled capillary with varied protein concentrations $[L]_t$) is compared to the negative peak area arising from the injection of the NP sample (A_{NP}) in order to calculate the bound protein concentration $[L]_b$.

By other side, the ratio ν for NP interaction with ApoE was derived from the variations in migration time of the ZGO-PEG/APoE complex related to the ApoE concentration changes in the BGE (the so called ACE approach). The equation describing this ratio can be defined as [202, 244]:

$$\nu = \frac{[S]_b}{[S]_t} = \frac{\mu_L - \mu_0}{\mu_{max} - \mu_0} \qquad \text{Eq. 5.2}$$

where μ_L is the observed electrophoretic mobility of the complex at determined L protein concentration, μ_0 the electrophoretic mobility of the NPs in free protein-BGE and μ_{max} the maximal electrophoretic mobility reached a saturation conditions.

In both HDCE and ACE methods we assume that the NP saturation by proteins was reached at the analyzed concentrations. These results were adequately fitted to a hyperbolic binding isotherm using nonlinear regression (Figure 5.2A and 5.2C, respectively).

As previously defined in Chapter III for results obtained by means of the HDCE method, the fraction of proteins actually bound per nanoparticle can then be defined as "r" [294] in order to obtain the binding parameters for the complex ZGO-PEG/HSA (Eq. 5.3):

$$r = \frac{[L]_b}{[S]_t} = n\frac{[L].K_a}{[L].K_a + 1} \qquad \text{Eq. 5.3}$$

The "r" value varying from 0 to n. Eq. 5.3 can be linearized as follows (Eq. 5.4):

$$\frac{r}{[L]} = -K_a r + K_a n \qquad \text{Eq. 5.4}$$

When plotting r/[L] versus r, one can access to the Scatchard plot, allowing for K_a determination (slope in absolute value) and n (x-intercept) (See Figure 5.2B).

In order to obtain the binding parameters for the complex ZGO-PEG/ApoE from the results obtained by ACE, we can also assume a system in which the protein (L) bound to a multiple independent binding sites in the nanoparticle surface (S). Here the variable for association "ν"

defined as the fractional saturation of the nanoparticles, as said, the number of bound nanoparticles over the total number of binding sites is [244]:

$$\nu = \frac{S_{bound}}{S_{total}} = \frac{[L]^n}{[L]^n + K_d}$$

Eq. 5.5

where K_d is the microscopic dissociation equilibrium constant (the inverse value of K_a). Rearranging equation 5.6 into a lineal form is obtained the Hill equation:

$$\log\left[\frac{\nu}{(1-\nu)}\right] = n\log[L] - \log K_d$$

Eq. 5.6

The plot of log [P] versus log [v/ (1-v)] is known as Hill plot, and is presented in the Figure 5.2D. Based on the equation, the Hill's plot should have a slope of n. However, the experimentally determined slope actually reflects not the number of binding sites but the degree of interaction between them. The slope of a Hill plot is therefore denoted by n_H, (the Hill coefficient), which is a measure of the degree of cooperativity The "n_H" parameter represents the binding cooperativeness, called Hill´s coefficient. The values of $n_H > 1$ and $n_H < 1$, represents positive and negative cooperativity, respectively, while $n_H = 1$ means to non cooperativity [346].

The Hill's plot corresponding to ZGO-PEG saturation by ApoE is shown in the Figure 5.2D. By means of that curve the binding constants (Ka_{Hill}) and the cooperativity values (n_H) were obtained and summarized in the Table 5-1.
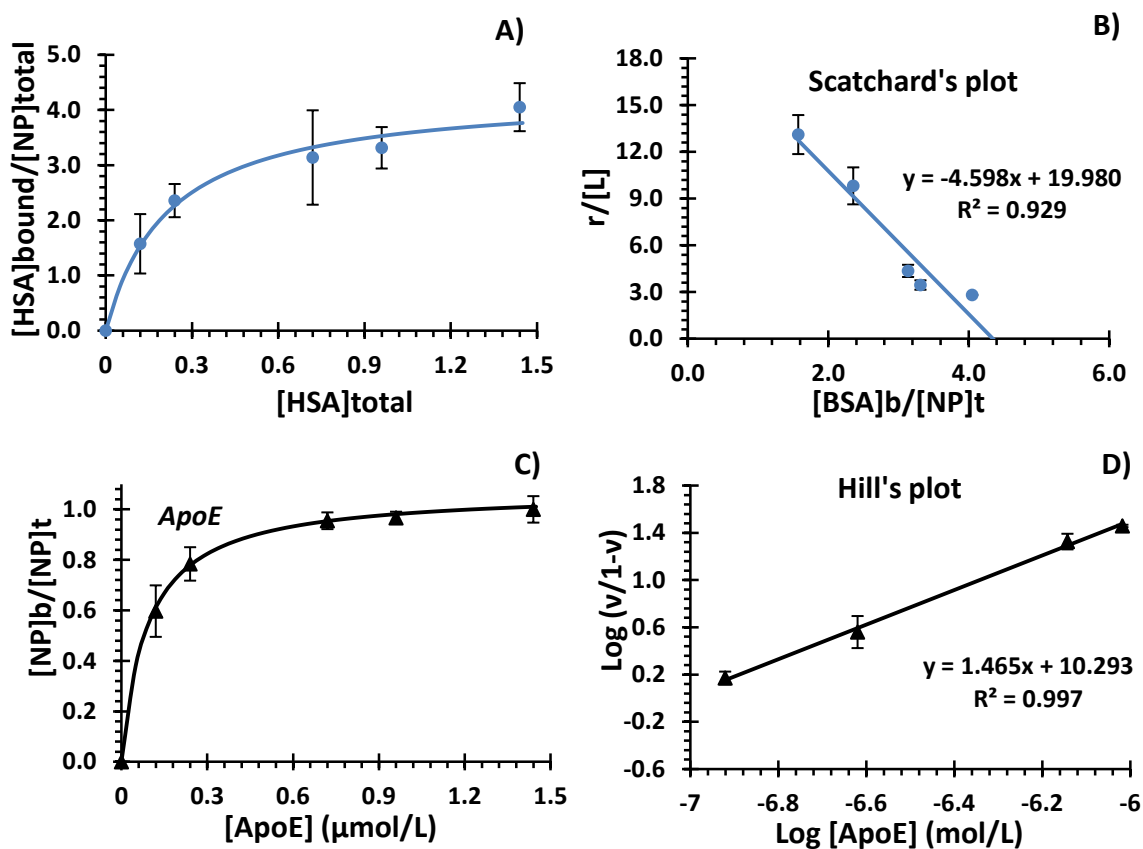
Fig. 5. 2. *A) Model fitting curves for ZGO-PEG interactions with* **HSA** *and* **B)** *corresponding Scatchard's plot for the ZGO-PEG/HSA binding.* **C)** *Model fitting curves for ZGO-PEG interactions with* **ApoE** *and* **D)** *corresponding Hill's plot for the ZGO-PEG/ApoE binding.* **BGE:** *ammonium carbonate buffer (pH 8.0) at 30 mM ionic strength. Error bars indicate the ± standard deviation of four sets of samples prepared by separate at each protein concentration.*

Table 5- 1. *Summary of model fitting parameters according HD-CE analysis for HSA/ZGO-PEG, and ACE for ApoE/ZGO-PEG complexes in ammonium carbonate buffer pH 8.0 at 30 mM ionic strength.*

	$Ka_{Scatchard}$ (M^{-1})	n_H
HSA		
	$4.60 \pm 0.41 \times 10^6$	4.35 ± 0.24
	Ka_{Hill} (M^{-1})	n
ApoE		
	$1.96 \pm 0.25 \times 10^{10}$	1.47 ± 0.07

The stronger ZGO-PEG/ApoE association compared to ZGO-PEG/HSA was verified by these calculi, resulting in a difference in Ka of four orders of magnitude. No cooperative association was detected for interactions with ApoE (n_H= 1.47).

Increased PEG density negatively impacts the detection of NPs by cellular elements, likely inhibiting the endogenous ApoE-mediated targeting mechanism [330]. Although the adsorption of ApoE can be drastically reduced when increasing the length of the PEG chain, the adsorption of this protein has been verified by 2D-PAGE analysis [317]. There is an indication about antibody formation against PEG and thus interaction of the immune system also with PEGylated NPs [347], so PEGylation does not exclude the NPs to completely interact with proteins. It has been shown by 2D-PAGE that the PEGylation of poly-hexadecylylcyanoacrylate (PHDCA) NPs increase the ApoE adsorption (from 0.15 to 0.23 %) of the total amount of proteins adsorbed in serum, while the albumin adsorption decrease from (9.83 to 8.85 %)[347]. Similar results were found for PHDCA NPs, in which ApoE adsorption increased from 2.17 to 3.82 % when they were PEGylated, while albumin adsorption decreases from 18.28 to 17.83 % after PEGylation [69]. In addition, if we consider the relative composition of the serum, albumin is by far more abundant that the ApoE, this observation from results obtained by independent groups suggests a higher affinity of PEGylated NP surfaces for ApoE adsorption compared to HSA.

5.3.3. ZGO-PEG interaction with a mixture of proteins in the BGE

In order to compare the ZGO-PEG/protein interactions in a system containing both HSA and ApoE proteins, we preconditioned the capillary with mixtures of proteins and then ZGO-PEG were injected. In Figure 5.3 we show a full panorama about ZGO-PEG interactions with HSA/ApoE mixtures at different ratios.

In Figure 5.3A the ZGO-PEG interactions with pure ApoE are presented to afterwards facilitate the comparison of the effects of the addition of a second protein in the system. As previously described, the increase in the ApoE concentration in the BGE produces the formation of the stable ZGO-PEG/ApoE complexes, and thereby the increase in migration time (i.e. increase in electrophoretic mobility in absolute value) due to the increase in charged groups around the NPs. No intrinsic signal for ApoE proteins was detected; however an increase in migration time as a concentration effect was verified when ApoE concentrations from 0 to 0.72 μM were present in the BGE. Interaction between ZGO-PEG and pure HSA are also presented in this figure to facilitate data interpretation (Figure 5.3B). As previously described, the increase in HSA concentration does not produce shift in the electrophoretic mobility of the ZGO-PEG, and but a variation in the area of the vacancy peak at the migration time of HSA due to its interaction with ZGO-PEG.

For the experiments of ZGO-PEG interactions with in a binary system of proteins, HSA and ApoE concentration ratios were varied, containing final concentrations from 0 to 0.72 μM for each one after considering dilution (Figures 5.3C and 5.3D). So as to help in the interpretation of the results obtained from Figure 5.3, a schematic representation of the phenomena occurring during the interaction studies with a mixture of HSA and ApoE is proposed in Figure 5.4.
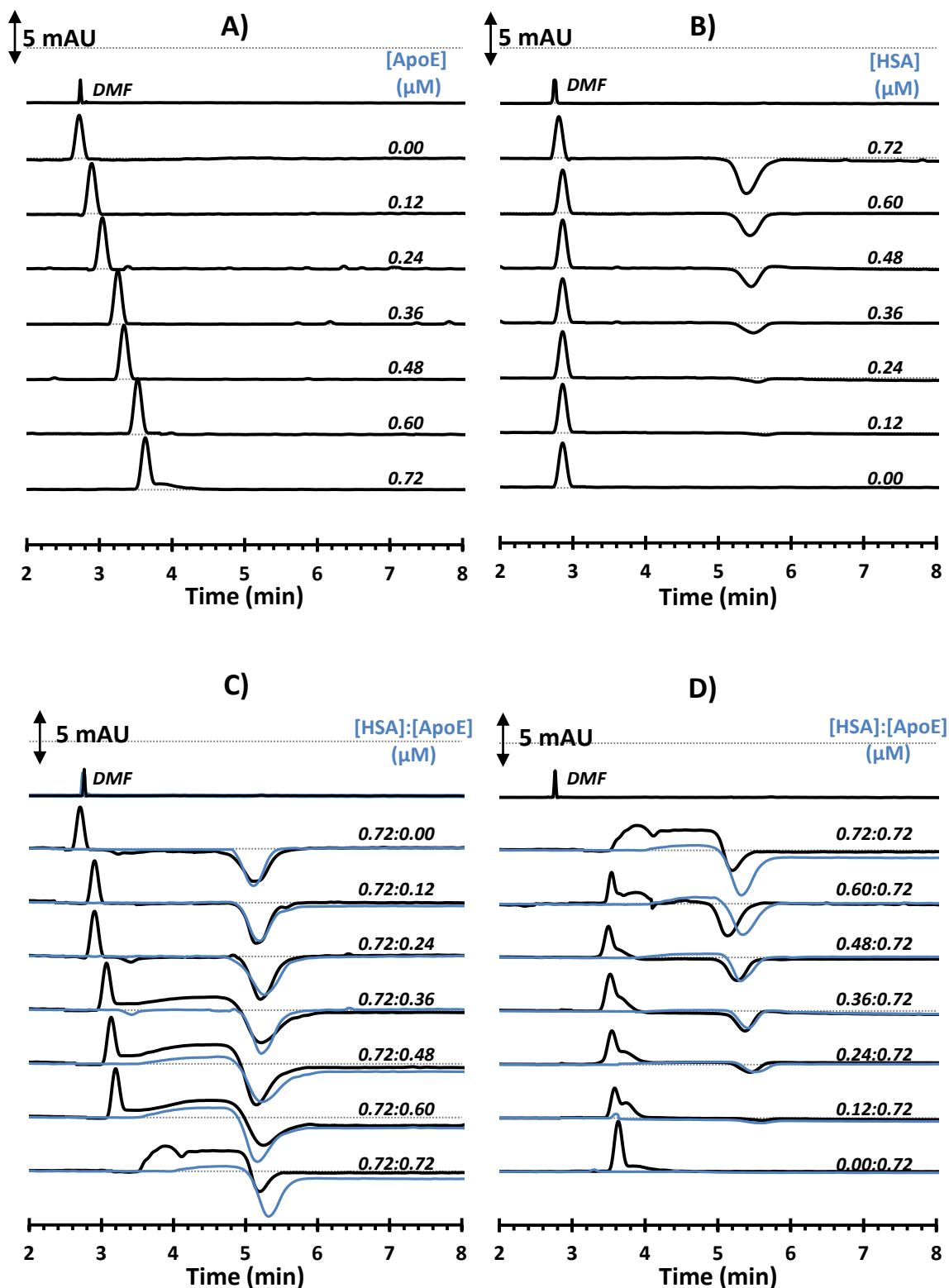
Fig. 5. 3. *Electropherograms for evaluation of interactions of ZGO-PEG and ApoE (A), ZGO-PEG and HSA (B), and ZGO-PEG with a mixture of ApoE and HSA: HSA concentration was fixed and ApoE varied (C), and HSA was varied and ApoE concentration remained constant (D). Signals in black correspond to ZGO-PEG injection for NP/proteins interactions, while superimposed blue lines in C) and D) correspond*

CHAPTER V

COMPETITIVE INTERACTIONS BETWEEN PEGYLATED PERSISTENT LUMINESCENCE NANOPARTICLES AND
APOLIPOPROTEIN-E VERSUS ALBUMIN: ANALYSIS IN A BINARY SYSTEM OF PROTEINS

to BGE injection, giving access to inter-protein interactions evaluation. The indicated values are the total protein concentration in the mixture considering the dilution. BGE: ammonium carbonate buffer solutions (pH 8.0) at 15 mM ionic strength. E=14.0 kV.
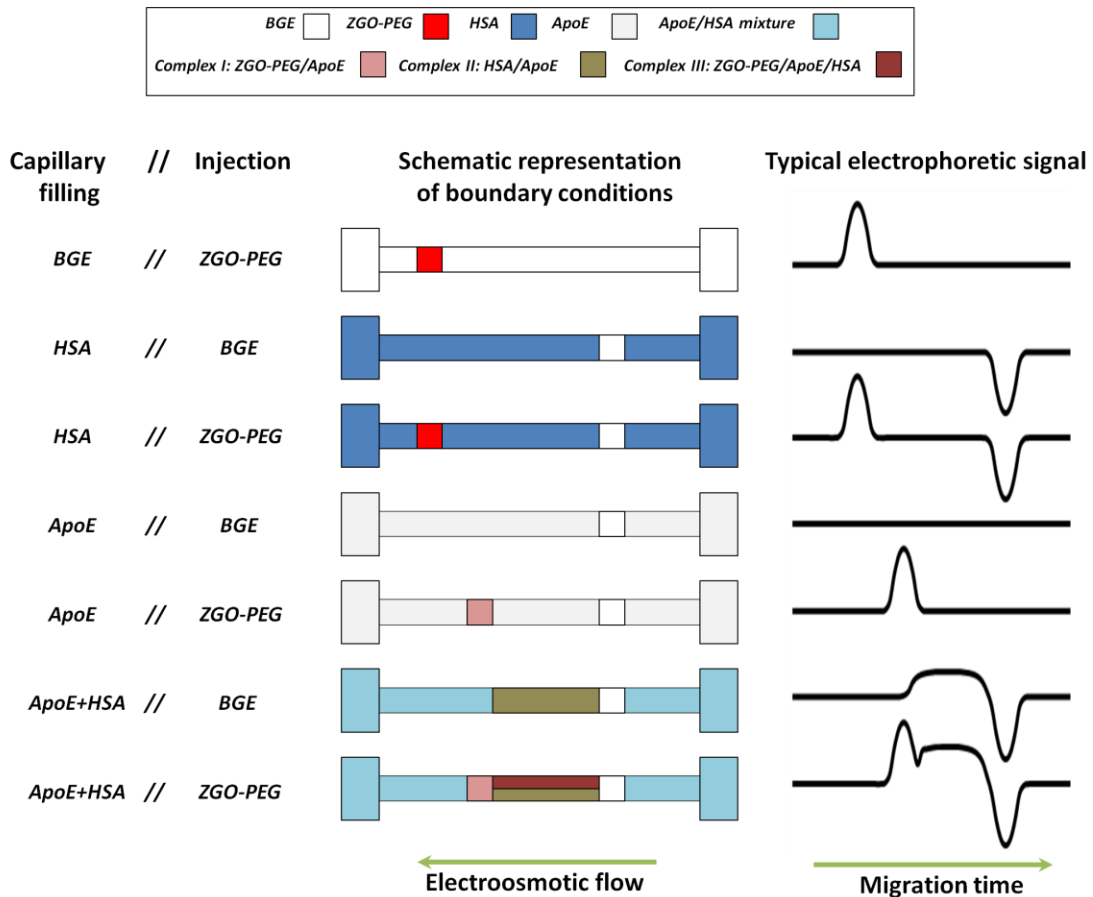
Fig. 5. 4. *Schematic representation for interpretation of interactions between ZGO-PEG and the binary system of proteins HSA:ApoE.*

The superimposed blue lines in Figures 5.3C and 5.3D represent the injection of a zone of BGE instead of ZGO-PEG, in the capillary pre-conditioned as indicated. These experiments allow demonstrating an interaction between HSA and ApoE, evidenced by the formation of a positive broad peak (a plateau) with a mixture of proteins containing concentrations higher than 0.36 μM of anyone of the proteins when the concentration of the other is fixed at 0.72 μM. As previously indicated in the literature, this association can occur since more than thirty-five proteins were found to be associated to HSA including both known high and low abundant proteins (e.g., apolipoproteins, angiotensinogen, ceruloplasmin, clusterin, hemoglobin (Hb), plasminogen, prothrombin, and transferring) [348].

When the HSA concentration in the pre-conditioned capillary was fixed at 0.72 μM and that ApoE concentration was varied (Figure 5.3C), the same shift in the electrophoretic profile of ZGO-PEG/ApoE complex occurred for ApoE concentrations lower than 0.36 μM as for the equivalent electropherograms obtained in the system in which the same NPs were injected in a capillary containing exclusively ApoE (Figure 5.3A). Until these ApoE/HSA ratios no modification was detected to the vacancy peak at the migration time corresponding to HSA. This observation demonstrates that the presence of HSA does not revert the ZGO-PEG affinity for interactions with ApoE at these protein concentrations, and that ZGO-PEG/ApoE interaction is strongly favored compared to ZGO-PEG/HSA.

However, when ApoE concentration was higher than 0.36 μM, a plateau connecting the ZGO-PEG/ApoE peak and the HSA vacancy peak was evidenced, with higher intensity than when only BGE is injected (blue lines). This seems to indicate not only a HSA/ApoE interaction but probably an additional interaction leading to a ternary complex ZGO-PEG/ApoE/HSA. This complex could be favored by the initial HSA/ApoE association or by a more complex mechanism. At these concentrations, the precise determination of the HSA vacancy peak was not evident due to the superposition of the complex signal and the vacancy peaks, and the consequently variation in baseline.

By analyzing the variations in electrophoretic mobility of the complex ZGO-PEG/ApoE observed when ApoE concentration was increased (Figure 5.3C) in the background electrolyte containing a fixed concentration of HSA (0.72 μM), and considering that saturation of the NP surface was reached, the binding constant was calculated as described before. The association parameters of Ka= 2.60 x10^8 M^{-1}, and n$_H$=1.37 were calculated. By comparing these result with the values obtained in a system containing only ApoE (Ka= 1.96 x10^{10} M^{-1}, and n$_H$=1.47), the binding constant for the complex ZGO-PEG/ApoE decrease in presence of HSA. This can be due to the decrease in the ApoE disponibility derived to their association with HSA by means of inter-protein association demonstrated in Figures 5.3C and 5.3D.

In Figure 5.3D in which ApoE concentration in the separation suspension was fixed (at 0.72 μM) and HSA concentration was varied, a peak associated to the ZGO-PEG/ApoE complex was registered at 3.5 min (which is equal to the detected ZGO-PEG/ApoE complex detected for interactions in a capillary containing isolated ApoE at the same concentrations). Its electrophoretic mobility did not vary upon HSA concentration increase. No significant modification in the HSA vacancy peak area was either observed (black and blue lines). These results demonstrate again the stability of the ZGO-PEG/ApoE complex, even in the presence of HSA. However at higher HSA concentrations, a plateau appears, as previously hypothesized being due to the formation of the ZGO-PEG/ApoE/HSA complex.

This set of experiment clearly demonstrates the higher ZGO-PEG affinity for ApoE compared to HSA, and the stability of the ZGO_PEG complex, even when HSA concentration was higher than the ApoE one. It furthermore evidences a HSA/ApoE interaction that seems to lead to the formation of a more complex interaction system involving ZGO-PEG and the two proteins.

5.3.4. Pre-incubation effect on the comparative and competitive interactions between ZGO-PEG and Albumin or Apolipoprotein-E

In order to evaluate the interactions between ZGO-PEG and ApoE or HSA in another competitive system model, the particles were incubated with proteins at the most elevated concentration analyzed in this work (1.44 µM), guarantying the NP saturation, during 15 minutes just before their injection into the capillary for the separation (Figure 5.5). No effects due to the incubation time were detected in the range from 15 minutes to 2 hours at the saturation concentration.
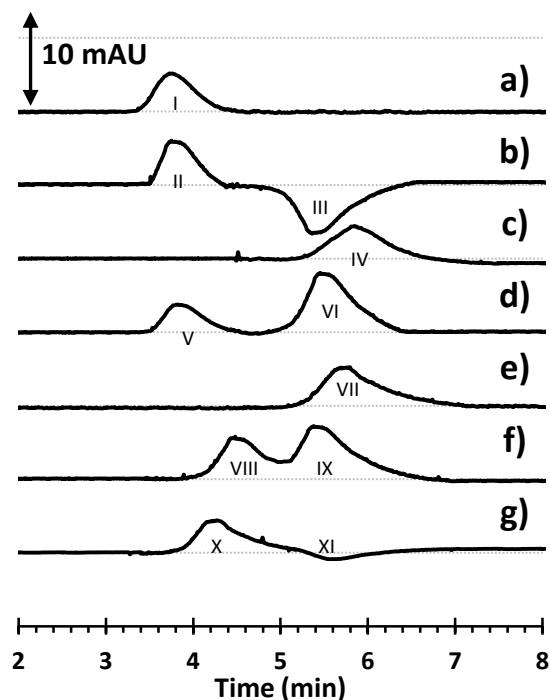
Fig. 5. 5. *Set of representative electropherograms obtained at λ = 200 nm for the various strategies employed to better understand the interaction mechanisms. a) Injection of ZGO-PEG in the capillary pre-conditioned with the BGE, b) injection of ZGO-PEG in the capillary pre-conditioned with the BGE containing HSA, c) injection of ZGO-PEG in the capillary pre-conditioned with the ApoE, d) injection of the pre-incubated ZGO-PEG/HSA in the capillary pre-conditioned with the BGE, e) injection of the pre-incubated ZGO-PEG/ApoE in the capillary pre-conditioned with the BGE, f) Injection of the pre-incubated ZGO-PEG/HSA in the capillary pre-conditioned with the ApoE, g) injection of the pre-incubated ZGO-PEG/ApoE in the capillary pre-conditioned with the HSA. Protein concentration was 1.44 µM for all cases. BGE: ammonium carbonate buffer solutions (pH 8.0) at 30 mM ionic strength. E=12.0 kV.*

The peak I in Figure 5.5a corresponds to ZGO-PEG and it will be used as a reference for the experiments described below. ZGO-PEG were injected in a capillary pre-conditioned with 1.44 µM HSA (5.5b) or 1.44 µM APoE (5.5c). In Figure 5.5b, a positive peak corresponding to ZGO-PEG

CHAPTER V

COMPETITIVE INTERACTIONS BETWEEN PEGYLATED PERSISTENT LUMINESCENCE NANOPARTICLES AND
APOLIPOPROTEIN-E VERSUS ALBUMIN: ANALYSIS IN A BINARY SYSTEM OF PROTEINS

(peak II), and a peak with negative absorbance due to the vacancy of the HSA (peak III) are present (as already described). In Figure 5.5c, the peak IV corresponds to the ZGO-PEG/ApoE complex.

Then, ZGO-PEG were incubated with HSA or ApoE and the incubation mixture was separated in a capillary filled with the BGE (Figures 5.5d and 5.5e, respectively) In Figure 5.5d two signals are observed, the peak V at the same electrophoretic mobility than ZGO-PEG (peak I) and the peak VI, at the electrophoretic mobility of HSA. This indicates that the complex ZGO-PEG/HSA is not stable even after pre-incubation. The variation in peak height for peaks I and V could be due to dissociation within the separation capillary or a possible aggregation during the pre-incubation step.

When ZGO-PEG was pre-incubated with ApoE (Figure 5.5e), the identified peak VII appears at the same electrophoretic mobility as IV in which NPs were injected in the capillary containing only ApoE. This indicates that the saturation was effectively obtained in our experimental conditions, probably due to steric hindrance.

The protein interactions in a competitive system are also presented. For this purpose the ZGO-PEG was first incubated with HSA or ApoE and then injected in a BGE containing APoE or HSA, respectively, at the same concentration as for pre-incubation (1.44 μM) (Figures 5.5f and 5.5 g, respectively). In Figure 5.5f two peaks were detected. The peak IX corresponds to HSA, and the peak VIII appears at an intermediary mobility between ZGO-PEG and ZGOPEG/ApoE. Both peaks are badly resolved. This could indicate a competition between HSA and ApoE when ZGO_PEG is previously incubated with HSA and/or the formation of a ternary peak upon injection of the incubated ZGO-PEG mixture in a capillary filled with ApoE. Anyway, it clearly appears from the peak height of HSA, that the ZGO-PEG/HSA complex is not stable in the experimental conditions.

Finally, in the Figure 5.5g, one can observe a very broad peak X (or a peak followed by a plateau), and a very slight negative peak XI. The peak X should correspond to the ZGO-PEG/ApoE complex; the plateau could be due to the ternary complex hypothesized previously ; and the peak XI to the vacancy of HSA. However, the negative peak area was very small in comparison to peak III. This could be due to the interaction of HSA in the ternary complex. .

To conclude on all these experiments it was clearly demonstrated that: (1) the ZGO-PEG/HSA complex is ruled by a fast association and dissociation kinetics, (2) the ZGO-PEG/ApoE is a stable complex, even in the presence of the competing HSA, and (3) an interaction between HSA and ApoE occurs. An hypothesis for a ternary complex ZGO-PEG/ApoE/HSA is furthermore established according to these results.

Since the mechanism for interactions between NPs and proteins remains unclear, theoretical docking studies can be used to obtain information about these interactions with PEGylated NPs [183]. This *in silico* methodologies can give information about the interactions between PEGylated nanoparticles and HSA and ApoE. The methodology used in the present work can also be potentially adapted to study other interacting molecules, such as nanoparticle with other specific

proteins. This work also opens the perspectives for the quantitative evaluation of NPs interaction in a binary system of proteins by means of the calculation of binding parameters.

5.4. PARTIAL CONCLUSIONS

Because the BBB represents such an insurmountable obstacle for NPs an effective protein mediated active transport can be addressed in order to send the persistent luminescence nanoparticles into the brain zone and then to obtain quality images by optical imaging. The presented CE methodologies can be used to compare the affinity of NPs for different plasma proteins and the applicability to obtain information about interactions in a mixture of two proteins. These experiments demonstrate the higher ZGO-PEG affinity for ApoE compared to HSA in the three analyzed interaction models, considering first the interaction with pure proteins in the capillary and comparing by means of the calculated binding constant (Ka), then a competitive protein mixture in the capillary, even when HSA concentration was higher than the ApoE one, and finally in pre-incubated system. A fast association/dissociation for the complex ZGO-PEG/HSA, and a slow dissociation for the complex ZGO-PEG/ApoE were also demonstrated. The formation of a possible ternary complex still remains to study. Pre-formation of an ApoE protein corona around the ZGO-PEG, by means of a simple pre-incubation step can therefore be exploited as a strategy for their translocation across the BBB. This strategy could be extrapolated for another kind of PEGylated NPs. Once *in vivo* the new entity formed by pre-incubated nanoparticles with ApoE could be able to cross through the BBB, representing a new strategy to delivery NPs used for multiple purposes into the brain region.

CHAPTER VI.

PHOTO-ACTIVATION ENHANCE THE TOXICITY OF PERSISTENT LUMINESCENCE NANOPARTICLES IN BREAST CANCER CELLS
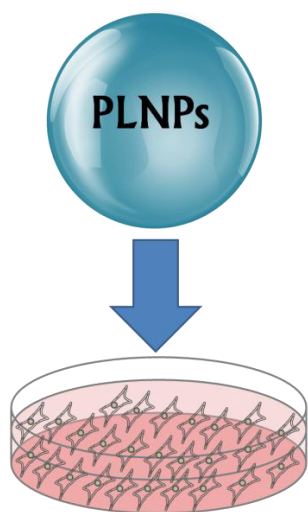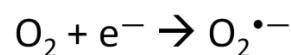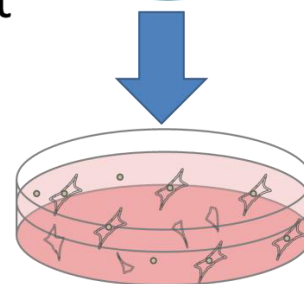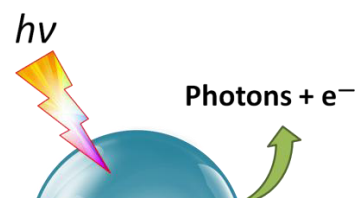
The persistent luminescence nanoparticles are innovative materials with potential applications in biological imaging. They emit photons during long periods of time after the end of the excitation by light at adequate wavelength. On these phenomena, the most part of the energy is emitted as photons, however, some of the electrons in the conduction band can reduce the molecular oxygen to produce superoxide anion ($O_2^{\bullet-}$). In this chapter, we evaluated the light effect on the reactive oxygen species production by irradiated or non-irradiated $ZnGa_{1.995}Cr_{0.005}O_4$ persistent luminescence nanoparticles. Their influence in oxidative stress induction and their cytotoxic effect on MCF-7 and MDA-MB-231 human breast cancer cells were also analyzed. The results indicated that reactive oxygen species production was stimulated by exposition of the hydroxylated persistent luminescence nanoparticle to UV and visible light, and the corresponded oxidative stress induced in cells after internalization can be directly related with their dose-dependent inhibition of cell viability. In other hand, PEGylated nanoparticles were not uptake by cells, and cell viability was not altered by these nanoparticles. This study reveals the importance of consideration of light irradiation for the study of luminescent nanoparticles toxicity, and a novel possible application in photodynamic therapy.

6.1. BACKGROUND AND JUSTIFICATION

Nanoparticles have a great potential for cancer therapy and diagnosis because they allow the *in vivo* detection and monitoring of this pathology [349, 350]. However, optical imaging is limited in sensitivity due to autofluorescence and light scattering in depth biological tissues, and by these reason more sensitive tools are necessary [351].

The persistent luminescence is the optical phenomena in which light emission remains for extended periods of time (some hours) after the irradiation source is switched off [16, 23]. These materials overcome the disadvantages of conventional optical markers such as quantum-dots and organic dyes mainly due to a non negligible autofluorescence signals, providing many conveniences for optical imaging [13, 352].

In our group, a series of persistent luminescence nanoparticles (PLNPs) have been developed and applied in the biomedical field as contrast agents for near infra-red *in vivo* imaging [7, 254-256, 258, 259]. The innovative chromium-doped zinc gallate $ZnGa_{1.995}Cr_{0.005}O_4$ nanoparticles (ZGO-NPs) have denoted attractive optical properties due to its long persistent luminescence activated by UV or visible light, besides its capacity to be re-activated *in vivo* through living tissues using highly penetrating low-energy orange/red photons [33]. Due to its photonic emission at the region of the tissue transparency window, this material has demonstrated its application for optical imaging of vascularization, tumors and grafted cells [33].

The complexity and great diversity of new engineering nanomaterials and their properties imply that the complete mechanisms of nanoparticle toxicity are far to be understood [353]. At this

day, the secondary effects of the most part of nanoparticles, including the PLNPs in living organisms are not well known, and exhaustive toxicological studies are paramount [354].

Only as an example, one of the most important causes of nanoparticle toxicity is frequently attributed to reactive oxygen species (ROS) production inducement, and the resulting oxidative stress [94]. In the literature, the described mechanisms for ROS production by nanoparticles are the followings [94, 98]: 1) direct generation as a result of nanoparticles exposition to an acidic environment (such in the lysosomes)[99, 100], 2) alteration of subcellular functions by interaction with organelles such as mitochondria [101], 3) interaction of nanoparticles with the redox active proteins such as NADPH oxidase, and 4) interaction with cell surface receptors and activation of intracellular signaling pathways [98]. In all these cases, the ROS production depends of direct interactions between cells and nanoparticles.

In recent studies it has been demonstrated that the irradiation of some nanoparticles by light enhances the ROS production, and this property has been applied principally in photocatalytic antimicrobial treatments for water disinfection [355-357]. On these cases, the nanoparticle surface acts as photonsensitizer, a molecule that produce a chemical change in another molecule after light stimulation [358, 359]. Upon irradiation, an activated photosensitizer transfers its excited-state energy to surrounding oxygen, resulting in ROS production, such as singlet oxygen ($^1O_2$), hydroxyl radical ($OH^{\bullet}$) or superoxide radical ($O_2^{\bullet-}$), which can to become cytotoxic in a well localized area [360-362].

The integrative diagnosis−therapy systems based on nanoparticles applications represent an emerging approach to cancer treatment [363]. By this reason, and remarking the importance of consideration in toxicity studies of the emerging properties of nanoparticles such persistent luminescence, we evaluated the cytotoxic effect of ZGO-NPs using the MCF-7 and MDA-MB-231 cell lines derived from human breast cancer. This work was focused in the differences in ROS production by photo-stimulated or non light irradiated nanoparticles *in vitro*, and in contact with cells in order to reveal the possible mechanisms of breast cancer cell death induced by exposure to ZGO-NPs.

6.2. MATERIALS AND METHODS

$ZnGa_{1.995}Cr_{0.005}O_4$ nanoparticles were synthesized and functionalized according to the previously reported method [33], as described in the Materials section of the Chapter II.

Particle size and zeta potential was characterized to measure and control nanoparticle dimensions in the biological test medium before administration by Dynamic light Scattering (DLS) and Laser Doppler Electrophoresis (LDE) measurements with a Nano ZS Zetasizer instrument (Malvern Instruments, Southborough, MA. Adequate colloidal stability control was also performed by means of the techniques described in the Chapter II.

Cells were routinely maintained in DMEM culture media without phenol red, supplemented at 10 % with fetal bovine serum and 1 % of penicillin/streptomycin. Cells were grown and maintained in cell culture 24 well plates at 37 ◦C in a 5% CO_2 humidified incubator. To make easier administration, a suspension of ZGO- NPs was prepared using the culture media and dispersed for 1 minute by using a sonication cube to prevent aggregation. The effects of 0, 0.01, 0.05, 0.25 and 0.50 mg/mL ZGO-NPs concentrations in breast cancer cell toxicity were tested on this study.

Nanoparticles were reserved in darkness 1 week before use, and manipulation was performed in safelight conditions to avoid excitation by natural visible light. A parallel set of cells was treated with pre-irradiated nanoparticles, which were exposed to an UV-lamp (UVP, inc. Model UVGL-25) at 254 nm wavelength during 5 minutes just before administration in culture cell media.

Cell viability was measured by the Trypan Blue viability test [364] by using a TC20 Automated Cell Counter from BioRad.

The peroxydation levels in organs were measured with a Peroxi-Detect kit (PD1 KT, Sigma), which is based on the oxidation of Fe^{2+} into Fe^{3+} ions by peroxides under acidic conditions. The resulting Fe^{3+} ions form a colored adduct with xylenol-orange, which is measured at 560nm. This assay was carried out in accordance with the manufacturer's protocol.

NO levels were measured by Griess method as described by the manufacturers of the colorimetric assay kit (NB98, Oxford Biomedical Research). This method is based on an enzymatic reduction of nitrate into nitrite, which reacts with sulfanilamide and naphthylethylenediamine to generate a colored azo compound, which is measured at 540 nm.

The uptake of ZGO nanoparticles by cells was analyzed by confocal microscopy imaging. MDA-MB-231 cells were grown in DMEM media on a glass cover slide with dimensions of 1 x 1 cm for 24 h. Then the ZGO-OH or ZGO-PEG nanoparticles (0.05 mg/mL) were added and the cells were incubated for 24 h. The cells were washed and fixed with p-formaldehyde and then observed with confocal microscope (Zeiss LSM 510 Meta/ AxioVert 200 Confocal Microscope) using an excitation wavelength of 561 nm, and emission of 564-700 nm. None extra fluorescent marker was added to the test.

The determination of $O_2^{\bullet-}$ produced by nanoparticles was carried out by suspending ZGO-OH or ZGO-PEG in 100 μM XTT (2,3-bis(2-methoxy-4-nitro-5-sulfophehyl)-2H-tetrazolium-5-carboxanilide) as indicator[356, 357] (purchased from Sigma-Aldrich). Nanoparticles concentration was 5.0 mg/L. After UV or visible light irradiation (λ=254 nm) or visible light (20W fluorescent lamp, from Philips) for different periods of time, a sample of the orange-colored XTT-formazan (the product resulting from the reduction of XTT by $O_2^{\bullet-}$) was measured into a quartz vial with a Varian, Cary 50 UV-Vis spectrophotometer at 470 nm. The experiments were also carried out in the dark to determine the background $O_2^{\bullet-}$ production without photo-stimulation. A control consisted in the XTT solution without nanoparticles irradiated under the same conditions in parallel.

All the experiments were repeated three separate times. Statistical analysis of the mean differences between multiple groups was determined by one-way analysis of variance followed by Tukey–Kramer multiple comparison tests. The version 8 JMP software from SAS was used. The alpha level for all tests was 0.05.

6.3. RESULTS AND DISCUSION

In order to guarantee the quality of our synthesized nanoparticles, we used a conventional light scattering technique (Zetasizer) to measure the zeta potentials and hydrodynamic size of the ZGO-NPs. These properties are summarized in Table 6-1.

Table 6- 1. ZnGa$_{1.995}$Cr$_{0.005}$O$_4$ characterization in pH 7.4 phosphate buffer solution.

	ZGO-OH	ZGO-PEG
Hydrodinamic Size (nm)	82 (pdi = 0.102)	174 (pdi = 0.098)
Surface charge	Negative	Neutral
Zeta potential (mV)	-40.2 ± 4.8	-1.8 ± 0.4

The same nanoparticle core, but with different molecules into their surface (hydroxyl and polyethylene glycol groups) were tested. The initial ZGO-OH with negative zeta potential and colloidal stability by electrostatic repulsions were transformed into ZGO-PEG by proper functionalization reactions, obtaining the neutral charged nanoparticles stabilized by steric hindrance. A further characterization study in terms of colloidal stability and physicochemical properties of the ZGO-NPs was recently reported by us [193].

6.3.1. Light exposure effect on ROS production by ZGO nanoparticles

This work was focused on the photo-induced toxicological effects of the PLNPs. As indicated before, the nanoparticles can enhance the ROS production by cellular components. However, the possibility of ZGO-NPs reaction with aqueous media after light stimulation can also contribute to the increase in ROS concentrations. To verify this hypothesis, the ROS production by ZGO-NPs in absence of cells was analyzed by using the tetrazolium dye XTT, which is reduced to their soluble formazan by superoxide radicals under standard conditions (See Figure 6.1), and the induced change in the color determined by means of a simple UV-Vis spectrometry measure.
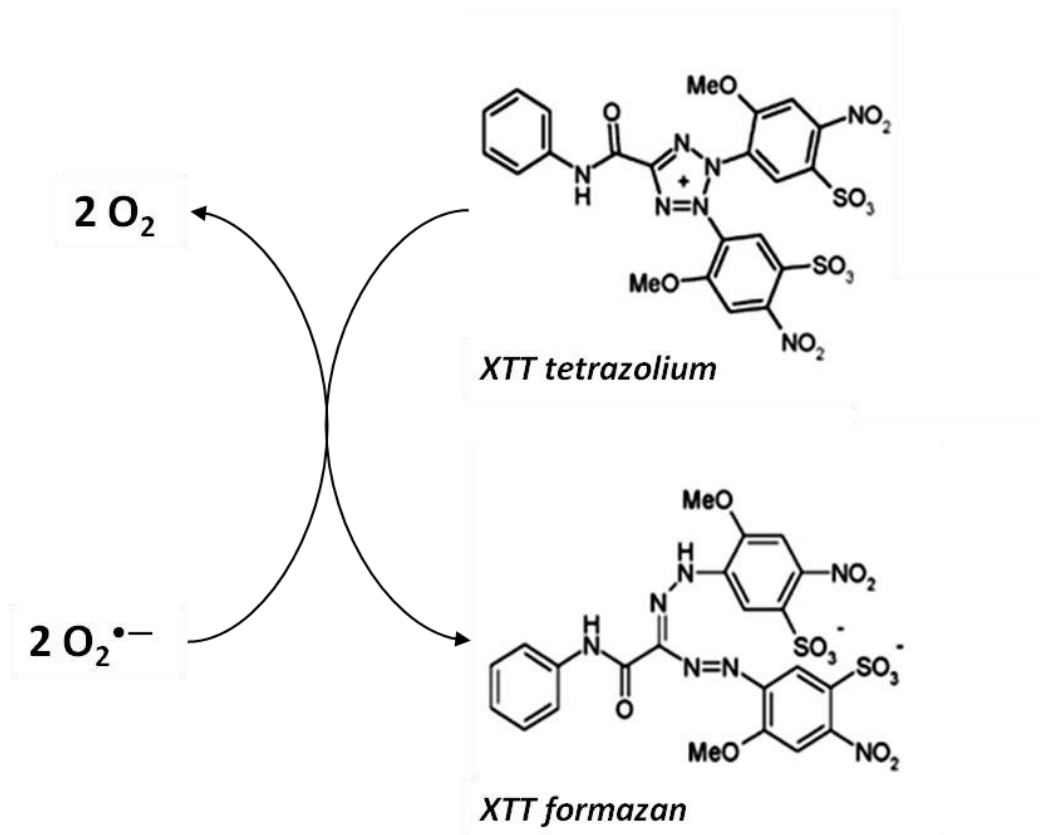
Fig. 6. 1. Reaction for the reduction of XTT tetrazolium to XTT formazan by superoxide radicals.

In the Figure 6.2 are presented the UV-Visible spectra for evaluation of the $O_2^{\bullet-}$ generation by ZGO-NPs across the time, and then the comparison of the light type effects.

In the Figure 6.2A the changes in the absorption spectrum of the nanoparticle suspension in XTT along the first two hours of UV irradiation are shown.

The visible-light irradiation effect was also tested and shown in Figure 6.2B. In both cases, a clear peak with maximum absorbance at $\lambda=470$ nm was present, and its intensity was increased with the time within the first two hours. The increased absorption at this wavelength indicates an augmentation in the $O_2^{\bullet-}$ production. In the Figure 6.2C is compared the light type effect in superoxide production by visible and UV light respect to its darkness counterpart. Only non significant differences were found in the spectrum with photo-stimulated ZGO-OH, while a clear difference was present respect to ZGO-OH nanoparticles kept in darkness. ROS generation is dictated by an interfacial electron transfer process. When electrons are promoted from the valence band to the conduction band, a concomitant hole is also generated in the valence band. The holes and excited electrons are then capable to react with an electron donor or acceptor, respectively [356]. On this work, the photo-excited electrons react with the dissolved molecular oxygen to produce $O_2^{\bullet-}$. No variation in absorption peaks were detected for all ZGO-PEG nanoparticle

suspensions by action of light within the two first hours of irradiation respect to in dark conditions (Figure 6.2D). The decrease in ROS generation by PEGylation respect to their hydroxylated counterpart is likely due to their lower direct interaction between nanoparticle surface and solution due to the presence of long polyethylene glycol chains (5000 Da).
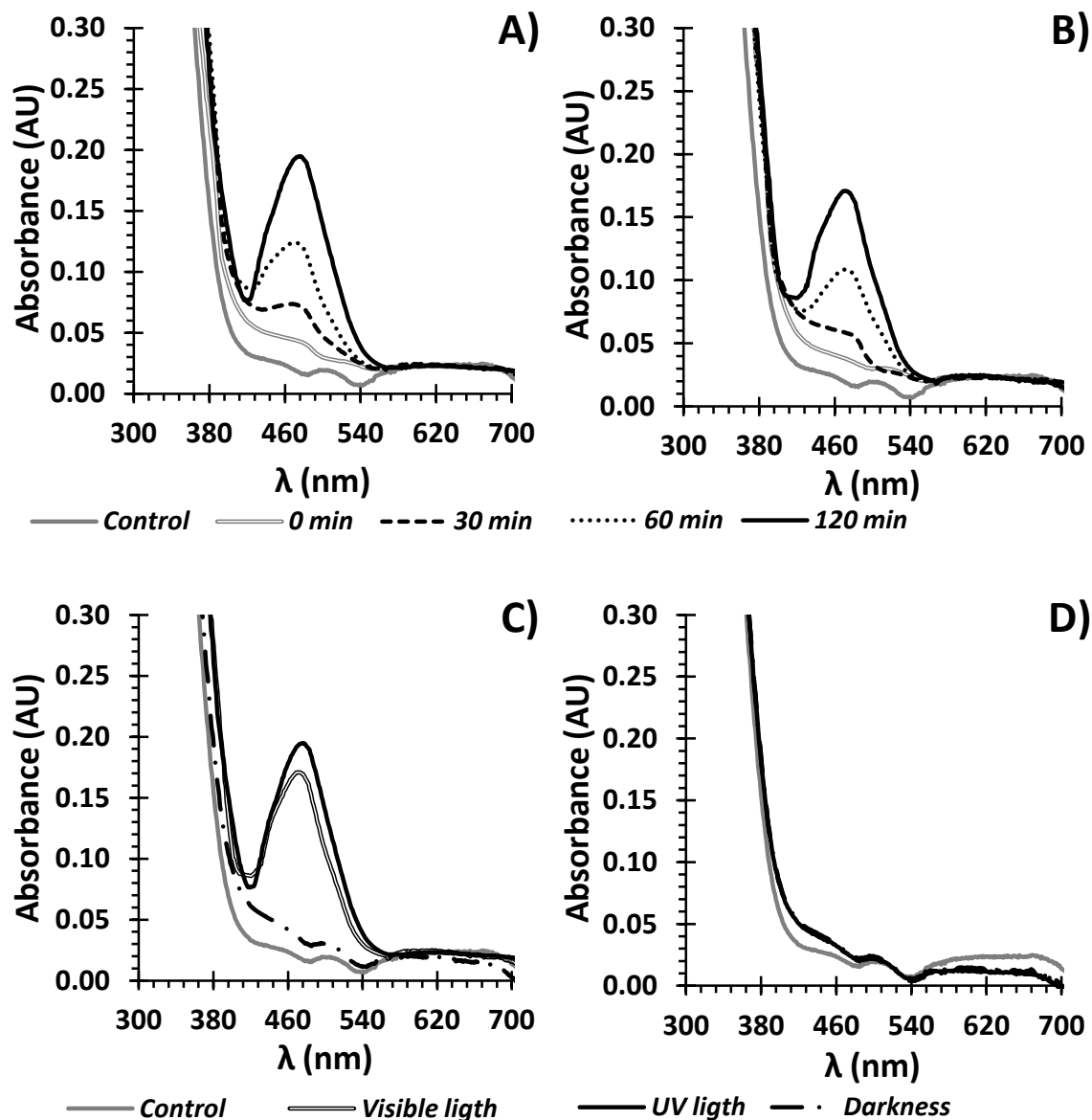
Fig. 6. 2. UV-Visible spectra for evaluation of the $O_2^{\cdot-}$ generation in time by A) ZGO-OH under UV ligth irradiation, B) ZGO-OH under visible light irradiation. Light type effect on UV-Visible spectra for evaluation of $O_2^{\cdot-}$ generation by C) ZGO-OH and D) ZGO-PEG two hours after UV light irradiation as indicated by the reduction of 100 μM XTT.

The absorbance at 470 nm was continuously recorded and transformed into molar concentration using an extinction coefficient of 2.16×10^4 $M^{-1}cm^{-1}$ [365]. In Figure 6.3 are shown the kinetics of superoxide production by ZGO-OH and ZGO-PEG.
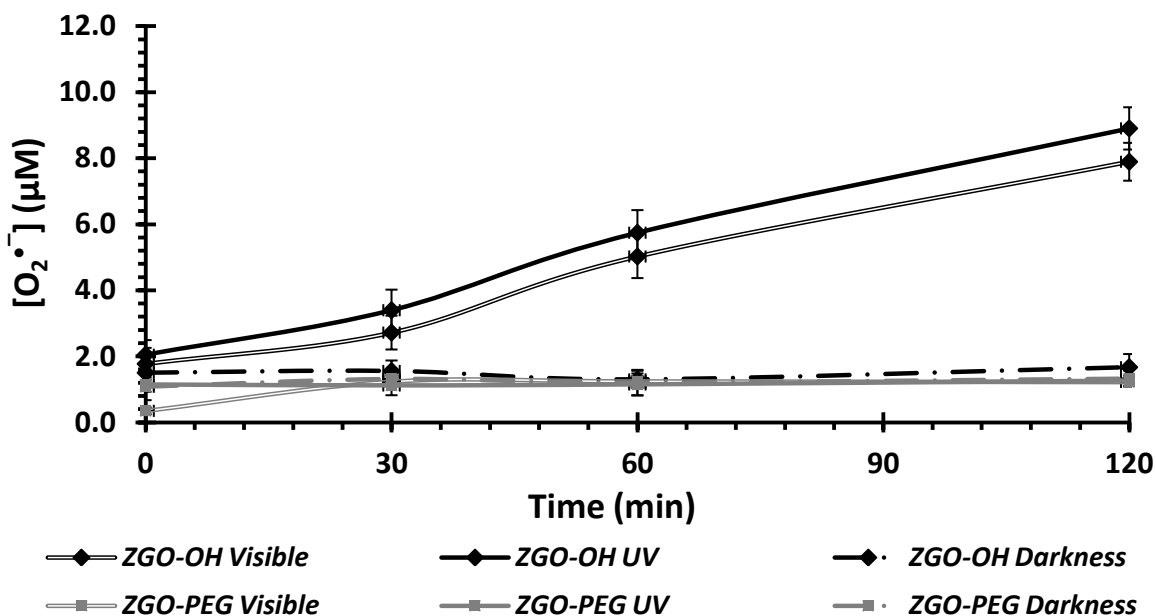
Fig. 6. 3. Kinetics for the $O_2^{\bullet -}$ generation by ZGO-PEG and ZGO-OH NPs under UV or visible-ligth irradiation and compared with their darkness counterpart as indicated by the reduction of 100 µM XTT. * Represents significant differences respect to control measure (time=0 minutes) according Tukey-Kramer test (p<0.05).

In this figure the effect of light irradiation in $O_2^{\bullet -}$ production by ZGO-OH within the time is clear, and an almost linear increase is observed during the first two hours of light irradiation. Not significant differences between the light source type (UV or visible light) were found.

6.3.2. Breast cancer cell viability alteration by pre-irradiated ZGO nanoparticles

Regarding the application of the ZGO-NPs, tumor cells seemed to be an important target for toxicity studies, and MCF-7 and MDA-MB-231 are standard cell lines derived from breast cancer tumors for *in vitro* research [366]. ZGO nanoparticles were administrated to MCF-7 and MDA-MB-231 cell cultures in varied concentrations (pre-irradiated with UV light or not), and different parameters as cell viability, ROS and NOS production, and cellular uptake were measured. The cells were never exposed to UV irradiation.

We examined the effect of ZGO-NP on the cell viability of human breast cancer cells using a conventional trypan blue assay. This method is based on the principle that live cells possess intact cell membranes that exclude certain dyes (trypan blue), whereas dead cells do not [364].

Colorimetric assay (such MTT) was not used in order to avoid a possible reaction between ZGO-NPs and the colorimetric indicator, giving false results.

The results shown in Figures 6.4A and 6.4B revealed a dose-dependent cytotoxicity by ZGO-OH nanoparticles after 24 hours of incubation, while cell viability was not altered by ZGO-PEG at the same doses and period of time. By its side, no significant alterations in cellular viability were observed when ZGO-PEG were added to the culture media.
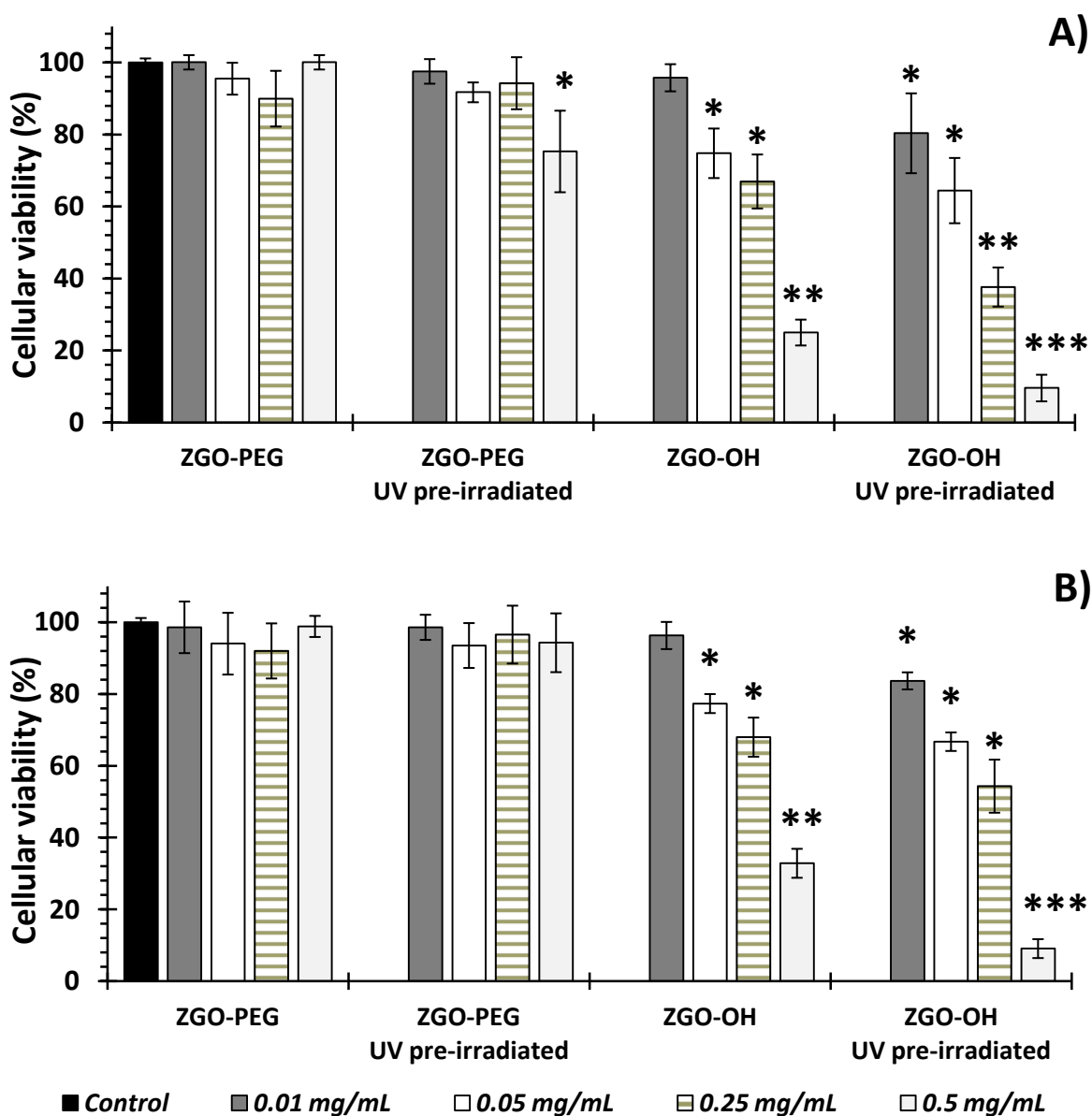
Fig. 6. 4. ZGO-NP and UV light irradiation effect on cell viability 24 hours after incubation. A) MDA-MB-231, and B) MCF-7 breast cancer cells 50000 cell/well. * Represents significant differences respect to control (viability= 100 %) according Tukey-Kramer test (p<0.05). Nanoparticles were administered after 5 minutes of UV irradiation or without irradiation.

Culture cells without nanoparticles were used as control for this experiment. Due to the ability of the PLNP to save photonic energy during long periods of time, the ZGO-NPs were keep in darkness one week before the experiments to avert photostimulation by natural light. In the same tables, we can appreciate the UV-light pre-stimulation effect on ZGO-OH toxicity, revealing a significant increase in cell death respect to non photostimulated nanoparticles.

6.3.3. In vitro oxidative stress evaluation: Aqueous peroxides and nitric oxide metabolites measurement

In Figure 6.5, aqueous peroxide [POx] generation in breast cancer cells culture media after ZGO-NP administration were quantified by colorimetric commercially disposable test after their lysis. The results indicated significant reactive oxygen species generation in both MDA-MB-231 and MCF-7 cell lines at 0.25 and 0.50 mg/mL ZGO-OH concentrations. Peroxide concentrations were increased in cells treated with pre-irradiated nanoparticles respect to non-irradiated nanoparticles. No significant increase in peroxide generation was measured at all ZGO-PEG concentrations tested respect to control.

The increased peroxide concentrations in the cellular environment can result in alteration and damage of cellular components, such as lipids, proteins, and DNA. The augmented peroxide concentrations in culture cells by addition of photostimulated PLNPs is well correlated with the increase in cell death.
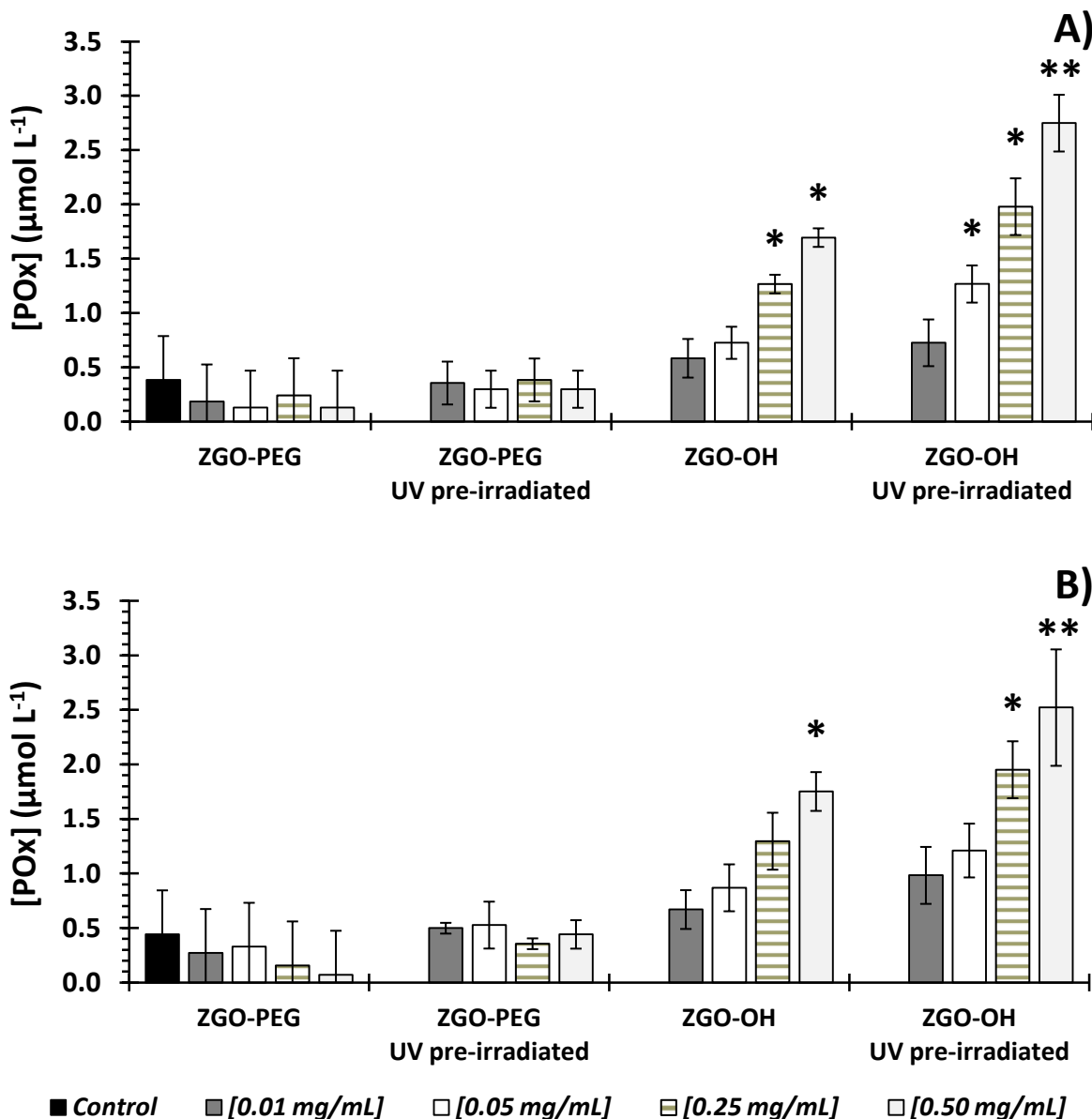
Fig. 6. 5. Effect of ZGO-NP on superoxide production (quantified as peroxides by colorimetric assay) by A) MDA-MB-231, and B) MCF-7 breast cancer cells after 24 hours of incubation in culture media (10000 cell/well). Nanoparticles were administered after 5 minutes of UV irradiation or without irradiation.

In the Figure 6.6, the nitric oxide metabolites concentrations were analyzed in breast cancer cells after ZGO-NPs treatment.
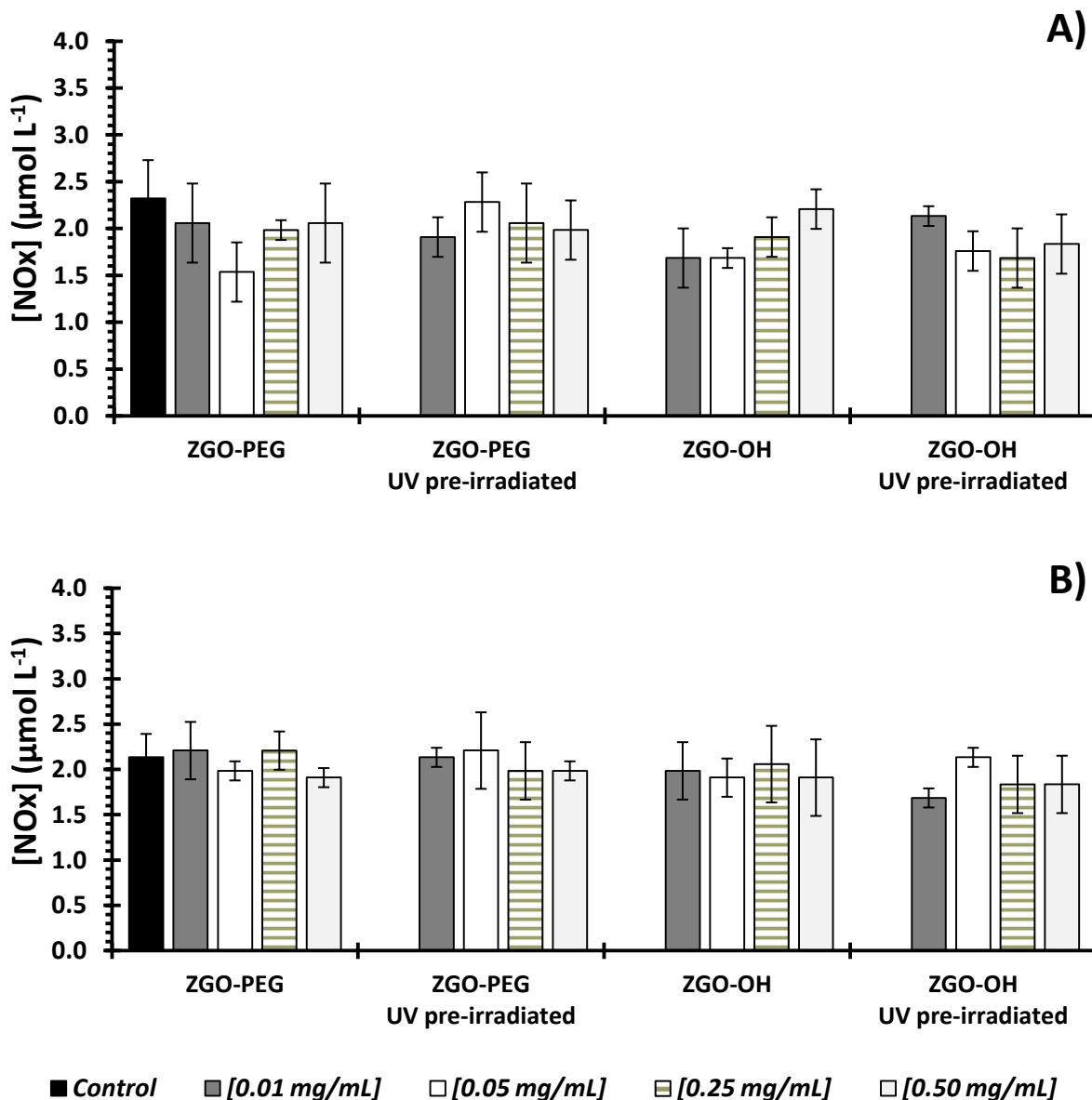
Fig. 6. 6. Effect of ZGO-NP on nitric oxide production (quantified as stable nitric oxide metabolites by Griess colorimetric assay) in A) MDA-MB-231, and B) MCF-7 breast cancer cells after 24 hours of incubation in culture media (10000 cell/well). Nanoparticles were administered after 5 minutes of UV irradiation or without irradiation.

The interest in the detection of nitric oxide arises from its identification as a bio-molecule that plays an important role in oxidative stress injury. In other work, high concentration of NO was cytotoxic and could induce the apoptosis of tumor cells, preventing tumors from metastasizing and assisting macrophage to kill tumor cells [367]. Nitric oxide is a cell signaling molecule that can be a potent inducer of cell death in cancers at elevated concentrations [368]. However, no significant

variations in nitric oxide metabolites concentrations were detected (Limit of detection: 1 µmol/L) in both hydroxylated and pegylated ZGO-NP treated cells. By this observation is shown that only ROS are implicated in the toxicity mechanisms of ZGO-NPs and not another free radical species.

In the Table 6-2 the inhibitory concentrations 50 % (IC50) for the light irradiated or not ZGO-OH and ZGO-PEG in both MDA-MB-231 and MCF-7 lines are indicated, resulting in statistically significant differences between photostimulated and not irradiated ZGO-OH.

Table 6- 2. IC50 $_{values}$ (µg/mL) of the nanoparticle cytotoxicity to different cells by trypan blue assay.

Nanoparticle configuration	MDA-MB-231	MCF-7
ZGO-OH	325 ± 19	370 ± 62
ZGO-OH UV	182 ± 40 *	224 ± 35 *
ZGO-PEG	> 0.5	> 0.5
ZGO-PEG UV	> 0.5	> 0.5

This observation denoted the importance of photo-induced toxicity.

6.3.4. Uptake of ZGO-NPs by cells

In order to justify the differences in toxicity between ZGO-OH and ZGO-PEG, we analyzed the nanoparticles uptake by breast cancer cells. With this purpose, adequate nanoparticle concentrations were incubated with MDA-MB-231 cells. We take advantage of the bio-labeling application of ZGO-NP for the cellular internalization studies by using confocal microscopy (Figure 6.7).

This technique was used to analyze the potentially toxicological effects of ZGO-NPs at cellular level without necessity of additional fluorescent biomarkers. In basis of the absorption/emission ZGO-NPs spectra[33], adequate excitation (λ=561 nm) and emission (λ=564-700 nm) filters were used in order to detect the ZGO-NPs luminescence. This confocal microscopy image provides assistance in the morphological and ultrastructural analysis of breast cancer cells. At cellular level, it is possible to see the aggregation of ZGO-OH treated breast cancer cells, while at ultra-structural scale, is possible to determine that nanoparticles were dispersed in the cytoplasm, but not in the nucleus of the cells. We found that the ZGO-OH nanoparticles were uptake by cells and then deposited into the cytoplasm (nucleus are indicated by arrows) (Figure 6.6A).
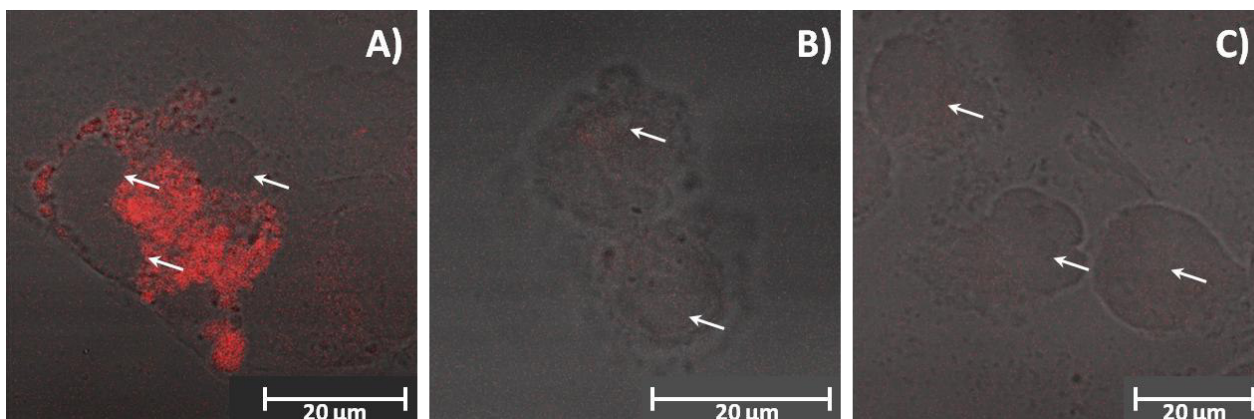
Fig. 6. 7. In vitro cellular uptake of A) ZGO-OH, B) ZGO-PEG and C) Control at [0.05 mg/mL] by MDA-MB-231 24 hours after administration. The arrows indicate the cell nucleus.

However, PEG-functionalized nanoparticles practically were not internalized by cells (Figure 6.6B). These PEGylated nanoparticles remained in the culture cell media, and were removed during the corresponding cell washing procedure before the confocal microscopy analysis.

Nanoparticle´s ability to bypass cellular membranes influences its capacity to induce toxic effects. This parameter is controlled principally by the variations in the size and shape, ligand type and by the surface chemistry [44, 87, 88]. In this work, the protective effect of polyethylene glycol against cellular uptake and toxicity has been demonstrated, and is caused by the decrease in nanoparticle interactions with proteins or cellular components due to steric hindrance.

The ZGO-OH uptake and their *in vitro* induced oxidative stress are well correlated with their cytotoxicity. Unlike ZGO-PEG, only ZGO-OH stimulates the peroxides production by cultured cells, which is well correlated with the reduction on cell viability. In addition, the superoxide production by isolated ZGO-OH was also demonstrated on this work, indicating the relevance of photo-induced effects of PLNPs in cell toxicity.

Complementary studies are required for the evaluation of the use of ZGO-NPs in photodynamic therapy, in which this material can acts as nanoprobe, and possibly as photosensitizer, which can means a bimodal alternative for cancer detection and treatment.

6.4. PARTIAL CONCLUSIONS

The photo-stimulation of persistent luminescence nanoparticles plays an important role in their toxicity. The determinant role of nanoparticle functionalization on *in vitro* effects of ZGO-NP has also been shown. The protective effect of nanoparticle surface functionalization by polyethylene glycol was demonstrated, resulting in non toxic ZGO-PEG nanoprobes for breast cancer cells.

Oxidative stress conditions were presented on these cells, which were induced by the ROS production by cell machinery due to the interaction of nanoparticles with cytoplasm organelles. The direct superoxide production by nanoparticles in consequence to photochemical effects after stimulation by UV and visible light has also an important contribution in the ROS formation.

CHAPTER VII.

ACUTE, SHORT AND LONG-TERM TOXICITY OF PERSISTENT NANOPHOSPHORS IN MICE
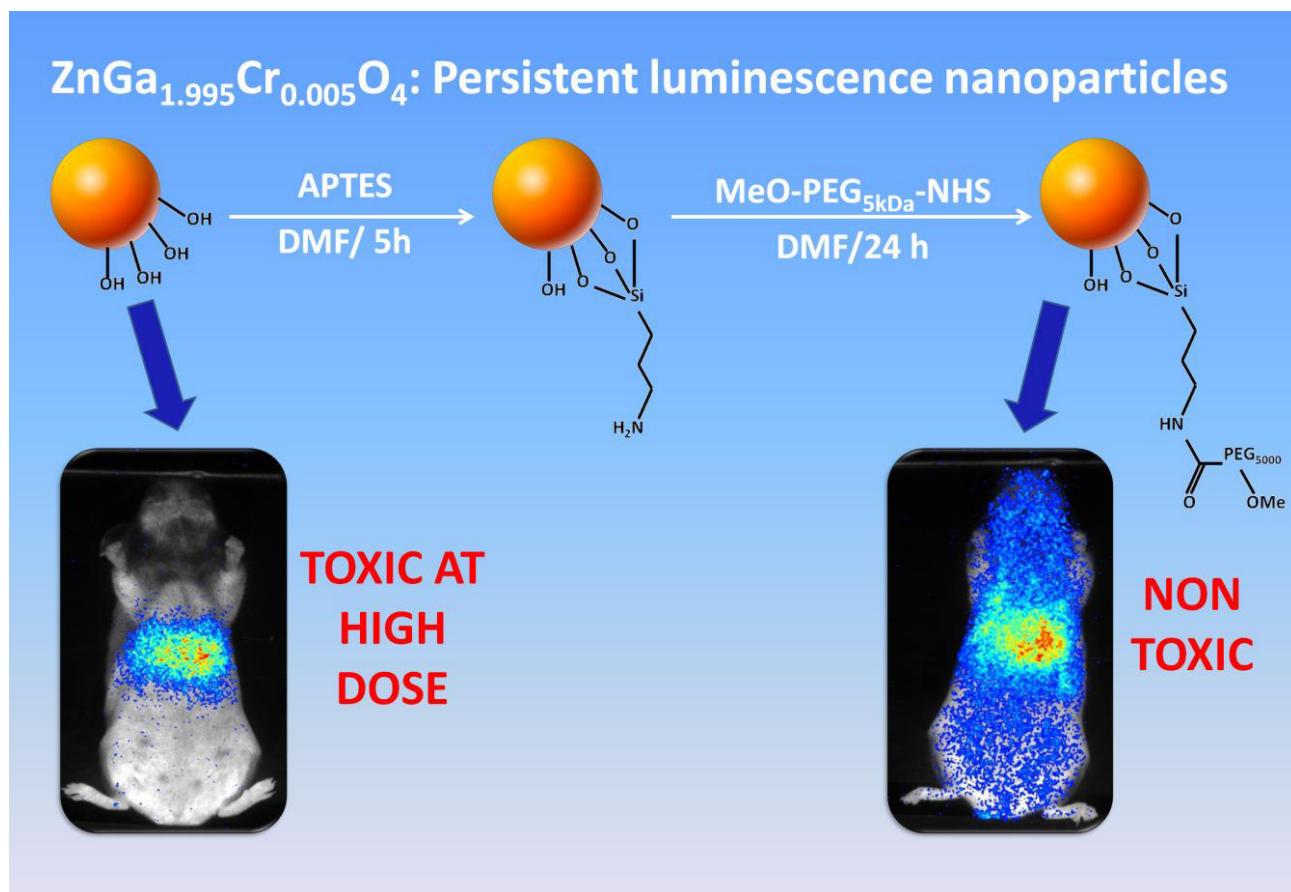
Persistent luminescence nanoparticles offer the promise of revolutionary tools for biological imaging with applications such as cellular tracking or tumor detection. They can be re-excited through living tissues by visible photons, allowing observations without any time constraints and avoiding auto-fluorescence signals. However, their uses demand extensive toxicological evaluation. In this part of the work, a complete set of mice were treated with a single intravenous administration of hydroxylated or PEGylated nanoparticles at different concentrations and then a set of standard tests were carried out 1 day, 1 month and 6 months after the administration in order to evaluate the acute, sub-chronic and long term *in vivo* effects of the $ZnGa_{1.995}Cr_{0.005}O_4$ persistent luminescence nanoprobes. Hydroxylated nanoparticles induced some important health alterations at the higher dose both at short and at long term exposition. High concentrations of hydroxylated nanoparticles generate structural alterations at histology level, endoplasmic reticulum damage and oxidative stress in liver, as well as rising in white blood cells counts. On the contrary, no clinical sign related to PEGylated nanoprobes treatments were noted during our *in vivo* experiments, denoting the protective effect of PEG-functionalization and thereby their potential as safe *in vivo* diagnostic probes.

7.1. BACKGROUND AND JUSTIFICATION

The use of non-invasive luminescent systems as tools for tagging pathologies in animal models is of great interest in biomedical research [369]. Some fluorescent probes, such as quantum dots [370-372], metal nanoparticles [373-375], fluorescent proteins [376, 377] and organic fluorophores[378, 379] have been used in optical imaging. Luminescent bioimaging based on nanoprobes has shown to be a highly selective, sensitive and non-invasive powerful tool for visualizing *in vivo* or *in vitro* molecular events[380]. However, fast photobleaching, poor signal-to-noise[381] ratio and toxicity can limit their practical applications [94, 382].

Persistent luminescence nanoparticles (PLNPs) are innovative materials in which the excitation energy can be stored in traps before being slowly released by thermal activation producing photonic emission which can last for several hours [14, 23, 254, 383]. Some advantages of persistent luminescence nanoparticles for biological imaging include detection and imaging without concomitant external illumination, avoiding auto-fluorescence signals produced by the tissues, resulting in high target to background ratio images [33].

Optical imaging for biological applications requires more sensitive tools. The recently reported $ZnGa_{1.995}Cr_{0.005}O_4$ persistent luminescence nanoparticles (ZGO-NPs) represent a new generation of optical nanoprobes, whose persistent luminescence can be activated before administration on live systems, as well as *in vivo* through living tissues [33]. This *in situ* re-activation in the therapeutic window, contrary to the previous PLNPs only excitable *in vivo* with UV light [14, 23], results in the ability to make observations of the probe without any time constraints, opening new perspectives for a great variety of diagnosis applications [33].

The surface functionalization of persistent luminescence nanoparticles is necessary to enhance its biocompatibility, avoid or delay their capture by the reticulo-endotelial system cells and for various biomedical applications [44, 254]. Aminosilane functionalized ZGO-NPs have been applied to monitor labeled cells, while PEGylated ZGO-NPs were used for *in vivo* passive tumor targeting [33]. In addition to their possible applications, the resulting toxicological response is greatly affected by the surface functional modification [384].

Because the same properties that are desirable and potentially useful from a biomedical perspective can also give rise to unexpected and hazardous toxicities, systematic toxicological studies are essential to design adequate nanomaterials for optical imaging or biomedical applications in order to avoid their adverse effects on health [385].

In the present chapter, we have evaluated the *in vivo* potential toxic effects of hydroxylated and PEGylated ZGO-NPs in mice after acute, short term and long term exposures at different doses, which is paramount for their further uses as biological imaging probes.

7.2. MATERIALS AND METHODS

$ZnGa_{1.995}Cr_{0.005}O_4$ nanoparticles were synthesized and functionalized according to the previously reported method [33], as described in the materials section of the Chapter II of this work.

Particle size and zeta potential were characterized to measure and control nanoparticle dimensions in biological test medium before administration by Dynamic light Scattering (DLS) and Laser Doppler Electrophoresis (LDE) measurements with a Nano ZS Zetasizer instrument (Malvern Instruments, Southborough, MA), and by capillary electrophoresis (CE) with a 7100 model capillary electrophoresis system (Agilent Technologies, Waldbronn, Germany) as further described in the Chapter II.

All experiments were conducted under the Mexican Official Regulations guidelines for use and care of laboratory animals and were approved by the University Animal Inspectorate. All animal were kept in stress-free, hygienic, and animal-friendly conditions. Sterilized food for mice and water were supplied *ad libitum*. In order to evaluate the potential *in vivo* toxicity, 4-week-old male BALB/c mice were once injected through the caudal vein with 200 μL of ZGO-NP suspensions at different concentrations (0, 1, 2, 4 and 8 mg/mouse) in 5 % [w/v] sterile glucose. Control mice received only glucose. Animals were weighed three times per week to control its growth and development. Twenty four hours, 30 days, and 6 months after PLNPs administration, mice were anesthetized with sodium pentobarbital (25.2 mg kg^{-1}) and then euthanized. Complete blood collected via the heart was realized for the different analyzes. Organs were excised and weighed accurately for *ex vivo* biodistribution studies, structural and histological analysis. A small piece of tissue from each organ was used immediately for aqueous peroxides (POx) and nitric oxide metabolites (NOx) quantification.

The lowest quantity of the ZGO-NPs permitting a good signal/noise rate (2 mg/mouse) was used to evaluate the main organs in which nanoparticles were accumulated. The *ex vivo* excitation of ZGO-NPs was carried out by nanoparticle exposition for 2 minutes under 254 nm ultraviolet light. After 1 or 4 hours, persistent luminescence from ZGO-NPs was re-activated by animal exposition under an orange/red LED lamp during 2 minutes. Persistent luminescence signals were then acquired using a photon-counting system based on a cooled GaAs intensified charge-coupled device camera (Optima, Biospace) (acquisition time: 3 minutes).

The entire organs from ZGO-NP treated mice were carefully removed and then stored at -20 °C until analysis. The *ex vivo* excitation was carried out by organ exposition for 5 minutes under LED excitation. Persistent luminescence signals were then acquired under the same precedent described conditions.

The peroxydation levels in organ homogenates were measured with a Peroxi-Detect kit (PD1 KT, Sigma), which is based on the oxidation of Fe^{2+} into Fe^{3+} ions by peroxides under acidic conditions. The resulting Fe^{3+} ions form a colored adduct with xylenol-orange, which is measured at 560nm. This assay was carried out in accordance with the manufacturer's protocol.

Nitric oxide levels were measured by Griess method as described by the manufacturer of the colorimetric assay kit (NB98, Oxford Biomedical Research). This method is based on an enzymatic reduction of nitrate into nitrite, which reacts with sulfanilamide and naphthyl ethylenediamine to generate a colored azo-compound, which is measured at 540 nm.

Blood was obtained by cardiac puncture using sodium heparin (Inhepar) as anticoagulant. Hematic biometry was carried out using a whole blood analyzer.

The alkaline comet assay was performed to evaluate the DNA damage from lymphocytes in blood samples of treated mice according on a previously described protocol [386]. Briefly, lymphocytes (2×10^4) with ~90 % viability (estimated by trypan blue exclusion) were mixed with 100 µL of low melting point agarose at 0.7 % [w/v], and the mixture was transferred onto a frosted slide (ES 370; Erie Scientific) pre-coated with normal-melting agarose at 1 % [w/v]. A cover slip was added and the slide was cooled on ice until correct gelification. After the embedding procedure, slides were treated for 1 h with cold lysis buffer (10 mM Tris pH 10, 2.5 M NaCl, 100 mM Ethylenediaminetetraacetic acid (EDTA), 200 mM NaOH, 1 % [v/v] Triton X-100, and 10% [v/v] Dimethyl sulfoxide (DMSO)). After lysis, slides were washed and immersed in cold alkaline electrophoresis solution (0.3 M NaOH and 1 mM EDTA in de-ionized water, pH 13.5) for 30 min and subjected to electrophoresis for 30 min at a constant voltage of 25V. All procedures were carried out in the dark. The slides were then neutralized with 0.04 M Tris–HCl (pH 7.5) for 10 min. The slides were stained with DAPI (4´,6-diamidino-2-phenylindole) just prior to images analysis. DNA migration was assessed by fluorescence microscopy.

Samples of liver, spleen, lung and kidney were collected and then fixed with 10 % [v/v] buffered formalin. Tissues sections were examined under an Olympus BX50 light microscope at ×40 and x100 magnifications with standard hematoxylin and eosin staining.

Mice were treated with intra-cardiac perfusion of 0.9 % NaCl [w/v], pH 7.4 cacodylate buffer and 4 % [v/v] para-formaldehyde, in respective order for adequate internal organ fixation and tissues stabilization. Ultramicrotome sections of the organ samples (liver and spleen) were evaluated for structural alterations using a JEOL JEM-1010 Transmission Electron Microscope (TEM) equipped with an ORIUS digital camera, by GATAN. In order to evaluate the ZGO-NP effects, the TEM images of injected mice organs were compared to the corresponding organs of non-injected animals.

Statistical analysis of the mean difference between multiple groups was determined by one-way analysis of variance followed by Tukey–Kramer multiple comparison tests by using the version 8 JMP software from SAS. The alpha level for all tests was 0.05.

7.3. RESULTS AND DISCUSSION

We used a light scattering technique to measure the zeta potentials and hydrodynamic diameter of the ZGO-NPs. These nanoparticles had zeta potentials of -38.5 ± 5.1 mV (ZGO-OH) and -1.8 ± 0.7 mV (ZGO-PEG) in phosphate buffer 30 mM. Their corresponding hydrodynamic radii were 92 ± 8 nm and 178 ± 14 nm, respectively. In our previously reported work (further details are described in Chapter II), the functionalization sequence of these nanoparticles was extensively studied and optimized in terms of colloidal stability in physiological conditions, guarantying the quality of the ready to use nano-objects [193]. No aggregation or sedimentation were observed in the dispersions used for these experiments.

This study was conducted in three setups in which mice were exposed to a single ZGO-NPs injection and the effects analyzed after an acute (24 hours), short-term (30 days) or long-term (6 months) exposition in order to observe *in vivo* potential toxic effects.

7.3.1. *In vivo* nanoparticle biodistribution

The aim of this part of the work was to investigate the acute, short and long term toxicological effects of recently discovered hydroxylated and PEGylated ZGO-NPs. The study of their potential toxicity is crucial for their safe biomedical applications. The biodistribution, histopathology, structural cytotoxicity, genotoxicity and general biocompatibility of the synthesized ZGO-NPs are among the most important factors to be analyzed. In order to reach a clearer conclusion about the potential toxic effect, we have injected increasing doses of ZGO-NPs, including a maximum of 8 times the required doses for *in vivo* optical imaging applications [37].

For the evaluation of *in vivo NP* biodistribution into the first hours after injection, persistent luminescence signal acquisition was performed immediately, 1 hour, and 4 hours after the injection of ZGO nanoparticles in healthy mouse (Figure 7.1).
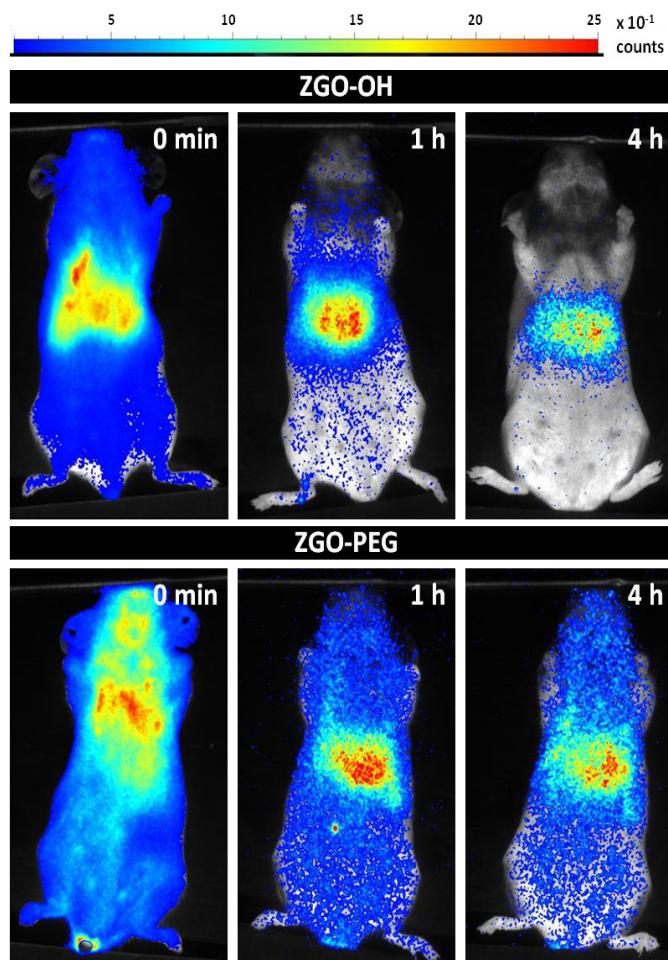
Fig. 7. 1. Biodistribution of UV pre-excited ZGO-NPs after intravenous injection of 2 mg/mouse and in situ activated at time 1hour and 4 hours. (1 unit= 2800 photons/s·cm^2·steradians).

Optical imaging examination showed that ZGO-OH were rapidly and mainly captured by the reticuloendothelial system cells (RES) of the liver and spleen. On the contrary, ZGO-PEG remains in blood circulation at least 4 hours after injection. The liver, which is the primary organ of metabolism, might act as a major target organ for ZGO nanoparticles after they entry into the body [37].

For short term imaging (imaging during the first few hours after their injection), the persistent luminescence nanoparticles must be pre-excited with UV. For this reason, mice were always treated with UV pre-excited particles and then the acute, short and long term effects were analyzed.

7.3.2. Mice weight control

Body weights were monitored three times every week. The representative tendency of the gained weight is presented in Figure 7.2 considering monthly measurements.
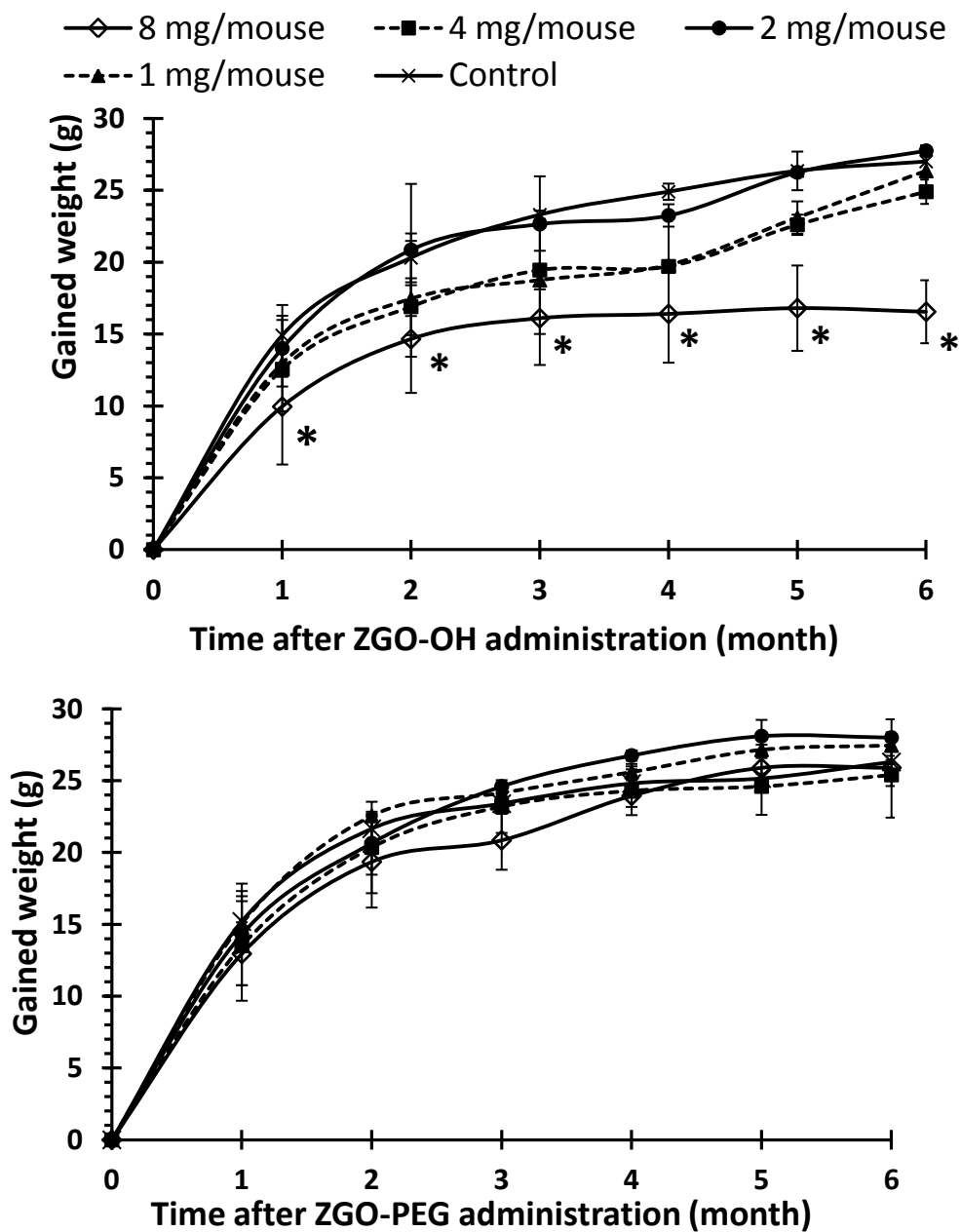
*Fig. 7. 2. Mean body gained weight ± SD of mice after chronic ZGO-NPs administration (over 6 months). * Represents significant statistical differences by Tukey HSD respect to control (p < 0.05), (n=6).*

The fluctuations were no greater after treatment at various concentrations with respect to the control, only at very elevated concentration of ZGO-OH nanoparticles, suggesting minimal systemic effects. ZGO-PEG did not cause variations in animal weight whatever the injected amount. No behavioral changes were observed in any group of mice. Organ coefficient (the ratio of

weight of the organ with respect to total animal weight) alterations were not detected during our experiments (results not shown).

7.3.3. Biodistribution in organs by persistent luminescence analysis

Three different possible fates for the ZGO-NPs can be imagined after their *in vivo* injection: i) Total elimination by the body, ii) Partial degradation and biodisponibility of their components for a determinated time, and finally iii) Intact prevalence and integrity of the nanocrystals in the body. The persistent luminescence signals detected by means of the *ex vivo* optical imaging analysis of the organs (Figure 7.3) has shown that nanoparticles remain in the body for at least 6 months. The bio-labeling application of ZGO-NPs for the biodistribution studies by optical imaging was used to analyze their potential toxic effects at systemic level without resorting to additional fluorescent biomarkers. A progressive decrease in luminescence signals seems to be evidenced by a qualitative analysis of the images.

According to the literature, systemically administered nanoparticles are commonly accumulated in the reticuloendothelial system, including liver, spleen and lymphatic system of small animals [387]. This was confirmed in this study (Figures 7.1 and 7.3). By that reason, further toxicity studies in this work were addressed to these organs.

ZGO-OH nanoparticles accumulated preferentially in liver, but also in lung and spleen. The liver has important function in metabolism of toxic substances. Particularly, in the production of metallothioneins that have toxic metal detoxification function. Metallothioneins are proteins possessing a high amount of Cys residues, which confers them a high capacity for metal binding [388]. As ZGO-OH nanoparticles are suspected to undergo stronger interactions with cellular components, they are likely to better interact with metallothioneins, which have demonstrated to be implicated in negative effects (decrease in resistance to metal-based compounds) due to the coercive connection between zinc(II) ions, reactive oxygen species and heavy metal ions [388], all of them already observed in the mouse/ZGO-NP system. This subject will be further analyzed in upcoming studies.

At this moment, the results obtained in this progressing work allowed to evidence the principal target organs implicated in the passive capture of ZGO-NPs and the presence of the latter as functional persistent luminescence nanoprobes in organs at least 6 months after administration.
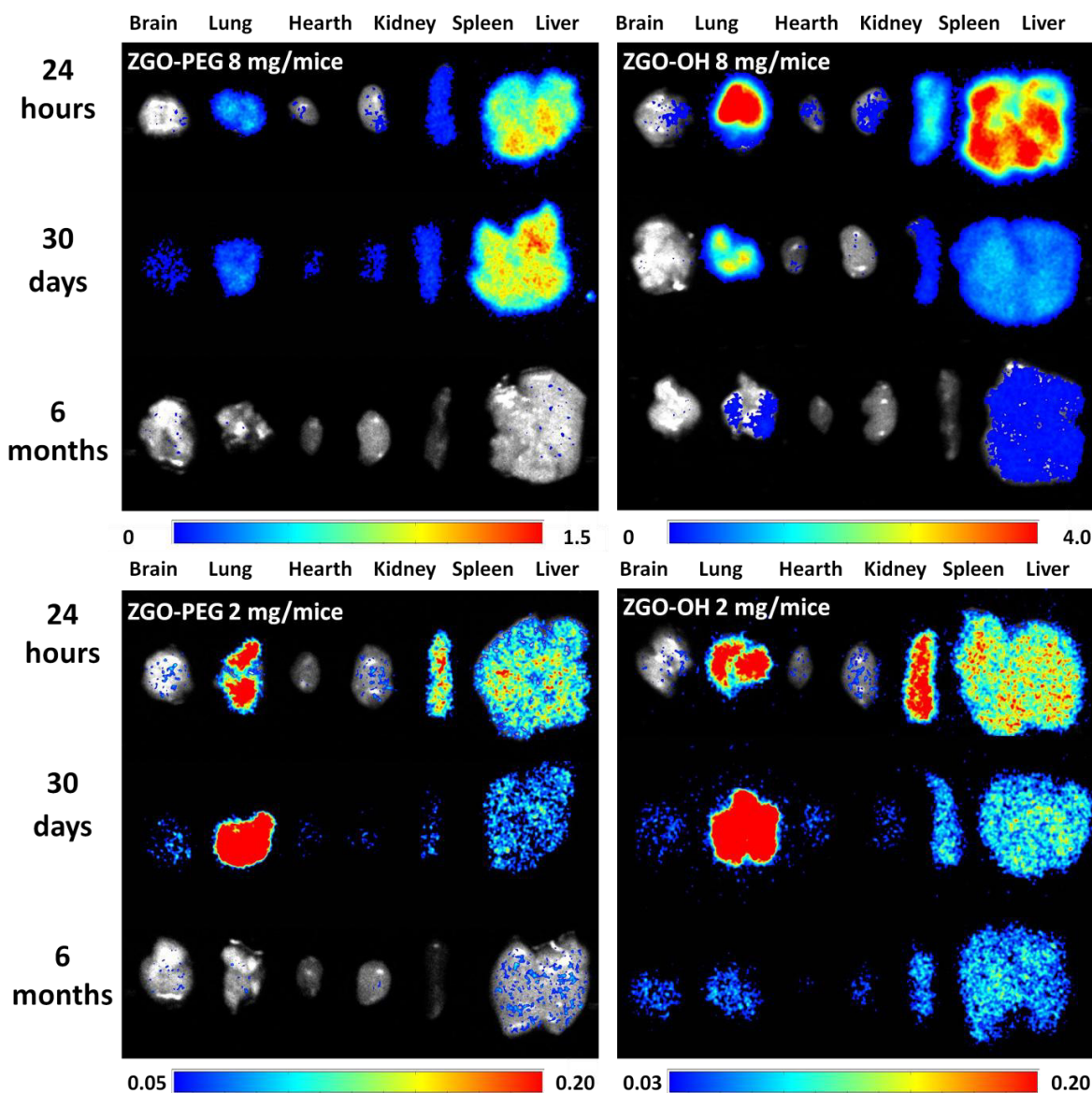
Fig. 7. 3. Ex vivo biodistribution of ZGO-OH and ZGO-PEG (2 or 8 mg/mouse) at different periods after intravenous injection. Persistent luminescence intensity is expressed in false color units (1 unit D 2,800 photons s^{-1} cm^2 sr) for all images.

About the analysis of *ex vivo* optical imaging data collected in the principal organs of treated mice, the decrease in luminescence intensity may be associated to a progressive and slow degradation of the superficial crystal structure of nanoparticles. This hypothesis is pretended to be demonstrated in a near future by an extensive biodistribution analysis, in which persistent luminescence of nanoparticles would be quantitatively evaluated using other techniques such as inductive coupled plasma.

7.3.4. Oxidative and nitrosative stress evaluation

In order to reveal possible mechanisms of cell death induced by exposure of ZGO-NPs in liver, lungs and spleen, peroxide generation was investigated (See Figure 7.4 A-C), which correspond to the organs displaying the highest content of nanoparticles. Oxidative stress was only detected in the livers of the ZGO-OH treated mice and only at the most elevated concentrations (4 and 8 mg/mouse 24 hours after injection, and 8 mg/mouse 6 months after injection). The peroxide production by organs of ZGO-OH treated mice at lower concentrations as well as ZGO-PEG treated mice across all the range of doses were not affected by the presence of the nanoparticles.

Nitric oxide levels remained unchanged with respect to the control in all tested conditions (Results not shown).

ZGO-OH accumulation and oxidative stress are well correlated with the lost of weight induced by this kind of nanoparticles. Reactive oxygen species (ROS) are known to mediate cell death in a variety of cell types [389]. ZGO-NPs can persist in organ tissues and directly interact with the living environment. ZGO-NP dissolution can lead to the release of Zn^{2+} in living media, which has proved capable to generate reactive oxygen species [390, 391]. Only ZGO-OH stimulated peroxide production by hepatic cells, which can potentially cause liver damage.
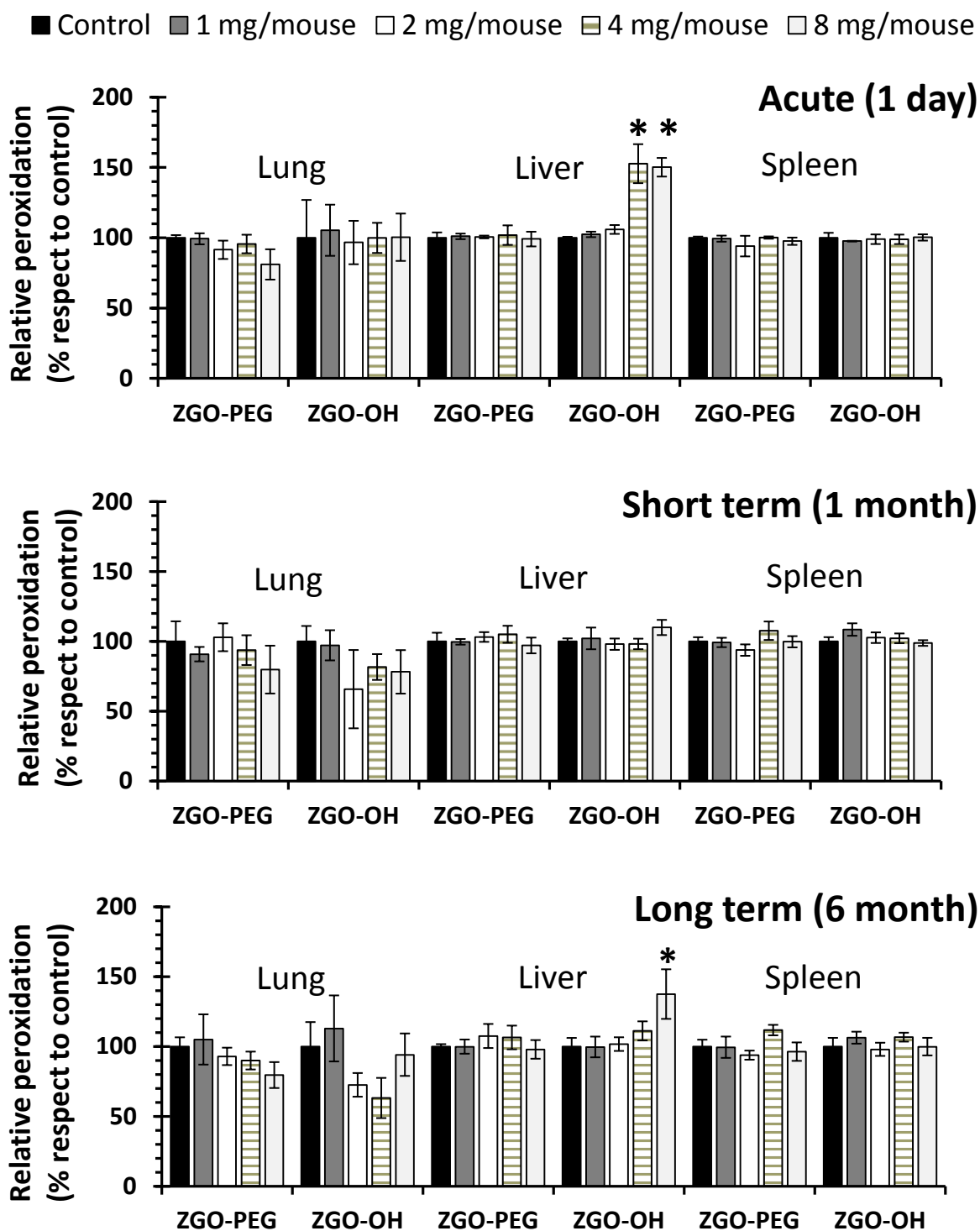
*Fig. 7. 4. Aqueous peroxide production by mouse organs after acute, sub-chronic and chronic administration of ZGO-NPs. Quantification by colorimetric assay. * Represents significant statistical differences by Tukey HSD respect to control (p < 0.05). (n=4).*

7.3.5. DNA damage study by comet assay

No DNA breakage in lymphocytes could be detected with ZGO-OH nor with ZGO-PEG treated mice (Figure 7.5). The DNA tail intensity was not modified by ZGO-NPs at all tested concentrations. Positive control (8.8 % [v/v] H_2O_2 treated cells) was also included in all analyses to ensure the reliability of the results. The presence of comet tails was not detected, indicating absence of fragmented DNA, by which no ZGO-NP genotoxicity is expected at least in lymphocyte cells.
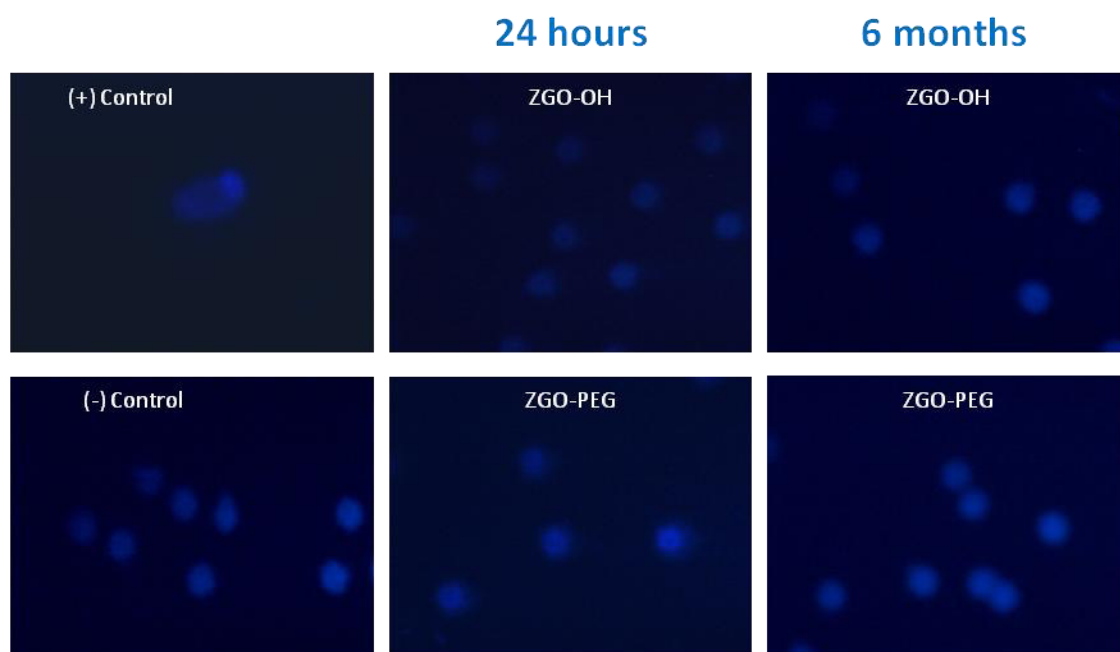
Fig. 7. 5. Comet assay from blood sample of ZGO-PEG and ZGO-OH acute and at long-term treated mice (8 mg/mouse). H_2O_2 (8.8 % [v/v]) treated cells were used as positive control.

7.3.6. Complete blood count analysis

ZGO-OH nanoparticles produced rising in white blood cell counts, principally lymphocytes and granulocytes after acute and long-term treatments at elevated concentrations (Table 7-1). However, hematic biometry parameters did not show any alteration 30 day after ZGO-NP administration. Other parameters of hematic biometry remained unaffected by the nanoparticles. Cell counts were not affected by ZGO-PEG nanoparticle administration whatever the injected doses.

*Table 7- 1. Hematic biometry of ZGO-NPs treated mice at short and long term after administration (n=2); WBC, white blood cells; LYM, lymphocytes; GRAN, granulocytes; RBC, red blood cells; HGB, hemoglobin; HCT, hematocrit; PLT, platelets. *Statistically different vs. the control (p<0.05) by Tukey-HSD test, (n=4).*

		24 hours after administration							
Dose/ mouse	**Control 0 mg**	**ZGO-OH (dose/mouse)**				**ZGO-PEG (dose/mouse)**			
		1 mg	**2 mg**	**4 mg**	**8 mg**	**1 mg**	**2 mg**	**4 mg**	**8 mg**
WBC (x10^3)/µL	8.7 ± 0.1	8.6 ± 0	8.9 ±0.4	**10.3 *** **± 0.1**	**12.5 **** **± 1.0**	8.5 ± 0.1	8.8 ± 0	8.5 ± 0.4	**10.5 *** **± 0.1**
LYM (x10^3)/µL	6.0 ± 0.6	5.7 ± 0.4	6.2 ± 0.6	6.7 ± 0.4	**8.0 *** **± 0.3**	6.0 ± 0	5.6 ± 0	4.6 ± 2.1	**7.5 *** **± 0.1**
GRAN (x10^2)/µL	7.0 ± 1.4	7.0 ± 1.4	8.0 ± 2.8	**13.0 *** **± 1.4**	**18.0 **** **± 0**	10.0 ± 2.8	7.0 ± 1.4	7.0 ± 1.4	**11.0 *** **± 1.4**
RBC (x10^6)/µL	9.1 ± 0.1	9.3 ± 0.7	9.1 ± 0.1	9.1 ± 1.0	9.2 ± 0.1	9.1 ± 0.1	8.6 ± 1.0	8.9 ± 1.2	9.1 ± 0
HGB (g/dL)	14.7 ± 0.4	15.0 ± 1.1	15.0 ±0.3	14.6 ± 0.3	15.3 ± 1.3	15.3 ± 0.7	14.9 ± 1.8	15.3 ± 1.6	14.7 ± 0.4
HCT (%)	52.4 ± 0.6	50.5 ± 2.1	53.0 ± 3.4	49.8 ± 2.8	52.5 ± 4.4	51.7 ± 0.7	51.5 ± 4.4	54.0 ± 1.4	51.2 ± 2.8
PLT (x10^5)/µL	6.7 ± 1.3	6.1 ± 1.4	5.6 ± 0.5	6.1 ± 0.2	6.7 ± 0.3	6.4 ± 0.2	6.1 ± 0.1	6.0 ± 1.2	7.2 ± 1.2
		30 days after administration							
WBC (x10^3)/µL	8.5 ± 0.4	8.3 ± 1.0	9.3 ± 1.3	8.7 ± 0.1	9.2 ± 0	8.6 ± 0.6	8.7 ± 0.4	8.4 ± 0.3	9.2 ± 0.6
LYM (x10^3)/µL	6.4 ± 0.6	6.0 ± 1.1	6.4 ± 0.3	6.1 ± 0.4	6.6 ± 0.6	5.7 ± 0.1	5.8 ± 0	6.0 ± 0	5.7 ± 0.7
GRAN (x10^2)/µL	8.0 ± 0	7.0 ± 1.4	8.0 ± 0	7.0 ± 1.4	6.0 ± 0	7.0 ± 1.4	7.0 ± 1.4	8.5 ± 2.1	7.0 ± 1.4
RBC (x10^6)/µL	9.4 ± 0.2	9.4 ± 1.3	9.2 ± 0.2	9.1 ± 1.0	9.3 ± 0.1	9.1 ± 0.1	8.7 ± 1.1	8.9 ± 1.2	9.1 ± 0.7
HGB (g/dL)	15.7 ± 0.4	15.3 ± 0.7	15.2 ± 0.6	14.8 ± 1.7	15.4 ± 1.4	15.2 ± 0.8	15.1 ± 3.3	15.4 ± 0.3	15.3 ± 0.7
HCT (%)	52.0 ± 2.8	51.4 ± 0.8	51.8 ± 2.8	52.3 ± 0.7	51.5 ± 2.7	52.2 ± 0.8	50.1 ± 0.7	52.1 ± 0.1	50.4 ± 1.1
PLT (x10^5)/µL	6.3 ± 1.3	5.6 ± 1.1	5.6 ± 0.5	5.8 ± 0.7	6.3 ± 0.2	6.2 ± 0.8	5.8 ± 0.5	6.3 ± 0.7	6.6 ± 0.6
		6 month after administration							
WBC (x10^3)/µL	8.7 ± 0.4	8.4 ± 0.8	9.5 ± 1.3	8.7 ± 0.1	**12.0 *** **± 1.1**	8.0 ± 0.3	8.7 ± 0.4	8.3 ± 0.5	8.5 ± 0.7
LYM (x10^3)/µL	6.0 ± 0.3	5.5 ± 0.4	6.3 ± 0.4	5.7 ± 0.1	**7.3 *** **± 0.1**	5.7 ± 0.1	5.6 ± 0.3	5.5 ± 0.7	5.7 ± 0.7
GRAN (x10^2)/µL	7.0 ± 1.4	7.0 ± 1.4	9.0 ± 1.4	**11.0 *** **± 1.3**	**15.0 **** **± 1.5**	7.0 ± 1.4	7.0 ± 1.4	6.5 ± 2.1	7.0 ± 1.4
RBC (x10^6)/µL	9.4 ± 0.2	9.4 ± 1.3	9.2 ± 0.2	9.1 ± 1.0	9.3 ± 0.1	9.1 ± 0.1	8.7 ± 1.1	8.9 ± 1.2	9.1 ± 0.7
HGB (g/dL)	15.9 ± 0.7	15.0 ± 1.1	14.7 ± 0.1	15.2 ± 2.0	15.4 ± 1.4	15.8 ± 0	14.5 ± 4.1	16.1 ± 3.3	16.1 ± 0.4
HCT (%)	52.0 ± 2.8	51.4 ± 0.8	51.6 ± 3.1	49.3 ± 3.5	52.5 ± 4.4	52.2 ± 0.8	51.5 ± 4.4	51.3 ± 3.3	53.4 ± 5.4
PLT (x10^5)/µL	6.7 ± 1.5	5.6 ± 1.1	5.6 ± 0.5	6.5 ± 0.3	6.7 ± 0.3	6.5 ± 0.7	6.0 ± 0.2	6.0 ± 1.1	7.2 ± 1.1

The increase in white blood cells during the first 24 hours after administration can be due to a primary immune response against nanoparticles. Because of the similarity in size between nanoparticles and viruses or large proteins, they may affect the immune system or induce an inflammatory response, which would be correlated with changes in blood cell counts [392]. After a long term residence of nanoparticles into the mice (6 months), the possible dissolution of the nanoparticles could generate biodisponibility of their elements.

7.3.7. Histopathological examination of principal organs

In Figure 7.6, the histopathological examination of the tissues indicated that intravenous administration of high doses of ZGO-OH could induce hepatic pathological lesions for long-term exposure.

For mice treated with ZGO-OH nanoparticles severe alterations at cellular and histological level were observed in the liver, that is to say inflammatory changes and congestive dilated central veins. Marked nuclear pleomorphism, increase in nuclei volume, abnormal chromatin distribution and lymphoid infiltrates have been observed in hepatocytes. A dose-response relationship for ZGO-NP induced toxicity was evidenced in this study. However, as seen under the microscope, no obvious abnormalities in histology could be observed in the spleen, lung and kidneys of ZGO-OH nanoparticle treated mice. No obvious pathological effects were observed in the organs of ZGO-PEG nanoparticle treated mice under the same treatment and observation conditions.

According to the literature, ZnO nanoparticles cause endoplasmic reticulum stress by ROS generation due to Zn^{2+} overconcentration [391]. Our results can indicate that ZGO-NPs perhaps activate the endoplasmic reticulum stress pathway as effect of Zn^{2+} ions releasing.

The protective effect of polyethylene glycol molecules onto nanoparticle surface was also demonstrated at a histopathological level, since only negligible alterations were observed for ZGO-PEG NPs in comparison with unmodified ZGO-OH NPs, for which severe alterations were observed, mainly due to the incessant presence of the nanoparticles into the liver structure.
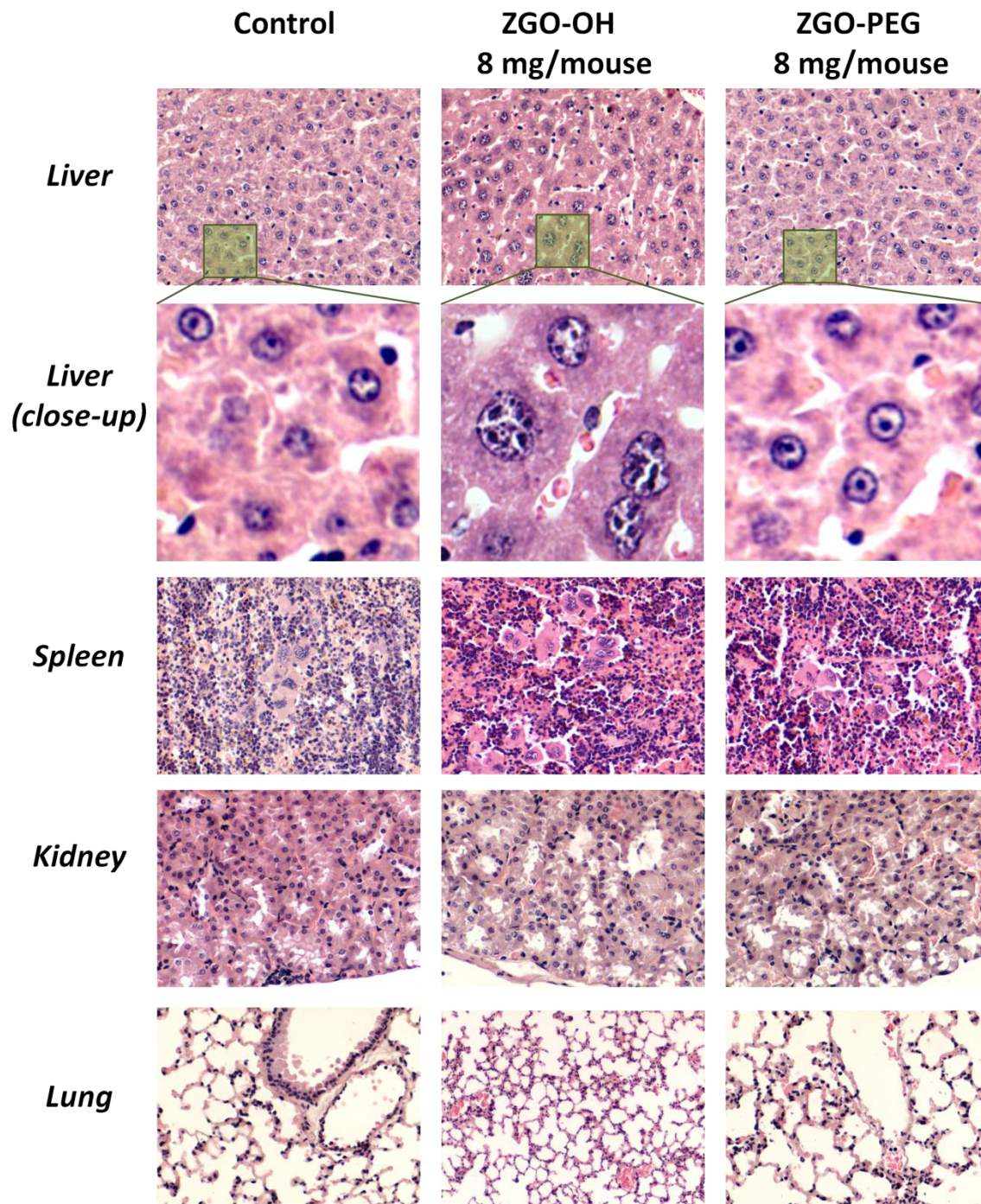
Fig. 7. 6. Hematoxylin and eosin stains on liver, spleen, kidney and lung under optical microscope for histopathological morphology analysis at 6 months after ZGO-NPs injection.

7.3.8. Evaluation of structural alterations by TEM

The ultra-microtome sections of the principal organs of the reticulum endothelial system, liver and spleen, were thoroughly analyzed. In Figure 7.7, the results of TEM analysis indicated that ZGO-OH nanoparticles at very elevated concentrations (8 mg/mouse) present endoplasmic reticulum (ER) alterations, but no damages were detected at lower concentrations or when using the PEGylated nanoparticles. ZGO-OH nanoparticles induced swelling of the ER and ribosome degranulation. The ER structures are marked with arrows, and we can note the disorder in their structures in the case of the livers of ZGO-OH treated mice, by comparison with the corresponding control.

Endoplasmic reticulum swelling is associated with endoplasmic reticulum stress. This organelle is sensitive to oxidative stress and has important functions such as proteins folding and assembly, lipids and sterols synthesis as well as calcium release [393]. Endothelial reticulum stress refers to an important cellular self protection mechanism, which can be activated to counteract situations of stress induced by an overload of unfolded proteins or come from direct endoplasmic reticulum damage [393].
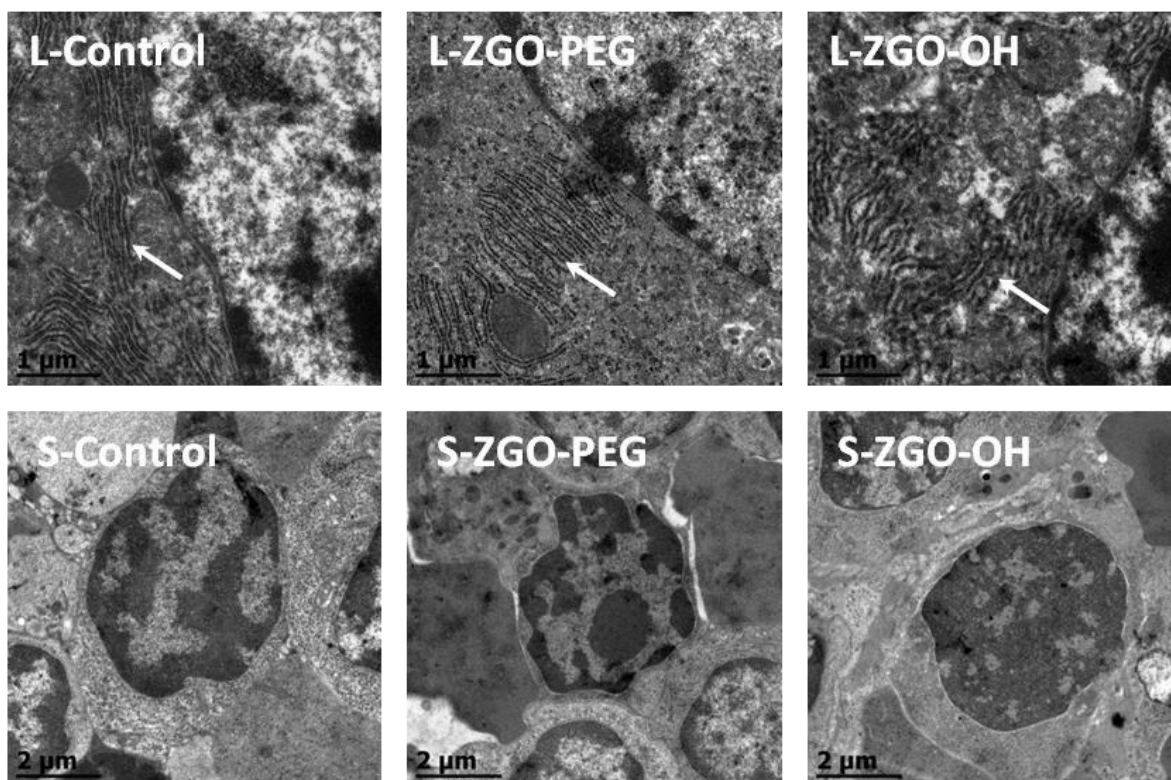
Fig. 7. 7. TEM images of liver (L) and spleen (S) of mice 6 months after injection of ZGO-NP at 8 mg/mouse. Single staining was used for all TEM analysis. Arrows in the images show endoplasmic reticulum.

In contrast no alterations were observed in control liver. Besides, no alterations were observed in nucleus, nuclear membrane, mitochondria, and other organelles. Likewise, no structural damage was observed in any spleen structures.

We hypothesized that exposure to high doses of ZGO-OH NPs induces oxidative stress and endothelial reticulum (ER) stress involved in chronic liver damage. In any case, no organelle and cellular membrane alterations could be observed in mice treated with ZGO-OH or ZGO-PEG NPs.

Only very elevated concentrations of ZGO-OH nanoparticles (8 mg/mouse) showed noticeable toxic effects in mice after long-term exposure at ultra-structural transmission electron microscopy level. No toxic effects were detected at functional doses of ZGO-NPs (<2 mg/mouse) used to biological imaging. As an example, a 2 mg/mouse dose of ZGO-PEG has been used for *in vivo* tumor passive detection [33].

Surface functionalization plays a determinant role on the *in vivo* interactions with blood components and cellular elements, and therefore on the ZGO-NP toxicity. The ability of NPs to bypass cellular membranes influences its capacity to induce toxic effects. The nanoparticle surface or coating with additional biocompatible molecules (antibody, peptide, and small ligands) is useful to control toxicity [389, 394-396]. In the literature, it has been shown that PEGylation reduces the toxicity of nanoparticles with respect to non-PEGylated ones [87, 397]. Polyethylene glycol is the most widely used polymer in the drug delivery field. This inert polymer prevents interactions with components of the cells. PEGylation is a method that promotes long circulation and thus reduces accumulation in organs. The protective effect of PEG-functionalization has been verified again in this study.

7.4. PARTIAL CONCLUSIONS

This study has shown a determinant role of nanoparticle functionalization on the *in vivo* effects of ZGO-NPs. Protective effect of nanoparticle surface functionalization was demonstrated. PEG-functionalized $ZnGa_{1.995}Cr_{0.005}O_4$ probes are non-toxic to live mice even at elevated doses. Only very elevated concentrations of ZGO-OH nanoparticles produce toxic effects on this animal model, indicating low toxicity index. Increased white blood cell counts, elevation of peroxydation levels on liver and alterations of endoplasmic reticulum on hepatocytes could only be observed at doses as high as 8 mg/mouse. Severe histopathological damage characterized by prominent nucleus and abnormal chromatin distribution was detected in livers of mice treated with ZGO-OH nanoparticles. No DNA damage in mice lymphocytes could be detected by comet assay, whatever the nanoparticle dose involved. No toxic effects were detected at functional doses of ZGO-NPs (<2 mg/mouse) used for biological imaging. Nanoparticles were not totally eliminated by the body during the first 6 months after administration. Using the general toxicology parameters investigating clinical signs (hematology, genotoxicity, stress oxidative assessment and morphological study by TEM) no significant effects could be evidenced on any of the groups tested with ZGO-PEG nanoparticles as collected values were all within the normal range when compared to non-treated

animals and cells. From all these results, no serious toxicological phenomenon was observed. These ZGO-NPs are promising materials able to use *in vivo* in safe conditions. Further experiments are planned to evaluate the effect of such PLNPs at very long term after administration as well as to determine their possible biodegradation.

GENERAL CONCLUSIONS

The physicochemical characterization of nanoparticles is paramount to correlate their properties with their *in vivo* fate. The interest of employing capillary electrophoresis for nanoparticle characterization was demonstrated in this study, allowing a very quick and easy characterization with minimal amount of nanoparticles and reliable results.

The characterization of the $ZnGa_{1.995}Cr_{0.005}O_4$ persistent luminescence nanoparticles with different functional groups at their surface allowed to verify the effective functionalization, to optimize the different steps in terms of reaction conditions and washing procedures, to identify the best conditions to mimic physiological ones and allow colloidal stability. Some parameters such as polydispersity, size characterization and zeta potential were determined in various buffers. The dispersion media properties, for example charge nature, pH and ionic strength impacted the colloidal properties of these nanoparticles. The understanding of the effects of these variables can help in the formulation of new nanomaterials, and in the particular case of the $ZnGa_{1.995}Cr_{0.005}O_4$ nanoparticles, this results were fundamentals to guaranty the nanoparticle quality for posterior analysis.

A main challenge in developing biomedical nanoprobes is to ensure their biocompatibility, bioreactivity and *in vivo* stability. A determinant role of nanoparticle functionalization in toxicity was evidenced by means of the *in vivo* effects of $ZnGa_{1.995}Cr_{0.005}O_4$ nanoparticles. Only very elevated concentrations of ZGO-OH nanoparticles produced toxic effects on mice, while protective effect of polyethylene glycol surface functionalization was demonstrated, resulting ZGO-PEG to be non-toxic to live mice even at elevated doses. Further experiments must be performed in order to evaluate the effect of such nanoparticles at very long term after administration as well as to determine their possible biodegradation.

The photo-stimulation of persistent luminescence nanoparticles plays an important role in their toxicity in culture cells. The direct superoxide production by nanoparticles in consequence to photochemical effects after stimulation by UV and visible light has been demonstrated, and the application as a photodynamic therapy agent is actually evaluated.

Because the biomolecule adsorption by nanoparticles once they are in contact with physiological fluids provides them a new identity and new properties, we considered the importance of the development of new methodologies for the analysis of interactions between nanoparticles and proteins. The Hummel-Dreyer method for a deeper and fast characterization of the adsorption of proteins on nanoparticles has shown to be sufficiently sensitive to detect small changes in the magnitude of association parameters. This methodology opens the way for a better understanding of the nanoparticle/proteins interactions and for a prediction of nanoparticle behavior in biological systems. This could guide future nanoparticle syntheses and functionalization for the design and performance improvement of new nanomaterials in various domains such as diagnostic biosensors, biomedical imaging and targeted therapy, and even allow control of the structural features of the adsorbed proteins, whose bio-reactivity could be modified, leading to new therapeutic effects.

It was also demonstrated that capillary electrophoresis was a powerful tool to compare the affinity of nanoparticles for different plasma proteins in a mixture of two proteins. The resulting higher ZGO-PEG affinity for Apolipoprotein-E respect to Human Serum Albumin in different interaction models opens the perspective for the analysis of the pre-formation of an Apolipoprotein-E protein corona around the PEGylated nanoparticles by means of a simply pre-incubation step, which can be exploited as a strategy for their translocation across the blood brain barrier. Even if the presence of only two proteins is far from the real protein composition in a physiological sample, at the current state of the research in which the interactions between nanoparticles and single proteins is normally considered, the analysis of interactions in a binary system of proteins represents a great advance in the simulation of physiologically relevant conditions.

Despite the developing of adequate methodologies to accurately predict the *in vivo* nanoparticle fate is still a challenge, the knowledge of the physicochemical properties of nanoparticles could therefore help to interpret the information of experimental data and extract general rules that can be applied to studies of design, modification, biocompatibility, and applications of novel and safe, engineered nanoparticles intended for biomedical applications.

PERSPECTIVES

The analysis and characterization of different nanoparticle physicochemical parameters in more complex media is suggested in order to obtain more accurate information for the prediction of the *in vivo* nanoparticle performance.

The developed methodologies in this work can be used to characterize other kinds of nanoparticles in terms of colloidal properties, which could enhance their applications.

The application of many other CE modes disposable for evaluation of binding parameters such as vacancy affinity capillary electrophorsis (VACE), vacancy peak method (VPM), non-equilibrium CE of equilibrium mixtures (NECEEM) and others remain unexplored and could be potentially exploited in order to obtain different and complementary information about binding parameters between nanoparticles and biomolecules.

The evaluation of the interactions between nanoparticles and other kinds of biomolecules, such as lipids and carbohydrates could provide important information about the *in vivo* nanoparticle fate and thereby, for new biomedical applications.

It appears important to evaluate the PEGylated nanoparticle pre-incubation with Apolipoprotein-E effect in the translocation of the nanoparticles through the blood brain barrier. As predicted by the results obtained by capillary electrophoresis, it can represent a new strategy for nanoparticle vectorization to the brain zone.

The study of complementary toxicological parameters to determine the $ZnGa_{1.995}Cr_{0.005}O_4$ nanoparticle biocompatibility is paramount. Some tests to determine the nanoparticle biodegradation and clearance, as for example by inductive coupled plasma are indispensable to understand the *in vivo* nanoparticle effects. The precise localization of the nanoparticles at cellular level is also necessary in order to determine the toxicity or innocuousness mechanisms according to the functional groups present in the nanoparticle surface.

The study of protective effects of some functional groups or molecules against toxicity induced by nanoparticles is also of great interest in order to increase the biocompatibility of new engineered nanoparticles.

The evaluation of the photo-activation effects on the reactive oxygen species production by $ZnGa_{1.995}Cr_{0.005}O_4$ nanoparticles with *in vivo* models is also an exciting perspective that can open the possibility to a new strategy for photodynamic therapy and cancer treatment.

Despite the great advances in the research of nanomaterials, awesome mysteries of the nanoworld remain unexplored, and we are susceptible to be impressed by it...

REFERENCES

1. Byrne, W.L., et al., *Use of optical imaging to progress novel therapeutics to the clinic.* Journal of Controlled Release, 2013. **172**(2): p. 523-534.

2. Rudin, M. and R. Weissleder, *Molecular imaging in drug discovery and development.* Nat Rev Drug Discov, 2003. **2**(2): p. 123-131.

3. Massoud, T.F. and S.S. Gambhir, *Molecular imaging in living subjects: seeing fundamental biological processes in a new light.* Genes Dev, 2003. **17**(5): p. 545-80.

4. Weissleder, R., *Molecular imaging in cancer.* Science, 2006. **312**(5777): p. 1168-1171.

5. Weissleder, R., *A clearer vision for in vivo imaging.* Nat Biotechnol, 2001. **19**(4): p. 316-7.

6. Koba, W., et al., *Imaging devices for use in small animals.* Semin Nucl Med, 2011. **41**(3): p. 151-65.

7. Maldiney, T., et al., *In Vitro Targeting of Avidin-Expressing Glioma Cells with Biotinylated Persistent Luminescence Nanoparticles.* Bioconjugate Chemistry, 2012. **23**(3): p. 472-478.

8. VMCHLab. *http://www.wichlab.com/research/*. 2016 [cited 2016.

9. Banterle, N. and E.A. Lemke, *Nanoscale devices for linkerless long-term single-molecule observation.* Curr Opin Biotechnol, 2016. **39**: p. 105-112.

10. Zarschler, K., et al., *Ultrasmall inorganic nanoparticles: state-of-the-art and perspectives for biomedical applications.* Nanomedicine: Nanotechnology, Biology and Medicine.

11. Quek, C.-H. and K.W. Leong, *Near-Infrared Fluorescent Nanoprobes for in Vivo Optical Imaging.* Nanomaterials, 2012. **2**(2): p. 92.

12. Wolfbeis, O.S., *An overview of nanoparticles commonly used in fluorescent bioimaging.* Chemical Society Reviews, 2015. **44**(14): p. 4743-4768.

13. Richard, C., et al., *Persistent Luminescence Nanoparticles for Bioimaging*, in *Advances in Bio-Imaging: From Physics to Signal Understanding Issues*, N. Loménie, D. Racoceanu, and A. Gouaillard, Editors. 2012, Springer Berlin Heidelberg. p. 37-53.

14. de Chermont, Q.L., et al., *Nanoprobes with near-infrared persistent luminescence for in vivo imaging.* Proceedings of the National Academy of Sciences of the United States of America, 2007. **104**(22): p. 9266-9271.

15. Yu, M., et al., *Citrate-gel synthesis and luminescent properties of $ZnGa_2O_4$ doped with Mn^{2+} and Eu^{3+}.* Materials Letters, 2002. **56**(6): p. 1007-1013.

16. le Masne de Chermont, Q., et al., *Silicates doped with luminescent ions: useful tools for optical imaging applications*, in *Colloidal Quantum Dots for Biomedical Applications IV*2009, Proc. of SPIE. p. 1-9.

17. Jorma, H., *Persistent Luminescence Beats the Afterglow: 400 Years of Persistent Luminescence.* The electrochemical society Infera, 2009(Winter): p. 42-45.

18. Harvey, E.N., *A history of luminescence from the earliest times until 1900*. 1957, Philadelphia: American Philosophical Society.

19. Matsuzawa, T., et al., *A new long phosphorescent phosphor with high brightness, $SrAl_2O_4:Eu^{2+},Dy^{3+}$.* Journal of the Electrochemical Society, 1996. **118**: p. 930-933.

20. Van den Eeckhout, K., D. Poelman, and P. Smet, *Persistent Luminescence in Non-Eu2+-Doped Compounds: A Review.* Materials, 2013. **6**(7): p. 2789.

21. Viana, B., et al., *Long term in vivo imaging with Cr3+ doped spinel nanoparticles exhibiting persistent luminescence.* Journal of Luminescence.

22. Liu, Y.L., B.F. Lei, and C.S. Shi, *Luminescent properties of a white afterglow phosphor $CdSiO_3 : Dy^{3+}$.* Chemistry of Materials, 2005. **17**(8): p. 2108-2113.

23. Maldiney, T., et al., *Controlling Electron Trap Depth To Enhance Optical Properties of Persistent Luminescence Nanoparticles for In Vivo Imaging.* Journal of the American Chemical Society, 2011. **133**(30): p. 11810-11815.

24. Viana, B., et al., *Long term in vivo imaging with Cr3+ doped spinel nanoparticles exhibiting persistent luminescence.* Journal of Luminescence, 2016. **170, Part 3**: p. 879-887.

25. Aitasalo, T., et al., *Persistent luminescence of Eu^{2+} and Na^+ doped alkaline earth aluminates.* Radiation Effects and Defects in Solids, 2003. **158**(1-6): p. 89-96.

26. Pedroza-Montero, M., et al., *Dose effects on the long persistent luminescence properties of beta irradiated $SrAl_2O_4$:Eu^{2+}, Dy^{3+} phosphor.* Radiation Measurements, 2010. **45**(3-6): p. 311-313.

27. Castano, A.P., T.N. Demidova, and M.R. Hamblin, *Mechanisms in photodynamic therapy: part one—photosensitizers, photochemistry and cellular localization.* Photodiagnosis and Photodynamic Therapy, 2004. **1**(4): p. 279-293.

28. Shi, Q., et al., *Luminescence of Cr^{3+}-doped $ZnGa_2O_4$ thin films deposited by pulsed laser ablation.* Thin Solid Films, 2012. **520**(23): p. 6845-6849.

29. Bessiere, A., et al., *ZnGa2O4:Cr3+: a new red long-lasting phosphor with high brightness.* Optics Express, 2011. **19**(11): p. 10131-10137.

30. Kim, J.S., et al., *The origin of emission color of reduced and oxidized ZnGa2O4 phosphors.* Solid State Communications, 2004. **129**(3): p. 163-167.

31. Wu, S.H. and H.C. Cheng, *Preparation and characterization of nanosized $ZnGa_2O_4$ phosphors.* Journal of the Electrochemical Society, 2004. **151**(7): p. H159-H163.

32. Hirano, M., *Hydrothermal Synthesis and Characterization of $ZnGa_2O_4$ Spinel Fine Particles.* J. Mater. Chem., 2000. **10**(2): p. 469-472.

33. Maldiney, T., et al., *The in vivo activation of persistent nanophosphors for optical imaging of vascularization, tumours and grafted cells.* Nat Mater, 2014. **13**(4): p. 418-426.

34. Bessière, A., et al., *Storage of Visible Light for Long-Lasting Phosphorescence in Chromium-Doped Zinc Gallate.* Chemistry of Materials, 2014. **26**(3): p. 1365-1373.

35. Mikenda, W., *N-lines in the luminescence spectra of Cr3+ -doped spinels (III) partial spectra.* Journal of Luminescence, 1981. **26**(1–2): p. 85-98.

36. Nie, W., et al., *New results on optical properties and term-energy calculations in Cr3+-doped ZnAl2O4.* Journal of Luminescence, 1990. **46**(3): p. 177-190.

37. Maldiney, T., et al., *Controlling aminosilane layer thickness to extend the plasma half-life of stealth persistent luminescence nanoparticles in vivo.* Journal of Materials Chemistry B, 2015.

38. Chen, Z.G., et al., *Versatile synthesis strategy for carboxylic acid-functionalized upconverting nanophosphors as biological labels.* Journal of the American Chemical Society, 2008. **130**(10): p. 3023-3029.

39. Xiong, L.Q., et al., *Synthesis, characterization, and in vivo targeted imaging of amine-functionalized rare-earth up-converting nanophosphors.* Biomaterials, 2009. **30**(29): p. 5592-600.

40. Erathodiyil, N. and J.Y. Ying, *Functionalization of inorganic nanoparticles for bioimaging applications.* Acc Chem Res, 2011. **44**(10): p. 925-35.

41. Maldonado, C.R., et al., *Nano-functionalization of metal complexes for molecular imaging and anticancer therapy.* Coordination Chemistry Reviews, 2013. **257**(19–20): p. 2668-2688.

42. Duchêne, D. and R. Gref, *Small is beautiful: Surprising nanoparticles.* International Journal of Pharmaceutics, 2016. **502**(1–2): p. 219-231.

43. Gu, H.W., et al., *Study of amino-functionalized mesoporous silica nanoparticles (NH2-MSN) and polyamide-6 nanocomposites co-incorporated with NH2-MSN and organo-montmorillonite.* Microporous and Mesoporous Materials, 2013. **170**: p. 226-234.

44. Maldiney, T., et al., *Effect of Core Diameter, Surface Coating, and PEG Chain Length on the Biodistribution of Persistent Luminescence Nanoparticles in Mice.* Acs Nano, 2011. **5**(2): p. 854-862.

45. Bazak, R., et al., *Cancer active targeting by nanoparticles: a comprehensive review of literature.* J Cancer Res Clin Oncol, 2015. **141**(5): p. 769-84.

46. Bertrand, N., et al., *Cancer nanotechnology: the impact of passive and active targeting in the era of modern cancer biology.* Adv Drug Deliv Rev, 2014. **66**: p. 2-25.

47. Nakamura, H., F. Jun, and H. Maeda, *Development of next-generation macromolecular drugs based on the EPR effect: challenges and pitfalls.* Expert Opin Drug Deliv, 2015. **12**(1): p. 53-64.

48. Iyer, A.K., et al., *Exploiting the enhanced permeability and retention effect for tumor targeting.* Drug Discovery Today, 2006. **11**(17–18): p. 812-818.

49. Yamashita, F. and M. Hashida, *Pharmacokinetic considerations for targeted drug delivery.* Advanced Drug Delivery Reviews, 2013. **65**(1): p. 139-147.

50. Kamaly, N., et al., *Targeted polymeric therapeutic nanoparticles: design, development and clinical translation.* Chemical Society Reviews, 2012. **41**(7): p. 2971-3010.

51. Byrne, J.D., T. Betancourt, and L. Brannon-Peppas, *Active targeting schemes for nanoparticle systems in cancer therapeutics.* Advanced Drug Delivery Reviews, 2008. **60**(15): p. 1615-1626.

52. Arppe, R., et al., *Photon upconversion sensitized nanoprobes for sensing and imaging of pH.* Nanoscale, 2014. **6**(12): p. 6837-6843.

53. Wang, X.-d. and O.S. Wolfbeis, *Optical methods for sensing and imaging oxygen: materials, spectroscopies and applications.* Chemical Society Reviews, 2014. **43**(10): p. 3666-3761.

54. Yang, L., et al., *Luminescent Ru(bpy)3 2+-doped silica nanoparticles for imaging of intracellular temperature.* Microchimica Acta, 2013. **181**(7): p. 743-749.

55. Love, S.A., et al., *Assessing nanoparticle toxicity.* Annu Rev Anal Chem (Palo Alto Calif), 2012. **5**: p. 181-205.

56. Cheng, C.J., et al., *A holistic approach to targeting disease with polymeric nanoparticles.* Nat Rev Drug Discov, 2015. **14**(4): p. 239-247.

57. Bednarski, M., et al., *The influence of the route of administration of gold nanoparticles on their tissue distribution and basic biochemical parameters: In vivo studies.* Pharmacological Reports, 2015. **67**(3): p. 405-409.

58. Li, S.D. and L. Huang, *Pharmacokinetics and biodistribution of nanoparticles.* Mol Pharm, 2008. **5**(4): p. 496-504.

59. Surugau, N. and P.L. Urban, *Electrophoretic methods for separation of nanoparticles.* J Sep Sci, 2009. **32**(11): p. 1889-906.

60. Monopoli, M.P., et al., *Biomolecular coronas provide the biological identity of nanosized materials.* Nat Nano, 2012. **7**(12): p. 779-786.

61. Saptarshi, S.R., A. Duschl, and A.L. Lopata, *Interaction of nanoparticles with proteins: relation to bio-reactivity of the nanoparticle.* J Nanobiotechnology, 2013. **11**: p. 26.

62. Nel, A.E., et al., *Understanding biophysicochemical interactions at the nano-bio interface.* Nat Mater, 2009. **8**(7): p. 543-557.

63. Walkey, C.D. and W.C. Chan, *Understanding and controlling the interaction of nanomaterials with proteins in a physiological environment.* Chem Soc Rev, 2012. **41**(7): p. 2780-99.

64. Walkey, C.D., et al., *Nanoparticle Size and Surface Chemistry Determine Serum Protein Adsorption and Macrophage Uptake.* Journal of the American Chemical Society, 2012. **134**(4): p. 2139-2147.

65. Gunawan, C., et al., *Nanoparticle-protein corona complexes govern the biological fates and functions of nanoparticles.* Journal of Materials Chemistry B, 2014. **2**(15): p. 2060-2083.

66. Kim, H.R., et al., *Analysis of plasma protein adsorption onto PEGylated nanoparticles by complementary methods: 2-DE, CE and Protein Lab-on-chip system.* Electrophoresis, 2007. **28**(13): p. 2252-61.

67. Brambilla, D., et al., *New method based on capillary electrophoresis with laser-induced fluorescence detection (CE-LIF) to monitor interaction between nanoparticles and the amyloid-beta peptide.* Anal Chem, 2010. **82**(24): p. 10083-9.

68. Andrieux, K. and P. Couvreur, *Polyalkylcyanoacrylate nanoparticles for delivery of drugs across the blood-brain barrier.* Wiley Interdiscip Rev Nanomed Nanobiotechnol, 2009. **1**(5): p. 463-74.

69. Kim, H.R., et al., *Translocation of poly(ethylene glycol-co-hexadecyl)cyanoacrylate nanoparticles into rat brain endothelial cells: role of apolipoproteins in receptor-mediated endocytosis.* Biomacromolecules, 2007. **8**(3): p. 793-9.

70. Lesniak, A., et al., *Effects of the presence or absence of a protein corona on silica nanoparticle uptake and impact on cells.* ACS Nano, 2012. **6**(7): p. 5845-57.

71. Iversen, T.-G., T. Skotland, and K. Sandvig, *Endocytosis and intracellular transport of nanoparticles: Present knowledge and need for future studies.* Nano Today, 2011. **6**(2): p. 176-185.

72. Zhao, F., et al., *Cellular uptake, intracellular trafficking, and cytotoxicity of nanomaterials.* Small, 2011. **7**(10): p. 1322-37.

73. Verma, A. and F. Stellacci, *Effect of surface properties on nanoparticle-cell interactions.* Small, 2010. **6**(1): p. 12-21.

74. Conner, S.D. and S.L. Schmid, *Regulated portals of entry into the cell.* Nature, 2003. **422**(6927): p. 37-44.

75. Ishimoto, H., et al., *Single-cell observation of phagocytosis by human blood dendritic cells.* Jpn J Infect Dis, 2008. **61**(4): p. 294-7.

76. Liu, Y., et al., *The effect of Gd@C82(OH)22 nanoparticles on the release of Th1/Th2 cytokines and induction of TNF-alpha mediated cellular immunity.* Biomaterials, 2009. **30**(23-24): p. 3934-45.

77. Wei, L., et al., *The translocation of fullerenic nanoparticles into lysosome via the pathway of clathrin-mediated endocytosis.* Nanotechnology, 2008. **19**(14): p. 145102.

78. Harush-Frenkel, O., et al., *Targeting of nanoparticles to the clathrin-mediated endocytic pathway.* Biochem Biophys Res Commun, 2007. **353**(1): p. 26-32.

79. Harush-Frenkel, O., et al., *Surface charge of nanoparticles determines their endocytic and transcytotic pathway in polarized MDCK cells.* Biomacromolecules, 2008. **9**(2): p. 435-43.

80. Rappoport, J.Z., *Focusing on clathrin-mediated endocytosis.* Biochem J, 2008. **412**(3): p. 415-23.

81. Kirkham, M. and R.G. Parton, *Clathrin-independent endocytosis: new insights into caveolae and non-caveolar lipid raft carriers.* Biochim Biophys Acta, 2005. **1745**(3): p. 273-86.

82. McIntosh, D.P., et al., *Targeting endothelium and its dynamic caveolae for tissue-specific transcytosis in vivo: a pathway to overcome cell barriers to drug and gene delivery.* Proc Natl Acad Sci U S A, 2002. **99**(4): p. 1996-2001.

83. Contreras, J., et al., *Intracellular uptake and trafficking of difluoroboron dibenzoylmethane-polylactide nanoparticles in HeLa cells.* ACS Nano, 2010. **4**(5): p. 2735-47.

84. Partlow, K.C., G.M. Lanza, and S.A. Wickline, *Exploiting lipid raft transport with membrane targeted nanoparticles: a strategy for cytosolic drug delivery.* Biomaterials, 2008. **29**(23): p. 3367-75.

85. Wang, Z., et al., *Size and dynamics of caveolae studied using nanoparticles in living endothelial cells.* ACS Nano, 2009. **3**(12): p. 4110-6.

86. Choi, H.S. and J.V. Frangioni, *Nanoparticles for biomedical imaging: fundamentals of clinical translation.* Mol Imaging, 2010. **9**(6): p. 291-310.

87. Tan, S.J., et al., *Surface-Ligand-Dependent Cellular Interaction, Subcellular Localization, and Cytotoxicity of Polymer-Coated Quantum Dots.* Chemistry of Materials, 2010. **22**(7): p. 2239-2247.

88. Bozich, J.S., et al., *Surface chemistry, charge and ligand type impact the toxicity of gold nanoparticles to Daphnia magna.* Environmental Science: Nano, 2014. **1**(3): p. 260-270.

89. Gratton, S.E., et al., *The effect of particle design on cellular internalization pathways.* Proc Natl Acad Sci U S A, 2008. **105**(33): p. 11613-8.

90. Zhang, L.W. and N.A. Monteiro-Riviere, *Mechanisms of quantum dot nanoparticle cellular uptake.* Toxicol Sci, 2009. **110**(1): p. 138-55.

91. Lewinski, N., V. Colvin, and R. Drezek, *Cytotoxicity of nanoparticles.* Small, 2008. **4**(1): p. 26-49.

92. Zhang, F., et al., *Ion and pH sensing with colloidal nanoparticles: influence of surface charge on sensing and colloidal properties.* Chemphyschem, 2010. **11**(3): p. 730-5.

93. See, V., et al., *Cathepsin L digestion of nanobioconjugates upon endocytosis.* ACS Nano, 2009. **3**(9): p. 2461-8.

94. Soenen, S.J., et al., *Cellular toxicity of inorganic nanoparticles: Common aspects and guidelines for improved nanotoxicity evaluation.* Nano Today, 2011. **6**(5): p. 446-465.

95. Diaz, B., et al., *Assessing methods for blood cell cytotoxic responses to inorganic nanoparticles and nanoparticle aggregates.* Small, 2008. **4**(11): p. 2025-34.

96. Nel, A., et al., *Toxic potential of materials at the nanolevel.* Science, 2006. **311**(5761): p. 622-7.

97. Xia, T., N. Li, and A.E. Nel, *Potential health impact of nanoparticles.* Annu Rev Public Health, 2009. **30**: p. 137-50.

98. Pisanic T.R., J.S., Shubayev V.I., , *Nanotoxicity: From in vivo and in vitro models to health risks*. 2009, London: John Wiley & Sons, Ltd.

99. Stroh, A., et al., *Iron oxide particles for molecular magnetic resonance imaging cause transient oxidative stress in rat macrophages.* Free Radic Biol Med, 2004. **36**(8): p. 976-84.

100. Jain, T.K., et al., *Biodistribution, clearance, and biocompatibility of iron oxide magnetic nanoparticles in rats.* Mol Pharm, 2008. **5**(2): p. 316-27.

101. Soto, K., K.M. Garza, and L.E. Murr, *Cytotoxic effects of aggregated nanomaterials.* Acta Biomater, 2007. **3**(3): p. 351-8.

102. Soenen, S.J., et al., *The role of nanoparticle concentration-dependent induction of cellular stress in the internalization of non-toxic cationic magnetoliposomes.* Biomaterials, 2009. **30**(36): p. 6803-13.

103. Soenen, S.J., et al., *High intracellular iron oxide nanoparticle concentrations affect cellular cytoskeleton and focal adhesion kinase-mediated signaling.* Small, 2010. **6**(7): p. 832-42.

104. Wu, X., et al., *Toxic effects of iron oxide nanoparticles on human umbilical vein endothelial cells.* Int J Nanomedicine, 2010. **5**: p. 385-99.

105. Singh, N., et al., *NanoGenotoxicology: the DNA damaging potential of engineered nanomaterials.* Biomaterials, 2009. **30**(23-24): p. 3891-914.

106. Pisanic, T.R., 2nd, et al., *Nanotoxicity of iron oxide nanoparticle internalization in growing neurons.* Biomaterials, 2007. **28**(16): p. 2572-81.

107. Soenen, S.J., et al., *Intracellular nanoparticle coating stability determines nanoparticle diagnostics efficacy and cell functionality.* Small, 2010. **6**(19): p. 2136-45.

108. Miller, I.S., et al., *Surface-induced cell signaling events control actin rearrangements and motility.* J Biomed Mater Res A, 2010. **93**(2): p. 493-504.

109. Kedziorek, D.A., et al., *Gene expression profiling reveals early cellular responses to intracellular magnetic labeling with superparamagnetic iron oxide nanoparticles.* Magn Reson Med, 2010. **63**(4): p. 1031-43.

110. Lunov, O., et al., *Lysosomal degradation of the carboxydextran shell of coated superparamagnetic iron oxide nanoparticles and the fate of professional phagocytes.* Biomaterials, 2010. **31**(34): p. 9015-22.

111. Mahendra, S., et al., *Quantum Dot Weathering Results in Microbial Toxicity.* Environmental Science & Technology, 2008. **42**(24): p. 9424-9430.

112. Mancini, M.C., et al., *Oxidative Quenching and Degradation of Polymer-Encapsulated Quantum Dots: New Insights into the Long-Term Fate and Toxicity of Nanocrystals in Vivo.* Journal of the American Chemical Society, 2008. **130**(33): p. 10836-10837.

113. Gagné, F., et al., *Cytotoxicity of aged cadmium-telluride quantum dots to rainbow trout hepatocytes.* Nanotoxicology, 2008. **2**(3): p. 113-120.

114. Wiogo, H.T., et al., *Stabilization of magnetic iron oxide nanoparticles in biological media by fetal bovine serum (FBS).* Langmuir, 2011. **27**(2): p. 843-50.

115. Yen, H.J., S.H. Hsu, and C.L. Tsai, *Cytotoxicity and immunological response of gold and silver nanoparticles of different sizes.* Small, 2009. **5**(13): p. 1553-61.

116. Lin, J., et al., *Penetration of lipid membranes by gold nanoparticles: insights into cellular uptake, cytotoxicity, and their relationship.* ACS Nano, 2010. **4**(9): p. 5421-9.

117. Johannsen, M., et al., *Magnetic nanoparticle hyperthermia for prostate cancer.* Int J Hyperthermia, 2010. **26**(8): p. 790-5.

118. Schafer, R., et al., *Functional investigations on human mesenchymal stem cells exposed to magnetic fields and labeled with clinically approved iron nanoparticles.* BMC Cell Biol, 2010. **11**: p. 22.

119. Mortensen, L.J., et al., *In vivo skin penetration of quantum dot nanoparticles in the murine model: the effect of UVR.* Nano Lett, 2008. **8**(9): p. 2779-87.

120. Samia, A.C.S., X. Chen, and C. Burda, *Semiconductor Quantum Dots for Photodynamic Therapy.* Journal of the American Chemical Society, 2003. **125**(51): p. 15736-15737.

121. Radomska, A., J. Leszczyszyn, and M.W. Radomski, *The Nanopharmacology and Nanotoxicology of Nanomaterials: New Opportunities and Challenges.* Adv Clin Exp Med, 2016. **25**(1): p. 151-62.

122. Erbis, S., et al., *Review of Research Trends and Methods in Nano Environmental, Health, and Safety Risk Analysis.* Risk Anal, 2016.

123. Bitounis, D., et al., *Detection and analysis of nanoparticles in patients: A critical review of the status quo of clinical nanotoxicology.* Biomaterials, 2016. **76**: p. 302-12.

124. Azhdarzadeh, M., et al., *Nanotoxicology: advances and pitfalls in research methodology.* Nanomedicine (Lond), 2015. **10**(18): p. 2931-52.

125. Soo Choi, H., et al., *Renal clearance of quantum dots.* Nat Biotech, 2007. **25**(10): p. 1165-1170.

126. Wang, B., et al., *Metabolism of nanomaterials in vivo: blood circulation and organ clearance.* Acc Chem Res, 2013. **46**(3): p. 761-9.

127. He, X., et al., *Lung deposition and extrapulmonary translocation of nano-ceria after intratracheal instillation.* Nanotechnology, 2010. **21**(28): p. 285103.

128. Zhu, M.T., et al., *Particokinetics and extrapulmonary translocation of intratracheally instilled ferric oxide nanoparticles in rats and the potential health risk assessment.* Toxicol Sci, 2009. **107**(2): p. 342-51.

129. Geiser, M., *Update on macrophage clearance of inhaled micro- and nanoparticles.* J Aerosol Med Pulm Drug Deliv, 2010. **23**(4): p. 207-17.

130. Alexis, F., et al., *Factors affecting the clearance and biodistribution of polymeric nanoparticles.* Mol Pharm, 2008. **5**(4): p. 505-15.

131. Osmond-McLeod, M.J., et al., *Durability and inflammogenic impact of carbon nanotubes compared with asbestos fibres.* Part Fibre Toxicol, 2011. **8**: p. 15.

132. Liu, J., et al., *Renal clearable inorganic nanoparticles: a new frontier of bionanotechnology.* Materials Today, 2013. **16**(12): p. 477-486.

133. Deen, W.M., M.J. Lazzara, and B.D. Myers, *Structural determinants of glomerular permeability.* Am J Physiol Renal Physiol, 2001. **281**(4): p. F579-96.

134. Yamagishi, Y., et al., *Acute and chronic nephrotoxicity of platinum nanoparticles in mice.* Nanoscale Res Lett, 2013. **8**(1): p. 395.

135. Sebekova, K., et al., *Comprehensive assessment of nephrotoxicity of intravenously administered sodium-oleate-coated ultra-small superparamagnetic iron oxide (USPIO) and titanium dioxide (TiO2) nanoparticles in rats.* Nanotoxicology, 2014. **8**(2): p. 142-57.

136. Sadauskas, E., et al., *Kupffer cells are central in the removal of nanoparticles from the organism.* Part Fibre Toxicol, 2007. **4**: p. 10.

137. Sorensen, K.K., et al., *The scavenger endothelial cell: a new player in homeostasis and immunity.* Am J Physiol Regul Integr Comp Physiol, 2012. **303**(12): p. R1217-30.

138. Bargheer, D., et al., *The distribution and degradation of radiolabeled superparamagnetic iron oxide nanoparticles and quantum dots in mice.* Beilstein J Nanotechnol, 2015. **6**: p. 111-23.

139. Braet, F. and E. Wisse, *Structural and functional aspects of liver sinusoidal endothelial cell fenestrae: a review.* Comp Hepatol, 2002. **1**(1): p. 1.

140. Caballero-Díaz, E., et al., *The Toxicity of Silver Nanoparticles Depends on Their Uptake by Cells and Thus on Their Surface Chemistry.* Particle & Particle Systems Characterization, 2013. **30**(12): p. 1079-1085.

141. Kreyling, W.G., et al., *In vivo integrity of polymer-coated gold nanoparticles.* Nat Nano, 2015. **10**(7): p. 619-623.

142. Kolosnjaj-Tabi, J., et al., *The One Year Fate of Iron Oxide Coated Gold Nanoparticles in Mice.* ACS Nano, 2015. **9**(8): p. 7925-39.

143. Pan, Y., et al., *Gold nanoparticles of diameter 1.4 nm trigger necrosis by oxidative stress and mitochondrial damage.* Small, 2009. **5**(18): p. 2067-76.

144. Panas, A., et al., *Screening of different metal oxide nanoparticles reveals selective toxicity and inflammatory potential of silica nanoparticles in lung epithelial cells and macrophages.* Nanotoxicology, 2013. **7**(3): p. 259-73.

145. Park, E.J. and K. Park, *Oxidative stress and pro-inflammatory responses induced by silica nanoparticles in vivo and in vitro.* Toxicol Lett, 2009. **184**(1): p. 18-25.

146. Sahay, G., D.Y. Alakhova, and A.V. Kabanov, *Endocytosis of nanomedicines.* J Control Release, 2010. **145**(3): p. 182-95.

147.   Wu, L., J. Zhang, and W. Watanabe, *Physical and chemical stability of drug nanoparticles.* Advanced Drug Delivery Reviews, 2011. **63**(6): p. 456-469.

148.   Kim, C.-j., *Advanced pharmaceutics : physicochemical principles*. 2004, Boca Raton, Fla. ; London: CRC.

149.   Van Eerdenbrugh, B., G. Van den Mooter, and P. Augustijns, *Top-down production of drug nanocrystals: Nanosuspension stabilization, miniaturization and transformation into solid products.* International Journal of Pharmaceutics, 2008. **364**(1): p. 64-75.

150.   Patravale, V.B., A.A. Date, and R.M. Kulkarni, *Nanosuspensions: a promising drug delivery strategy.* Journal of Pharmacy and Pharmacology, 2004. **56**(7): p. 827-840.

151.   Yang, W., J.I. Peters, and R.O. Williams, 3rd, *Inhaled nanoparticles--a current review.* Int J Pharm, 2008. **356**(1-2): p. 239-47.

152.   Sung, J.C., B.L. Pulliam, and D.A. Edwards, *Nanoparticles for drug delivery to the lungs.* Trends Biotechnol, 2007. **25**(12): p. 563-70.

153.   Misra, S.K., et al., *The complexity of nanoparticle dissolution and its importance in nanotoxicological studies.* Science of the Total Environment, 2012. **438**: p. 225-232.

154.   Rabinow, B.E., *Nanosuspensions in drug delivery.* Nat Rev Drug Discov, 2004. **3**(9): p. 785-96.

155.   Choi, J.-Y., et al., *Role of polymeric stabilizers for drug nanocrystal dispersions.* Current Applied Physics, 2005. **5**(5): p. 472-474.

156.   Uskokovic, V., et al., *Dynamic light scattering and zeta potential of colloidal mixtures of amelogenin and hydroxyapatite in calcium and phosphate rich ionic milieus.* Archives of Oral Biology, 2011. **56**(6): p. 521-532.

157.   Li, H., et al., *Surface Potential Dependence of the Hamaker Constant.* Journal of Physical Chemistry C, 2009. **113**(11): p. 4419-4425.

158.   Bergman, L., et al., *On the complexity of electrostatic suspension stabilization of functionalized silica nanoparticles for biotargeting and imaging applications.* Journal of Nanomaterials, 2008.

159.   Doane, T.L., et al., *Nanoparticle ζ -Potentials.* Accounts of Chemical Research, 2012. **45**(3): p. 317-326.

160.   Kosmulski, M., *pH-dependent surface charging and points of zero charge. IV. Update and new approach.* Journal of Colloid and Interface Science, 2009. **337**(2): p. 439-448.

161.   Kaasalainen, M., et al., *Effect of isotonic solutions and peptide adsorption on zeta potential of porous silicon nanoparticle drug delivery formulations.* International Journal of Pharmaceutics, 2012. **431**(1-2): p. 230-236.

162.   Rosenholm, J.M. and M. Linden, *Wet-chemical analysis of surface concentration of accessible groups on different amino-functionalized mesoporous SBA-15 silicas.* Chemistry of Materials, 2007. **19**(20): p. 5023-5034.

163.   Hirn, S., et al., *Particle size-dependent and surface charge-dependent biodistribution of gold nanoparticles after intravenous administration.* European Journal of Pharmaceutics and Biopharmaceutics, 2011. **77**(3): p. 407-416.

164.   Delgado, A.V., et al., *Measurement and interpretation of electrokinetic phenomena.* Journal of Colloid and Interface Science, 2007. **309**(2): p. 194-224.

165.   Pyell, U., et al., *Characterization of gold nanoparticles with different hydrophilic coatings via capillary electrophoresis and Taylor dispersion analysis. Part I: determination of the zeta potential employing a modified analytic approximation.* J Colloid Interface Sci, 2015. **450**: p. 288-300.

166.   Montoro Bustos, A.R., J. Ruiz Encinar, and A. Sanz-Medel, *Mass spectrometry for the characterisation of nanoparticles.* Anal Bioanal Chem, 2013. **405**(17): p. 5637-43.

167. Trapiella-Alfonso, L., et al., *Chapter 8 - Mass Spectrometry for the Characterization of Gold Nanoparticles*, in *Comprehensive Analytical Chemistry*, V. Miguel and I.L.-L. Ángela, Editors. 2014, Elsevier. p. 329-356.

168. Maiolo, D., et al., *Nanomedicine delivery: does protein corona route to the target or off road?* Nanomedicine (Lond), 2015. **10**(21): p. 3231-47.

169. Aleksenko, S.S., et al., *Interactions of tumour-targeting nanoparticles with proteins: potential of using capillary electrophoresis as a direct probe.* Metallomics, 2012. **4**(11): p. 1141-8.

170. Lapresta-Fernández, A., et al., *A General Perspective of the Characterization and Quantification of Nanoparticles: Imaging, Spectroscopic, and Separation Techniques.* Critical Reviews in Solid State and Materials Sciences, 2014. **39**(6): p. 423-458.

171. Laborda, F., et al., *Detection, characterization and quantification of inorganic engineered nanomaterials: A review of techniques and methodological approaches for the analysis of complex samples.* Anal Chim Acta, 2016. **904**: p. 10-32.

172. Lopez-Serrano, A., et al., *Nanoparticles: a global vision. Characterization, separation, and quantification methods. Potential environmental and health impact.* Analytical Methods, 2014. **6**(1): p. 38-56.

173. Ban, E., Y.S. Yoo, and E.J. Song, *Analysis and applications of nanoparticles in capillary electrophoresis.* Talanta, 2015. **141**: p. 15-20.

174. Hoo, C.M., et al., *A comparison of atomic force microscopy (AFM) and dynamic light scattering (DLS) methods to characterize nanoparticle size distributions.* Journal of Nanoparticle Research, 2008. **10**(1): p. 89-96.

175. Sapsford, K.E., et al., *Analyzing Nanomaterial Bioconjugates: A Review of Current and Emerging Purification and Characterization Techniques.* Analytical Chemistry, 2011. **83**(12): p. 4453-4488.

176. Brar, S.K. and M. Verma, *Measurement of nanoparticles by light-scattering techniques.* TrAC Trends in Analytical Chemistry, 2011. **30**(1): p. 4-17.

177. Somers, R.C., M.G. Bawendi, and D.G. Nocera, *CdSe nanocrystal based chem-/bio-sensors.* Chemical Society Reviews, 2007. **36**(4): p. 579-591.

178. Pons, T., et al., *Hydrodynamic dimensions, electrophoretic mobility, and stability of hydrophilic quantum dots.* Journal of Physical Chemistry B, 2006. **110**(41): p. 20308-20316.

179. Espada, A. and M. Molina-Martin, *Capillary electrophoresis and small molecule drug discovery: a perfect match?* Drug Discov Today, 2012. **17**(7-8): p. 396-404.

180. Mischak, H., et al., *Capillary electrophoresis-mass spectrometry as a powerful tool in biomarker discovery and clinical diagnosis: an update of recent developments.* Mass Spectrom Rev, 2009. **28**(5): p. 703-24.

181. Altria, K.D., M.A. Kelly, and B.J. Clark, *Current applications in the analysis of pharmaceuticals by capillary electrophoresis. I.* Trac-Trends in Analytical Chemistry, 1998. **17**(4): p. 204-214.

182. Harstad, R.K., et al., *Capillary Electrophoresis.* Analytical Chemistry, 2016. **88**(1): p. 299-319.

183. Brambilla, D., et al., *PEGylated Nanoparticles Bind to and Alter Amyloid-Beta Peptide Conformation: Toward Engineering of Functional Nanomedicines for Alzheimer's Disease.* ACS Nano, 2012. **6**(7): p. 5897-5908.

184. Song, X., et al., *Highly efficient size separation of CdTe quantum dots by capillary gel electrophoresis using polymer solution as sieving medium.* ELECTROPHORESIS, 2006. **27**(7): p. 1341-1346.

185. Rudnev, A.V., et al., *Characterization of calcium hydroxyapatite polycrystalline nanoparticles by capillary zone electrophoresis and scanning electron microscopy.* Journal of Analytical Chemistry, 2012. **67**(6): p. 565-571.

186. Krupke, R., et al., *Separation of metallic from semiconducting single-walled carbon nanotubes.* Science, 2003. **301**(5631): p. 344-347.

187. Radko, S.P. and A. Chrambach, *Separation and characterization of sub-mu m- and mu m-sized particles by capillary zone electrophoresis.* Electrophoresis, 2002. **23**(13): p. 1957-1972.

188. Lopez-Lorente, A.I., B.M. Simonet, and M. Valcarcel, *Electrophoretic methods for the analysis of nanoparticles.* Trac-Trends in Analytical Chemistry, 2011. **30**(1): p. 58-71.

189. Winzor, D.J., *Determination of binding constants by affinity chromatography.* Journal of Chromatography A, 2004. **1037**(1–2): p. 351-367.

190. Heegaard, N.H.H., *Applications of affinity interactions in capillary electrophoresis.* Electrophoresis, 2003. **24**(22-23): p. 3879-3891.

191. Desai, M.J. and D.W. Armstrong, *Separation, identification, and characterization of microorganisms by capillary electrophoresis.* Microbiol Mol Biol Rev, 2003. **67**(1): p. 38-51, table of contents.

192. Trapiella-Alfonso, L., F. d'Orlyé, and A. Varenne, *Recent advances in the development of capillary electrophoresis methodologies for optimizing, controlling, and characterizing the synthesis, functionalization, and physicochemical, properties of nanoparticles.* Analytical and Bioanalytical Chemistry, 2016: p. 1-7.

193. Ramirez-Garcia, G., et al., *Functionalization and characterization of persistent luminescence nanoparticles by dynamic light scattering, laser Doppler and capillary electrophoresis.* Colloids Surf B Biointerfaces, 2015. **136**: p. 272-281.

194. Carrillo-Carrion, C., et al., *Capillary electrophoresis method for the characterization and separation of CdSe quantum dots.* Anal Chem, 2011. **83**(7): p. 2807-13.

195. Pyell, U., *Characterization of nanoparticles by capillary electromigration separation techniques.* Electrophoresis, 2010. **31**(5): p. 814-31.

196. Ohshima, H., *Approximate Analytic Expression for the Electrophoretic Mobility of a Spherical Colloidal Particle.* J Colloid Interface Sci, 2001. **239**(2): p. 587-590.

197. Ibrahim, A., et al., *Determination of effective charge of small ions, polyelectrolytes and nanoparticles by capillary electrophoresis.* J Chromatogr A, 2012. **1247**: p. 154-64.

198. Taylor, G., *Dispersion of Soluble Matter in Solvent Flowing Slowly through a Tube.* Proceedings of the Royal Society of London A: Mathematical, Physical and Engineering Sciences, 1953. **219**(1137): p. 186-203.

199. Saux, T.L. and H. Cottet, *Size-based characterization by the coupling of capillary electrophoresis to Taylor dispersion analysis.* Anal Chem, 2008. **80**(5): p. 1829-32.

200. Oukacine, F., et al., *Physico-chemical characterization of polymeric micelles loaded with platinum derivatives by capillary electrophoresis and related methods.* J Control Release, 2014. **196**: p. 139-45.

201. Pyell, U., *CE characterization of semiconductor nanocrystals encapsulated with amorphous silicium dioxide.* Electrophoresis, 2008. **29**(3): p. 576-89.

202. Boulos, S.P., et al., *Nanoparticle-protein interactions: a thermodynamic and kinetic study of the adsorption of bovine serum albumin to gold nanoparticle surfaces.* Langmuir, 2013. **29**(48): p. 14984-96.

203. d'Orlye, F., A. Varenne, and P. Gareil, *Size-based characterization of nanometric cationic maghemite particles using capillary zone electrophoresis.* Electrophoresis, 2008. **29**(18): p. 3768-78.

204. Pyell, U., et al., *Characterization of hydrophilic coated gold nanoparticles via capillary electrophoresis and Taylor dispersion analysis. Part II: Determination of the hydrodynamic radius distribution - Comparison with asymmetric flow field-flow fractionation.* J Colloid Interface Sci, 2015. **457**: p. 131-40.

205. López-Lorente, Á.I., M.L. Soriano, and M. Valcárcel, *Analysis of citrate-capped gold and silver nanoparticles by thiol ligand exchange capillary electrophoresis.* Microchimica Acta, 2014. **181**(15): p. 1789-1796.

206. Franze, B. and C. Engelhard, *Fast separation, characterization, and speciation of gold and silver nanoparticles and their ionic counterparts with micellar electrokinetic chromatography coupled to ICP-MS.* Anal Chem, 2014. **86**(12): p. 5713-20.

207. Qu, H., T.K. Mudalige, and S.W. Linder, *Capillary Electrophoresis/Inductively-Coupled Plasma-Mass Spectrometry: Development and Optimization of a High Resolution Analytical Tool for the Size-Based Characterization of Nanomaterials in Dietary Supplements.* Analytical Chemistry, 2014. **86**(23): p. 11620-11627.

208. Liu, L., et al., *Identification and accurate size characterization of nanoparticles in complex media.* Angew Chem Int Ed Engl, 2014. **53**(52): p. 14476-9.

209. Li, L., et al., *A novel dark-field microscopy technique coupled with capillary electrophoresis for visual analysis of single nanoparticles.* Analyst, 2013. **138**(13): p. 3705-10.

210. Bouri, M., et al., *A novel approach to size separation of gold nanoparticles by capillary electrophoresis-evaporative light scattering detection.* RSC Advances, 2015. **5**(22): p. 16672-16677.

211. Stanisavljevic, M., et al., *Capillary electrophoresis of quantum dots: minireview.* Electrophoresis, 2014. **35**(14): p. 1929-37.

212. Sang, F., X. Huang, and J. Ren, *Characterization and separation of semiconductor quantum dots and their conjugates by capillary electrophoresis.* Electrophoresis, 2014. **35**(6): p. 793-803.

213. Voracova, I., et al., *Determination of zeta-potential, charge, and number of organic ligands on the surface of water soluble quantum dots by capillary electrophoresis.* Electrophoresis, 2015. **36**(6): p. 867-74.

214. McCormick, R.M., *Characterization of Silica Sols Using Capillary Zone Electrophoresis.* Journal of Liquid Chromatography, 1991. **14**(5): p. 939-952.

215. Vanifatova, N.G., et al., *Investigation of iron oxide nanoparticles by capillary zone electrophoresis.* Talanta, 2005. **66**(3): p. 605-610.

216. Hu, Q., et al., *Capillary electrophoretic study of amine/carboxylic acid-functionalized carbon nanodots.* J Chromatogr A, 2013. **1304**: p. 234-40.

217. Duffy, E., et al., *Separation and characterisation of detonation nanodiamond by capillary zone electrophoresis.* Electrophoresis, 2014. **35**(12-13): p. 1864-72.

218. Astefanei, A., et al., *Aggregation behavior of fullerenes in aqueous solutions: a capillary electrophoresis and asymmetric flow field-flow fractionation study.* Anal Bioanal Chem, 2015. **407**(26): p. 8035-45.

219. Astefanei, A., O. Nunez, and M.T. Galceran, *Characterisation and determination of fullerenes: A critical review.* Anal Chim Acta, 2015. **882**: p. 1-21.

220. Ibrahim, A., et al., *Size and charge characterization of polymeric drug delivery systems by Taylor dispersion analysis and capillary electrophoresis.* Anal Bioanal Chem, 2013. **405**(16): p. 5369-79.

221. Liu, T., et al., *Monitoring surface functionalization of dendrigraft poly-L-lysines via click chemistry by capillary electrophoresis and Taylor dispersion analysis.* J Chromatogr A, 2013. **1273**: p. 111-6.

222. Oukacine, F., et al., *Size-based characterization of nanoparticle mixtures by the inline coupling of capillary electrophoresis to Taylor dispersion analysis.* J Chromatogr A, 2015. **1426**: p. 220-5.

223. Franzen, U. and J. Østergaard, *Physico-chemical characterization of liposomes and drug substance–liposome interactions in pharmaceutics using capillary electrophoresis and electrokinetic chromatography.* Journal of Chromatography A, 2012. **1267**(0): p. 32-44.

224. You, J., et al., *Quaternized cellulose-supported gold nanoparticles as capillary coatings to enhance protein separation by capillary electrophoresis.* Journal of Chromatography A, 2014. **1343**: p. 160-166.

225. Wang, X., et al., *Determination of ascorbic acid in individual liver cancer cells by capillary electrophoresis with a platinum nanoparticles modified electrode.* Journal of Electroanalytical Chemistry, 2014. **712**: p. 139-145.

226. Gong, Z.-S., L.-P. Duan, and A.-N. Tang, *Amino-functionalized silica nanoparticles for improved enantiomeric separation in capillary electrophoresis using carboxymethyl-β-cyclodextrin (CM-β-CD) as a chiral selector.* Microchimica Acta, 2015. **182**(7): p. 1297-1304.

227. Zhang, Z., et al., *Horseradish peroxidase and antibody labeled gold nanoparticle probe for amplified immunoassay of ciguatoxin in fish samples based on capillary electrophoresis with electrochemical detection.* Toxicon, 2015. **96**: p. 89-95.

228. Girardot, M., et al., *Aptamer-conjugated nanoparticles: Preservation of targeting functionality demonstrated by microchip electrophoresis in frontal mode.* Analytical Biochemistry, 2013. **435**(2): p. 150-152.

229. Streich, C., et al., *Influence of ligands in metal nanoparticle electrophoresis for the fabrication of biofunctional coatings.* Applied Surface Science, 2015. **348**: p. 92-99.

230. Sharma, B., et al., *Selective biophysical interactions of surface modified nanoparticles with cancer cell lipids improve tumor targeting and gene therapy.* Cancer Letters, 2013. **334**(2): p. 228-236.

231. Ba-Abbad, M.M., et al., *The effect of process parameters on the size of ZnO nanoparticles synthesized via the sol–gel technique.* Journal of Alloys and Compounds, 2012. **550**: p. 63-70.

232. Jensen, H. and J. Østergaard, *Flow Induced Dispersion Analysis Quantifies Noncovalent Interactions in Nanoliter Samples.* Journal of the American Chemical Society, 2010. **132**(12): p. 4070-4071.

233. Semete, B., et al., *Effects of protein binding on the biodistribution of PEGylated PLGA nanoparticles post oral administration.* International Journal of Pharmaceutics, 2012. **424**(1–2): p. 115-120.

234. Aggarwal, P., et al., *Nanoparticle interaction with plasma proteins as it relates to particle biodistribution, biocompatibility and therapeutic efficacy.* Advanced Drug Delivery Reviews, 2009. **61**(6): p. 428-437.

235. Gao, X., et al., *In vivo cancer targeting and imaging with semiconductor quantum dots.* Nat Biotech, 2004. **22**(8): p. 969-976.

236. Abhilash, M., *Potential applications of nanoparticles.* International Journal of Pharma and Bio Sciences, 2010. **1**(1-12).

237. Jedlovszky-Hajdú, A., et al., *Surface Coatings Shape the Protein Corona of SPIONs with Relevance to Their Application in Vivo.* Langmuir, 2012. **28**(42): p. 14983-14991.

238. Estephan, Z.G., P.S. Schlenoff, and J.B. Schlenoff, *Zwitteration As an Alternative to PEGylation.* Langmuir, 2011. **27**(11): p. 6794-6800.

239. Blab, G.A., et al., *Optical readout of gold nanoparticle-based DNA microarrays without silver enhancement.* Biophysical Journal, 2006. **90**(1): p. L13-L15.

240. Rabanel, J.-M., P. Hildgen, and X. Banquy, *Assessment of PEG on polymeric particles surface, a key step in drug carrier translation.* Journal of Controlled Release, 2014. **185**(0): p. 71-87.

241. Rundlett, K.L. and D.W. Armstrong, *Methods for the determination of binding constants by capillary electrophoresis.* Electrophoresis, 2001. **22**(7): p. 1419-27.

242. Ramírez-García, G., et al., *Electrokinetic Hummel-Dreyer characterization of nanoparticle-plasma protein corona: the non-specific interactions between PEG-modified persistent luminescent nanoparticles and albumin.* Submitted.

243. Wang, J., et al., *In-capillary self-assembly study of quantum dots and protein using fluorescence coupled capillary electrophoresis.* Electrophoresis, 2015. **36**(14): p. 1523-8.

244. Li, N., et al., *Probing nanoparticle--protein interaction by capillary electrophoresis.* Anal Chem, 2010. **82**(17): p. 7460-6.

245. Zhang, Z., et al., *Ultrasensitive and accelerated detection of ciguatoxin by capillary electrophoresis via on-line sandwich immunoassay with rotating magnetic field and nanoparticles signal enhancement.* Analytica Chimica Acta, 2015. **888**: p. 27-35.

246. Matczuk, M., et al., *Speciation of metal-based nanomaterials in human serum characterized by capillary electrophoresis coupled to ICP-MS: a case study of gold nanoparticles.* Metallomics, 2015. **7**(9): p. 1364-70.

247. Wang, J., et al., *Studies on multivalent interactions of quantum dots–protein self-assemble using fluorescence coupled capillary electrophoresis.* Journal of Nanoparticle Research, 2014. **16**(7): p. 1-7.

248. Zhang, M.Z., et al., *Targeted quantum dots fluorescence probes functionalized with aptamer and peptide for transferrin receptor on tumor cells.* Nanotechnology, 2012. **23**(48): p. 485104.

249. Girardot, M., et al., *Determination of binding parameters between lysozyme and its aptamer by frontal analysis continuous microchip electrophoresis (FACMCE).* J Chromatogr A, 2011. **1218**(26): p. 4052-8.

250. Girardot, M., et al., *Aptamer–Target Interaction: A Comprehensive Study by Microchip Electrophoresis in Frontal Mode.* Chromatographia, 2012. **76**(7): p. 305-312.

251. Wang, J. and J. Xia, *Preferential binding of a novel polyhistidine peptide dendrimer ligand on quantum dots probed by capillary electrophoresis.* Anal Chem, 2011. **83**(16): p. 6323-9.

252. Stanisavljevic, M., et al., *Interactions between CdTe quantum dots and DNA revealed by capillary electrophoresis with laser-induced fluorescence detection.* Electrophoresis, 2014. **35**(18): p. 2587-92.

253. Stanisavljevic, M., et al., *Study of Streptavidin-Modified Quantum Dots by Capillary Electrophoresis.* Chromatographia, 2013. **76**(7-8): p. 335-343.

254. Maldiney, T., et al., *Synthesis and functionalization of persistent luminescence nanoparticles with small molecules and evaluation of their targeting ability.* International Journal of Pharmaceutics, 2012. **423**(1): p. 102-107.

255. Maldiney, T., et al., *In vivo imaging with persistent luminescence silicate-based nanoparticles.* Optical Materials, 2013. **35**(10): p. 1852-1858.

256. Maldiney, T., et al., *Mesoporous persistent nanophosphors for in vivo optical bioimaging and drug-delivery.* Nanoscale, 2014. **6**(22): p. 13970-6.

257. Teston, E., et al., *Non-aqueous sol-gel synthesis of ultra small persistent luminescence nanoparticles for near-infrared in vivo imaging.* Chemistry, 2015. **21**(20): p. 7350-4.

258. Teston, E., et al., *Design, Properties, and In Vivo Behavior of Super-paramagnetic Persistent Luminescence Nanohybrids.* Small, 2015.

259. Maldiney, T., et al., *Gadolinium-Doped Persistent Nanophosphors as Versatile Tool for Multimodal In Vivo Imaging.* Advanced Functional Materials, 2015. **25**(2): p. 331-338.

260. le Masne de Chermont, Q., et al., *Nanoprobes with near-infrared persistent luminescence for in vivo imaging.* Proc Natl Acad Sci U S A, 2007. **104**(22): p. 9266-71.

261. Woodward, R.C., et al., *A comparison of methods for the measurement of the particle-size distribution of magnetic nanoparticles.* Journal of Applied Crystallography, 2007. **40**(s1): p. s495-s500.

262. Holoubek, J., *Some applications of light scattering in materials science.* Journal of Quantitative Spectroscopy and Radiative Transfer, 2007. **106**(1–3): p. 104-121.

263. Hunter, R.J., *Foundations of Colloid Science*. 2nd ed. 2001, New York: Oxford University Press.

264. d'Orlye, F., et al., *Charge-based characterization of nanometric cationic bifunctional maghemite/silica core/shell particles by capillary zone electrophoresis.* Electrophoresis, 2009. **30**(14): p. 2572-2582.

265. Fourest, B., N. Hakem, and R. Guillaumont, *Characterization of Colloids by Measurement of Their Mobilities*, in *Radiochimca Acta*1994. p. 173.

266. Vanifatova, N.G., et al., *Size separation of silica nanospheres by means of capillary zone electrophoresis.* Talanta, 2003. **59**(2): p. 345-53.

267. Ducatte, G.R., et al., *Separation and characterization of oxide particles by capillary electrophoresis.* Journal of Microcolumn Separations, 1996. **8**(6): p. 403-412.

268. Morneau, A., et al., *Analysis of ferrofluids by capillary electrophoresis.* Colloids and Surfaces A: Physicochemical and Engineering Aspects, 1999. **154**(3): p. 295-301.

269. Melanson, J.E., N.E. Baryla, and C.A. Lucy, *Double-chained surfactants for semipermanent wall coatings in capillary electrophoresis.* Anal Chem, 2000. **72**(17): p. 4110-4.

270. Kuzovkov, V.N. and E.A. Kotomin, *Static and dynamic screening effects in the electrostatic self-assembly of nano-particles.* Physical Chemistry Chemical Physics, 2014. **16**(46): p. 25449-25460.

271. Franzen, U., et al., *Physicochemical characterization of a PEGylated liposomal drug formulation using capillary electrophoresis.* ELECTROPHORESIS, 2011. **32**(6-7): p. 738-748.

272. Huff, B.V. and G.L. McIntire, *Determination of the electrophoretic mobility of polystyrene particles by capillary electrophoresis.* Journal of Microcolumn Separations, 1994. **6**(6): p. 591-594.

273. Mikhaylova, M., et al., *BSA Immobilization on Amine-Functionalized Superparamagnetic Iron Oxide Nanoparticles.* Chemistry of Materials, 2004. **16**(12): p. 2344-2354.

274. Ma, P.C., J.K. Kim, and B.Z. Tang, *Functionalization of carbon nanotubes using a silane coupling agent.* Carbon, 2006. **44**(15): p. 3232-3238.

275. Asenath Smith, E. and W. Chen, *How To Prevent the Loss of Surface Functionality Derived from Aminosilanes.* Langmuir, 2008. **24**(21): p. 12405-12409.

276. Lim, M.H. and A. Stein, *Comparative studies of grafting and direct syntheses of inorganic-organic hybrid mesoporous materials.* Chemistry of Materials, 1999. **11**(11): p. 3285-3295.

277. Vandenberg, E.T., et al., *Structure of 3-aminopropyl triethoxy silane on silicon oxide.* Journal of Colloid and Interface Science, 1991. **147**(1): p. 103-118.

278. Lyklema, J., *Coagulation by simple multivalent counterions.* Colloids and Surfaces A: Physicochemical and Engineering Aspects, 2014. **460**: p. 468-472.

279. Okamoto, Y., F. Kitagawa, and K. Otsuka, *Separation of cationic polymer particles and characterization of avidin-immobilized particles by capillary electrophoresis.* Electrophoresis, 2006. **27**(5-6): p. 1031-1040.

280. Wei, G.-T., et al., *Separation of Nanostructured Gold Particles by Capillary Zone Electrophoresis.* Journal of the Chinese Chemical Society, 1998. **45**(1): p. 47-52.

281. Templeton, A.C., D.E. Cliffel, and R.W. Murray, *Redox and Fluorophore Functionalization of Water-Soluble, Tiopronin-Protected Gold Clusters.* Journal of the American Chemical Society, 1999. **121**(30): p. 7081-7089.

282. Jacobs, C. and R.H. Muller, *Production and characterization of a budesonide nanosuspension for pulmonary administration.* Pharm Res, 2002. **19**(2): p. 189-94.

283. Pardeike, J. and R.H. Müller, *Nanosuspensions: A promising formulation for the new phospholipase A2 inhibitor PX-18.* International Journal of Pharmaceutics, 2010. **391**(1–2): p. 322-329.

284. Eastman, J., *Colloid Stability*, in *Colloid Science*. 2009, Blackwell Publishing Ltd. p. 36-49.

285. Sperling, R.A. and W.J. Parak, *Surface modification, functionalization and bioconjugation of colloidal inorganic nanoparticles.* Philos Trans A Math Phys Eng Sci, 2010. **368**(1915): p. 1333-83.

286. Zhang, Z., et al., *Synthesis of poly(ethylene glycol) (PEG)-grafted colloidal silica particles with improved stability in aqueous solvents.* J Colloid Interface Sci, 2007. **310**(2): p. 446-55.

287. Nune, S.K., et al., *Nanoparticles for biomedical imaging.* Expert Opin Drug Deliv, 2009. **6**(11): p. 1175-94.

288. Peng, Q. and H. Mu, *The potential of protein–nanomaterial interaction for advanced drug delivery.* Journal of Controlled Release, 2016. **225**: p. 121-132.

289. Treuel, L., et al., *The influence of surface composition of nanoparticles on their interactions with serum albumin.* Chemphyschem, 2010. **11**(14): p. 3093-9.

290. Brewer, S.H., et al., *Probing BSA Binding to Citrate-Coated Gold Nanoparticles and Surfaces.* Langmuir, 2005. **21**(20): p. 9303-9307.

291. Dominguez-Medina, S., et al., *In situ measurement of bovine serum albumin interaction with gold nanospheres.* Langmuir, 2012. **28**(24): p. 9131-9.

292. Iosin, M., et al., *Study of protein–gold nanoparticle conjugates by fluorescence and surface-enhanced Raman scattering.* Journal of Molecular Structure, 2009. **924–926**: p. 196-200.

293. Jiang, C. and D.W. Armstrong, *Use of CE for the determination of binding constants.* Electrophoresis, 2010. **31**(1): p. 17-27.

294. Yan, W. and C.L. Colyer, *Investigating noncovalent squarylium dye–protein interactions by capillary electrophoresis–frontal analysis.* Journal of Chromatography A, 2006. **1135**(1): p. 115-121.

295. Beale, S.C., *Capillary electrophoresis.* Anal. Chem., 1998. **70**: p. 279-300.

296. Chen, Z. and S.G. Weber, *Determination of binding constants by affinity capillary electrophoresis, electrospray ionization mass spectrometry and phase-distribution methods.* TrAC Trends in Analytical Chemistry, 2008. **27**(9): p. 738-748.

297. Galievsky, V.A., A.S. Stasheuski, and S.N. Krylov, *Capillary Electrophoresis for Quantitative Studies of Biomolecular Interactions.* Analytical Chemistry, 2015. **87**(1): p. 157-171.

298. Ram Boppana, V.B., D.J. Doren, and R.F. Lobo, *Analysis of Ga coordination environment in novel spinel zinc gallium oxy-nitride photocatalysts.* Journal of Materials Chemistry, 2010. **20**(43): p. 9787-9797.

299. McCarthy, S.A., G.L. Davies, and Y.K. Gun'ko, *Preparation of multifunctional nanoparticles and their assemblies.* Nat Protoc, 2012. **7**(9): p. 1677-93.

300. François, Y., et al., *New integrated measurement protocol using capillary electrophoresis instrumentation for the determination of viscosity, conductivity and absorbance of ionic liquid–molecular solvent mixtures.* Analytica Chimica Acta, 2006. **562**(2): p. 164-170.

301. Busch, M.H., et al., *Comparison of five methods for the study of drug-protein binding in affinity capillary electrophoresis.* J Chromatogr A, 1997. **777**(2): p. 311-28.

302. Michalcova, L. and Z. Glatz, *Comparison of various capillary electrophoretic approaches for the study of drug-protein interaction with emphasis on minimal consumption of protein sample and possibility of automation.* J Sep Sci, 2015. **38**(2): p. 325-31.

303. Hage, D.S., et al., *CHROMATOGRAPHIC ANALYSIS OF DRUG INTERACTIONS IN THE SERUM PROTEOME.* Analytical methods : advancing methods and applications, 2011. **3**(7): p. 10.1039/C1AY05068K.

304. Gargouri, M., B. Gallois, and J. Chaudiere, *Binding-equilibrium and kinetic studies of anthocyanidin reductase from Vitis vinifera.* Arch Biochem Biophys, 2009. **491**(1-2): p. 61-8.

305. Norde, W., et al., *Protein adsorption at solid-liquid interfaces: Reversibility and conformation aspects.* Journal of Colloid and Interface Science, 1986. **112**(2): p. 447-456.

306. Kulikova, G.A., et al., *Calorimetric study of adsorption of human serum albumin onto silica powders.* Thermochimica Acta, 2010. **503–504**(0): p. 65-69.

307. Peters Jr, T., *3 - Ligand Binding by Albumin*, in *All About Albumin*. 1995, Academic Press: San Diego. p. 76-132.

308. Shen, C., S. Guo, and C. Lu, *Degradation behaviors of monomethoxy poly(ethylene glycol)-b-poly(ε-caprolactone) nanoparticles in aqueous solution.* Polymers for Advanced Technologies, 2008. **19**(1): p. 66-72.

309. Allouni, Z.E., et al., *The effect of blood protein adsorption on cellular uptake of anatase TiO2 nanoparticles.* Int J Nanomedicine, 2015. **10**: p. 687-95.

310. Karmali, P.P. and D. Simberg, *Interactions of nanoparticles with plasma proteins: implication on clearance and toxicity of drug delivery systems.* Expert Opin Drug Deliv, 2011. **8**(3): p. 343-57.

311. Pozzi, D., et al., *The biomolecular corona of nanoparticles in circulating biological media.* Nanoscale, 2015.

312. Yallapu, M.M., et al., *Implications of protein corona on physico-chemical and biological properties of magnetic nanoparticles.* Biomaterials, 2015. **46**: p. 1-12.

313. Tenzer, S., et al., *Rapid formation of plasma protein corona critically affects nanoparticle pathophysiology.* Nat Nano, 2013. **8**(10): p. 772-781.

314. Liu, L., et al., *Decreased reticuloendothelial system clearance and increased blood half-life and immune cell labeling for nano- and micron-sized superparamagnetic iron-oxide particles upon pre-treatment with Intralipid.* Biochim Biophys Acta, 2013. **1830**(6): p. 3447-53.

315. Yu, M. and J. Zheng, *Clearance Pathways and Tumor Targeting of Imaging Nanoparticles.* ACS Nano, 2015. **9**(7): p. 6655-74.

316. Sheng, Y., et al., *In vitro macrophage uptake and in vivo biodistribution of PLA-PEG nanoparticles loaded with hemoglobin as blood substitutes: effect of PEG content.* J Mater Sci Mater Med, 2009. **20**(9): p. 1881-91.

317. Gref, R., et al., *'Stealth' corona-core nanoparticles surface modified by polyethylene glycol (PEG): influences of the corona (PEG chain length and surface density) and of the core composition on phagocytic uptake and plasma protein adsorption.* Colloids Surf B Biointerfaces, 2000. **18**(3-4): p. 301-313.

318. Amoozgar, Z. and Y. Yeo, *Recent advances in stealth coating of nanoparticle drug delivery systems.* Wiley Interdiscip Rev Nanomed Nanobiotechnol, 2012. **4**(2): p. 219-33.

319. Li, S.D. and L. Huang, *Stealth nanoparticles: high density but sheddable PEG is a key for tumor targeting.* J Control Release, 2010. **145**(3): p. 178-81.

320. Jokerst, J.V., et al., *Nanoparticle PEGylation for imaging and therapy.* Nanomedicine, 2011. **6**(4): p. 715-728.

321. Maeda, H., K. Tsukigawa, and J. Fang, *A Retrospective 30 Years After Discovery of the EPR Effect of Solid Tumors: Next-Generation Chemotherapeutics and Photodynamic-therapy-Problems, Solutions, Prospects.* Microcirculation, 2015.

322. Liu, X., et al., *Mixed-Charge Nanoparticles for Long Circulation, Low Reticuloendothelial System Clearance, and High Tumor Accumulation.* Advanced Healthcare Materials, 2014. **3**(9): p. 1439-1447.

323. Liu, J., et al., *Passive Tumor Targeting of Renal-Clearable Luminescent Gold Nanoparticles: Long Tumor Retention and Fast Normal Tissue Clearance.* Journal of the American Chemical Society, 2013. **135**(13): p. 4978-4981.

324. Torrisi, V., et al., *Preventing Corona Effects: Multiphosphonic Acid Poly(ethylene glycol) Copolymers for Stable Stealth Iron Oxide Nanoparticles.* Biomacromolecules, 2014. **15**(8): p. 3171-3179.

325. Maffre, P., et al., *Effects of surface functionalization on the adsorption of human serum albumin onto nanoparticles - a fluorescence correlation spectroscopy study.* Beilstein J Nanotechnol, 2014. **5**: p. 2036-47.

326. Trapiella-Alfonso, L.R.-G., Gonzalo; d'Orlyé, Fanny; Varenne, Anne, *Electromigration separation methodologies for the characterization of nanoparticles and the evaluation of their behaviour in biological systems* Submitted.

327. Zhu, M., M.Z. Lerum, and W. Chen, *How to prepare reproducible, homogeneous, and hydrolytically stable aminosilane-derived layers on silica.* Langmuir, 2012. **28**(1): p. 416-23.

328. Bhonsle, H.S., et al., *Albumin competitively inhibits glycation of less abundant proteins.* Protein Pept Lett, 2008. **15**(7): p. 663-7.

329. Pozzi, D., et al., *Effect of polyethyleneglycol (PEG) chain length on the bio-nano-interactions between PEGylated lipid nanoparticles and biological fluids: from nanostructure to uptake in cancer cells.* Nanoscale, 2014. **6**(5): p. 2782-92.

330. Kumar, V., et al., *Shielding of Lipid Nanoparticles for siRNA Delivery: Impact on Physicochemical Properties, Cytokine Induction, and Efficacy.* Mol Ther Nucleic Acids, 2014. **3**: p. e210.

331. Maldiney, T., et al., *Controlling aminosilane layer thickness to extend the plasma half-life of stealth persistent luminescence nanoparticles in vivo.* Journal of Materials Chemistry B, 2015. **3**(19): p. 4009-4016.

332. Zolnik, B.S., et al., *Nanoparticles and the immune system.* Endocrinology, 2010. **151**(2): p. 458-65.

333. Mohammad, A.K. and J.J. Reineke, *Quantitative Detection of PLGA Nanoparticle Degradation in Tissues following Intravenous Administration.* Molecular Pharmaceutics, 2013. **10**(6): p. 2183-2189.

334. Shi, B. and M. Abrams, *Technologies for investigating the physiological barriers to efficient lipid nanoparticle-siRNA delivery.* J Histochem Cytochem, 2013. **61**(6): p. 407-20.

335. Florence, A.T., *"Targeting" nanoparticles: The constraints of physical laws and physical barriers.* Journal of Controlled Release, 2012. **164**(2): p. 115-124.

336. Kristensen, M., D. Birch, and H. Morck Nielsen, *Applications and Challenges for Use of Cell-Penetrating Peptides as Delivery Vectors for Peptide and Protein Cargos.* Int J Mol Sci, 2016. **17**(2).

337. Meyers, J.D., et al., *Nanoparticles for imaging and treating brain cancer.* Nanomedicine (Lond), 2013. **8**(1): p. 123-43.

338. Begley, D.J., *Understanding and circumventing the blood-brain barrier.* Acta Paediatr Suppl, 2003. **92**(443): p. 83-91.

339. Gabathuler, R., *Approaches to transport therapeutic drugs across the blood-brain barrier to treat brain diseases.* Neurobiol Dis, 2010. **37**(1): p. 48-57.

340. Yamamoto, M., et al., *Increased expression of low density lipoprotein receptor-related protein/alpha2-macroglobulin receptor in human malignant astrocytomas.* Cancer Res, 1997. **57**(13): p. 2799-805.

341. Elzoghby, A.O., et al., *Natural polymeric nanoparticles for brain-targeting: Implications on drug and gene delivery.* Curr Pharm Des, 2016.

342. Kreuter, J., et al., *Passage of peptides through the blood-brain barrier with colloidal polymer particles (nanoparticles).* Brain Res, 1995. **674**(1): p. 171-4.

343. Michaelis, K., et al., *Covalent linkage of apolipoprotein e to albumin nanoparticles strongly enhances drug transport into the brain.* J Pharmacol Exp Ther, 2006. **317**(3): p. 1246-53.

344. Kreuter, J., et al., *Apolipoprotein-mediated transport of nanoparticle-bound drugs across the blood-brain barrier.* J Drug Target, 2002. **10**(4): p. 317-25.

345. Wagner, S., et al., *Uptake mechanism of ApoE-modified nanoparticles on brain capillary endothelial cells as a blood-brain barrier model.* PLoS One, 2012. **7**(3): p. e32568.

346. Weiss, J.N., *The Hill equation revisited: uses and misuses.* FASEB J, 1997. **11**(11): p. 835-41.

347. Peracchia, M.T., et al., *Visualization of in vitro protein-rejecting properties of PEGylated stealth polycyanoacrylate nanoparticles.* Biomaterials, 1999. **20**(14): p. 1269-75.

348. Fanali, G., et al., *Human serum albumin: from bench to bedside.* Mol Aspects Med, 2012. **33**(3): p. 209-90.

349. Fukumori, Y. and H. Ichikawa, *Nanoparticles for cancer therapy and diagnosis.* Advanced Powder Technology, 2006. **17**(1): p. 1-28.

350. Brigger, I., C. Dubernet, and P. Couvreur, *Nanoparticles in cancer therapy and diagnosis.* Advanced Drug Delivery Reviews, 2012. **64, Supplement**: p. 24-36.

351. Coll, J.-L., *Cancer optical imaging using fluorescent nanoparticles.* Nanomedicine (London, England), 2011. **6**(1): p. 7-10.

352. Palner, M., et al., *Semiconducting Polymer Nanoparticles with Persistent Near-infrared Luminescence for In Vivo Optical Imaging.* Angew Chem Int Ed Engl, 2015.

353. Djurišić, A.B., et al., *Toxicity of Metal Oxide Nanoparticles: Mechanisms, Characterization, and Avoiding Experimental Artefacts.* Small, 2015. **11**(1): p. 26-44.

354. Hofmann-Amtenbrink, M., D.W. Grainger, and H. Hofmann, *Nanoparticles in medicine: Current challenges facing inorganic nanoparticle toxicity assessments and standardizations.* Nanomedicine: Nanotechnology, Biology and Medicine.

355. Xiao, G., et al., *Visible-light-mediated synergistic photocatalytic antimicrobial effects and mechanism of Ag-nanoparticles@chitosan–TiO2 organic–inorganic composites for water disinfection.* Applied Catalysis B: Environmental, 2015. **170–171**: p. 255-262.

356. Li, Y., et al., *Mechanism of Photogenerated Reactive Oxygen Species and Correlation with the Antibacterial Properties of Engineered Metal-Oxide Nanoparticles.* ACS Nano, 2012. **6**(6): p. 5164-5173.

357. Brunet, L., et al., *Comparative Photoactivity and Antibacterial Properties of C60 Fullerenes and Titanium Dioxide Nanoparticles.* Environmental Science & Technology, 2009. **43**(12): p. 4355-4360.

358. Zhang, L.e., et al., *Inorganic photosensitizer coupled Gd-based upconversion luminescent nanocomposites for in vivo magnetic resonance imaging and near-infrared-responsive photodynamic therapy in cancers.* Biomaterials, 2015. **44**: p. 82-90.

359. Levy, J.G., *Photosensitizers in photodynamic therapy.* Semin Oncol, 1994. **21**(6 Suppl 15): p. 4-10.

360. Macdonald, I.J. and T.J. Dougherty, *Basic principles of photodynamic therapy.* Journal of Porphyrins and Phthalocyanines, 2001. **5**(2): p. 105-129.

361. Kolarova, H., et al., *Production of reactive oxygen species after photodynamic therapy by porphyrin sensitizers.* Gen Physiol Biophys, 2008. **27**(2): p. 101-5.

362. Kochevar, I.E. and R.W. Redmond, *Photosensitized production of singlet oxygen.* Methods Enzymol, 2000. **319**: p. 20-8.

363. Ling, D., et al., *Multifunctional Tumor pH-Sensitive Self-Assembled Nanoparticles for Bimodal Imaging and Treatment of Resistant Heterogeneous Tumors.* Journal of the American Chemical Society, 2014. **136**(15): p. 5647-5655.

364. Strober, W., *Trypan blue exclusion test of cell viability.* Curr Protoc Immunol, 2001. **Appendix 3**: p. Appendix 3B.

365. Sutherland, M.W. and B.A. Learmonth, *The tetrazolium dyes MTS and XTT provide new quantitative assays for superoxide and superoxide dismutase.* Free Radic Res, 1997. **27**(3): p. 283-9.

366. Speirs, V., et al., *Short-term primary culture of epithelial cells derived from human breast tumours.* Br J Cancer, 1998. **78**(11): p. 1421-9.

367. Ekmekcioglu, S., C.-H. Tang, and E.A. Grimm, *NO News is not Necessarily Good News in Cancer.* Current Cancer Drug Targets, 2005. **5**(2): p. 103-115.

368. Duan, S., et al., *Multi-arm polymeric nanocarrier as a nitric oxide delivery platform for chemotherapy of head and neck squamous cell carcinoma.* Biomaterials, 2012. **33**(11): p. 3243-3253.

369. Ntziachristos, V., *Fluorescence molecular imaging.* Annu Rev Biomed Eng, 2006. **8**: p. 1-33.

370. Ji, X., et al., *Fluorescent quantum dots: synthesis, biomedical optical imaging, and biosafety assessment.* Colloids Surf B Biointerfaces, 2014. **124**: p. 132-9.

371. Byers, R.J. and E.R. Hitchman, *Quantum dots brighten biological imaging.* Prog Histochem Cytochem, 2011. **45**(4): p. 201-37.

372. Smith, A.M., et al., *Bioconjugated quantum dots for in vivo molecular and cellular imaging.* Adv Drug Deliv Rev, 2008. **60**(11): p. 1226-40.

373. Ricciardi, L., et al., *Multifunctional material based on ionic transition metal complexes and gold-silica nanoparticles: synthesis and photophysical characterization for application in imaging and therapy.* J Photochem Photobiol B, 2014. **140**: p. 396-404.

374. Nam, J., et al., *Surface engineering of inorganic nanoparticles for imaging and therapy.* Adv Drug Deliv Rev, 2013. **65**(5): p. 622-48.

375. Pan, Z.Y., et al., *The application of ZnO luminescent nanoparticles in labeling mice.* Contrast Media Mol Imaging, 2011. **6**(4): p. 328-30.

376. Xenopoulos, P., S. Nowotschin, and A.K. Hadjantonakis, *Live imaging fluorescent proteins in early mouse embryos.* Methods Enzymol, 2012. **506**: p. 361-89.

377. Yang, X., et al., *Molecular imaging of small animals with fluorescent proteins: from projection to multimodality.* Comput Med Imaging Graph, 2012. **36**(4): p. 259-63.

378. Ptaszek, M., *Rational design of fluorophores for in vivo applications.* Prog Mol Biol Transl Sci, 2013. **113**: p. 59-108.

379. Lemasters, J.J. and V.K. Ramshesh, *Imaging of mitochondrial polarization and depolarization with cationic fluorophores.* Methods Cell Biol, 2007. **80**: p. 283-95.

380. Niu, J., et al., *Luminescent nanoprobes for in-vivo bioimaging.* TrAC Trends in Analytical Chemistry, 2014. **58**: p. 112-119.

381. Wu, B.Y., et al., *Fluorescence resonance energy transfer inhibition assay for alpha-fetoprotein excreted during cancer cell growth using functionalized persistent luminescence nanoparticles.* J Am Chem Soc, 2011. **133**(4): p. 686-8.

382. Soenen, S.J., et al., *The effect of nanoparticle degradation on poly(methacrylic acid)-coated quantum dot toxicity: The importance of particle functionality assessment in toxicology.* Acta Biomaterialia, 2014. **10**(2): p. 732-741.

383. Sun, M., et al., *Persistent luminescent nanoparticles for super-long time in vivo and in situ imaging with repeatable excitation.* Journal of Luminescence, 2014. **145**: p. 838-842.

384. Ye, L., et al., *A pilot study in non-human primates shows no adverse response to intravenous injection of quantum dots.* Nat Nano, 2012. **7**(7): p. 453-458.

385. Gnach, A., et al., *Upconverting nanoparticles: assessing the toxicity.* Chemical Society Reviews, 2015. **44**(6): p. 1561-1584.

386. Collins, A.R., S.J. Duthie, and V.L. Dobson, *Direct enzymic detection of endogenous oxidative base damage in human lymphocyte DNA.* Carcinogenesis, 1993. **14**(9): p. 1733-5.

387. Derfus, A.M., W.C.W. Chan, and S.N. Bhatia, *Probing the Cytotoxicity of Semiconductor Quantum Dots.* Nano Letters, 2004. **4**(1): p. 11-18.

388. Babula, P., et al., *Mammalian metallothioneins: properties and functions.* Metallomics, 2012. **4**(8): p. 739-50.

389. Tiwari, D.K., T. Jin, and J. Behari, *Bio-distribution and toxicity assessment of intravenously injected anti-HER2 antibody conjugated CdSe/ZnS quantum dots in Wistar rats.* Int J Nanomedicine, 2011. **6**: p. 463-75.

390. Xia, T., et al., *Comparison of the mechanism of toxicity of zinc oxide and cerium oxide nanoparticles based on dissolution and oxidative stress properties.* ACS Nano, 2008. **2**(10): p. 2121-34.

391. Aillon, K.L., et al., *Effects of nanomaterial physicochemical properties on in vivo toxicity.* Adv Drug Deliv Rev, 2009. **61**(6): p. 457-66.

392. Ho, C.C., et al., *Quantum dot 705, a cadmium-based nanoparticle, induces persistent inflammation and granuloma formation in the mouse lung.* Nanotoxicology, 2013. **7**(1): p. 105-15.

393. Garg, A.D., et al., *ER stress-induced inflammation: does it aid or impede disease progression?* Trends Mol Med, 2012. **18**(10): p. 589-98.

394. Baumann, J., et al., *The coating makes the difference: acute effects of iron oxide nanoparticles on Daphnia magna.* Sci Total Environ, 2014. **484**: p. 176-84.

395. Merdzan, V., et al., *The effects of different coatings on zinc oxide nanoparticles and their influence on dissolution and bioaccumulation by the green alga, C. reinhardtii.* Sci Total Environ, 2014. **488-489**: p. 316-24.

396. Yu, T., et al., *Influence of geometry, porosity, and surface characteristics of silica nanoparticles on acute toxicity: their vasculature effect and tolerance threshold.* ACS Nano, 2012. **6**(3): p. 2289-301.

397. Kubiak, T., *[The use of shells made of poly(ethylene glycol) and chitosan to ensure the biocompatibility of nanoparticles in biomedical applications].* Polim Med, 2014. **44**(2): p. 119-27.

ANEXE I. RÉSUMÉ GÉNÉRALE EN FRANÇAIS

Caractérisation physicochimique des nanoparticules à luminescence persistante et étude de leur biocompatibilité pour des applications précliniques de diagnostic

Les nanoparticules à luminescence persistante de gallate de zinc dopée chrome ($ZnGa_{1.995}Cr_{0.005}O_4$) sont des matériaux innovants avec des propriétés optiques particulières qui permettent leur utilisation pour l'imagerie optique *in vivo*. Elles peuvent être excitées dans la fenêtre de transparence des tissus par des photons visibles et émettre de la lumière pendant quelques heures après la fin de l'excitation. Ce phénomène permet d'observer la sonde sans contraintes de temps et en l'absence de signaux d'autofluorescence produits par les tissus biologiques. Malgré les propriétés optiques des $ZnGa_{1.995}Cr_{0.005}O_4$, leur utilisation exige une vaste caractérisation physicochimique et l'évaluation de leur biocompatibilité. L'utilisation de différentes méthodes pour contrôler le processus de synthèse et de fonctionnalisation des nanoparticules et caractériser ces objets est impérative pour mieux comprendre les interactions ultérieures avec des éléments biologiques. Dans cet objectif, le design, la synthèse et la fonctionnalisation des nanoparticules de $ZnGa_{1.995}Cr_{0.005}O_4$ ont été réalisées. Leur caractérisation physico-chimique a été effectuée afin d'optimiser les différentes étapes de synthèse, d'obtenir les propriétés physico-chimiques de ces objets et d'estimer leur stabilité colloïdale en vue de leur application en bioimagerie. La caractérisation des nanoparticules a été effectuée en parallèle par les méthodes classiquement employées (diffusion dynamique de lumière (DLS), électrophorèse laser doppler (LDE)) et par une méthode émergente dans ce domaine, l'électrophorèse capillaire. Les études ont été effectuées sur les trois étapes de la fonctionnalisation de la surface des NPs : surface hydroxylée, cette surface ayant été modifiée par aminosilanisation, et enfin cette surface aminée fonctionnalisée par des chaines PEG. Les résultats ont démontré le potentiel important de cette méthode pour garantir le contrôle et la qualité des nanosondes appliquées dans les études de toxicité ultérieures et dans l'analyse de leurs interactions avec des protéines. Un ensemble général des tests de toxicité a été réalisé *in vitro* (cellules du cancer du sein) et *in vivo* (souris) après administration aiguë des $ZnGa_{1.995}Cr_{0.005}O_4$, (soit hydroxylées, soit PEGylées) à court et à long terme afin d'évaluer leur biocompatibilité. Lors de l'administration de nanoparticules hydroxylés, différentes conséquences négatives ont été notées. Cependant, l'administration des nanoparticules PEGylés n'a pas mis en évidence de conséquences dommageables. Ainsi, l'effet protecteur du polyéthylène glycol (PEG) fonctionnalisé en surface des NPs a été démontré. La production de radicaux libres *in vitro* comme effet de la stimulation des nanoparticules par la lumière a attiré notre attention indiquant la possible application des $ZnGa_{1.995}Cr_{0.005}O_4$ hydroxylés comme agents théranostiques pour l'imagerie optique et la thérapie photodynamique. En raison de l'importance des interactions des nanoparticules avec les protéines plasmatiques lors de leur administration, influençant ainsi leur biodistribution et biocompatibilité, nous avons évalué et appliqué pour la première fois la méthode électrocinétique de Hummel-Dreyer pour la détermination des interactions non spécifiques entre les nanoparticules PEGylés et des protéines. La constante d'interaction et le nombre de sites d'interaction ont été calculés dans des solutions de force ionique variée, en milieu de pH physiologique, ce qui a démontre la sensibilité de

cette technique pour détecter de petites différences dans le degré d'interaction. Une fois ce procédé optimisé sur l'albumine de sérum bovin (BSA), il a été employé pour étudier l'influence du temps d'aminosilanation (réaction intermédiaire utilisée au cours de la séquence de fonctionnalisation pour obtenir des nanoparticules PEGylés) sur l'interaction avec l'albumine de serum humain (HSA). Cette méthodologie peut être utile pour favoriser le développement de nouveaux nanomatériaux furtifs dans le système circulatoire. Finalement, l'évaluation des interactions entre les $ZnGa_{1.995}Cr_{0.005}O_4$ et un système binaire de protéines (albumine de sérum humain et Apolipoprtoéine E) a été effectuée par méthode électrocinétique. Ces analyses ont montré une affinité plus forte entre la surface des nanoparticules PEGylés et l'apolipoprotéine-E par rapport à l'albumine, ce qui pourrait représenter une stratégie novatrice pour la vectorisation des nanoparticules vers la région du cerveau. Toutes les méthodes mentionnées ci-dessus peuvent être extrapolées pour l'analyse des autres nanoparticules avec plusieurs des applications.

A1. Introduction

L'imagerie optique est un champ de recherche actuel visant l'évaluation non invasive des maladies et leur progression *in vivo*, l'évaluation du comportement pharmacocinétique des médicaments ou l'identification de biomarqueurs moléculaires des maladies [1]. La préparation des matériaux pour surmonter les inconvénients des marqueurs optiques conventionnels (tels que les classiques Quantum dots et les fluorophores organiques) principalement dus aux signaux d'autofluorescence venant de chromophores endogènes aussi excités lors de l'utilisation de telles sondes *in vivo*, est actuellement étudiée intensivement. Dans ce contexte, des matériaux dont l'émission de la lumière reste pendant des périodes prolongées de temps (jusqu'à plusieurs heures) après que l'excitation lumineuse est arrêtée ont été synthétisés, et sont connus comme matériaux à luminescence persistante [16, 23, 37, 254-259]. Les matériaux à base de gallate de zinc dopé chrome ($ZnGa_2O_4$: Cr (III)) ont attiré l'attention en raison de leur luminescence persistante dans la région proche à l'infrarouge après l'excitation par la lumière ultraviolet [29]. Les propriétés optiques du gallate de zinc non dopé ont été également étudiées dans les matériaux à l'échelle nanométrique [31, 32]. Ainsi, les nanoparticules de gallate de zinc dopé chrome avec formule optimisé $ZnGa_{1.995}Cr_{0.005}O_4$ (ZGO-NPs) développées récemment ont montré des propriétés optiques intéressantes en raison de leur longue luminescence persistante en plus de leur capacité d'être réactives *in vivo* à travers des tissus biologiques en utilisant des photons orange/rouges de faible énergie [33].

Pour une utilisation optimisée des nanoparticules comme sondes luminescentes *in vivo*, leurs propriétés de surface doivent être soigneusement contrôlées. La fonctionnalisation de la surface doit tout d'abord fournir aux nanoparticules une bonne dispersabilité, stabilité dans des solutions aqueuses, une prévention de leur détection naturelle par les cellules immunitaires, et finalement permettre la conjugaison avec des molécules biologiquement actives [38, 39, 260]. Les progrès récents dans le développement de nanoparticules fonctionnelles et polyvalentes a conduit à la nécessité de développer des méthodes permettant la détermination précise des propriétés physico-

chimiques des nanoparticules [172]. L'électrophorèse capillaire (EC) a été appliquée à la caractérisation des nanoparticules [200, 203, 207, 210, 213, 264], en fournissant des informations sur la charge, la densité des groupes fonctionnels, la taille, la stabilité colloïdale selon le milieu de dissolution et les interactions avec des autres objets d'intérêt.

Ces études physicochimiques doivent ensuite être complétées par des études toxicologiques systématiques dans une perspective d'applications biomédicales. Ainsi les NPs peuvent donner lieu à des processus toxiques dangereux, les études toxicologiques systématiques sont donc essentielles pour concevoir des nanomatériaux adéquats pour l'imagerie optique ou des autres applications biomédicales afin d'éviter leurs effets néfastes sur la santé [385].

Pour aller plus loin dans les potentiels biomédicaux de ces nanoparticules, il est nécessaire d'évaluer leurs interactions avec les protéines plasmatiques, qui peuvent impacter sur leur temps de circulation dans le sang, leur biodistribution, leur dégradation, leur accessibilité, l'efficacité des agents de ciblage possibles sur leur surface et leur internalisation cellulaire [37, 44, 233, 234]. Ces interactions dépendent de la nature des groupes fonctionnels sur la surface et de la densité de charge superficielle [44, 230]. En absence d'adsorption non spécifique de protéines sériques, les temps de résidence des NPs dans le sang est augmenté, ce qui favorise le ciblage passif des tumeurs [235, 236]. Afin d'éviter l'adsorption des protéines, la passivation de la surface des NPs est donc un défi crucial [237-239]. L'une des stratégies les plus couramment appliquées implique l'utilisation des recouvrements de polyéthylène glycol pour limiter ces interactions [44, 64, 240].

Cette précieuse information qualitative et quantitative des interactions entre NPs et biomolecules peut être évaluée par diverses méthodologies dont différents modes en électrophorèse capillaire (CE) [173, 182, 246]. Principalement, le mode d'électrophorèse d'affinité a été utilisé pour l'analyse des interactions entre de nombreux types de NPs et de biomolecules. Divers paramètres d'interaction tels le pourcentage de conjugaison, la constante d'interaction, la cinétique d'interaction, le taux de saturation de l'échantillon et le nombre de sites d'interaction ont été obtenus [169, 243, 244, 246]. Le développement de nouvelles méthodologies pour évaluer ces interactions peut favoriser la découverte de nouveaux nanomatériaux avec des applications biomédicales.

L'objectif de ce travail de thèse est d'effectuer (1) une caractérisation physico-chimique poussées des ces nouvelles NPs à luminescence persistante, (2) une étude toxicologique approfondie de ces NPs dont la synthèse a été optimisée dans la première étape, (3) une étude de l'interaction de protéines plasmatiques avec ces NPs (appelé effet de couronne de protéines (protéine-corona)). La première étape est axé sur l'utilisation combinée de la diffusion dynamique de lumière (DLS), l'électrophorèse laser doppler (LDE) et électrophorèse capillaire de zone (CZE) pour contrôler et optimiser la synthèse et fonctionnalisation des ZGO-NPs et déterminer leur stabilité colloïdale et leurs propriétés physico-chimiques lorsque elles sont dispersées dans différents tampons physiologiquement importants. La densité de charge de surface (potentiel zeta) et le diamètre hydrodynamique ont été déterminés à chaque étape de la fonctionnalisation de la surface. Plusieurs tests de toxicité ont ensuite été effectués *in vitro* et *in vivo* chez la souris afin

d'évaluer la biocompatibilité des ZGO-NPs depuis une exposition aiguë, à court terme et à long terme. Enfin, une nouvelle méthodologie a été développée pour étudier les interactions non spécifiques entre les nanoparticules à luminescence persistante et des protéines du plasma. L'interaction entre les NPs et l'albumine de sérum bovin (BSA) a été déterminée par optimisation de la méthode électrocinétique en mode Hummel-Dreyer. Ce développement employé pour la première fois pour ce type de caractérisations a été conçu et optimisé afin d'accéder à la constante d'interaction et le nombre de sites d'interaction de protéines liées sur les NPs. Après optimisation, la première application de cette méthode a été l'évaluation de l'effet de deux temps d'aminosilanisation (3 et 5 heures), deuxième étape lors de la fonctionnalisation des NPs, sur les interactions avec des protéines. Cette étape d'aminosilanisation ayant un impact sur l'étape de PEGYlation, les résultats ont permis d'optimiser cette deuxième étape afin d'optimiser la permanence des nanoparticules dans la circulation sanguine. Enfin, une étude totalement novatrice de l'interaction de deux protéines plasmatiques (albumine de sérum humain(HSA) et Apolipoprotéine E (ApoE)) simultanément avec les NPs a permis de mettre en évidence une interaction plus forte de l' ApoE que l'HSA, ainsi qu'une interaction entre HSA et ApoE, ce qui pourrait représenter une stratégie novatrice pour la vectorisation des nanoparticules vers la région du cerveau.

A2. Résultats et discussion

Les résultats obtenus dans ce travail sont remarquables dans deux sens: d'abord, le développement de méthodologies pour l'analyse des propriétés des nanoparticules et l'évaluation de leurs interactions avec les protéines, et d'autre part, l'application de ces méthodes en combinaison avec un ensemble complet d'études de biocompatibilité pour caractériser les nanoparticules de $ZnGa_{1.995}Cr_{0.005}O_4$.

A2.1. Synthèse, fonctionnalisation et caractérisation des $ZnGa_{1.995}Cr_{0.005}O_4$

Les nanoparticules de $ZnGa_{1.995}Cr_{0.005}O_4$ ont été préparées en utilisant le procédé de synthèse hydrothermale décrit par *Maldiney et al.* [33]. Une séquence classique de fonctionnalisation a été appliquée pour obtenir ZGO-NPs avec de surfaces chimiques variées: ZGO-OH, puis ZGO-NH$_2$, et finalement ZGO-PEG (Figure A-2.1.1).
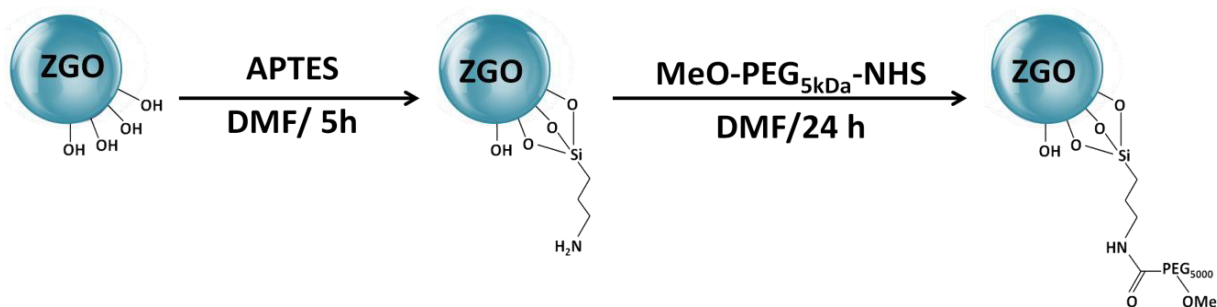
Fig. A-2.1. 1. Fonctionnalisation séquentiel des nanoparticles de $ZnGa_{1.995}Cr_{0.005}O_4$.

La fonctionnalisation séquentielle de la surface de ces NPs a été caractérisée par la détermination d'un certain nombre de paramètres physico-chimiques tels que leur potentiel zêta (par CE et LDE), diamètre hydrodynamique (par DLS), point de charge nulle (PZC) (par EC et LDE) et la stabilité colloïdale (par CE et DLS) dans divers milieux aqueux.

La caractérisation et l'optimisation de cette séquence de fonctionnalisation classique a été explorée pour la première fois par électrophorèse capillaire, permettant ainsi de caractériser la nature des nanoparticules avec différentes densités de charge de surface, comme indiqué dans la Figure A-2.1.2.
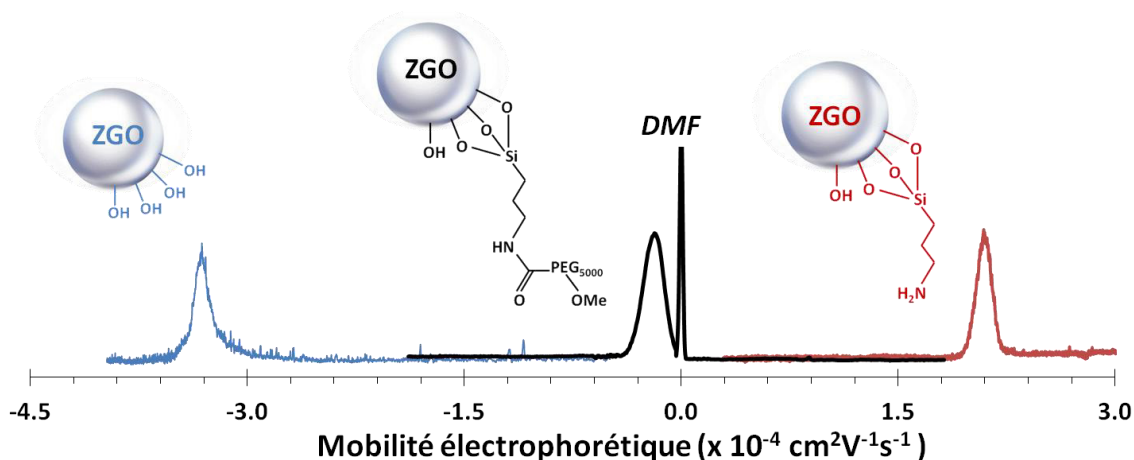
Fig. A-2.1. 2. Réponses électrophorétiques pour la caractérisation des ZGO fonctionnalisés avec des groupes fonctionnels variés.

Dans ce travail, l'équation d'Ohshima-Pyell [165] a été utilisée pour convertir la mobilité électrophorétique (μ_E) en potentiel zeta (ζ). Cette expression permet de faire la distinction entre la forte influence de la mobilité du contre ion et l'influence plus faible de la mobilité du co-ion, permettant l'applicabilité dans des électrolytes tamponnés [165].

Comme prévu dans notre travail, en augmentant la force ionique et la concentration des NPs, les valeurs absolues du potentiel zeta diminuent. En effet, une réduction de l'épaisseur de la couche diffuse (en raison de l'écrantage de la charge de surface) en augmentant la force ionique est prédite par la théorie de la double couche électrique. Concomitamment, les concentrations de NPs plus élevées facilitent les interactions entre les particules dues à une plus grande proximité entre eux [147, 270]. Ces résultats sont en bon accord avec les mesures de la taille des particules, et montrent une stabilité colloidale d'autant plus importante que le potentiel zeta est élevé.

L'effet du pH sur la stabilité colloïdale a été également étudié dans un tampon phosphate de sodium de force ionique 30 mM avec diverses valeurs de pH entre 6 et 8, y compris le pH physiologique 7,4 (Figure A-2.1.3).
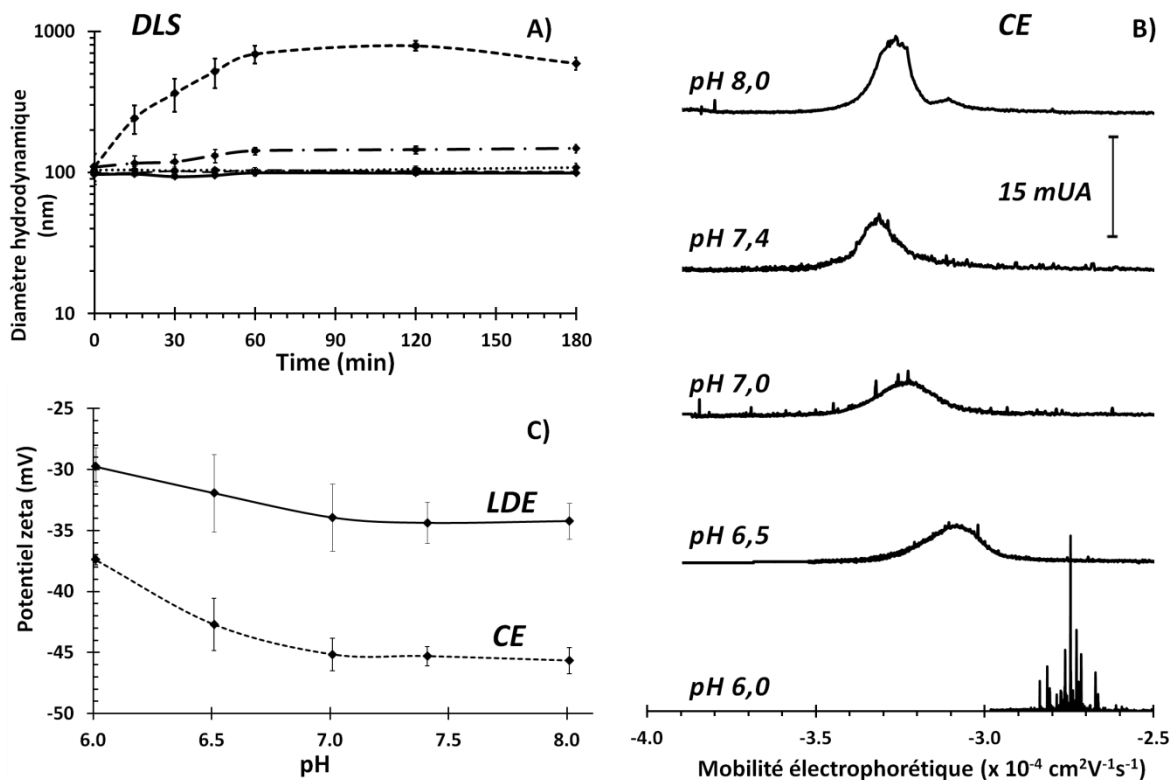
Fig. A-2.1. 3. Diamètre hydrodynamique (à 1,0 mg/mL) à des valeurs de pH variées (pH 6,0 -----, 6,5 –·–, 7,0 ·······, 7,4 ——, and 8,0 ——) estimés par DLS (A), profils électrophorétiques (à 0,2 mg/mL) obtenues par CZE (B) et potentiel zeta de ZGO-OH dans tampon phosphate 30 mM dérivée des mesures de mobilité, soit par CZE (ligne en pointillé) ou par LDE (ligne continue) (C). Conditions de séparation: capillaire de silice fondue: 50,0 µm d.i., 35,0 cm de longueur totale, 26,5 cm de longueur effective; injection: 10 s à 20 mbar; tension appliquée: 12 kV; détection par absorption UV à 200 nm; température capillaire: 25 ∘C. (n = 4 répétitions, et les barres d'erreur représentent l'écart-type).

Concernant les NPs hydroxylées, une augmentation progressive du diamètre hydrodynamique au cours du temps a été mis en évidence à des valeurs de pH de 6,5 et au-dessous (Figure A-2.1.3A), indiquant le début de l'agrégation des particules. Outre le déplacement des pics électrophorétiques (Figure A-2.1.3B), une agrégation sévère à pH 6,0 a été mise en évidence par l'apparition de pics artefacts correspondant à des agrégats qui migrent à une vitesse aléatoire. Les potentiels zeta déterminés à partir des mesures de mobilité à la fois par LDE et EC ont été constants sur tout l'intervalle de pH 7,0-8,0 (Figure A-2.1.3C). Il doit être noté que ces valeurs du potentiel zêta déterminées par LDE et EC pour ZGO-OH dans les mêmes conditions (tampon phosphate 30 mM dans un gradient de pH) présentent la même évolution, mais pas la même valeur. Les valeurs absolues du potentiel zêta dérivée de mesures de mobilité par CE étaient environ 11,0 mV supérieures par rapport à ceux obtenus par LDE. Cette divergence est généralement observée dans la littérature, où une tendance à des valeurs absolues plus élevées de mobilité électrophorétique déterminée par EC est remarque par rapport aux valeurs de LDE ou des autres techniques similaires comme la vélocimétrie laser Doppler (LDV) [265, 271, 272].

Puis des séparations successives de ZGO-NH$_2$ par CZE aux différentes étapes du traitement ont été effectués dans des capillaires modifiés avec du bromure de didodécyldiméthylammonium (DDABr) (pour éviter d'adsorption des NPs à la surface du capillaire) en utilisant d'acide (N-(2-hydroxyéthyl pipérazine-N'-(2-éthanesulfonique) (HEPES) ou d'acide 3-(N-morpholino) propane sulfonique (MOPS) comme électrolyte support. Lors de l'aminosilanisation, l'application d´une étape de température de 100 ou 150 ° C semble améliorer la liaison de l'APTES initialement absorbée à la surface de la nanoparticule, et comme conséquence la stabilité des ZGO-NH$_2$.

En ce qui concerne les NPs finales PEGylées (ZGO-PEG), la stabilité colloïdale a été étudiée dans des tampons phosphate, MOPS et HEPES dans la gamme de force ionique de 30-150 mM. Le diamètre hydrodynamique des ZGO-PEG était constant (environ 180 nm) au moins pendant les 3 premières heures après l´arrêt de la sonication dans ces deux types de tampons (anioniques et zwitterioniques).

À cette gamme de force ionique et dispersées dans un tampon phosphate à pH 7,4, les ZGO-PEG migrent à une valeur de mobilité (très légèrement négative proche de celle de l'électroosmose, qui est en accord avec une densité de charge quasi-neutre des ZGO-PEG due à la présence de la couche de PEG. Lorsque la force ionique est augmentée (de 30 à 150 mM), les profils électrophorétiques des particules et leur mobilité n'ont pas été modifiés, indiquant la conservation des propriétés des particules en termes de taille hydrodynamique et de charge de surface ainsi que de stabilité colloïdale.

Les techniques de CE et LDE ont permis aussi d'étudier l'effet de la force ionique sur le potentiel zeta de ZGO-PEG dans des tampons phosphate et MOPS à ces forces ioniques. Seulement des légères différences de ζ ont été trouvées en comparant la EC et LDE (moins de 1,0 mV de différence). Par conséquence, la stabilité colloïdale ZGO-PEG dans le temps a été démontrée dans ces solutions de dispersion classiques.

A2.2. Évaluation des interactions entre ZGO-PEG et l'albumine par la méthode électrocinétique de Hummel-Dreyer

Etant donné que la tendance actuelle d'application des nanoparticules pour l'imagerie biomédicale semble prometteuse, des méthodes et des modèles permettant de mesurer et de manipuler leur pharmacocinétique, biodistribution et toxicité, méritent une attention particulière, entre autres au moyen de l'évaluation quantitative des interactions non spécifiques entre les nanoparticules et les protéines plasmatiques. Dans cette section, est présentée une méthode innovante pour l'évaluation de ces interactions: la méthode électrocinétique de Hummel-Dreyer. Cette section est divisée en deux parties. Tout d'abord, les aspects méthodologiques et la validation de la méthode Hummel-Dreyer (HDCE) pour l'évaluation des interactions entre ZGO-PEG et l'albumine de sérum bovin (BSA) et d'autre part, l'application de cette méthode pour l'optimisation du temps d'aminosilanization appliqué dans la séquence des réactions nécessaires pour obtenir des nanoparticules PEGylées avec permanence optimisée dans la circulation sanguine.

Différentes façons d'aborder les paramètres d'interaction entre un substrat et un ligand peuvent être développées, en fonction de la force et de la cinétique d'association/dissociation [169]. La méthode HDCE, basé sur des mesures d'aire des pics, a permis la caractérisation des interactions entre objets avec une cinétique de dissociation rapide [301].

Dans cette méthodologie le capillaire est rempli d'électrolyte de séparation contenant le ligand à des concentrations variables connues [L]. Un étalonnage externe est réalisé par injection et séparation d'un volume constant d'électrolyte dépourvu de ligand ou substrat. Un "pic négatif" apparaît en raison l'absence locale de [L] dans l'électrolyte de séparation (BGE, background électrolyte). Pour l'étude des interactions, le même volume de substrat à une concentration fixe ([S], inférieure à [L], dispersé dans le BGE est ensuite injecté et séparé, et deux pics peuvent apparaître dans l'électrophérogramme [241, 294, 301]. Le "pic positif" correspond au substrat libre, tandis qu'un "pic négatif" est provoqué par l'absence locale de [L] dans l'échantillon et par sa complexation avec le substrat (Figure A-2.2.1). À partir des mesure de l'aire du «pic négatif» de l'échantillon et de l'étalonnage externe, on peut accéder à la concentration du ligand lié au substrat, et donc à la constante d'interaction et au nombre de sites d'interaction de ligand sur le substrat. Dans notre cas, la NP est considérée de par sa taille comme le substrat, et la protéine comme le ligand.
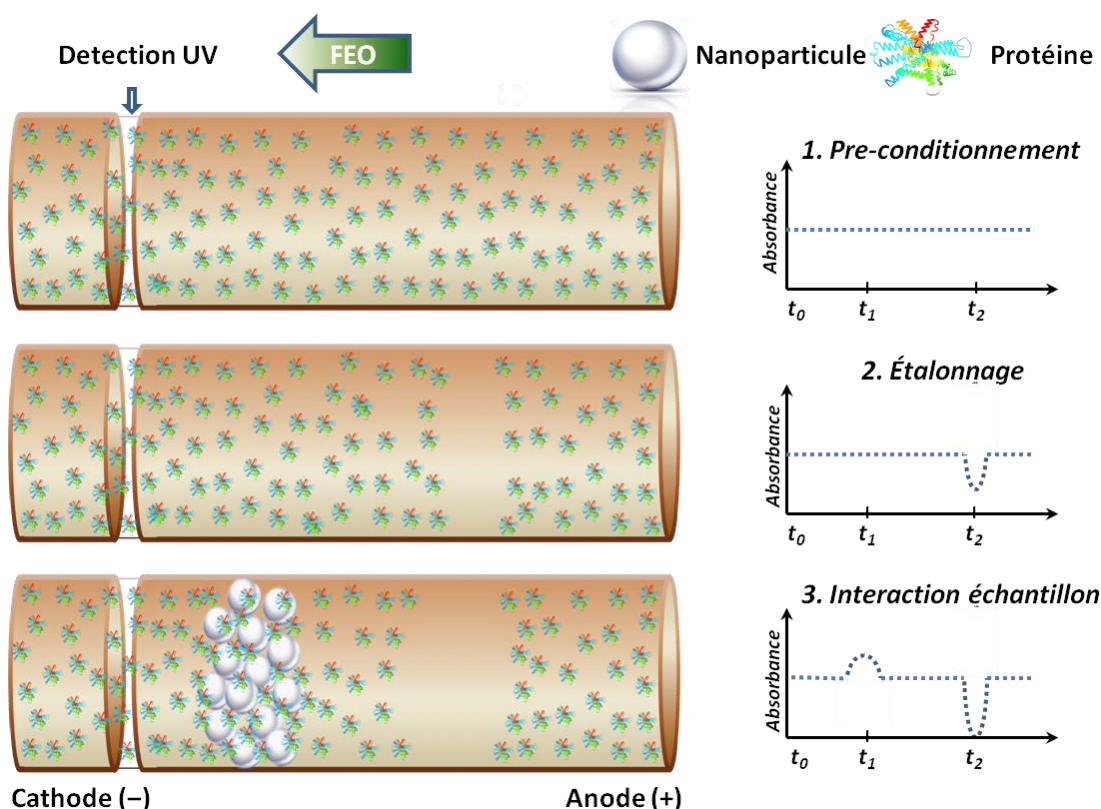
Fig. A-2.2. 1. Représentation schématique de la méthode électrocinétique de Hummel-Dreyer pour l'évaluation des interactions entre nanoparticles et protéines. EOF: Écoulement électroosmotique.

En supposant un système dans lequel une protéine peut potentiellement se lier à de multiples sites de liaison indépendants sur la surface des NPs, l'interaction peut être décrite sous la forme (Eq. A1):

$$S + nL \rightleftharpoons SLn \qquad \text{Eq. A1}$$

où n est le nombre total de sites de liaison. Si l'on considère que les n sites indépendants ont une énergie identique, l'interaction élémentaire (une molécule de protéine sur un site à la surface d'une NP) est définie par une constante de liaison Ka. La fraction de protéines effectivement liée par nanoparticule [294] peut être définie comme "r" (Eq. A2):

$$r = \frac{[L]_{bound}}{[S]_{total}} = n \; \frac{[L]Ka}{[L]Ka+1} \qquad \text{Eq. A2}$$

La valeur de "r" varie de 0 à n. Alors, l'équation 2 peut être linéalisée de la façon suivante (Eq. A3):

$$\frac{r}{[L]} = -K_a r + K_a n \qquad \text{Eq. A3}$$

S'on trace r/[L] en fonction de r, on peut accéder à la linéarisation de Scatchard, qui permet le calcul de la constante d'interaction (pente de la droite), et au nombre de sites d'interaction (intersection avec l'axis des abscisses) sur la surface des NPs.

La Figure A-2.2.2 présente à titre d'exemple les électrophérogrammes réalisés pour l'étalonnage externe correspondant à une force ionique 60 mM, comprenant une gamme de concentration de protéines entre 0 et 0,9 µM.
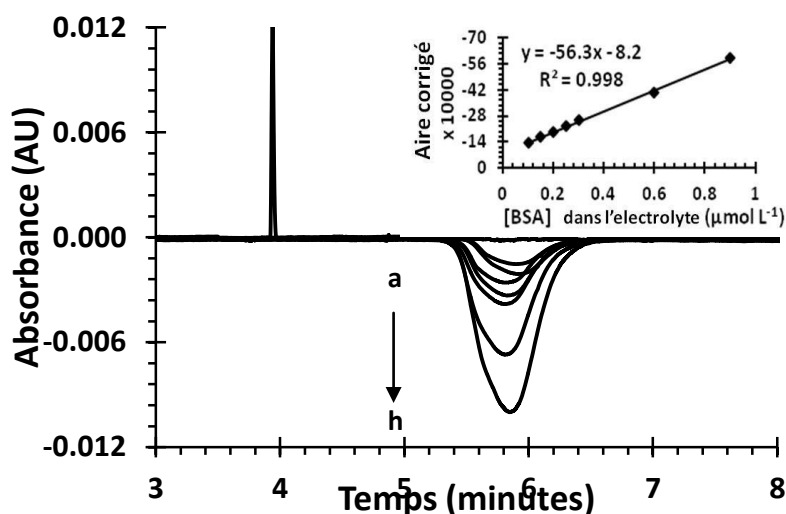
Fig. A-2.2. 2. Électrophérogrammes représentatifs à λ = 200 nm pour la calibration externe d'accord à la méthode de Hummel-Dreyer. Les pics de vacance correspondent à l'injection d'électrolyte support (tampon phosphate pH 7.4 à force ionique 60 mM) dans un capillaire rempli avec du BSA à des concentrations

différentes (a-DMF, b-0,10, c-0,15, d-0,20, e-0,25, f-0,30, g-0,60 et h-0,90 µmol L⁻¹). La courbe d'étalonnage insérée correspondant à ces mesures.

Pour évaluer les paramètres d'interaction avec les protéines, 10 nL d'une suspension 3,88 nM de ZGO-PEG ont été injectés dans les mêmes conditions que pour l'étalonnage (Figure A-2.2.3)
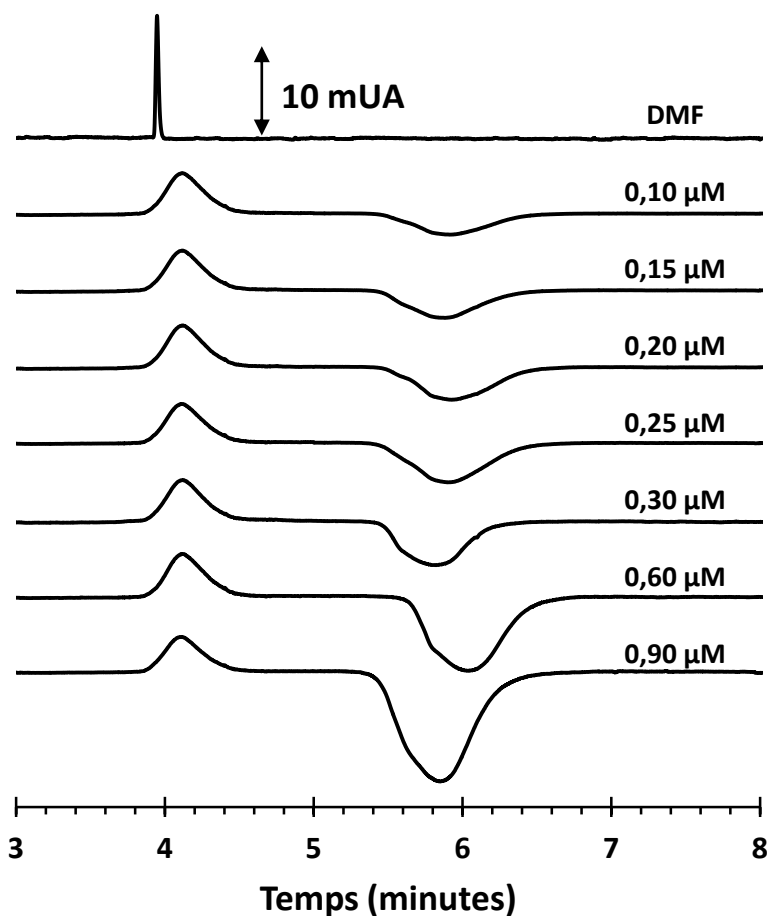
Fig. A-2.2. 3. Electrophérogrammes représentatifs obtenus à λ = 200 nm avec la méthode Hummel-Dreyer pour l'analyse des interactions BSA/ZGO-NP dans des tampons phosphate (pH 7.4) à force ionique 60 mM.

Un "pic positif" apparait à une mobilité de -1.2x10⁻⁵ cm²V⁻¹s⁻¹ correspondant à la mobilité des ZGO-PEG, quelle que soit la concentration des protéines dans le BGE. La forme de ce pic ne varie pas ni dans sa forme ni dans son intensité. Le "pic négatif" est dû à la vacance de la protéine provenant de l'interaction avec les NPs injectées et l'absence locale de protéines due à la présence du BGE. Comme le « pic positif » ne varie pas quelque soit la concentration de protéines, l'hypothèse d'une dissociation rapide de S-L semble valable.

A partir des aires des pics de vacance obtenues lors de l'étalonnage (A$_c$) et des aires des pic négatifs résultants de l'injection du substrat (A$_s$) dans les mêmes conditions expérimentales, la concentration de ligand lié [L]$_b$ peut être déterminée [294]. La quantification de [L]$_{liée}$ permet alors la détermination de l'isotherme d'absorption correspondant à r versus $[L]_t$ (Figure A-2.2.4A).

La valeur de [L]$_{liée}$ diminue lorsque la force ionique augmente, en raison de la compétition entre les contre-ions et la BSA pour l'interaction avec la surface des NPs, à savoir l'effet d'écrantage. La linéarisation de ces isothermes mène à la courbe de Scatchard (Figure A-2.2.4B). La bonne reproductibilité des mesures reflète la précision de cette méthodologie, et permet la détermination de la constante d'association et le nombre de sites de liaison (n) (Tableau A.2-1). Comme prévu de la Figure A-2.2.4A, les valeurs de Ka et n diminuent lorsque la force ionique augmente, en raison de la condensation des contre-ions et donc la compétition pour l'interaction, ce qui indique que des interactions électrostatiques se produisent entre les ZGO-PEG et la BSA.

Cette méthodologie HDCE permet alors de déterminer rapidement et facilement les paramètres de liaison pour ce type de complexes. Contrairement à d'autres méthodes proposées, elle permet d'atteindre l'équilibre directement dans le capillaire sans étapes supplémentaires de pré-incubation, ce qui peut altérer l'intégrité chimique des groupes fonctionnels autour des nanoparticules, par exemple par des réactions d'hydrolyse [308].
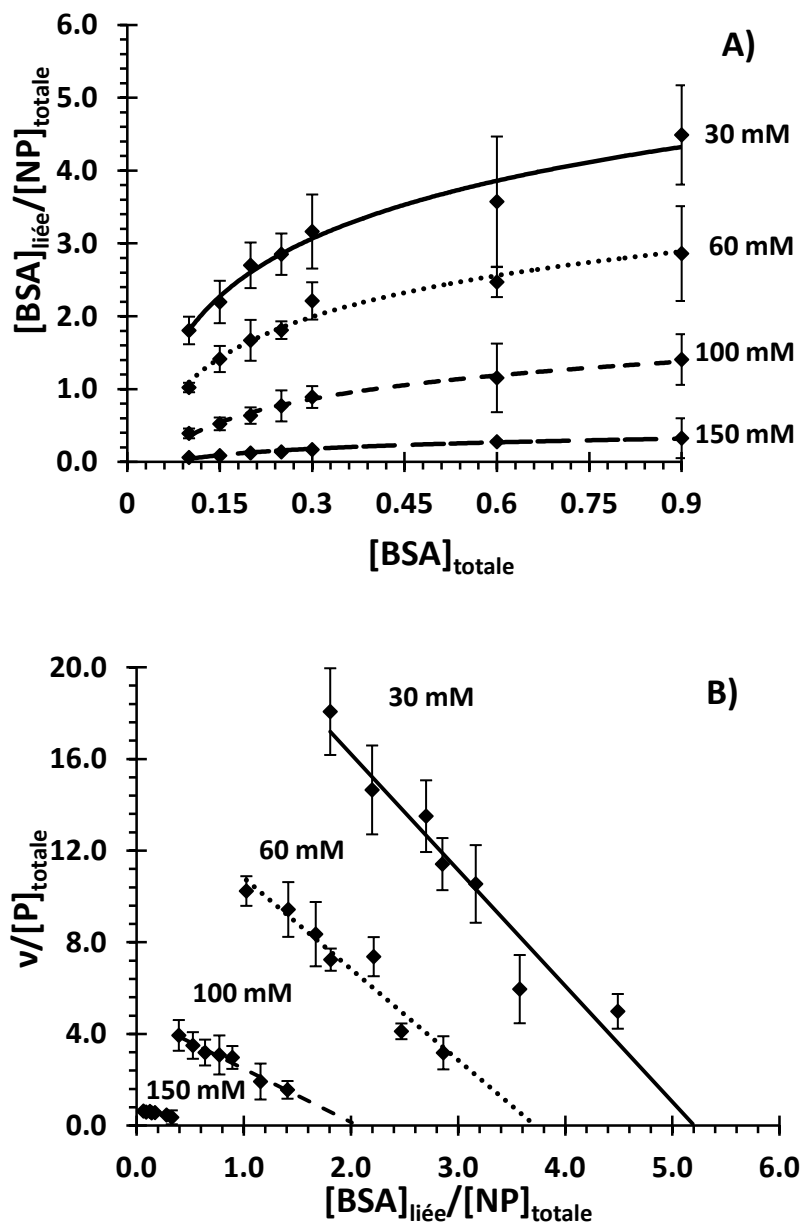
Fig. A-2.2. 4. A) Courbes d'association pour des interactions entre la BSA et les ZGO-PEG dans le tampon phosphate (pH 7.4) à force ionique variée. B) Courbes obtenues d'accord à l'équation de Scatchard. Les barres d'erreur indiquent ± écart type de quatre mesures.

Tableau A.2- 1. *Résumé des paramètres d'ajustement selon la méthode Hummel-Dreyer pour les complexes BSA/ZGO-PEG obtenues par l'équation de Scatchard.*

Paramètre	Force ionique			
	30 mM	**60 mM**	**100 mM**	**150 mM**
Ka $_{Scatchard}$ (M^{-1})	$5.06 \pm 0.64 \times 10^6$	$3.98 \pm 0.38 \times 10^6$	$2.33 \pm 0.23 \times 10^6$	$9.53 \pm 0.18 \times 10^5$
n	5.21 ± 0.27	3.71 ± 0.13	2.06 ± 0.22	0.74 ± 0.15

Un paramètre facilement contrôlable pour obtenir des ZGO-PEG avec différents degrés d'affinité pour les protéines est le temps de réaction pour l'étape d'aminosilanisation. Dans notre séquence de fonctionnalisation ZGO-OH → ZGO-NH$_2$ → ZGO-PEG, le temps de reaction entre les ZGO-OH et le (3-aminopropyl) triéthoxysilane (APTES) (3 ou 5 heures) a été fixé à 3 h (ZGO-NH$_2$ (3h)) ou 5 h (ZGO-NH$_2$(5h)) La dernière étape, le couplage des molécules de PEG à partir de ces NPs ZGO-NH2 a ensuite été réalisée en parallèle dans les mêmes conditions et temps de réaction (ZGO-PEG$_{3h}$ ou ZGO-PEG$_{5h}$). La caractérisation colloïdale de ces objets a été effectuée après chaque étape de fonctionnalisation en termes de diamètre hydrodynamique et potentiel zêta. Les électrophérogrammes représentatifs pour l'évaluation des interactions entre ces objets et dans ce cas l'albumine sérique humaine (HSA) sont présentés à la Figure A-2.2.5.
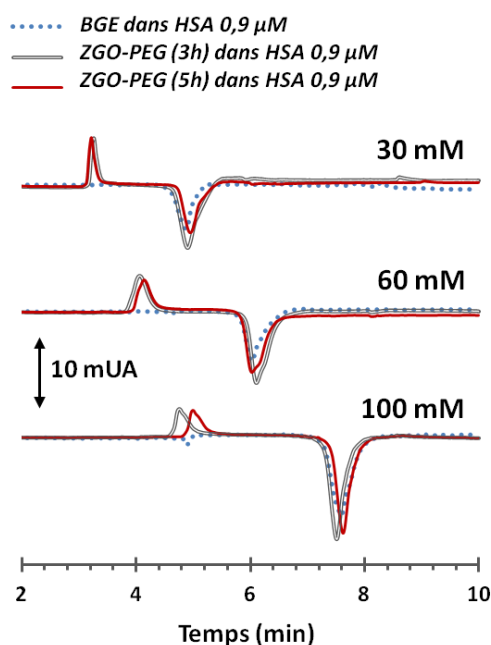
Fig. A-2.2. 5. Électrophérogrammes représentatifs pour l'évaluation des interactions entre ZGO-PEG$_{3h}$ ou ZGO-PEG$_{5h}$ et la HSA selon la méthode Hummel-Dreyer à forces ionique différentes. La concentration de la HSA pour cet exemple est de 0,9 μM.

Pour l'analyse stœchiométrique des interactions, les concentrations de HSA ont été variées dans la gamme de 0,1 à 0,9 µM. Nous avons pu distinguer les différences de grandeur pour les absorbances négatives entre les électrophérogrammes de l'étalonnage (injection de BGE dans le capillaire rempli de protéines) et les signaux obtenus quand les ZGO-PEG$_{3h}$ ou ZGO-PEG$_{5h}$, ont été injectés dans le capillaire pré-conditionné de la même façon. Grâce à l'intégration de ces pics négatifs, les aires ont été obtenues et comparées avec l'étalonnage.

Un bilan des paramètres obtenus selon l'équation de Scatchard est regroupée dans le Tableau A.2-2.

Tableau A.2- 2. Paramètres d'interaction d'accorde à la méthode Hummel-Dreyer pour l'étude des complexes HSA/ZGO-PEG$_{3-5h}$.

Paramètre	Force ionique					
	30 mM		60 mM		100 mM	
	3 h	5 h	3 h	5 h	3 h	5 h
Ka $_{Scatchard}$ (x10^6/M)	6.64±0.42	5.33±0.44	5.63±0.52	4.10±0.44	3.63±1.09	1.63±0.50
n	7.13±0.05	5.67±0.20	4.41±0.47	3.67±0.72	2.81±0.32	2.55±0.61

De nouveau, comme pour l'analyse des interactions avec la BSA, l'effet de la force ionique a été mis en évidence, induisant une interaction plus faible à force ionique plus élevée.. En outre, des valeurs plus élevées pour la constant d'association ont été obtenues pour les interactions ZGO-PEG$_{3h}$/HSA par rapport à ZGO-PEG$_{5h}$/HSA. Ainsi une aminosilanisation de 5h permet d'obtenir un recouvrement par les chaînes PEG générant une passivation de la surface légèrement plus efficace qu'une aminosilanisation de 3h. Des différences significatives dans le degré de saturation et le nombre de molécules de protéines en interaction par chaque nanoparticule ont été déterminées. La méthodologie utilisée dans ce travail peut aider à l'optimisation et le contrôle de la production de nanoparticules fonctionnalisées avec l'objectif d'augmenter leur permanence dans la circulation sanguine avant l'analyse *in vivo*.

A2.3. Évaluation des interactions entre ZGO-PEG et deux protéines plasmatiques l'Apolipoprotéine E et l'albumine de sérum humain : effets compétitifs

La EC a démontré être un outil performant pour la caractérisation des NP dans des milieux physiologiquement pertinents, et pour l'évaluation des interactions des NPs avec des biomolécules, dans le but d'une compréhension fine de la couronne de protéines plasmatiques.

Ici, une étude a été menée sur non plus une protéine plasmatique unique, mais un mélange de deux protéines : l'albumine de sérum humain, protéine plasmatique de concentration élevée, et l'Apolipoprotéine E, dont il a été démontré qu'elle était liée au transport actif de nanoparticules ou de molécules à travers la barrière hemato-encéphalique. Trois stratégies différentes ont été utilisées pour comparer étudier ces deux interactions possibles par électrophorèse capillaire EC: i) Evaluation des interactions des NPs avec les protéines individuelles dans les mêmes conditions d'analyse, et comparaison de leurs constantes d'interaction, ii) incubation des NPs avec l'une des protéines et injection du mélange incubé dans un milieu de séparation comprenant la deuxième protéine, et vice versa, et iii) injection de la NP dans un électrolyte contenant le mélange des deux protéines à des rapports de concentration variés.

Tout d'abord, une méthode consistant en l'injection des NPs dans un capillaire préalablement préconditionné avec une protéine à des concentrations variées a été appliquée pour l'analyse des interactions. Les profiles électrophorétiques sont différents lors de l'injection de HSA ou ApoE dans les mêmes conditions analytiques (Figure A-2.3.1). L'interaction avec l'HSA donne des profils électrophorétiques identiques à ceux pour la BSA : un « pic positif » et un « pic négatif » à des mobilités qui restent constantes quelle que soit la concentration de la protéine (Figure A-2.3.1A). Par contre, concernant l'ApoE, il n'apparait qu'un pic positif dont la mobilité électrophorétique évolue en fonction de la concentration en protéine (Figure A-2.3.1B). Ainsi, le même protocole permet de générer soit le mode Hummel-Dreyer (pour HSA) soit le mode affinité (pour ApoE), selon la force et la cinétique des interactions.
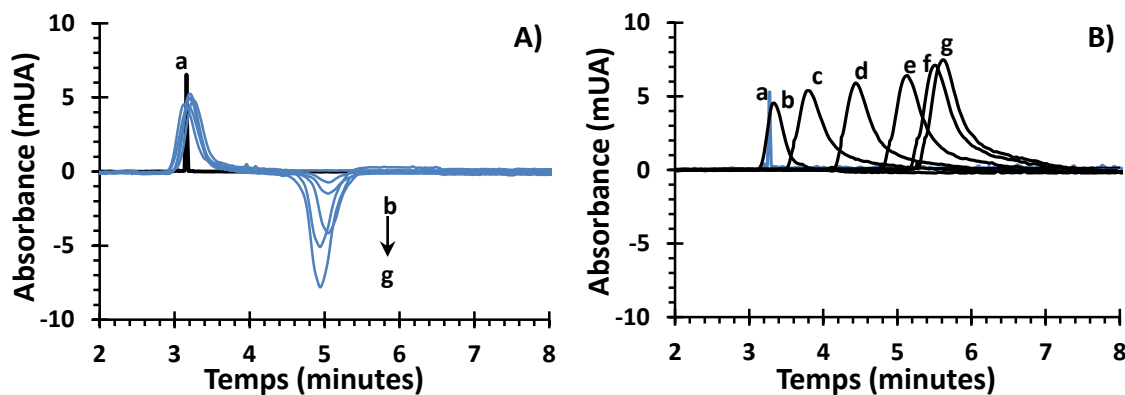
Fig. A-2.3. 1. Électrophérogrammes représentatifs pour l'évaluation des interactions selon la méthode Hummel-Dreyer pour A) HSA/ZGO-PEG et B) ApoE/ZGO-PEG dans le tampon de carbonate d'ammonium (pH 8.0) à force ionique 30 mM. E=14 kV. Identification des pics: a) DMF, b) 0, c) 0,12, d) 0,24, e) 0,72, f) 0,96, et g) 1,44 µM de la protéine correspondante.

Dans ce cas, un signal spécifique pour l'ApoE ou leur vacance n'a pas été détecté à la longueur d'onde analysé. Selon la loi de Beer-Lambert, les coefficients d'extinction molaire déterminés dans les conditions d'analyse utilisées par électrophorèse capillaire de zone (ACB 30 mM, et tension appliqué de 14 kV dans un capillaire de diamètre intérieur de 50 µm) à 200 nm sont $\varepsilon = 1.48 \times 10^6$ cm^{-1}M^{-1} pour la HSA et $\varepsilon = 1.17 \times 10^5$ cm^{-1}M^{-1} pour l'ApoE. Les valeurs obtenues pour

ApoE sont un ordre de grandeur plus faible par rapport à ceux de la HSA, ce qui peut expliquer l'absence de détection d'un signal de l'ApoE à ces concentrations.

D'après ces évolutions électrophorétiques, il apparait une stabilité plus importante du complexe ZGO- PEG/ApoE par rapport au complexe ZGO-PEG/HSA. Ceci peut être relié à une cinétique de dissociation du complexe plus importante pour la HSA, puisque les profiles électrophorétiques suivent le mode de Hummel-Dreyer, et donc aucun pic de complexe n'est mis en évidence.

La carence de changements dans la mobilité électrophorétique des pics de ZGO-PEG quand ils ont été soumis à une interaction avec des concentrations croissantes de HSA, à différence des profils électrophorétiques obtenus pour les interactions de ZGO-PEG avec l'ApoE est un premier indicateur de la stabilité plus forte des complexes ZGO- PEG/ApoE par rapport à leur complexe homologue ZGO-PEG/HSA. Ceci est une nette différence dans la cinétique de liaison puisque le complexe ZGO-PEG/HSA n'a pas été détectée, ce qui indique également une dissociation relativement plus rapide par rapport au complexe ZGO-PEG/ApoE.

Afin d'obtenir les paramètres d'interaction, les modèles de linéarisation des isothermes de Scatchard et de Hill ont été employés et résumées dans le Tableau A.2-3.

Tableau A.2- 3. Résumé des paramètres d'interaction obtenues d accord a l'analyse HD-CE pour HSA/ZGO-PEG, et ACE pour les complexes ApoE/ZGO-PEG dans le tampon de carbonate d'ammonium pH 8.0 à force ionique 30 mM.

	$Ka_{Scatchard}$ (M^{-1})	Numéro de saturation (n)
HSA	$4.60 \pm 0.41 \times 10^{6}$	4.35 ± 0.24
	Ka_{Hill} (M^{-1})	Coopérativité (n_H)
ApoE	$1.96 \pm 0.25 \times 10^{10}$	1.47 ± 0.07

Une association plus forte pour ZGO-PEG/ApoE par rapport à ZGO-HSA a été vérifiée par ces calculs, ce qui entraîne une différence de Ka de quatre ordres de grandeur. La valeur de n indique que 4,35 molécules de HSA on été en interaction pour chaque nanoparticule, tandis que la valeur de n_H indique un faible coopérativité ($n_H > 1$).

Dans la littérature, il a été montré par 2D-PAGE que la PEGylation des NPs de poly-hexadecylylcyanoacrylate (PHDCA) induit une augmentation de l'adsorption de l'ApoE (de 0,15 à 0,23% de la quantité totale de protéines adsorbées dans le sérum), et au contraire une diminution de l'adsorption de l'albumine (de 9,83 à 8,85 %) [347]. Des résultats similaires ont été trouvés pour des NPs de PHDCA, pour lesquelles l'adsorption de l'ApoE a augmenté de 2,17 à 3,82% quand ils étaient PEGylées, tandis que l'adsorption de l'albumine diminue de 18,28 à 17,83% après la

PEGylation [69]. Cette observation à partir des résultats obtenus par des groupes indépendants suggère une plus grande affinité des surfaces des NPs PEGylées pour l'adsorption de l'ApoE par rapport à la HSA, ce qui est bien corrélé avec nos observations.

Afin de comparer les interactions ZGO-PEG/protéine dans un système contenant les deux protéines HSA et ApoE, les trois stratégies décrites précédemment ont été mises en œuvre. Dans la Figure A-2.3.2, nous montrons un panorama complet de ces études d'interactions ZGO-PEG avec un mélange HSA/ApoE à des rapports variés.
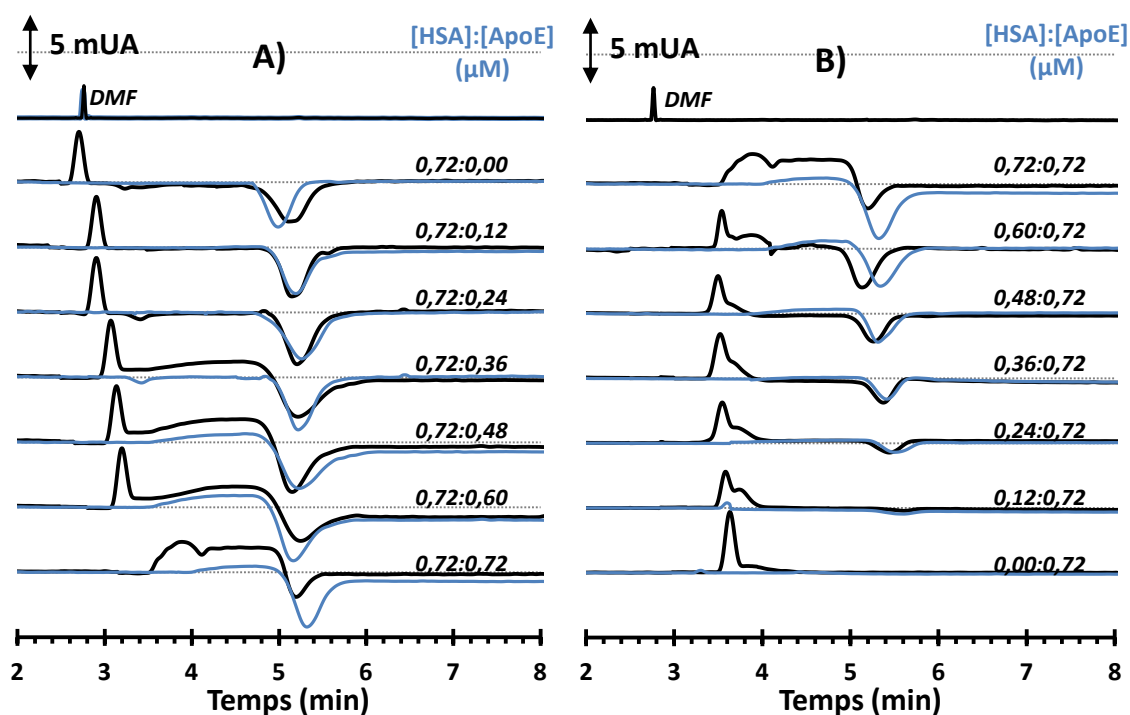
Fig. A-2.3. 2. Electropherogrammes pour l'évaluation des interactions entre ZGO-PEG avec des mélanges d'ApoE et HSA: en A) la concentration de la HSA a été fixé et l'ApoE variée. En B), la HSA a été variée, tandis que la concentration d'ApoE reste constante. Les signales en lignes noires correspondent à l'injection des NPs pour l'évaluation des interactions, tandis que les lignes bleus correspondent à l'injection d'électrolyte support. Pour l'étalonnage les valeurs indiquent les concentrations totales des protéines dans le mélange des protéines en considérant la dilution. BGE: tampon de carbonate d'ammonium (pH 8.0) à force ionique 15 mM. E=14.0 kV.

Dans les Figures A-2.3.2A et 2.3.2B les lignes bleues superposées montrent clairement une interaction entre la HSA et l'ApoE, générant un pic positif entre les deux pics de la NP et de la HSA. Ces résultats sont concordants avec la littérature qui a démontré une association de la HSA avec plus de 35 protéines , dont les apolipoprotéines, l'angiotensinogène, la céruloplasmine, la clustérine, l'hémoglobine, le plasminogène, la prothrombine et la transferrine [348]. Ainsi, dans notre système d'étude, le système d'interaction est à trois partenaires : les NPs, la HSA et l'ApoE,

chacun des protagonistes pouvant interagir avec les deux autres, ce qui complexifie les électrophérogrammes.

Lorsque la concentration en HSA dans le capillaire pré-conditionné a été fixée à 0,72 µM et la concentration de l'ApoE varie de 0 à 0,72 µM (Figure A-2.3.2A), il apparait pour les faibles concentrations en ApoE (inférieures à 0,36 µM) une évolution de la mobilité du pic de NPs, montrant une interaction ZGO-PEG/ApoE, ainsi que la présence du « pic négatif », à une mobilité constante, de HSA, indiquant une vacance en HSA, pouvant résulter uniquement de l'injection d'une zone exempte de HSA ou accompagnée d'une interaction ZGO-PEG/HSA.

Si pas d'évolution du pic de HSA : Ainsi, à ces faibles concentrations, l'interaction entre NPs et ApoE prédomine par rapport à celle entre NPs et HSA.

Si évolution : Ainsi, à ces faibles concentrations, l'interaction entre NPs et ApoE prédomine par rapport à celle entre NPs et HSA, mais les deux coexistent.

Lorsque la concentration en ApoE est supérieure à 0,36 µM, un « plateau » situé entre le pic de ZGO-PEG/ApoE et le pic de vacance de HSA a été mis en évidence, en comparaison avec un système dans lequel seul le tampon carbonate d'ammonium a été injecté dans le capillaire contenant le mélange de protéines. Deux hypothèses peuvent alors être avancées : ce plateau peut être généré par l'interaction entre les deux protéines, comme la littérature l'indique. Le plateau qui apparait aux mêmes mobilités et avec un profil identiques lorsque seul le BGE est injecté semble indiquer que cette hypothèse est recevable. La deuxième hypothèse serait une interaction entre les deux protéines qui génère ensuite un complexe triple NP/HSA/ApoE ou NP/ApoE/HSA, qui est favorisé par cette interaction entre les protéines.

Lorsque l'expérience symétrique est effectuée, c'est-à-dire lorsque la concentration en ApoE dans le capillaire pré-conditionné a été fixée à 0,72 µM et la concentration en HSA varie de 0 à 0,72 µM ((Figure A-2.3.2B), il semble que le complexe ZGO-PEG/ApoE reste présent quelques soient les conditions expérimentales. De plus, un pic de vacance de HSA apparait (vérifier sur les intensités pour voir si c'est juste de la vacance ou aussi interaction) ainsi que le plateau mis en évidence précédemment.

Ces expériences croisées démontrent une affinité plus élevé des ZGO-PEG pour l'ApoE par rapport à la HSA dans un mélange protéique compétitif, même lorsque la concentration de HSA est supérieure à l'ApoE.

La méthodologie utilisée dans le présent ouvrage peut également être potentiellement adaptée pour étudier d'autres molécules interagissant, comme d'autres types de nanoparticules avec d'autres protéines spécifiques. Ce travail ouvre également des perspectives pour l'évaluation quantitative de l'interaction des NPs dans un système binaire de protéines au moyen du calcul des paramètres de liaison.

A2.4. Effets de la photo-activation de $ZnGa_{1.995}Cr_{0.005}O_4$ sur la toxicité des cellules de cancer du sein

Cette partie du travail a été focalisée sur les effets toxicologiques photo-induits des nanoparticules à luminescence persistante. Comme indiqué précédemment, les nanoparticules peuvent stimuler la production des radicaux libres par des composants cellulaires. Cependant, la possibilité d'une réaction des ZGO-NPs avec des milieux aqueux après stimulation lumineuse peut également contribuer à l'augmentation des concentrations de ROS. Pour vérifier cette hypothèse, la production de radicaux libres par ZGO-NPs en absence de cellules a été analysée en utilisant le colorant tétrazolium XTT, qui est réduit à leur forme soluble (formazan) par les radicaux superoxydes dans conditions standard.

Sur la Figure A-2.4.1A sont montrés les changements dans le spectre d'absorption des suspensions des nanoparticules en utilisant le XTT pendant les deux premières heures d'irradiation UV.

L'effet de l'irradiation par la lumière visible a été également testé, et les résultats sont présentés Figure A-2.4.1B. Dans les deux cas, un pic avec une absorbance maximale à $\lambda = 470$ nm était présent, et son intensité a augmenté avec le temps dans les deux premières heures. L'augmentation de l'absorption à cette longueur d'onde indique une augmentation de la production de $O_2^{\bullet-}$.

Dans la Figure A-2.4.1C est comparé l'effet du type de lumière (visible et UV) sur la production de superoxyde par rapport à l'obscurité. Aucune différence significative n'a été observée dans le spectre des ZGO-OH photo-stimulés, alors qu'une différence nette était présente par rapport aux nanoparticules ZGO-OH maintenues dans l'obscurité. La génération des ROS est déterminée par un procédé de transfert interfacial d'électrons. Quand les électrons sont promus à partir de la bande de valence vers la bande de conduction, un trou est également généré de manière concomitante dans la bande de valence. Les trous et les électrons excités sont alors capables de réagir avec un donneur ou accepteur d'électrons, respectivement [356]. Dans ce travail, les électrons photo-excités réagissent avec l'oxygène moléculaire dissous pour produire $O_2^{\bullet-}$. Aucune variation des pics d'absorption n'a été détectée pour toutes les suspensions de ZGO-PEG par action de la lumière dans les deux premières heures d'irradiation, par rapport a celles gardées dans l'obscurité (Figure A-2.4.1D). La diminution de la production de ROS par des ZGO-PEG par rapport à leur homologue hydroxylé est probablement due à la diminution des interactions directes entre la surface des nanoparticules et de la solution due à la présence de chaînes longues de polyéthylène glycol (5000 Da).
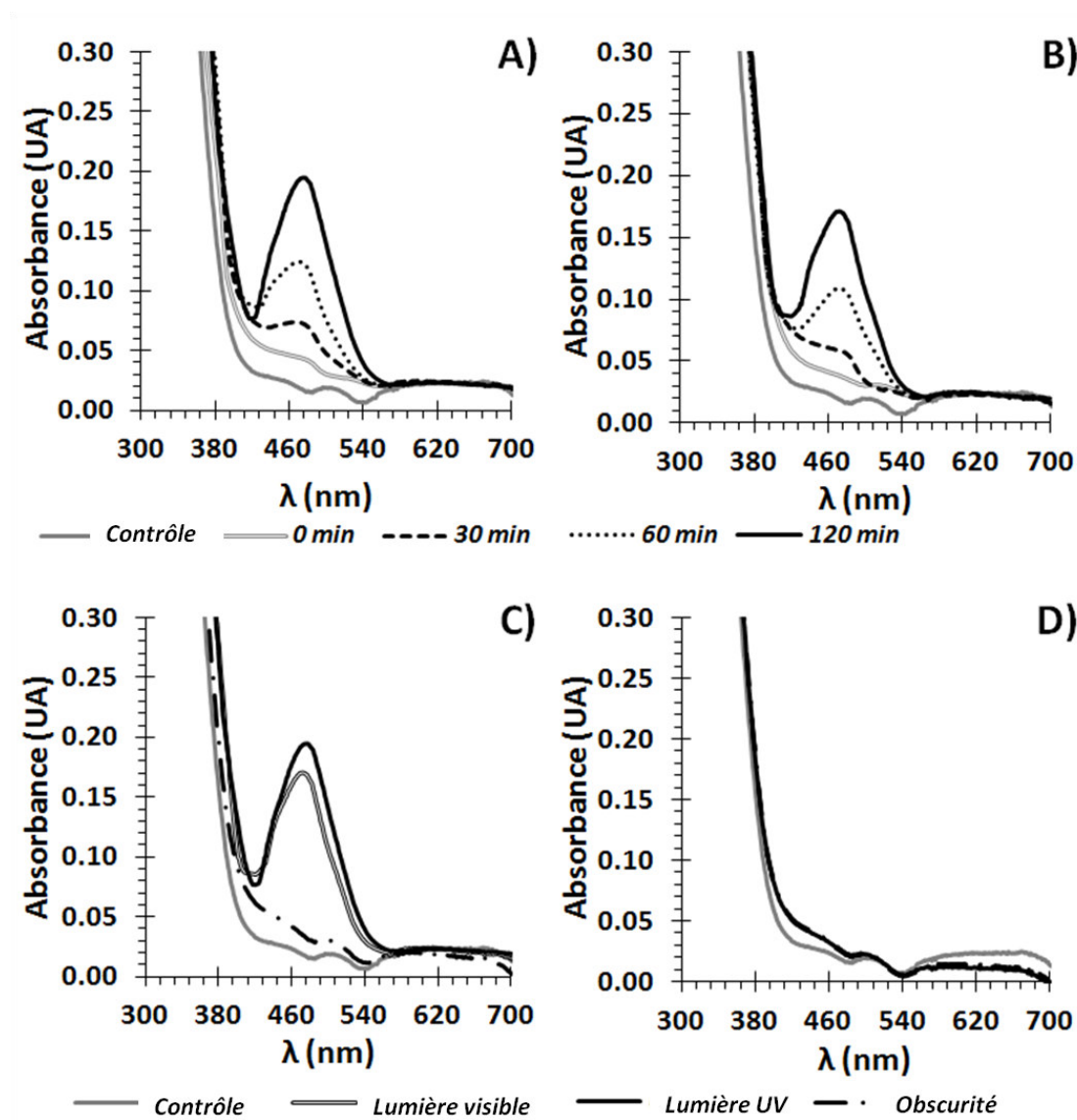
Fig. A-2.4. 1. Spectre UV-Visible pour l'évaluation de la production de $O_2^{\cdot-}$ dans le temps. A) ZGO-OH stimulé par la lumière UV, B) ZGO-OH stimulé par la lumière visible. Effet du type de la lumière sur le spectre UV-Visible pour l'évaluation de la génération de $O_2^{\cdot-}$ par C) ZGO-OH et D) ZGO-PEG après deux heures d'excitation comme indiqué par la réduction de XTT 100 μM.

En regardant l'application des ZGO-NPs, les cellules tumorales semblent être une cible importante pour les études de toxicité et les MCF-7 et MDA-MB-231 sont des lignées cellulaires standard pour la recherche *in vitro* du cancer du cancer du sein [366]. Pour cela, les ZGO-NPs ont été administrés aux cultures cellulaires de MCF-7 et MDA-MB-231 à des concentrations variées (pré-irradiés avec la lumière UV ou non irradiés), et les différents paramètres tels que la viabilité des cellules, la production des espèces réactives d'oxygène (ROS) et espèces réactives de nitrogène

(NOS) et l'internalisation cellulaire ont été évalués. Les cellules n'ont été jamais exposées à l'irradiation UV.

Les résultats de la viabilité cellulaire ont révélé une cytotoxicité dépendante de la dose de ZGO-OH après 24 heures d'incubation, tandis que la viabilité cellulaire n'a pas été modifiée par les ZGO-PEG aux mêmes doses et périodes de temps. En raison de la capacité des nanoparticules à luminescence persistante d'économiser l'énergie photonique pendant de longues périodes de temps, les ZGO-NPs ont été gardés dans l'obscurité une semaine avant les expériences pour éviter leur photostimulation par la lumière naturelle.

La génération des peroxydes aqueux [POx] au sein des milieux de culture de cellules cancéreuses après l'administration de ZGO-NP a été quantifiée par un essai colorimétrique commercialement disponible. Les résultats indiquent la production significative d'espèces d'oxygène par toutes les deux lignées cellulaires MDA-MB-231 et MCF-7 à des concentrations de 0,25 et 0,50 mg/mL de ZGO-OH. Les concentrations de peroxyde ont été augmentées dans les cellules traitées avec des nanoparticules pré-irradiées par rapport aux nanoparticules non irradiés. Aucune augmentation significative de la production de peroxyde n'a été détectée à toutes les concentrations de ZGO-PEG testées par rapport au contrôle. L'augmentation des concentrations de peroxyde dans les cellules par addition des nanoparticules de ZGO-OH photostimulées est bien corrélée avec l'augmentation de la mort cellulaire évaluée dans ce travail.

Afin de justifier les différences de toxicité entre les ZGO-OH et les ZGO-PEG, nous avons analysé l'internalisation des nanoparticules par les cellules de cancer du sein. À cet effet, les concentrations des nanoparticules appropriées ont été mises en incubation avec des cellules MDA-MB-231. Nous profitons des propriétés lumineuses des ZGO-NP pour les études d'internalisation cellulaire en utilisant la microscopie confocal (Figure A-2.4.2).
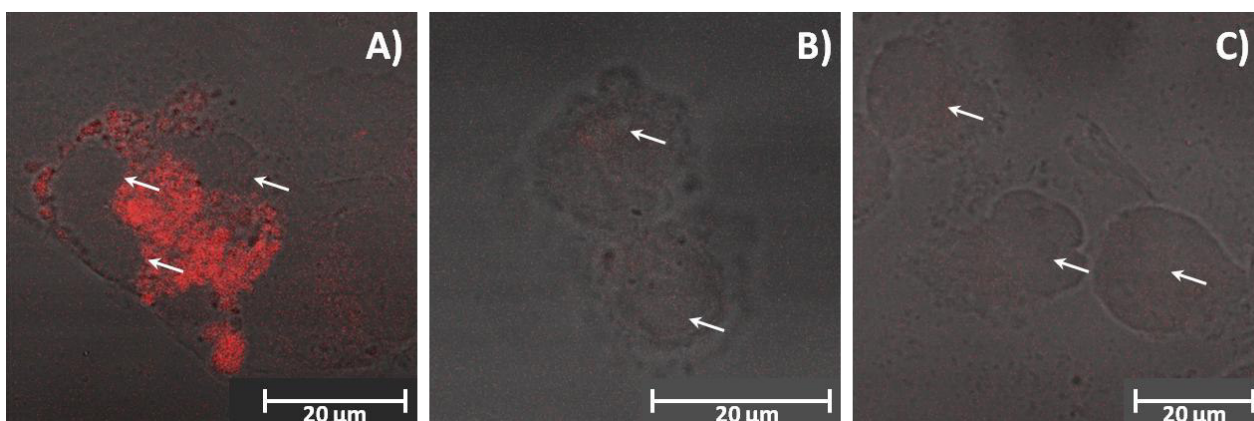
Fig. A-2.4. 2. Internalisation cellulaire in vitro de A) ZGO-OH, B) ZGO-PEG et C) Contrôle à [0,05 mg/mL] par MDA-MB-231 24 heures après l'administration. Les flèches indiquent les noyaux cellulaires.

Cette technique a été utilisée pour analyser les possibles effets toxiques des ZGO-NPs au niveau cellulaire sans nécessité de biomarqueurs fluorescents supplémentaires. Au niveau cellulaire, il est possible de voir l'agrégation des cellules de cancer du sein traitées avec des ZGO-OH, tandis qu'à l'échelle ultra-structurelle, il est possible de déterminer que les nanoparticules ont été dispersées dans le cytoplasme, mais pas dans le noyau des cellules. Nous avons constaté que les nanoparticules de ZGO-OH étaient internalisées par les cellules, puis déposées dans le cytoplasme (Figure A-2.4.2A). Cependant, les nanoparticules PEGylés n'ont été pratiquement pas internalisées par les cellules (Figure A-2.4.2B). Les nanoparticules PEGylées sont restées dans les milieux de culture cellulaire, et donc éliminés au cours du correspondant procédé de lavage des cellules avant l'analyse par la microscopie confocal.

Dans ce travail, l'effet protecteur du polyéthylène glycol en surface de la NP, contre l'absorption cellulaire et la toxicité, a été aussi démontré, probablement du à la diminution des interactions des nanoparticules avec des protéines ou des composants cellulaires en raison de l'encombrement stérique et aussi de l'augmentation de leur nature hydrophobe. L'absorption de ZGO-OH et leur induction de stress oxydant *in vitro* sont bien corrélées avec leur cytotoxicité. Contrairement aux ZGO-PEG, les ZGO-OH stimulent la production des peroxydes par les cellules, ce qui est bien en corrélation avec la réduction de la viabilité cellulaire. En outre, la production de superoxydes par les ZGO-OH en absence des cellules a été également démontrée dans ce travail, ce qui indique l'apport des effets photo-induits de nanoparticules à luminescence persistante sur la toxicité cellulaire. Des études complémentaires sont nécessaires pour l'évaluation de l'utilisation des ZGO-NPs en thérapie photodynamique, domaine dans lequel ce matériau peut agit comme nanosonde et photosensibilisateur, lequel peut signifier une alternative bimodale pour la détection et le traitement du cancer.

A2.5. Toxicité aiguë, à court et à long terme de nanosondes à luminescence persistante chez la souris

Le but de cette partie du travail était d'étudier les effets toxicologiques des ZGO-NPs. L'étude de leur potentielle toxicité est cruciale pour garantir leurs applications biomédicales. La biodistribution, génotoxicité, histopathologie, cytotoxicité structurelle et biocompatibilité générale des ZGO-NPs sont quelques uns des facteurs cruciaux à étudier. Afin de parvenir à une conclusion claire sur l'effet toxique potentiel de ces NPs, nous avons injecté des doses croissantes de ZGO-NPs (soit hydroxylées soit PEGylées), y compris un maximum de 8 fois les doses requises pour les applications d'imagerie optique *in vivo* [37]. Pour cella, certains tests toxicologiques ont été réalisés 1 jour, 1 mois et 6 mois après l'administration des NPs.

Pour l'évaluation de la biodistribution des NPs *in vivo* dans les premières heures après l'injection, l'acquisition du signal de luminescence persistante a été réalisée immédiatement, 1 heure et 4 heures après l'injection de nanoparticules ZGO chez la souris saine (Figure A-2.5.1).
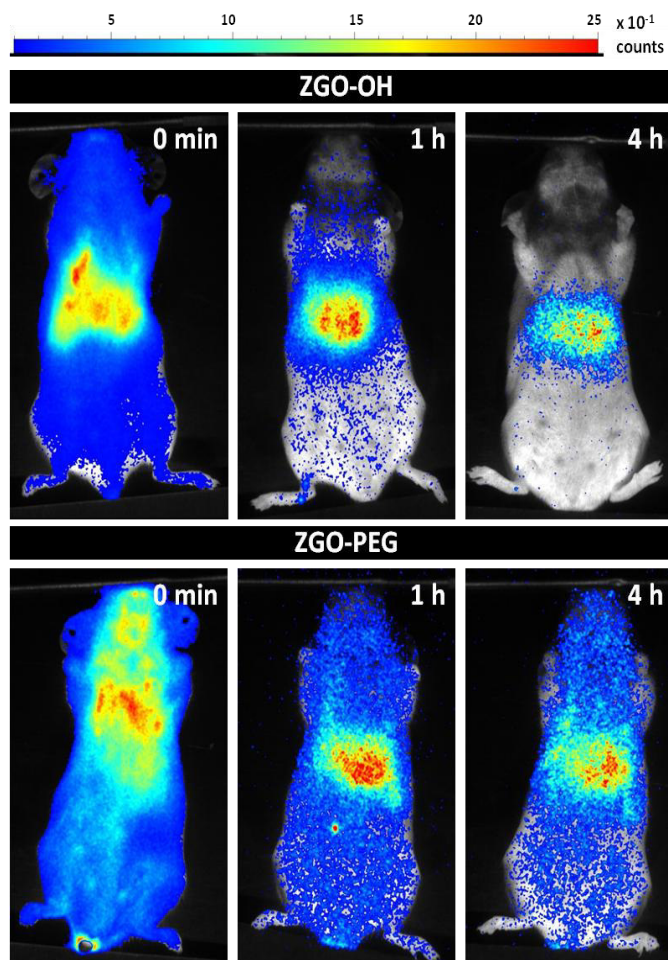
Fig. A-2.5. 1. Biodistribution des ZGO-NPs (ZGO-OH et ZGO-PEG) pré-exités lors de linjection intraveneuse de 2 mg/souri, et activation in situ après 1 heure et 4 heures. (1 unité= 2800 photons/s·cm^2·stéradians).

Les examens par imagerie optique ont montré que les ZGO-OH sont rapidement et essentiellement captés par les cellules du système réticulo-endothélial (RES) du foie et de la rate. Au contraire, les ZGO-PEG restent dans la circulation sanguine au moins 4 heures après l'injection. Le foie, qui est le principal organe chargé du métabolisme, semble jouer le rôle d'organe majeur cible pour les nanoparticules de ZGO après leur entrée dans le corps [37].

Les poids corporels ont été mesurés trois fois par semaine. Les fluctuations par rapport au contrôle n'étaient pas significatives après le traitement à diverses concentrations, seulement à une concentration très élevée de nanoparticules ZGO-OH (8 mg/souris), ce qui suggère des effets systémiques minimes. Les ZGO-PEG n'ont pas provoqué de variations de poids des animaux quelle que soit la quantité injectée (1-8 mg/souris).

La génération de peroxydes a été également étudiée pour révéler d'éventuels mécanismes de la mort cellulaire induite par l'exposition de ZGO-NP dans le foie, les poumons et la rate, qui correspondent aux organes présentant la teneur la plus élevée des nanoparticules. Le stress oxydatif

a été détecté uniquement dans les foies des souris traitées avec ZGO-OH et uniquement aux concentrations les plus élevées (4 et 8 mg/souris 24 heures après l'injection et 8 mg /souris 6 mois après l'injection). La production des peroxydes par les organes de souris traitées à des concentrations plus faibles de ZGO-OH, ainsi que les souris traitées avec des ZGO-PEG avec toute la gamme de doses ne sont pas affectés par la présence des nanoparticules.

L'accumulation de ZGO-OH et le stress oxydatif sont bien corrélés avec la perte de poids induite par ce type de nanoparticules. Les espèces réactives oxygénées (ROS) sont connues pour intervenir dans la mort cellulaire d'une grande variété de types cellulaires [389].

Les ZGO-NPs peuvent persister dans les tissus d'organes et interagir directement avec le milieu biologique. La dissolution des ZGO-NP peut conduire à la libération de Zn^{2+} dans les milieux vivants, lequel a prouvé sa capacité pour générer des espèces réactives de l'oxygène [390, 391]. Seulement les ZGO-OH ont stimulé la production de peroxyde par des cellules hépatiques, ce qui peut potentiellement causer des dommages au foie. Aucune rupture d'ADN dans des lymphocytes des souris traitées avec ZGO-OH ou ZGO-PEG n'a été montrée en utilisant le test des comètes.

En outre, les nanoparticules de ZGO-OH ont également produit l'augmentation du nombre de globules blancs, principalement des lymphocytes et des granulocytes après des traitements aigus et à long terme à des concentrations élevées. Cependant, les paramètres de la biométrie hématiques ne montrent aucune altération 30 jours après l'administration des ZGO-NP. D'autres paramètres de la biométrie hématique n'ont pas étés affectés par les nanoparticules. Les comptages de cellules ne sont pas affectés par l'administration de ZGO-PEG quelles que soient les doses injectées.

L'examen histopathologique des tissus a indiqué que l'administration intraveineuse de doses élevées de ZGO-OH peut induire des lésions pathologiques hépatiques pour une exposition à long terme. Pour les souris traitées avec des nanoparticules de ZGO-OH, de graves altérations au niveau cellulaire et histologique ont été observées dans le foie, c'est-à-dire des changements inflammatoires et la dilatation des veines centrales. Un pléomorphisme nucléaire marqué, une augmentation du volume des noyaux, la distribution anormale de la chromatine et des infiltrats lymphoïdes ont été observés dans des cellules hépatiques. Une relation dose-réponse pour la toxicité induite par les ZGO-NP a été mise en évidence dans cette étude. Cependant, comme on le voit au microscope, aucune anomalie histologique n'a été observée dans la rate, les poumons et les reins des souris traitées avec des nanoparticules de ZGO-OH. Aucun effet pathologique évident n'a été observé dans les organes de souris traitées avec des ZGO-PEG dans les mêmes conditions que pour ZGO-OH.

Selon la littérature, les nanoparticules de ZnO provoquent le stress du réticulum endoplasmique par la génération de ROS en raison de la surconcentration de Zn^{2+} [391]. Nos résultats peuvent indiquer que les ZGO-NPs peuvent activer la voie de stress du réticulum endoplasmique comme effet de la libération des ions Zn^{2+}. L'effet protecteur des molécules de polyéthylène glycol sur la surface des nanoparticules a également été démontrée à un niveau histopathologique, puisque seules des altérations négligeables ont été observés pour ZGO-PEG NPs

en comparaison avec les nanoparticules non modifiés de ZGO-OH, pour lesquelles des altérations sévères ont été observées, principalement en raison de l'incessante présence des nanoparticules dans la structure du foie.

Les sections d'ultra-microtome des principaux organes du système réticulum-endothéliale, le foie et la rate, ont été soigneusement analysées. Dans la Figure A-2.5.2, les résultats d'analyse par TEM indiquent que les nanoparticules de ZGO-OH à des concentrations très élevées (8 mg/souris) induisent des altérations du réticulum endoplasmique, mais aucun dégât n'a été détecté à des concentrations inférieures ou lors de l'utilisation des nanoparticules PEGylées. Les nanoparticules de ZGO-OH induisent le gonflement du réticulum endoplasmique et la dégranulation des ribosomes. Le gonflement du réticulum endoplasmique est associé au stress oxydant du réticulum endoplasmique [393]. Le stress du réticulum endothélial se réfère à un mécanisme d'auto protection cellulaire importante, qui peut être activé pour compenser les situations de stress induit par une surcharge de protéines dépliées ou proviennent directement des lésions du réticulum endoplasmique [393].
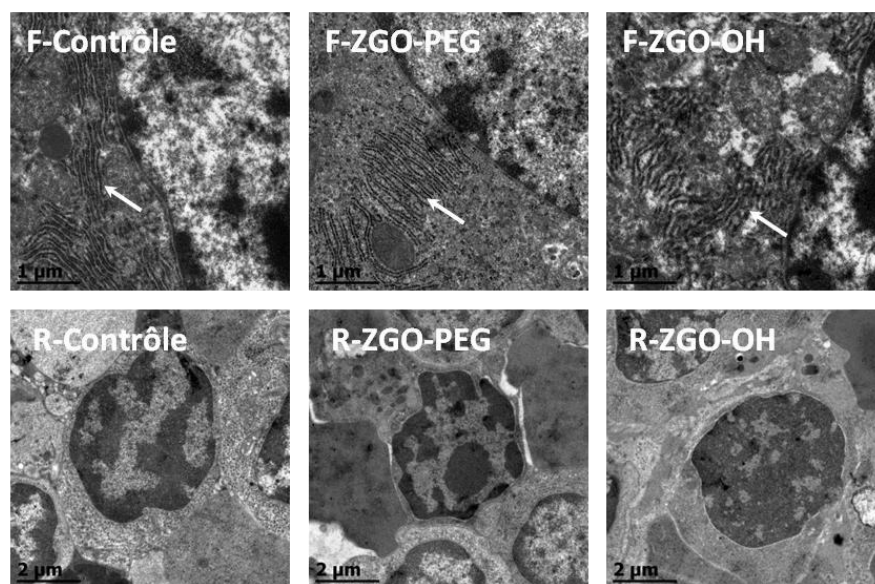
Fig. A-2.5. 2. Images de foie (F) et rate (R) des souris 6 mois après l'injection de ZGO-NP à des concentrations de 8 mg/souris. Les flèches dans les images signalent le réticulum endoplasmique.

D'ailleurs, aucune modification n'a été observée dans le noyau, la membrane nucléaire, les mitochondries, et les autres organites. De même, aucun dommage structurel n'a été observé dans toutes les structures de la rate. Seulement des concentrations très élevées de ZGO-OH (8 mg /souris) ont montré des effets toxiques notables chez la souris après l'exposition à long terme au niveau ultra-structurelle par la microscopie électronique à transmission. Aucun effet toxique n'a été détecté à des doses fonctionnelles de ZGO-NPs (<2 mg/souris) utilisés pour l'imagerie biologique. A titre d'exemple, une dose de 2 mg/souris de ZGO-PEG a été utilisée pour la détection passive des

tumeurs *in vivo* [33]. La fonctionnalisation de la surface joue un rôle déterminant sur les interactions *in vivo* avec des composants sanguins et des éléments cellulaires, et donc sur la toxicité des ZGO-NP. L'effet protecteur au niveau globale de la fonctionnalisation avec du PEG a été vérifié à nouveau dans cette étude.

A3. Conclusions

La caractérisation physico-chimique des nanoparticules est primordiale pour corréler leurs propriétés et prédire leur comportement *in vivo*. L'intérêt d'employer l'électrophorèse capillaire pour la caractérisation des nanoparticules a été démontré dans cette étude, ce qui permet une caractérisation très rapide et facile avec une quantité minimale de nanoparticules et des résultats fiables.

La caractérisation des nanoparticules à luminescence persistante de $ZnGa_{1.995}Cr_{0.005}O_4$ avec différents groupes fonctionnels sur leur surface a permis la vérification de l'efficace de la fonctionnalisation, afin d'optimiser les différentes étapes en termes de conditions de réaction et des procédures de lavage, ce qui aide fortement à l'identification des meilleures conditions pour la stabilité colloïdale.

Certains paramètres tels que la polydispersité, la taille et le potentiel zêta ont été déterminés dans différents tampons. Les propriétés des milieux de dispersion, par exemple la nature de la charge, le pH et la force ionique impactent sur les propriétés colloïdales des nanoparticules. La compréhension des effets de ces variables peut aider dans la formulation de nouveaux nanomatériaux, et dans le cas particulier des nanoparticules $ZnGa_{1.995}Cr_{0.005}O_4$, les résultats on été fondamentaux pour garantir la qualité des NPs pour les analyses postérieures.

Comme l'adsorption de biomolécules à la surface des nanoparticules lorsqu'elles sont injectées dans un fluide biologique leur donne une nouvelle identité et des nouvelles propriétés, nous avons considéré l'importance du développement des méthodologies innovantes pour l'analyse des interactions entre les nanoparticules et les protéines afin de caractériser plus finement la « couronne de protéines » (protéine corona). La méthode électrocinétique de Hummel-Dreyer a montré être suffisamment sensible pour détecter de petites variations dans les paramètres d'association pour l'adsorption des protéines sur des nanoparticules. Cette méthode ouvre les perspectives à une meilleure compréhension des interactions protéines/nanoparticules et pour une prédiction du comportement des nanoparticules dans les systèmes biologiques. Cela pourrait orienter les futures synthèses de nanoparticules et leur fonctionnalisation de surface pour la conception et l'amélioration des performances des nouveaux nanomatériaux dans divers domaines, conduisant à des nouveaux effets thérapeutiques.

On a également démontré l'application de l'électrophorèse capillaire pour comparer l'affinité des nanoparticules pour différentes protéines plasmatiques dans un mélange de deux protéines. La plus grande affinité des ZGO-PEG pour l'Apo-E par rapport à la HSA dans des modèles

d'interaction variés ouvre des perspectives pour l'analyse de la pré-formation d'une couronne d'apolipoprotéine-E autour des nanoparticules PEGylées au moyen d'une simple étape de pré-incubation, ce qui peut être exploité comme une stratégie pour la translocation des nanoparticules à travers de la barrière hémato-encéphalique. Même si la présence de seulement deux protéines est loin de la composition protéique réelle dans un échantillon physiologique, dans l'état actuel de la recherche dans lequel les interactions entre les nanoparticules et protéines individuelles sont normalement pris en compte, l'analyse des interactions dans un système binaire de protéines représente un grand progrès dans la simulation des conditions physiologiquement pertinentes.

La photo-stimulation des nanoparticules à luminescence persistante a joué un rôle important quant à leur toxicité sur des cellules en culture cellulaire. La production directe de superoxydes par des nanoparticules comme conséquence des effets photochimiques après la stimulation par la lumière UV et visible a été démontrée, et l'application comme un agent de thérapie photodynamique doit être évalué.

Un défi majeur dans le développement de nanosondes pour des applications biomédicales est de veiller à leur biocompatibilité, bioréactivité et leur stabilité *in vivo*. Un rôle déterminant de la fonctionnalisation des nanoparticules sur la toxicité a été mis en évidence par le biais des effets *in vivo* des nanoparticules de $ZnGa_{1.995}Cr_{0.005}O_4$ avec deux fonctionnalisations de surface, soit hydroxylées soit PEGylées Seules des concentrations très élevées de nanoparticules ZGO-OH ont produit des effets toxiques sur les souris. Par contre, l'effet protecteur de la fonctionnalisation de la surface avec de polyéthylène glycol a été démontré, même à des doses élevées. D'autres expériences complémentaires doivent être réalisées afin d'évaluer l'effet de ces nanoparticules à très long terme après l'administration, ainsi que de déterminer leur éventuelle biodégradation.

Ainsi, le développement de méthodologies adéquates pour prédire avec précision les effets des nanoparticules *in vivo* est encore un défi, et la connaissance des propriétés physico-chimiques des nanoparticules et de leurs interactions avec les protéines plasmatiques pourrait aider à mieux comprendre et mieux appréhender la formation de couronnes de protéines plasmatiques lorsque les nanosondes sont injectées in vivo. Ceci devrait permettre d'interpréter des données expérimentales et d'extraire des règles générales qui peuvent être appliquées à des études de conception, de modification de surface, de biocompatibilité et d'emploi de nouvelles nanoparticules manufacturées destinées à des applications biomédicales.